AES 2013

Advanced Electromagnetics Symposium

19-22 MARCH, SHARJAH - UAE

ISBN: 978-2-9545460-1-8

Proceedings of AES 2013

The 2nd Advanced Electromagnetics Symposium

ISBN: 978-2-9545460-1-8

March 19 – 22, 2013
Sharjah, United Arab Emirates

www.mysymposia.org

Proceedings of AES 2013

The 2nd Advanced Electromagnetics Symposium

ISBN: 978-2-9545460-1-8

Edited by

Said Zouhdi | Paris-Sud University, France
Hamid Al-Naimiy | University of Sharjah, United Arab Emirates

AES 2013 ORGANIZATION

AES 2013 General Chair

Said Zouhdi, Paris Sud University, France

AES 2013 General Co-Chairs

Hamid Al-Naimiy, University of Sharjah, UAE
Raj Mittra, Pennsylvania State University, USA

Organizing Committee

Hussein M. Elmehdi (Chair), UAE
Laurent Santandrea (Co-Chair), France

Nadjib Brahimi, UAE
Ihsan Shehadah, UAE
AbdulKadir Hamid, UAE
Muhammad Bawa'aneh, UAE
Omar Adwan, UAE
Rafea Haffa, UAE
Kifah Taqez, UAE
Khadijah Al Housani, UAE
Ghada Amer, UAE
Romain Corcolle, France
Mohamed Ahachad, Morocco
Mounia Ajdour, Morocco

International Advisory Committee

M. Al-Harthi, Saudi Arabia
H. M. K. Al-Naimiy, UAE
Y. Antar, Canada
P. Banerjee, India
A. Bossavit, France
M. Chandra, Germany
J. Chazelas, France
C. Christopoulos, UK
A. G. D'Assuncao, Brazil
P. de Maagt, Netherlands
V. Fouad Hanna, France
A. Georgiadis, Spain
Y. Hao, UK
N. Ida, USA
K. Ito, Japan
A. Karwowski, Poland
A. Kladas, Greece
K. Langenberg, Germany
E. Li, China
L.-W. Li, China
K. M. Luk, Hong Kong
J. Mao, China
C. Marchand, France
M. Ney, France
A. Razek, France
A. Sibille, France
A. Sihvola, Finland
P. Smith, Australia
G. Uhlmann, France
J. C. Vardaxoglou, UK

Technical Program Committee

X. Begaud (Chair), France
A. Alu, USA
S. E. Barbin, Brazil
M. S. Bawa'aneh, UAE
P. Coquet, France
C. Craeye, Belgium
T. J. Cui, China
R. Dkiouak, Morocco
H. M. Elmehdi, UAE
S. Gonzalez Garcia, Spain
J. Hu, China
T. Isernia, Italy
A. Khenchaf, France
K. Kitayama, Japan
A. Kishk, Canada
M Kuzuoglu, Turkey
J.-M. Lopez, France
A. Massa, Italy
N. Merabtine, Saudi Arabia
H. Ouslimani, France
O. Ozgun, Turkey
E. Pottier, France
C.-W. Qiu, Singapore
A. Raizer, Brazil
A. Shamim, Saudi Arabia
J.T. Sri Sumantyo, Japan
R. Staraj, France
G. Stojanovic, Serbia Montenegro
H. Süß, Germany
M. Tentzeris, USA
M. Tlidi, Belgium
N. Vallestero, USA
V. Y. Vu, Vietnam
T.-L. Wu, Taiwan
W.-Y. YIN,China
A. I. Zaghloul, USA

Special Session Organizers

Dave V. Giri, USA
Atif Shamim, Saudi Arabia
Mohammad S. Sharawi, Saudi Arabia

SPONSORS AND SUPPORTERS

We wish to thank the following organizations for their contribution to the success of this conference:

University of Sharjah, UAE
LGEP-SUPELEC, France
Paris-Sud University, France
Institut Français, UAE
Office of Naval Research Global, UK
IOP Publishing, UK
EPL, UK
CST-ME , Egypt
IEEE-APS, USA
URSI, Belgium

AES 2013 VENUE

AES 2013 will be held on March 19-22, 2013, at the University of Sharjah, Sharjah, United Arab Emirates.

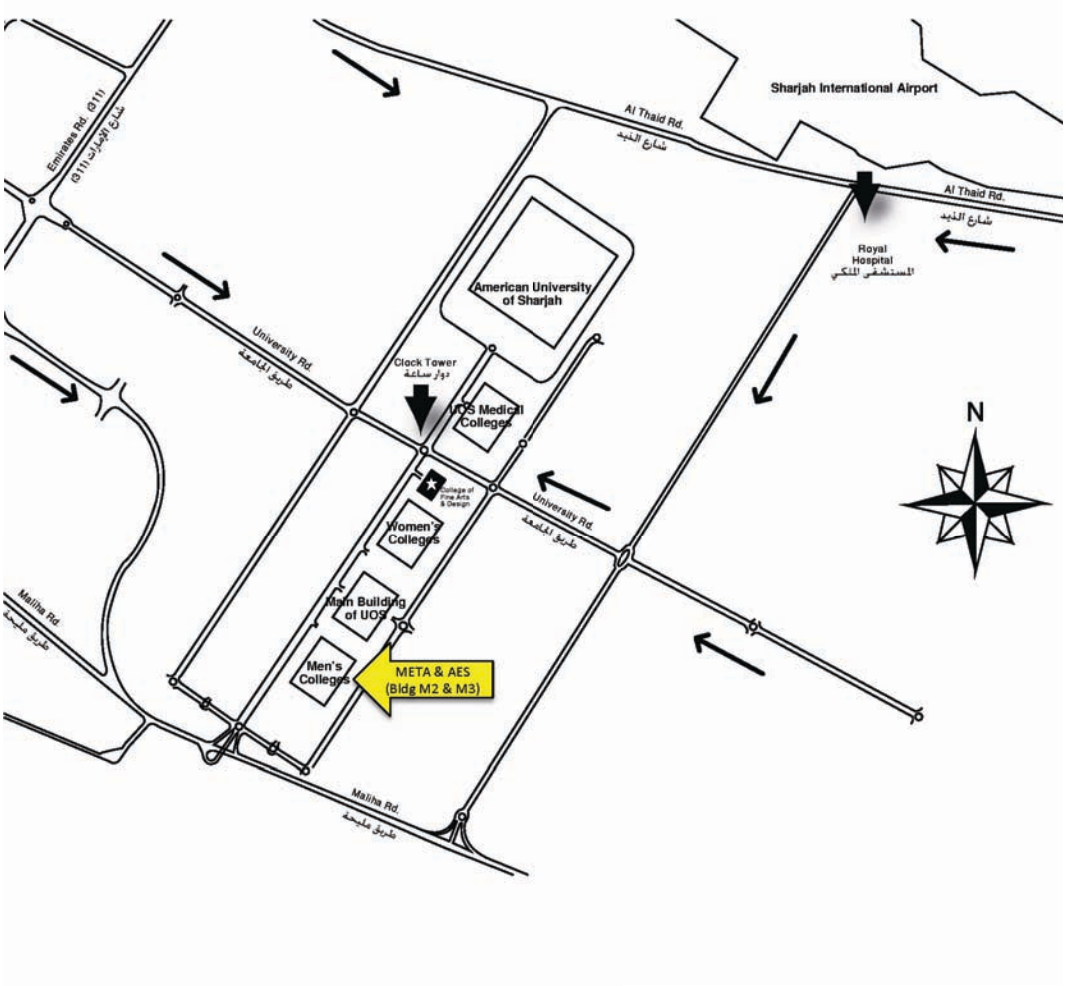

GUIDELINES FOR PRESENTERS

Oral Presentations

Each session room is equipped with a stationary computer connected to a LCD projector. Presenters must load their presentation files in advance onto the session computer. Technician personnel will be available to assist you.

Scheduled time slots for presentation are 20 mn for regular and invited prensentations, 45 mn for plenary talks, and 30 mn for keynote talks, including questions and discussions. Presenters are required to report to their session

room and to their session Chair at least 15 minutes prior to the start of their session.

The session chair must be present in the session room at least 15 minutes before the start of the session and must strictly observe the starting time and time limit of each paper.

Poster Presentations

Presenters are requested to stand by their posters during their session. One panel will be available for each poster. Pins or thumbtacks are provided to mount your posters on the board. All presenters are required to mount their papers one hour before the session and remove them at the end of their sessions.

TABLE OF CONTENTS

General Papers

Electromagnetic theory

Numerical methods

computational techniques applied to EM field problems

Radiation; Propagation and Diffraction

Scattering and inverse scattering

Electromagnetic compatibility (EMc)

Antenna theory and applications

Mobile antennas; Smart skin antennas

RF and wireless communication

Microwave and millimeter wave circuits and devices

Optics and photonics

Nanophotonics; THz technology

Experimental characterization techniques

Optical communications

Bioeffects of EM fields

Medical electromagnetics

Biological media; composite media; Random & structured materials

Advanced electromagnetic materials: Metamaterials; Plasmonics; Photonic crystals; chiral and Bianisotropic media

Wearable and Flexible Antennas, By A. Shamim

Electroactive and magnetoactive materials

Active materials and Structures, by L. Daniel & Y. Bernard

Printed MiMO Antenna implementations and challenges, by M. S. Sharawi

General Papers

A feasibility study for solar power plant to provide a domestic energy required for the citizens live in arid area

M.F.A.Alias *
Department of Physics, College of Science, University of Baghdad
P.O.Box. 47162, Jadiriya, Baghdad, Iraq
A. A.J. Al-Douri
Department of Applied Physics, College of Sciences,
University of Sharjah, sharjah ,UAE

Abstract

In the design and implementation of any system it is important to understand and appreciate the requirements for that system regarding performance, appearance and overall integration.

Photovoltaic systems are especially well suited to locations where accessing an electrical grid is either not feasible or expensive. In many such locations, photovoltaic technology is the least-cost option for meeting remote energy needs. Beside the fact that photovoltaic has proven to be a reliable source of power in an ever-growing number of applications.

The central fact that this photovoltaic system is an educational tool motivated many of the additional features, such as climatic monitoring, power output vs. building usage comparisons and of course overall system efficiency calculations.

In this paper a comprehensive study has been made to evaluate the feasibility of using PV generators, for peoples live in arid area that is located quite far distance - more than 30 km - away from the electricity grid terminals of Sharjah province at UAE.

The evaluation is made on the basis of comparing the cost of electrification alternatives consisting of: stand-alone PV system, diesel generator, and extension of the utility grid.

Pumping is one common use for these systems for purpose of agriculture and irrigation applications. For this purpose the pumping system designs were put according to the water demand requirement of the farm. A hydro storage technique has been recommended for the PV water lifting system, while storage batteries technique was also considered for the irrigation PV system.

In addition to total vertical lift, the design was carefully considering the effect of total horizontal run, water flow velocity, effects of pipeline size and fittings on total friction loss.

The current study also, taking into account the effect of solar cells temperature rise and the inclination angle of the solar cell on the peak power of the PV array throughout the year, along with the meteorological data of the site area.

The preliminary calculation and analysis of the performance of system operation showed encouraged results for using PV system in this kind of application and circumstance .It was also found out that distance from the national grid is the most crucial parameter to determining the most economical alternative taken in present study.

Keywords: *A feasibility study, PV-Pumping system, Utility grid, Energy in arid area.*

*Corresponding author. E-mail : **may_roza@yahoo.com**

Digital Holography- Step Towards Commercial 3D Displays.

***Salman Saeed Khan, Abdul Ahad Shams, Muhammad Sharjeel Javaid, Muhammad Ahsan Farooqui, Schazil Najam.**

*corresponding author: u2009245@giki.edu.pk

(Note: All authors have equal contribution)

Abstract-Holography unlike photography contains complete information of visual data, including both intensity and phase information. Various techniques are used to digitally imitate holography. This paper aims to artificially generate half parallax auto stereoscopic images. Fourier optics techniques are implemented to compute hologram pattern of given image. This paper presents algorithms and mathematical theory behind generation of diffraction pattern for the binary holograms. The algorithms are implemented on MATLAB™ and results obtained using He-Ne Laser as coherent light source are included.

Introduction:

Ever since the introduction of Holography by Dennis Gabor (1948) [1], the field has been explored in great detail. Subsequently Lohmann (1967) [2] presented the idea of generating holographic patterns with the aid of digital algorithms, thus setting the framework for computer generated holography (CGH). The evolution of three dimensional displays has once again invoked an interest in producing Holographic Visual displays at a commercial level. While the commercial 3d displays in the market offer only illusion of depth in image, holography has a promise for producing auto stereoscopic parallax visual displays, thus producing 3d generated visual images in the true sense of the word. Moreover CGH also has the promise for generating computer simulated images such as computer aided design (CAD).

Holograms include both the phase and intensity of the data, because of which it contains 3 dimensional information of the visual scene. Computer generated holography aims to imitate classical holography in digital domain. In classical holography it is only possible to generate 3D picture of objects with physical significance whereas computer generated holography we can generate holograms of artificial images.

The primary aim of the paper is to optimize the resolution and the computational time exploring different algorithms so as to successfully develop digital holograms at a commercial scale.

Fourier Holograms

In the first step towards computer generated holography a binary hologram of a 2 dimensional black and white image is computed using light field distribution [3]. In this algorithm each black pixel in image is modeled as a small aperture, which diffracts light passing through it. The region of observation of diffraction pattern is close to the object, therefore the diffraction is modeled as Fresnel diffraction. The light field distribution maps each pixel on the image to a hologram plane.

Mathematically the light field distribution can be expressed as:

$$H(x,y) = \sum_{k=1}^{N} A(k) exp(i2\pi r) \qquad (1.1)$$

Where 'N' denotes the total number of pixels in the image, 'A(k)' denotes the intensity of each pixel in image which is either one or zero (white-zero and black-one). 'r' is the distance between the k^{th} image pixel on the object plane and the pixel with coordinates (x,y) in hologram plane. The limitation of the algorithm is that image should be binary and the wavelength of coherent light source must be known beforehand. The basics behind the implemented equation (1.1) is the Fresnel diffraction. The electric field diffraction pattern at a point (x,y,z) is given by:

$$E(x,y) = \left(\frac{z}{j\lambda}\right) \iint_{\infty}^{\infty} E(x',y',0) \frac{e^{ikr}}{r^2} dx'dy' \qquad (1.2)$$

, where, $E(x', y', 0)$is the aperture. More formally r =$\sqrt{(x-x')^2+(y-y')^2+z^2}$ and z is the shortest distance between the object and image plane.

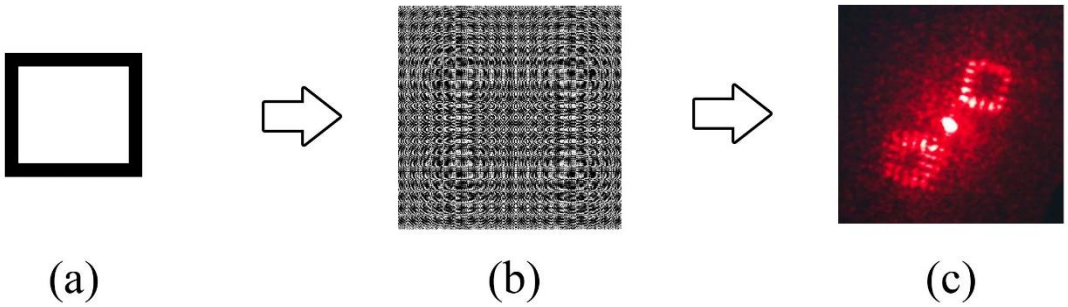

Figure 1 Practical results (Diagram not to scale)

Figure-1 shows the results of implementation of the aforementioned algorithm. Figure-1(a) is the input black and white image (object) of 12x11 pixels. Figure-1(b) shows the output hologram of size 600x600 pixels. The print of the diffraction pattern (Figure-1(b)) on transparency from a 600dpi (dots per inch) printer is used to reconstruct the image using a He-Ne laser (Figure-1(c)).

An additional algorithm to generate 2 dimensional holograms is obtained by taking two dimensional Fourier transform of image followed by incorporation of phase and amplitude information of the Fourier transform using detour phase algorithm [4]. To generate hologram each pixel of two dimensional Fourier transform is mapped to a larger cell in which a rectangular block is expanded or shifted on the basis of value of magnitude and phase of the Fourier transform of that pixel.

The size of each opening in a cell represents the magnitude of the Fourier transform, whereas the location of the opening within the cell signifies the phase. The size and location of this aperture is divided into discrete steps which define the spatial degree of freedom. The more freedom a cell has, the more refined hologram is reconstructed. The arrangement of the aperture in each cell is dependent on the wavelength of coherent light used for the reconstruction of the hologram. If 'λ' is the wavelength of coherent light used, and the spatial shift of aperture is 'Δε' then the associated phase shift of complex number will be '$(2\pi\Delta\varepsilon\cos\phi)/\lambda$'. Now reconstruction will occur at an angle of 'ϕ' to the optical axis of system, perpendicular to the hologram plane. This scheme of arrangement is implemented in detour phase method.

The focus of the research has been divided into three parallel paths. (a) To cascade a series of Fourier holograms such as to generate auto stereoscopic parallax holograms; (b) To optimize the algorithm for the mapping of image (or a series of images for producing a parallax reconstruction) so as to increase the computational efficiency; (c) To produce high resolution holograms. The aim of the research group is to find the optimum tradeoff between the three so as to produce high resolution hologram on a commercial scale

REFERENCES

1. Dennis Gabor [1971], Nobel prize for development of the holographic method
2. B.R. Brown and A.W. Lohmann (1969). "Computer-generated Binary Holograms". IBM Journal of Research and Development (IBM) 13: 160–168.
3. James B Wendt, "Computer Generated Holography", Bachelor thesis. Department of Physics Pomona College
4. Joseph W. Goodman "Introduction to Fourier Optics.2nded." The McGraw Hill Company, Singapore; 1996.

Trajectories of the lines equipotentielles for some profiles of magnetic poles

C. Farsi[1] , M. Zaoui[2]
Department of Mechanical Engineering, University of M'sila, 28000, M'sila, Algeria
cfarsi2000fr@yahoo.fr

Abstract:

The frequent use of the magnetic field in all industrial fields, and sought extensive especially on the increase of its gradient. The characteristics of the magnetic field are very important in magnetic separation of materials of low magnetic susceptibilities. This method is a method of filtration materials ground mixtures with water through layers of body magnet. The difficulty of the weakly magnetic particles from those non-magnetic separation is the distribution of the magnetic field, and the smoothness of their class to separate. This work is a comparison of some matrices of different forms of poles. magnetic. Following the distribution of the field was inside the space of separation, we have is the values of the magnetic induction, and then calculate the gradient of the field maximum point between the poles of separations.

Summary: Obtaining and the choice of new profiles of magnetic poles will enable the improvement of gradient no-homogeneous magnetic fields. Selected final forms were experimentally compared with those currently used worldwide the separator of John's and those of the French F.K.B. company matrices The advantage of this study is the possibility of opening the flocculate of the magnetic fraction for a good separation of the weakly magnetic products. Through the openings between the magnetic particles, the quality of the product extracted after the washing process is better and cleaner. The matrisse by a set of forms flat and sharp teeth is the result of several experiments have led us metritis and organize the final shapes and then have measured the magnetic field intensity of several points between its poles. As shown in the tables of measuring the intensity of the magnetic field; the force of the magnetic field Gradient h., the General Law on these forms is characterized by magnetic forces at the top of the matrix that are not optimal since it is ' a large concentrations of field.But for the lateral parts of teeth, field lines out of the bottom surfaces where the remaining empty space devoid of flocules magnetic separation. It is for this reason that the gradient: a decrease quickly in go down of teeth and the surface of the field distribution to reduce For the creation of good conditions of maximum values of the magnetic force H Grad get. H, must be used for profiles a matrix or the groups of convex teeth are faces of those concave, as the combination of sharp and flat teeth. In this way we obtain both convex and concave face to face of each pole or it is necessary that the axis of symmetry of convexity of one of the poles is confused with the bisector of the angle of the concavity of the other pole. For the improvement of the technology of preparations of these forms it is sufficient only to take the Summit in triangular form and the other teeth on the side map of flat shapes That of mathematical modelling with programs for the different possible forms of equipotential lines is the essential method of the optimal shape of magnetic nuclei a rapid demagnetization. The analysis of existing matrices pole forms shows us that narrow the focus of the field is located at the top of teeth.

REFERENCES

- Amikam Aharoni (2000). Introduction to the theory of ferromagnetism (2 ed.). Oxford University Press. p. 27.

- M Brian Maple et al. (2008). "Unconventional superconductivity in novel materials". In K. H. Bennemann, John B. Ketterson. Superconductivity. Springer. p. 640.
- Naoum Karchev (2003). "Itinerant ferromagnetism and superconductivity". In Paul S. Lewis, D. Di (CON) Castro. Superconductivity research at the leading edge. Nova Publishers. p. 169.
- C. Doran and A. Lasenby (2003) Geometric Algebra for Physicists, Cambridge University Press, p.233
- For a good qualitative introduction see: Feynman, Richard (2006). QED: the strange theory of light and matter. Princeton University Press.
- Serway, Raymond A.; Chris Vuille, Jerry S. Faughn (2009). College physics (8th ed.). Belmont, CA: Brooks/Cole, Cengage Learning. p. 628. ISBN 978-0-495-38693-3.

The Impact of Intelaminar Defects on The Characteristics of Piezoelectric Transducers

Waleed Ahmed[1]
[1] *United Arab Emirates University, Faculty of Engineering, EUR, Al Ain, UAE, w.ahmed@uaeu.ac.ae*

Abstract: In recent years, a rapid progress has been made in developing advanced materials with optical, mechanical and electromagnetic properties to meet the escalating demand in engineering applications. A piezoelectric material is considered as one of the advanced material that has been broadly used to produce an electrical charge from an applied mechanical force, and a mechanical force from an applied electrical field. In general, the characteristics of piezoelectric materials have made them particularly attractive for use in sensors, actuators, etc. In the present analysis interlaminar defect is proposed in piezoelectric beam to investigate its impact on the mechanical behavior. The beam is constructed of two layers loaded by opposite electric potentials which cause the beam to bend. Finite element technique is adopted through using two dimensional modeling. The defective zone is modeled as through thickness surface with different lengths along the beam.

Electromagnetic theory

Electromagnetic field in matter

M. Apostol[1,2,*], **L. Cune**[1], **S. Ilie**[2,3], **A. Petrut**[3], **M. Savu**[b], **and S. Toba**[3]

[1]Department of Theoretical Physics, Institute of Atomic Physics, Magurele-Bucharest MG-6, POBox MG-35, Romania

[2]MiraTechnologies Ltd, Teiul Doamnei 2, Bucharest

[3]MiraTelecom, Grigorescu 13, 075100 Otopeni-Bucharest

*corresponding author: apoma@theory.nipne.ro

Abstract— The polarization and magnetization degrees of freedom are included in the general treatment of the electromagnetic field in matter, and their governing equations are given. Particular cases of solutions are presented for polarizable, non-magnetic matter, including propagation, zero-point fluctuations of the eigenmodes, scattering by inhomogeneities or rough surfaces, plasmon transfer between nano-structures, etc.

With usual notations the Maxwell equations in matter read

$$div\mathbf{D} = 4\pi\rho_0 \ , \ div\mathbf{B} = 0 \ ,$$
$$curl\mathbf{E} = -\frac{1}{c}\frac{\partial\mathbf{B}}{\partial t} \ , \ curl\mathbf{H} = \frac{1}{c}\frac{\partial\mathbf{D}}{\partial t} + \frac{4\pi}{c}\mathbf{j}_0 \ , \tag{1}$$

where $\mathbf{E}$ is the electric field, $\mathbf{D}$ is the electric displacement, $\mathbf{B}$ is the magnetic induction and $\mathbf{H}$ is the magnetic field; ρ_0 is the external charge density and $\mathbf{j}_0$ is the external current density (obeying the continuity equation $\partial\rho_0/\partial t + div\mathbf{j}_0 = 0$). We have two independent Maxwell equations (1) (Faraday's and Maxwell-Ampere's equations) and four unknowns. In order to have a solution we introduce the quasi-phenomenological dielectric function ε and magnetic permeability μ, usually for the Fourier transforms. Apart from being unsatisfactory at the fundamental level, this procedure produce appreciable difficulties, especially with the finite size bodies.

Matter is polarizable, *i.e.* it consists of more-or-less mobile charges q, with mass m and concentration n (*e.g.*, electrons), which move against a neutralizing background of quasi-rigid charges $-q$ (*e.g.*, ions). A small displacement field $\mathbf{u}(t,\mathbf{r})$, which is a function of the time t and position $\mathbf{r}$, generates an imbalance $\delta n = -ndiv\mathbf{u}$ in the density of these charges, a charge density $\rho = -nqdiv\mathbf{u}$ and a corresponding current density $\mathbf{j} = nq\dot{\mathbf{u}}$. It is easy to see that the polarization is $\mathbf{P} = nq\mathbf{u}$ (density of the dipole moments) and the electric displacement is now represented as $\mathbf{D} = \mathbf{E} + 4\pi\mathbf{P}$. The displacement field obeys an equation of motion, which usually is Newton's equation

$$m\ddot{\mathbf{u}} = q\mathbf{E} - m\omega_c^2\mathbf{u} - m\gamma\dot{\mathbf{u}} \ ; \tag{2}$$

ω_c is a characteristic fequency (*e.g.*, for bound charges) and γ is a small damping coefficient. The magnetic term of the Lorentz force is usually absent in equation (2) (and the equation is non-relativistic), since the velocity of charges in matter is small, on one hand, and, on the other, the displacement $\mathbf{u}$ is sufficiently small to limit ourselves to linear terms only. This is the well-known Drude-Lorentz (plasma) model of polarizable matter. The point is that the equation of motion (2) provides a third equation for the four unknowns: $\mathbf{E}$, $\mathbf{u}$, $\mathbf{B}$ and $\mathbf{H}$

Matter is also magnetizable. The continuity equation allows for a "magnetic" current $\mathbf{j} = c\cdot curl\mathbf{M}$; as it is well-known the magnetization $\mathbf{M}$ obeys the equation of motion of the angular momentum

$$\frac{d\mathbf{M}}{dt} = \frac{q}{2mc}\mathbf{M}\times\mathbf{B} \ . \tag{3}$$

The magnetic induction is now represented as $\mathbf{B} = \mathbf{H} + 4\pi M$. We have now four equations:

$$curl\mathbf{E} = -\frac{1}{c}\frac{\partial\mathbf{B}}{\partial t} \ , \ curl\mathbf{H} = curl(\mathbf{B} - 4\pi\mathbf{M}) = \frac{1}{c}\frac{\partial\mathbf{E}}{\partial t} + \frac{4\pi}{c}nq\dot{\mathbf{u}} + \frac{4\pi}{c}\mathbf{j}_0 \tag{4}$$

and equations (2) and (3) and four unknowns: $\mathbf{E}$, $\mathbf{u}$, $\mathbf{B}$ and $\mathbf{M}$. These equations can provide the basis for treating the electromagnetic field on matter. Except for the important case of ferromagnetic (and related) matter, the usual matter is non-magnetic, so we may leave aside $\mathbf{M}$ and put $\mathbf{B} = \mathbf{H}$.

For the usual case of polarizable non-magnetic matter, we can find the plasmon and polariton eigenmodes, especially for infinite or semi-infinite (half-space) matter.[1, 2] We can thereby describe the propagation of electromagnetic field in matter, as well as the interaction of the electromagnetic field with finite-size bodies, both in the near-field (sub-wavelength, quasi-static) regime and the wave (radiation) zone. This can be done in complex situations, wher various fields are present for bodies with various shapes, a subject of high interest for nano-plasmonics. The plasmon and, respectively polariton eigenmodes are given by

$$\Omega_1 = \omega_L = \sqrt{\omega_c^2 + \omega_p^2}\ ,\ \Omega_2(K) \simeq \sqrt{\omega_L^2 + c^2K^2}\ ,\ \Omega_3(K) \simeq \omega_c cK/(\omega_L + cK)\ , \tag{5}$$

where $\omega_p = (4\pi nq^2/m)^{1/2}$ is the plasma wavevector and $\mathbf{K}$ is the wavevector. For a half-space we get a surface plasmon-polariton mode

$$\Omega^2 = \frac{2(2\omega_c^2 + \omega_p^2)c^2k^2}{\omega_c^2 + \omega_p^2 + 2c^2k^2 + \sqrt{(\omega_c^2 + \omega_p^2 + 2c^2k^2)^2 - 4(2\omega_c^2 + \omega_p^2)c^2k^2}} \tag{6}$$

for $c^2k^2 > \omega_c^2$, where $\mathbf{k}$ is the wavevector parallel with the surface; it goes from ω_c ($ck = \omega_c$) to $\sqrt{\omega_c^2 + \omega_p^2/2}$ ($k \to \infty$). This mode is localized with respect to the direction perpendicular to the surface.

The zero-point energy (vacuum fluctuations) of the polarization eigenmodes leads to molecular forces like van der Waals-London-Casimir forces acting between macroscopic bodies.[4] The behaviour of the polarization eigenmodes in non-inertial motions may lead to interesting new effects.[5] The electromagnetic coupling between nano-structures can also be treated by this method, leading to plasmon transfer and resonances, or to electromagnetic forces with a resonant character.[6] The scattering of the electromagnetic waves by small particles or inhomogeneities, including the rough surface of a semi-infinite solid,[7] is also amenable to such a treatment.

ACKNOWLEDGMENT

The authors are indebted to the members of the Seminar of the Institute of Atomic Physics and the Laboratory of Theoretical Physics, Magurele, Bucharest, for useful discussions and a careful reading of the manuscript. This work was supported by the Romanian Government Research Agency Grant #306/SMIS 26614.

REFERENCES

1. M. Apostol and G. Vaman, "Electromagnetic field interacting with a semi-infinite plasma," J. Opt. Soc. Am. A, Vol. 26, 1747-1753, 2009.
2. M. Apostol and G. Vaman, "Reflection and refraction of the electromagnetic field in a semi-infinite plasma," Opt. Commun., Vol. 282, 4329-4332, 2009.
3. M. Apsotol and G. Vaman, "Plasmons and diffraction of an electromagentic palne wave by a metalli sphere," Progr. Electrom., Res. (PIER), Vol. 98, 97-118, 2009.
4. M. Apostol, "On the molecular forces acting between macroscopic bodies," Physica B, Vol. 40, 57-62, 2013.
5. M. Apostol, "Non-inertial electromagnetic effects in matter. Gyromagnetic effect," Solid State Commun., Vol. 152, 1567-1571, 2012.
6. M. Apostol, S. Ilie, A. Petrut, M. Savu and Stefan Toba, "A generalization of the dipolar force," J. Appl. Phys. Vol. 12, 024905, 2012.
7. B. F. Apostol, "Scattering of the electromagnetic waves from a rough surface," J. Mod. Phys., Vol. 59, 1607-1616, 2012.

Near Fields for a Circular Loop Antenna above a Ground Plane

S. M. Ali Hamed[1*], **S. O. Bashir**[2]
[1]Nile Valley University, Sudan
[2]International Islamic University of Malaysia, Malaysia
[*]corresponding author: alihamed66@hotmail.com

Abstract- An exact electromagnetic near field expressions of a circular loop antenna over a ground plane are presented in this paper. The technique is based on the spherical Bessel functions and associated Legendre polynomials expansion.

The problem of radiation from circular loop antennas finds a considerable attention for its significance in geophysical probing, the problem of interaction between a loop antenna and a biological tissue, and RFID applications. A comprehensive results of researches on characteristics of a perfectly conducting thin-wire circular loop antenna are well documented by many researchers, e.g., [1 - 2]. The problem of near and far electromagnetic fields radiated from an isolated circular loop antenna, is investigated using various analytical and numerical techniques [3 - 5]. Recently, a technique that is based on the spherical functions expansions has been introduced to obtain general electromagnetic fields expressions for the circular loop antenna of arbitrary current distribution [6].

In this paper the work presented in [6] is extended to obtain the general electromagnetic field components, in near and far regions for a circular loop antenna over an infinite ground plane shown in Fig. 1a, and further to drive a simple and exact magnetic field expressions on the axis of the loop. The image theory is applied with the technique that is presented in [6].

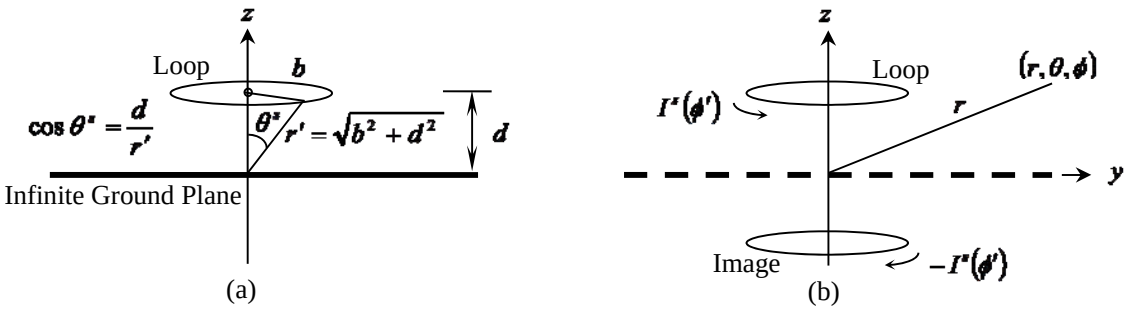

Fig. 1: Geometry of the problem. (a) Original problem. (b) Equivalent problem

Using the image theory the problem of the loop over the ground plane can be replaced by an equivalent problem of loop with its image as shown in Fig, 1b. The current on the loop over ground plane can be written as [7]

$$I^s(\phi') = \sum_{n=-\infty}^{\infty} I_n e^{jn\phi'} = \sum_{n=-\infty}^{\infty} \frac{V_0}{Z_n^{ss} - Z_n^{si}} e^{jn\phi'} \qquad (1)$$

Where Z_n^{ss} and Z_n^{si} are available as closed form expressions [7] and V_0 is the delta generator voltage of the loop. The current of the image is $I^i = -I^s$. Electromagnetic fields H and E radiated from the loop/ground plane problem at any point in the space above the ground can be obtained by superimposing the fields from the loop (H^s, E^s) and its image (H^i, E^i). By expressing the Green's function exp(-jβR)/R in terms of spherical Bessel functions and associated Legendre polynomials and following the technique presented in [6] exact electromagnetic fields components radiated from the loop/image can be obtained. With $\theta = 0$ and replacing the associated Legendre functions by their

equivalent Gegenbauer polynomials, expressions for total magnetic fields on the axis of the loop can be obtained using $H_q = H_q^s + H_q^i$, (q = *r*, θ, or ϕ) as

$$H_r = -j\frac{2\beta b}{r} I_0 \sum_{m=1}^{\infty} \frac{(2m+1)}{m(m+1)} C_{m-1}^{\frac{3}{2}}(1) C_{m-1}^{\frac{3}{2}}(\cos\theta^s) \begin{cases} j_m(\beta r') h_m^{(2)}(\beta r), & r > r' \\ h_m^{(2)}(\beta r') j_m(\beta r), & r < r' \end{cases} \quad (2)$$

$$H_\theta = j\frac{\beta b}{r} I_1 \cos\phi \sum_{m=0}^{\infty} (2m+1) C_m^{\frac{1}{2}}(1) C_m^{\frac{1}{2}}(\cos\theta^s) \begin{cases} j_m(\beta r')\left[\beta r h_{m-1}^{(2)}(\beta r) - (m+1) h_m^{(2)}(\beta r)\right], & r > r' \\ h_m^{(2)}(\beta r')\left[\beta r j_{m-1}(\beta r) - (m+1) j_m(\beta r)\right], & r < r' \end{cases} \quad (3)$$

$$H_\phi = -j\frac{\beta b}{r} I_1 \sin\phi \sum_{m=0}^{\infty} (2m+1) C_m^{\frac{1}{2}}(1) C_m^{\frac{1}{2}}(\cos\theta^s) \begin{cases} j_m(\beta r')\left[\beta r h_{m-1}^{(2)}(\beta r) - m h_m^{(2)}(\beta r)\right], & r > r' \\ h_m^{(2)}(\beta r')\left[\beta r j_{m-1}(\beta r) - m j_m(\beta r)\right], & r < r' \end{cases} \quad (4)$$

$C_m^{\alpha}(u)$ is the Gegenbauer polynomials. It is clear that the axial fields in (2) - (4) for loop/ground plane problem under study are depend only on modes ($n = 0, 1$) of the current given in (1). Figure 2 shows the magnetic field components on the axis of a resonant loop above a ground plane as a function of *r/b* with the height of the loop as a parameter. The values around singular points $r = r'$ are omitted from graphs.

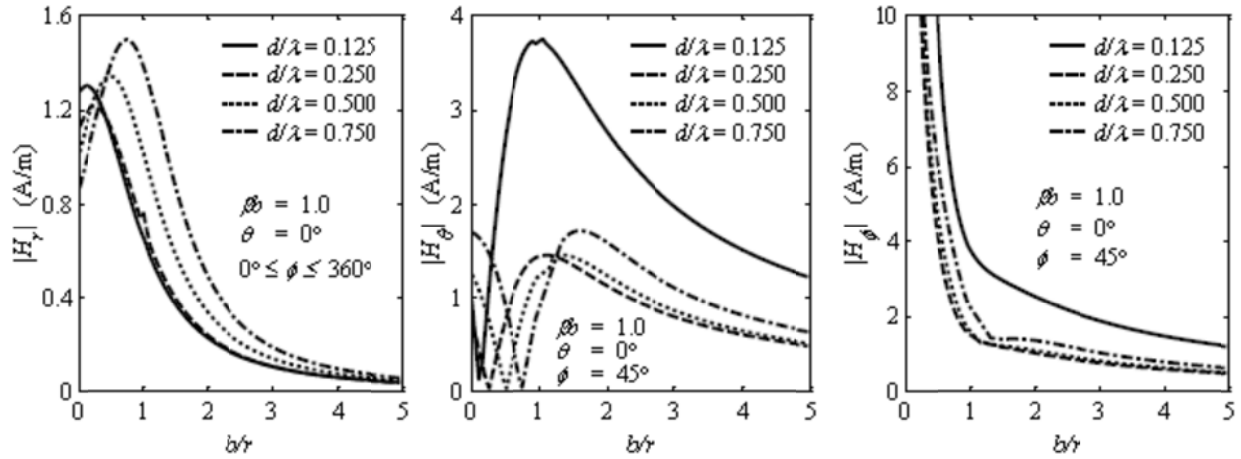

Fig. 2. Magnitude of axial magnetic fields components radiated from a circular loop above a ground plane.

REFERENCES

1. G. S. Smith, "loop antennas," in *Antenna Engineering Handbook*, R. C. Johnson and H. Jasik, Eds. New York: McGraw-Hill 2007, ch. 5.
2. Balanis, C. A. *Antenna Theory, Analysis, and Design*, New York: Harper and Row, 1982, ch. 5.
3. Overfelt, P. L. "Near fields of the constant current thin circular loop Antenna of arbitrary radius," *IEEE Trans. Antennas Propagat.*, Vol. AP-44, No. 2, 166-171, 1996.
4. Werner, D. H, "An exact integration procedure for vector potential of thin circular loop antenna," *IEEE Trans. Antennas Propagat.*, Vol. AP-44, No. 2, 157-165, 1996.
5. L. W. Li, C. P. Lim, M. S. Leong "Method of Moment analysis of electrically large circular loop antenna: Non-Uniform Currents," in *IEE Proc. Antennas Propagat.*, Vol. 146, No. 6, 416-420, 1999.
6. Ali Hamed, S. M. "Exact field expressions for circular loop antennas using spherical functions expansion", submitted to *IEEE Trans. Antennas and Propagation* .
7. Hejase, H. A. N., Gedney, S. D. and White, K. W. "Effect of a finite ground plane on radiated emission of a circular loop antenna, *IEEE Trans. on Electromagnetic Compatibility,* Vol. 36, 364-371, 1994.

Finite Conductivity Formulation of TE-TM Mode Conversion in Corrugated Circular Waveguides: A Multiple Scales Perturbation Approach

Omar R. Asfar, Senior Member, IEEE, and Nadiah H. Saba'neh
Department of Electrical Engineering
Jordan University of Science and Technology
Irbid, Jordan 22110

Abstract

It is shown in this paper that relaxing the perfect conductivity assumption leads to a consistent formulation of the boundary-value problem of TE-TM mode conversion in circular waveguides with periodically perturbed radius. Examination of the boundary conditions shows that these modes propagate independently in two-dimensional waveguides as well as in circular waveguides supporting circularly symmetric modes. For non-circularly symmetric modes, the boundary conditions for the TE (TM) mode cannot be satisfied without exciting the TM (TE) mode. Thus, the radial field component E_ρ of the TE_{11} mode is proportional to the axial electric field E_z of the TM_{11} mode. Since the latter should vanish at the boundary of a perfect conductor, we arrive at a contradiction. This inconsistency can be removed if we relax the perfect conductivity assumption allowing for nonzero values of the radial component of the electric field. This results in the TE_{11} mode becoming an HE_{11} mode that couples resonantly to the EH_{11} mode replacing the TM_{11} mode of the perfectly conducting guide. For a corrugation wavenumber k_w, resonant coupling requires the wavenumbers β_{TE} and β_{TM} to satisfy the condition $\beta_{TE} - \beta_{TM} = k_w$. The boundary-value problem for the hybrid modes inside the waveguide and in the conducting boundary is solved via the perturbation method of multiple scales. The resulting coupled mode equations are solved exactly and mode power conversion is studied for different wall conductivities and depth of corrugation for the case of an infinite waveguide.

Analysis of Electromagnetic Fields and Waves in Devices Containing Strong Chiral Nihility Material

M.WARDAN ALI, SHAHID HUSSAIN SHAH, USMAN MUSHTAQ, SAFIULLAH KHAN

Ghulam Ishaq Khan Institute of Engineering Sciences and Technology, Pakistan

corresponding author: u2009205@giki.edu.pk,safiullah.khan@hotmail.com

ABSTRACT

The realization of DB boundary conditions has been discussed for strong chiral-nihility medium. A DB spherical waveguide filled with strong chiral-nihility medium has been investigated in spherical coordinates and the resonance frequency has been calculated to depict the filtering behavior of spherical DB boundary. After determining resonant frequency electric and magnetic potential functions are derived, which leads to expressions of electric and magnetic field. Graphs showing the behavior of potential functions and different fields are also given.

SUMMARY

Chiral materials are those which cannot be superimposed on its mirror image. In chiral nihility materials, real parts of permittivity and permeability are zero. Research has already been done on PEC materials and strong chiral materials.
In this paper, a DB sphere filled with chiral nihility material is considered as shown in Figure 1. When a certain wave enters this medium, which is through a cavity in our case, the material absorbs wave at resonant frequency while the rest of frequencies remain unaffected. This filtering behavior is discussed.

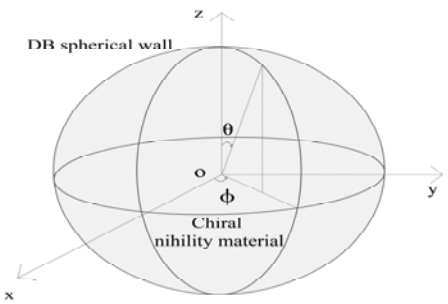

Figure 1

The electric and magnetic field at resonant frequency is found by calculating the resonant frequency, the electric and magnetic vector potentials and then fields at that resonant frequency. The electric and magnetic vector potentials and corresponding fields are analyzed by simulation. The chirality parameter in this case is

$$k^{+} = \omega k$$
$$k^{-} = -\omega k$$

By putting these values and the vector potential values in the corresponding field equations, we get the electric and magnetic field behavior.

Chiral nihility materials are used in optical applications and filtering techniques such as cavity resonator. Moreover, objects with DB boundary and possessing symmetry of certain type have zero back scattering. This property is used in stealth applications.

Acknowledgement:

We are thankful to Dr. Husnul Maab, Associate Professor at GIK Institute for helping us throughout this research work. We would also like to thank Mr. Sharjeel Javaid for his counseling and motivation.

References:

1. Ali, Muhammad. Mahmood. " Analysis of Electromagnetic Fields and Waves in Microwave Devices Containing Strong Chiral Metamaterial".
2. Hassan, Muhammad. Haseeb. "Realization and Applications of DB Boundaries in Chiral and Chiral-Nihility Medium".
3. R. F. Harrington, *Time-harmonic Electromagnetic Fields,* McGraw-Hill Inc., New York, 1961.

Numerical methods

Fast Waveguide Filter Synthesis, using the Mode Matching Method for Analysis and Practical Swarm Optimization.

I.BOUCHACHI and M.L.RIABI

Laboratory of Electromagnetism and Telecommunications, University of Constantine, Algeria

Email: fingroo@yahoo.fr ml.riabi@yahoo.fr

Abstract

In this paper, we give two examples of rectangular waveguide bandpass filter realizations. Starting from the filter specifications (order of the filter, position of zeros, band-edge frequencies, and passband return loss) our aim was to realize one program that makes all steps of the filter synthesis (calculate the coupling matrix, create the equivalent circuit, convert the equivalent circuit to waveguide structure, analyze this structure, and then optimize its dimensions), and doing this as fast as possible (less than two minutes in the first example). For the coupling matrix we used the Atia and Williams's method, for the analysis we used the mode matching method, which is the most adequate for this kind of structures, and for the optimization we used the Practical Swarm Optimization PSO. The complete combination has been successfully applied for several waveguide filters synthesis.

Methods and Techniques Background

In the early 1970s, Atia and Williams introduced the concept of the coupling matrix as applied to dual-mode symmetric waveguide filters. The circuit model they investigated was a bandpass prototype comprised of a cascade of lumped-element series resonators intercoupled by transformers, and each loop is theoretically coupled to every other loop through cross-mutual couplings between the mainline transformers [1].

The concept of matching modes at a junction was attempted in the late 1960s by A. Wexler. Because of the limited computer power available at that time it was not possible to do more than simple computations. The computational emphasis was on reducing the number of modes to the minimum so that a numerical solution could be obtained. It was the arrival of powerful computers that enabled the concept to be applied to the analysis of complicated structures [2].

Particle Swarm Optimization (PSO) is a relatively new technique, for optimization of continuous non-linear functions. It was first presented in 1995. Jim Kennedy discovered the method through simulation of a simplified social model, the graceful but unpredictable choreography of a bird swarm. PSO is a very simple concept, and paradigms are implemented in a few lines of computer code. It requires only primitive mathematical operators, so is computationally inexpensive in terms of both memory requirements and speed [3].

Numerical results

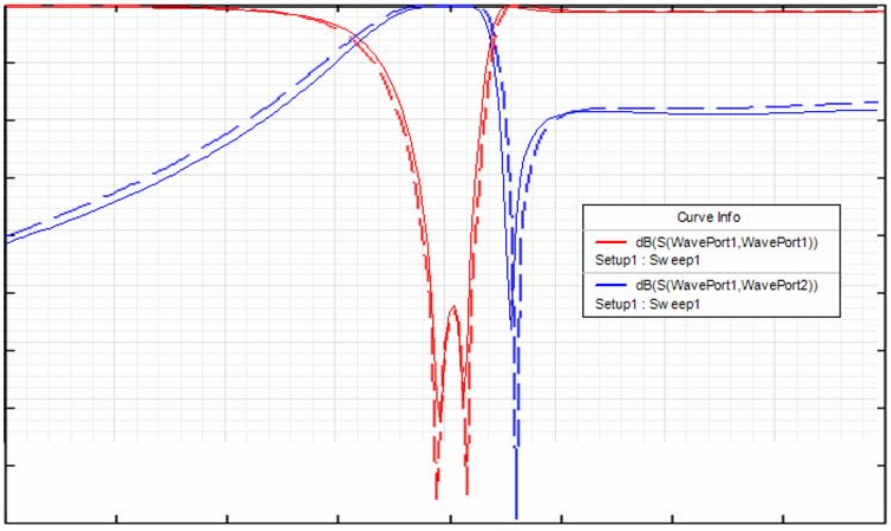

Fig.1. Our results (broken line) using Matlab program, and reference [4] ones on HFSS simulator.

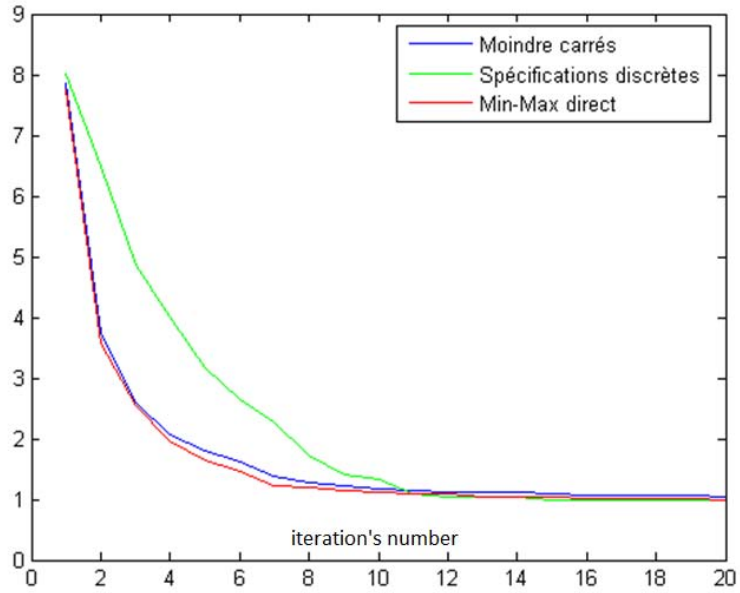

Fig.2. Comparing the convergence of the proposed fitness functions used in PSO.

[1] RICHARD J. CAMERON, CHANDRA M. KUDSIA, RAAFAT R. MANSOUR "MICROWAVE FILTERS FOR COMMUNICATION SYSTEMS" JOHN WILEY & SONS, INC., PUBLICATION 2007.
[2] Björn Widenberg "A General Mode Matching Technique applied to Bandpass Radomes" Gerhard Kristensson, Lund, August, 2001.
[3] Aleksandar Lazinica "Particle Swarm Optimization" In-Tech, January 2009
[4] P. JARRY, E. KERHERVE, O. ROQUEBRUN, M. GUGLTELMI, D. SCHMITT, J.M. PHAM "RECTANGULAR REALIZATIONS OF A NEW CLASS OF DUAL-MODE MICROWAVE FILTERS" Proceedings SBMO/IEEE MTT-S IMOC 2003 page 9-12

Wave Concept Iterative Procedure Analysis of Patch Antennas on Nanostructured Ceramic Substrates

V. P. Silva Neto*, C. F. L. Vasconcelos, M. R. M. L. Albuquerque, and A. G. D'Assunção
Federal University of Rio Grande do Norte, Caixa Postal 1655, CEP: 59078-970 Natal, RN, Brazil
*corresponding author: valdemir.neto@yahoo.com.br

Abstract- The wave concept iterative procedure (WCIP) is proposed to analyze rectangular and circular patch antennas on nanostructured ceramic substrate layers. Principles of WCIP are described and advantages are emphasized. The analysis of microstrip antennas on double layer substrates is performed in space and spectral domains. In addition Fast Fourier Transformation (FFT) is used to improve the efficiency of the method. WCIP simulated results are compared to HFSS software's ones. A good agreement is observed.

The wave concept iterative procedure (WCIP) is developed to analyze microstrip antennas on ceramic substrate layers. WCIP method uses the wave formulation for solving electromagnetic problems. Basically, this method uses a linear combination of tangential field and initial conditions to characterize the waves in a microwave circuit surface. This iterative method is suitable for microwave planar circuit analyses, as well as patch antennas [1] - [3]. Moreover, the WICP method uses FFT to reduce the required computing time and provide both versatility and reliable representation of the circuit structure.

In the WCIP method, the incident and reflected waves are defined in terms of combined electric fields and transverse electric current densities (or magnetic fields) [2]. For instance the incident, $\vec{A}_i$, and reflected, $\vec{B}_i$, waves at a circuit interface Ω are defined as:

$$\vec{A}_i = \frac{1}{2\sqrt{Z_{0i}}}\left[\vec{E}_i + Z_{0i}\left(\vec{H}_i \times \vec{n}_i\right)\right], \qquad \vec{B}_i = \frac{1}{2\sqrt{Z_{0i}}}\left[\vec{E}_i - Z_{0i}\left(\vec{H}_i \times \vec{n}_i\right)\right] \tag{1}$$

where Z_{0i} is the intrinsic impedance of the medium, $\vec{E}_i$ is the tangential component of the electric field, $\vec{H}_i$ is the tangential component of the magnetic field, and $\vec{n}_i$ is the outward unit vector normal to the interface. Therefore, the tangential components of the electric and magnetic fields $\left(\vec{J}_i = \vec{H}_i \times \vec{n}_i\right)$ are expressed as [2]:

$$\vec{E}_i = \sqrt{Z_{0i}}\left[\vec{A}_i + \vec{B}_i\right], \qquad \vec{J}_i = \frac{1}{\sqrt{Z_{0i}}}\left[\vec{A}_i - \vec{B}_i\right] \tag{2}$$

where $\vec{J}_i$ is the superficial current density.

Furthermore, this iterative procedure is based on the creation of a recurrence relationship between incident and reflected waves, and its repetition until the problem solution is reached. This iterative method can be

summarized by [2]:

$$\begin{cases} \vec{A} = \hat{S}\vec{B} + \vec{A}_{0i} \\ \vec{B} = \hat{\Gamma}\vec{A} \end{cases} \tag{3}$$

where $\hat{S}$ is the scattering operator at the interface, $\hat{\Gamma}$ is the reflection operator, $\vec{A}_{0i}$ is the wave created by the source in the space field, which is determined as a function of the total electrical field produced by the excitation source. The multilayer media is undertaken into the spectral operator.

Fig. 1 depicts return loss results for a rectangular patch antenna. Similarly, Fig. 2 shows results for a circular patch antenna. These patch antenna geometries were printed on double layer substrates. The top layer (region 1) is filled with a ceramic substrate (ε_{r1} = 20, h_1 = 1.57 mm), while the bottom layer (region 2) is filled with FR-4 (ε_{r2} = 4.4, h_2 = 1.57 mm). Other structural parameters are the rectangular patch width, W = 26.12 mm, and length, L = 35.11 mm, and the circular patch radius, R = 29 mm. HFSS software simulated results are included in Figs. 1 and 2 for comparison purpose.

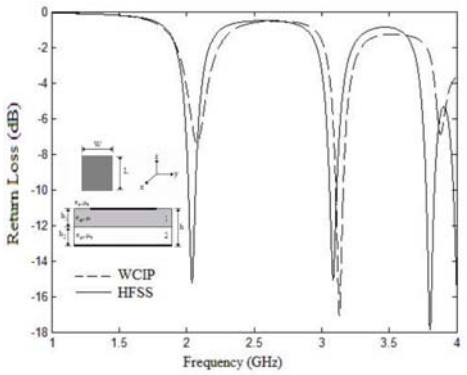

Figure 1. Return loss for a rectangular patch antenna.

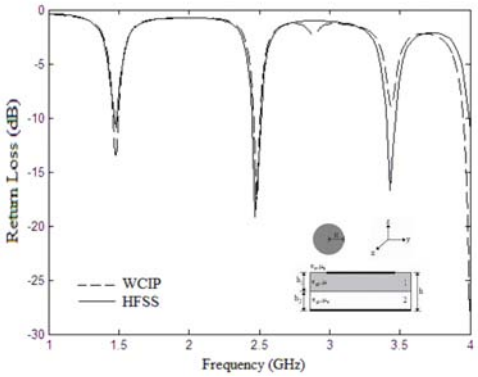

Figure 2. Return loss for a circular patch antenna.

As shown in Figs. 1 and 2 a very good agreement was observed between WCIP and HFSS results, illustrating the accuracy of the proposed WCIP method. Furthermore, the use of a FFT algorithm has improved the required computing time. Also this iterative method provides faster convergence than integral methods, such as the method of moments or the finite element method, because there is no need of matrix inversion and of large amount of memory space.

REFERENCES

1. Garssallah A., A. Mami, A. Zairi, and R. Douma, A. Gharbi, and H. Baudrand, "Analysis of a microstrip antenna with fractal multilayer substrate using iterative method," *RF and Microwave CAE*, Vol. 11, 212-218, 2001.
2. Akatimagool S., "Fast iterative method package for high frequency circuits analysis," in *Proceedings of ISCAS*, Bangkok, Thailand, May 2005, 5970-5973.
3. Raveu N., O. Pigaglio, G. Prigent, and H. Baudrand, "Improvement in the Wave Concept Iterative Procedure through Spectral Connection," in *Proceedings of 37th European Microwave Conference*, Munich, Germany, October 2007, 28-31.

computational techniques applied to EM field problems

Modeling strategy for conformal antenna coupling on aircraft

A. Piche[1], **G. P. Piau**[2], **O. Urrea**[2], **G. Peres**[1]
EADS Innovation Works, France
[1]: 18 rue Marius Terce, 31025 Toulouse [2]: 12 rue Pasteur, 92152 Suresnes Cedex
*corresponding author: alexandre.piche@eads.net

Abstract – The objective of this paper is to propose a modeling strategy for dealing with conformal antenna coupling on aircraft at several GHz.

A long term objective for aircraft manufacturer is the complete integration of antennas in fuselage in order to reduce the aerodynamic drag of aeronautic platforms. These conformal antennas could be composed of microstrip structures, metamaterials or high impedance surfaces. The modeling of a single planar antenna could be easily performed with commercial softs like HFSS or CST if the knowledge of the internal structure is sufficient (geometrical aspects, permittivity of substrates…). However, this knowledge is often limited for industrial reasons; the only observable always available by measurements is the reflection coefficient (i.e. input impedance). In this context, the main challenge is thus the behavior prediction of these antennas operating at several GHz when they are mounted on a complete aircraft. This paper presents a methodology for addressing coupling issues between conformal antennas, based on simulation for propagation aspects (S21) and measurements for antenna internal behavior (S11 and S22). To illustrate, we apply the methodology to an existing planar antenna; the radio altimeter (RA, 4/4.3GHz).

The first step consists in determining an equivalent antenna model which accurately reproduces the radiation. This step is more or less complex depending on the degree of knowledge of the antenna internal structure. In the case of the radio altimeter (figure 1), we know it is an array of 4 patches but we have no information on the feeding network. We use the EADS frequency domain software ASERIS BE which solves the Electric Field Integral Equation (EFIE) with a Boundary Element Method (BEM).

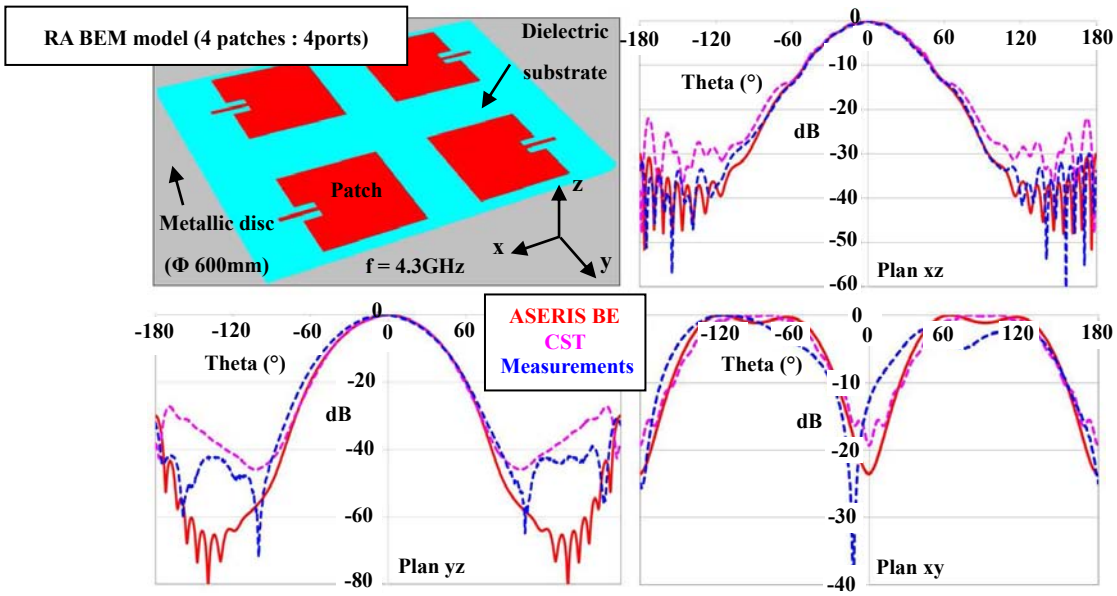

Figure 1: Equivalent RA BEM model, normalized radiation pattern ASERIS BE / CST / Measurements

We observe a very good correlation on the normalized radiation pattern between ASERIS BE and measurements. This equivalent model generates an accurate radiation pattern but its reflection coefficient is not representative (the feeding network is not taken into account). However, this last could be easily obtained by a simple VNA measurement on a large finite ground plane (S_{11meas} and S_{22meas} in the following). The equivalent model could now be used for predicting the coupling function between two RA antennas mounted on an aircraft. We note $[S_{simu}]$ the S matrix computed by simulation with the equivalent model and $[S_{meas}]$ the S matrix of the real configuration. The observable of interest S_{21meas} (i.e. equal to S_{12meas}) could be evaluated as follow:

$$|S_{21meas}| = |S_{21simu}| \frac{\sqrt{1-|S_{11meas}|^2}\sqrt{1-|S_{22meas}|^2}}{\sqrt{1-|S_{11simu}|^2}\sqrt{1-|S_{22simu}|^2}} \quad (1)$$

An iterative solver based on the fast multipole method (FMM) associated to a parallel computing capability on multi-processors is usually employed for extracting $[S_{simu}]$ for large problems (from several hundreds of thousands to several millions of unknowns). The FMM algorithm accelerates matrix-vector products in a controlled approximate way (computation time: nlog(n) instead n^2) but requires a mesh as homogeneous as possible (~λ/10). This constraint directly impacts conformal antennas with dielectric substrates where an important local refinement (λ/20, λ/30 or more) is necessary. So, the current trend is to treat this kind of problem with a H-matrix solver; a BEM Fast Direct solver based on space partitioning and low-rank approximations.

To validate the methodology, we compute in this paper the coupling function between two RA antennas mounted on a finite ground plane (1m x 1.5m) and we compare the results with VNA measurements. The distances between the two RA are 50cm in x-direction avec 5cm in y-direction (see figure 1). First, we determine with ASERIS BE the global 8x8 S matrix (i.e. 4 ports for RA1 and 4 ports for RA2) and we check some terms (S_{13}, S_{14}, S_{15} for example) with CST (temporal solver).

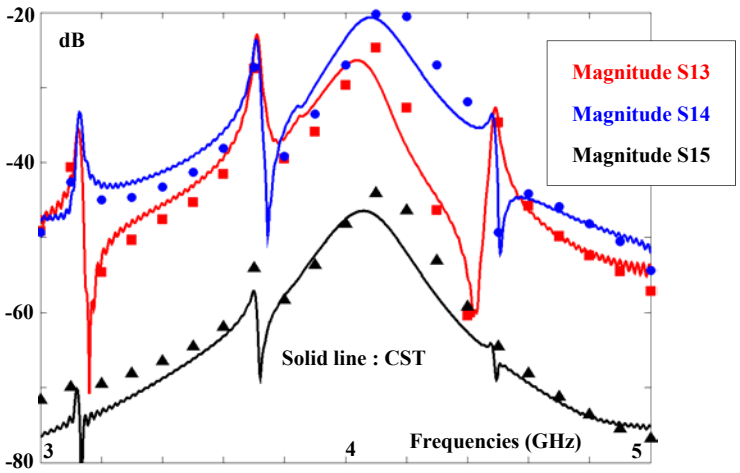

Figure 2: Comparison of S_{13}, S_{14} and S_{15} between ASERIS BE and CST

We observe a very close correlation between the two codes. In the final paper, we will combine the 4 ports of RA1 and RA2 to obtain the 2x2 S matrix $[S_{simu}]$, we will evaluate S_{21meas} thanks to (1) and we will compare the result with measurements to validate the global methodology.

[1] MOSIG, J.R "Numerical analysis of microstrip patch antennas", Handbook of microstrip antennas, Chap8

Computational Finite Element Software Assisted Development of a 3D Inductively Coupled Power Transfer System

P. R. Raval[1*], **D. Kacprzak**[1], **and A. P. Hu**[1]
[1]Deparment of Electrical and Computer Engineering
The University of Auckland, New Zealand.
[*]corresponding author: prav010@aucklanduni.ac.nz

Abstract-Inductively coupled power transfer systems have already many practical applications including battery charging. To date, a majority of current such systems only support uni- or bi-directional planar movement in load. This is due to a lack of magnetic field generation across a three-dimensional cubic volume. By use of modern finite element assisted computational software, this paper proposes primary and secondary magnetic structures as customized to support three-dimensional load movement for battery charging applications.

The technique of transmitting power across an air-gap without interconnecting wires is well established via the technique termed magnetic induction [1]. Such systems, referred to as inductively coupled power transfer systems (ICPT), are becoming ubiquitous in industry including monorail systems, people movers, biomedical implantation and low power consumer battery charging applications [1-2]. Regarding battery charging applications, current systems largely support only planar load displacements [2]. This is problematic for 3D load displacements. This paper proposes a 3D power transfer system for battery cell charging.

The structure of the proposed ICPT system is shown in Figure 1. A DC voltage is input to the power converter for inversion into high frequency resonant AC current at 155 kHz. The resonance is required to lower the input power rating [1]. This current is fed to the primary windings. The secondary magnetic structure intercepts the time varying flux for voltage induction into the secondary coils. This voltage is often weak and therefore resonated [1]. Furthermore, this voltage is noisy so AC rectification is required before application to a load [1].

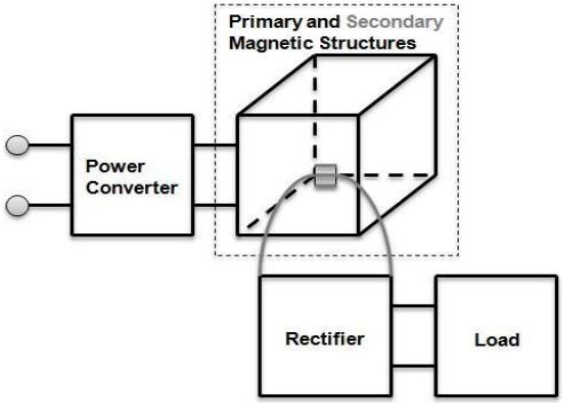

Figure 1: Structure of proposed system.

The methodology used for excitation of the proposed models is summarized in Equation 1. This method ensures the same magneto-motive force (MMF) in ampere-current turns (NI) ratio is used to account for coil sections i in one model and differing coil sections j of another model both of the same cross sectional area but different length l conveniently written in terms of the input FEM parameter the current density J .

$$\sum_{1}^{i}(NI)_i l_i = \sum_{1}^{j}(NI)_j l_j \Leftrightarrow \sum_{1}^{i} J_i l_i = \sum_{1}^{j} J_j l_j \tag{1}$$

The primary magnetic structure must provide a satisfactory magnetic flux density (MFD) distribution in

magnitude and uniformity in a 3D volume. Two primary structures are proposed. Firstly, the vertical field box is shown in Figure 2. It consists of winding structures with increasing coil turn density in the central region producing a net vertical field. This is to improve the central valley in MMF. This is verified by the simulated MFD contour visualizing a peak in the center zone. Notably, the currents are applied simultaneously in-phase. The averaged MFD in the cubic zone is 4.75e-05T. Secondly, the horizontal field box is shown in Figure 2. In this box, rectangular coils are placed on all 4 ferrite walls producing a horizontal field. The current in one coil pair encounters a 90 degrees phase shift with respect to the other pair. The result is a rotating magnetic field. The result is compared when a single pair of coils is switched on to reflect the scenario that occurs every cycle. This is justified as the averaged MFD in the cubic volume with all coils switched on does not increase in relative proportion compared to when one coil pair is switched on from 2.27e-05T to 1.74e-05T due to destructive interference by adjacent like poles. The MFD contour shows a central valley.

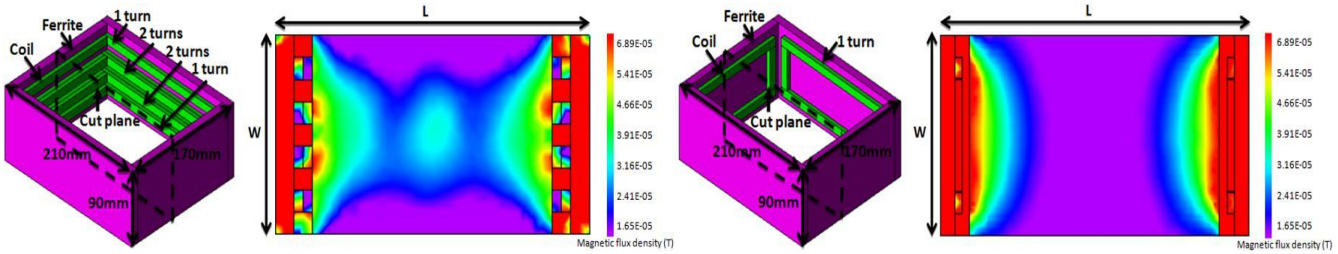

Figure 2: Vertical field box and MFD distribution (left) and Horizontal field box and MFD distribution.

The secondary magnetic structure, as customized around the shape of the chargeable battery, is shown in Figure 3. This consists of a ferromagnetic cylindrical core surrounded by rectangular blocks of ferrites. This requires three series pick-up coils to account for the planar and normal components of flux. The battery is placed in the air gap of the inner core. The power induced in the vertical orientation of the pick-up is tested through the center plane in both models also shown in Figure 3.

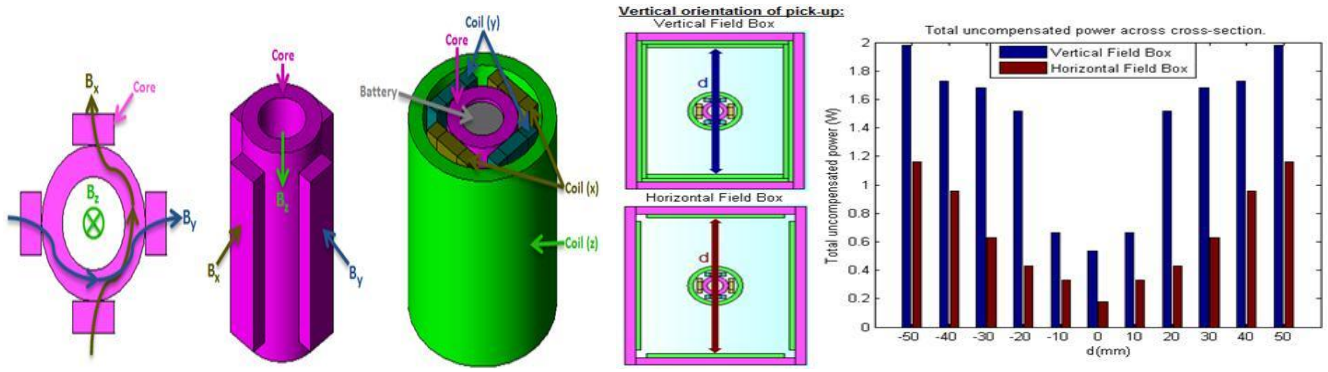

Figure 3: Pick-up core views (left) and Simulated uncompensated power level (right).

In conclusion, primary structures are proposed to generate a 3D power zone. In addition, a pick-up was customized for battery charging showing an average total uncompensated power level of 1.4W and 650mW with deviation of 101.3% and 150.08% for the vertical and horizontal field boxes.

REFERENCES

1. Green A. W. and Boys J. T., 10kHz inductively coupled power transfer concept and control, *IEEE PEVD conference*, London, pp694-699, 1994.
2. Hui R., Ho W., A new generation of universal contactless battery charging platform for portable consumer electronic equipment, *35th IEEE PES conference*, Aachen, Germany, pp638-644, 2004.

3D Numerical Analysis for Impedance Calculation and High Performance Consideration of Linear Induction Motor for Rail-guided Transportation

N. V. Cuong[1]*, **Y. Yamamoto**[1] and **T. Koseki**[1]
[1] The University of Tokyo, Japan
*corresponding author: ninh.cuong@koseki.t.u-tokyo.ac.jp

Abstract-In this paper, the authors describe the method of calculating the impedance of Linear Induction Motor for rail-guided transportation using magnetic vector potential which can be obtained from three-dimensional numerical analysis. Based on this method, high performance and power saving of some models of current research trends of Linear Induction Motor concerning the mechanical clearance and secondary reaction plate construction are discussed.

In recent years, the construction of new urban subway lines using Linear Induction Motor (LIM) has been developed, especially in Japan and Korea. Significant advantages of LIM are: direct thrust without gears and links, simple structure, easy maintenance as well as reduction of tunnel construction cost. However, different from rotating motor, LIM has special characteristics and inherent problems because of the non-continuity of the magnetic field. Longitudinal end effect and transverse edge effect are two major electromagnetic phenomena of LIM, which makes the analysis, design and control of this motor difficult.

The experiments for analysis and design are difficult to carry out due to the requirement of construction features. Since the longitudinal end effect is caused by finite length of primary that requires LIM the full modeling in analysis, and two-dimensional (2-D) analysis cannot express the influence of transverse edge effect which is caused by the finite widths of the primary and secondary part. Hence, in order to evaluate the characteristics of LIM, the three-dimensional (3-D) analysis with full length model is necessary.

In this paper, by using the 3-D numerical analysis, the method for calculating the impedance of LIM is described. In numerical analysis with a current source, the induced primary terminal voltages in each coil can be determined by direct integration over the coil length of the distribution of the magnetic vector potential which is obtained from the magnetic field analysis as shown in Eq. 1.

$$V_i = \int_s rot\overrightarrow{E_i} \cdot dS = \int_c \overrightarrow{E_i} \cdot d\vec{S} = -\int_s \frac{\partial \overrightarrow{B_i}}{\partial t} d\vec{S} = -\frac{\partial \varphi_i}{\partial t} = -j\omega \int_c \overrightarrow{A_i} \cdot d\vec{s} \quad (1)$$

Where, E_i is the electric field, B_i is the magnetic flux density, φ_i is the magnetic scalar potential and A_i is the magnetic field potential. From this result, the impedance of the power factor and efficiency is calculated. The model of the calculation method is shown in Fig.1.

Due to the great dependence of longitudinal end effect on mechanical clearance, transverse edge effect on the secondary reaction plate construction [4], reduction of mechanical clearance and re-construction of secondary reaction plate have been considered in order to get higher performance for LIM in Linear Metro

system in Japan. For this reason, the authors described the characteristics of different models of LIM by using the impedance calculation method mentioned above. As shown in Fig. 2, model **A** is the current type of LIM for Linear Metro system. Model **B** is the model of lower mechanical clearance (9 mm) under the same conditions as model **A**. Model **C** is the full-cap of secondary reaction plate under the same conditions as model **B**.

The analytical results of each model at constant slip frequency 2.1Hz (*s=0.1*) are shown in Table 1. The efficiency increases when mechanical clearance is reduced and the full-cap type is used. The details of calculation method as well as further discussion based on the analytical results will be described in the full paper.

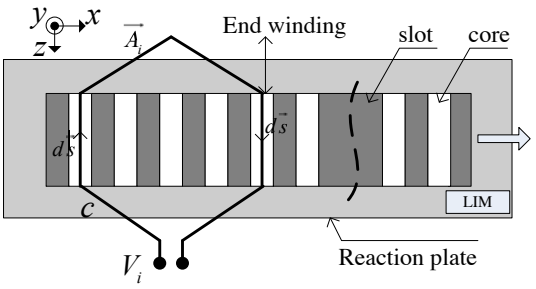

Fig. 1. Model for impedance calculation

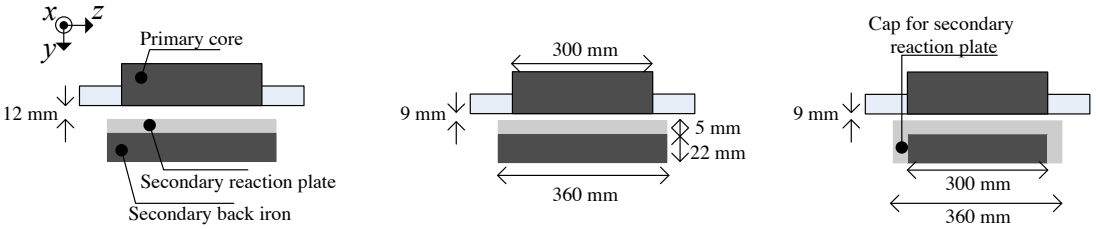

(**A**) 12 mm mechanical clearance & no cap

(**B**) 9 mm mechanical clearance & no cap

(**C**) 9 mm mechanical clearance & full-cap

Fig. 2. Different models of LIM

Table 1. Characteristics of different models of LIM by 3-D numerical analysis

Model	**A**	**B**	**C**
Thrust [kN]	11.2	12.1	12.3
Normal force [kN]	17.1	18.8	19.1
Joule heat [kW]	38.0	32.7	29.7
Power factor	0.47	0.43	0.49
Efficiency [%]	75.7	79.7	81.5

REFERENCES

1. Y. Yamamoto, N. V. Cuong, T. Koseki, "A numerical analysis on variation of forces and impedance of a single-sided linear induction motor to lateral displacement," in *Proceedings of the National Conference of Electrical Engineers*, Hiroshima, Japan, March 2012, 244-246 (In Japanese).
2. Y. Yamamoto, N. V. Cuong, T. Koseki, "Performance improvement and power-saving of linear induction motors for urban rail-guided transport considering their lateral edge effect," in *Proceedings of the National Conference of Electrical Engineers*, Tokyo, Japan, December 2012 (In Japanese)
3. T. Koseki, "Flux synthesizing Linear Induction Motor," The University of Tokyo, PhD. Thesis, 1991.12
4. S. Yamamura, *Theory of linear induction motors*, University of Tokyo press, 1978.

Proposal of C-core Type Transverse Flux Motor for Ship Propulsion -- Increasing Torque Density by Dense Stator Configuration --

Y. Yamamoto[1]*, **T. Koseki**[1] and **Y. Aoyama**[2]
[1] The University of Tokyo, Japan
[2] Hitachi research laboratory, Japan
*corresponding author: y_yamamoto@koseki.t.u-tokyo.ac.jp

Abstract – Direct-drive motors for electric ship propulsion are gaining popularity due to energy saving and low maintenance requirements. This application requires high-torque motors at low speed. In such situation, dense stator configuration is important for high torque density. Focused on increasing space factor in the stator, this paper describes a design method considering effects of leakage magnetic flux, magnetic saturation and pole-core combination based on magnetic-circuit theory. The validity of this proposed method has been verified through numerical analysis and experiments.

Transverse flux-type motor (TFM), one of the axial-flux types, is suitable for high-torque application at low speed due to the easily controllable pole pitch [1]. We took advantage of TFM in our proposed design. In the previous machine [2], an idea of pole-core combination which is one of the methods to reduce the cogging torque has been applied. We took the particular combination to apply concentrated winding on three teeth per phase in one lump while keeping relative positions between magnets and stator teeth. This peculiar combination, however, decreased the space factor in the stator side. The previous machine, therefore, did not achieve high torque density. Increasing the area that stator tooth faces field magnet is essential to realize high torque from the principle of generating torque in axial flux-type motor. Then, we use trapezoid-type stator teeth, field magnets and flat-type stator windings that are easy to increase space factor as found in conventional researches [3,4] and apply to the new motor design.

In TFM, unfortunately, three-dimensional numerical study is essential to estimate accurate performance because of its three-dimensional magnetic flux path. For that reason, it takes long time to analyze and it is not easy to confirm the validity of the analysis. Thus, it is necessary to obtain torque estimation beforehand using theoretical approach to design the motor quickly and easily. This paper proposes a simplified design method based on magnetic-circuit theory taking into account of the effect of leakage flux, magnetic saturation and pole-core combination. Furthermore, we design a new prototype model whose target torque density is fixed at 10Nm/l at rated current density of 5A/mm^2 while keeping the ratio of p-p cogging torque to rated torque at less than 3% and with natural air cooling.

In the C-core type TFM, fortunately, magnetic flux in each phase is isolated, so it is possible to estimate no-load flux and torque using 1-magnet 1-tooth modeling for each radial or axial direction as shown in Fig.1 (a), (b). In this modeling, the trade-off between magnetic and electric loading is expressed by regarding coil width as a parameter and using classical permeance method. In addition, leakage flux, magnetic saturation and pole-core combination are estimated using assumptive magnetic flux path method, regarding stator yoke as mmf loss and focusing on relative position between stator teeth and field magnets. Then, a leakage coefficient is defined as a

function of these effects and the effective flux into the C-type core tooth is determined by product the leakage coefficient and magnet flux without including any effects. Hence, torque T is simplified as shown in Eq.(1).

$$T = \frac{3}{2} p\phi AC \tag{1}$$

where, p, ϕ, AC stand for pole pair, peak value of no-load effective flux and that of armature magnetomotive force (mmf) per phase respectively. AC is calculated from current density, coil depth, coil width and coil factor. The effect of reducing effective flux by the pole-core combination is included using difference in electrical angle between relative positions of magnets and armature cores.

After theoretical calculation, FEM calculations are conducted to confirm some details such as cogging torque and iron loss in each analysis point and the design point is decided from the target torque density. In such ideal trapezoid-type stator teeth, however, it is impossible to make using not soft magnetic composite (SMC) but lamination steels. Hence, we apply stepped teeth to realize equivalent trapezoid structure as shown in Fig.1 (c). According to FEM simulation, the decrease in torque density in this equivalent structure is relatively negligible, so this configuration is applied to our new machine.

In the full paper, the details of the design method and experiment results will be clarified.

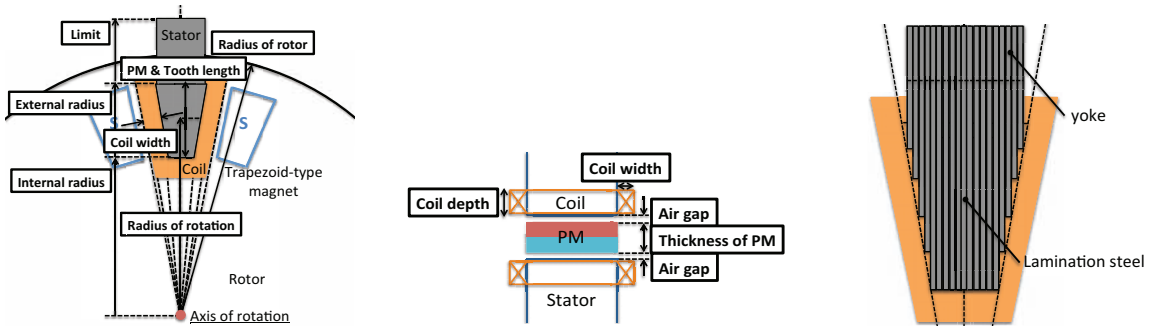

(a) Radial direction component (b) Axial direction component (c) Stepped tooth configuration

Fig.1. 1magnet-1tooth modeling for simplified calculation.

Table 1. Comparison between proposed and previous machines in our laboratory[2].

	Previous	*Proposed*
Peak-to-peak cogging torque / Rated torque [%]	0.24	1.6
Torque density [Nm/*l*]	5.5	9.4

References

1. Weh, H., H. Hoffman and J. Landrath, "New Permanent Magnet Excited Synchronous Machine with High Efficiency at Low Speeds", *Proceedings of the International Conference on Electrical Machines*, 1988.
2. Nakamura, T., K. Koseki and Y. Aoyama, "A low-speed high-torque permanent magnet synchronous motor – Reducing cogging torque and eddy current loss –", *Journal of the Japanese Society of Applied Electromagnetics and Mechanics*, Vol. 20, No. 2, pp.410–415, 2012.6.
3. Woolmer, T. J. and M. D. McCulloch, "Analysis of the Yokeless And Segmented Armature Machine", *IEEE International Conference on Electric Machines and Drive Conference 2007,* pp.704-708, 2007.
4. Tokoi, H., S. Kawamata and Y. Enomoto, "Study of High-Efficiency Motors Using Soft Magnetic Cores", *IEEJ Transactions on Industry Applications,* Vol. 132, No. 5, pp.574-580, 2012. (In Japanese)

Radiation; Propagation and Diffraction

Electromagnetic frequency selective surfaces on magnetic substrates: group-theoretical approach

Victor Dmitriev, Luis Paulo Vale Matos

Department of Electrical Engineering, University Federal of Para, PO Box 8619, Agencia UFPA, CEP 66075-900, Belem, Para, Brazil

Abstract-We investigate in this work electromagnetic frequency selective surfaces on magnetic substrates. Such surfaces can serve as controllable by magnetic field devices. We use the theory of magnetic groups to analyze some general properties of them. We present also an algorithm of calculations which allows one to reduce significantly the time and memory of the computer simulations. As an example, we consider a planar array of metal rings with square cell on a magnetized ferrite substrate for the cases of different orientation of magnetization.

Planar arrays consisting of resonating patches or apertures in a unit cell possess various electromagnetic wave responses and find many applications for frequencies ranging from microwave to optical regions. They serve as frequency selective surfaces (FSSs), polarizes, reflectarrays, absorbers, etc., [1]. It was shown in [2] that by using the group theory for the nonmagnetic array with square unit cell (the symmetry C_{4v}, the computation efficiency can be improved greatly: the memory occupation is reduced by 3/4 and the computation time is reduced by a factor 64. We will show that for magnetic arrays with symmetrical unit cell, one can also reduce significantly the time and memory of the computer simulations. The reduction depends on the magnetic symmetry which in its turn, depends on the direction of substrate magnetization.

Ferrite materials in a dc magnetic biasing field are described by a permeability tensor and manifest resonance ferromagnetic response which depends on the applied biasing field. It is known that by properly adjusting the applied biasing field, it is possible to shift the resonances of the metal arrays, to switch from a high level to a low level of the array transmission, to enhance the Faraday and Kerr rotation, etc., [3,4]. A possibility of tuning some electromagnetic parameters, such as resonance frequency, improve the capabilities of this type of arrays. As examples, we consider two magnetic symmetries of ferrite arrays with circular metal elements described by the groups $C_{4v}(C_4)$ which corresponds to normal magnetization, and the group $C_{2v}(C_s)$ for the in-plane magnetization. The permeability of the magnetized by a uniform dc magnetic field $\mathbf{H}_0$ ferrite substrate is a tensor of the second rank $\bar{\boldsymbol{\mu}}$ and the permittivity is a scalar ϵ. Without dc magnetic field, one can consider the ferrite substrate as dielectric one described by a scalar permeability $\mu = 1$. The square unit cell of the lattice has the period d in both the x- and the y-direction (Fig. 1a). The unit cell of the lattice is a square possessing the geometrical symmetry C_{4v} (in Schönflies notations [5]).

For the field $\mathbf{H}_0$ directed along the axis z (i.e. $\mathbf{H}_0 \parallel z$, Fig. 1a), the resulting group of symmetry of the system "2D square lattice + dc magnetic field" is $C_{4v}(C_4)$ which contains the following 8 elements: e is the identity element, C_2 is a rotation by π around the z-axis, C_4 and C_4^{-1} are rotations around the z-axis by $\pi/2$ and by by $-\pi/2$, respectively, $\boldsymbol{\mathcal{T}}\sigma_x$ and $\boldsymbol{\mathcal{T}}\sigma_y$ are the antireflections in the plane $x = 0$ and in the plane $y = 0$, respectively, $\boldsymbol{\mathcal{T}}\sigma_{(a-a)}$ and $\boldsymbol{\mathcal{T}}\sigma_{(b-b)}$ are the antireflections in the planes which pass through the axis z and the line $(a - a)$ and $(b - b)$, respectively. The Brillouin zone (BZ), the star and the basic domain of BZ for the magnetic groups are shown in Fig. 1b,c,d. We find the symmetry of the wave vector in different symmetry points of BZ. These symmetries are useful in discussing the possible stop- and pass-bands of the in-plane propagation in FSS.

For the diffraction problem, we consider the approach suggested in [2] for nonmagnetic arrays. In our case of magnetic structures, we consider magnetic groups and co-representations of them

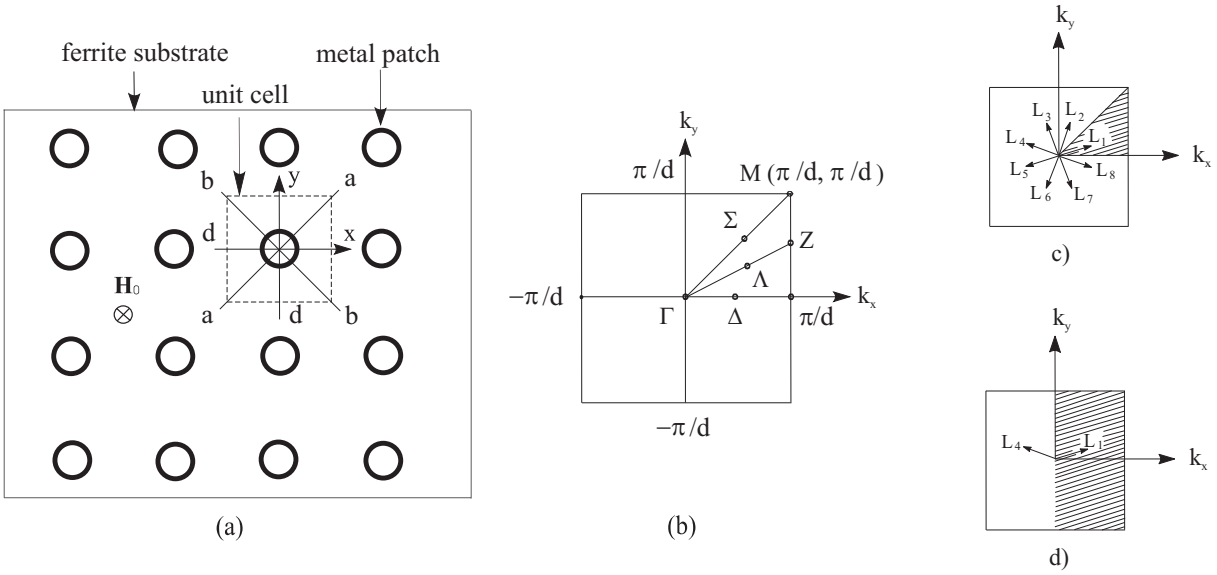

Figure 1: 2D periodical array on ferrite substrate with circular metal elements: a) front view, b) Brilloin zone. The star and the reduced Brillouin zone for magnetization: c) along the z-axis, group $C_{4v}(C_4)$, d) along the x-axis, group $C_{2v}(C_s)$.

and this is a principal difference in our approach. The following steps are the same as those discussed in [2]. We give some examples of numerical calculations with reduced computation time.

In conclusion, we have shown that magnetization of a magnetic substrate leads to a reduction of array symmetry. In spite of this, the magnetic group theory is useful not only to obtain a deep insight into the problems but also to improve the efficiency of numerical calculations.

Acknowledgment

This work was supported by Brazilian agency CNPq.

References

[1] R. Mittra, C. H. Chan and T. Cwik, "Techniques for Analyzing Frequency Selective Surfaces - A Review", Proceedings of the IEEE, Vol. ??, pp. 1593-1615, 1988.

[2] B. Bai and L. Li, "Reduction of computation time for crossed-grating problems: a group-theoretic approach," J. Opt. Soc. Am. A, Vol. 21, pp. 1886-1894, 2004.

[3] S. L. Prosvirnin and V. A. Dmitriev, "Electromagnetic wave diffraction by array of complex-shaped metal elements placed on ferromagnetic substrate," EPJ Appl. Phys., Vol. 49, pp. ??-??, 2010.

[4] T. K. Chang, R. J. Langley and E. A. Parker, "Frequency Selective Surfaces On Biased Ferrite Substrate," Electron. Lett., Vol. ??, pp. 1193–1194, 1994.

[5] Anatoly A. Barybin, Victor A. Dmitriev, *Modern Electrodynamics and Coupled-Mode theory: Application to Guided-Wave Optics*, Rinton Press, Princeton, New Jersey, 2002.

Detection of the bulk and leaky acoustic micro-waves in piezoelectric materials

[1]D. Benatia, [1]M. Garah and [2]M. Benslama

[1]Electronic Department, University of Batna. Algeria
[2]Electronic Department, University of Constantine, Algeria.
Corresponding author: dj_benatia@yahoo.fr

Abstract: In this paper, we propose a new method for the detection of an acoustic microwave in a piezoelectric substrate. For this, we based our analysis on the tensorial piezoelectric equations. In theses equations we have a very important parameter called acoustic velocity. Its importance is due to the fact that its variation permits to provoke singularities at the level of the wave. These singularities inform us of presence of bulk and leaky waves in piezoelectric materials. Some results are given; they lead to some interesting conclusions.

The investigation of bibliography in micro-acoustic area permits us to point the state of the art. Milson [1] in 1977 elaborates a relation based of the charge density. In spite of it, this method doesn't permit to distinguish easily the different modes of propagation. Yashiro and Goto [2] introduce the method of the stationary phase of Lightill [3] to calculate the singularities that inform us on the presence of bulk and leaky waves [4, 5]. In our case, we propose another approach for the modeling of the acoustic microwaves with a complementary vision to the literature mentioned above. In this approach we interested especially in the detection of singularities, directly at the level of penetration coefficient [6].

The signal to be treated will be applied to the electrodes of the transducer that generate the compression and dilatation, so a piezoelectric wave is generated and propagated in the X_1 direction with an acoustic velocity $\boldsymbol{V_S}$ (Fig.1).

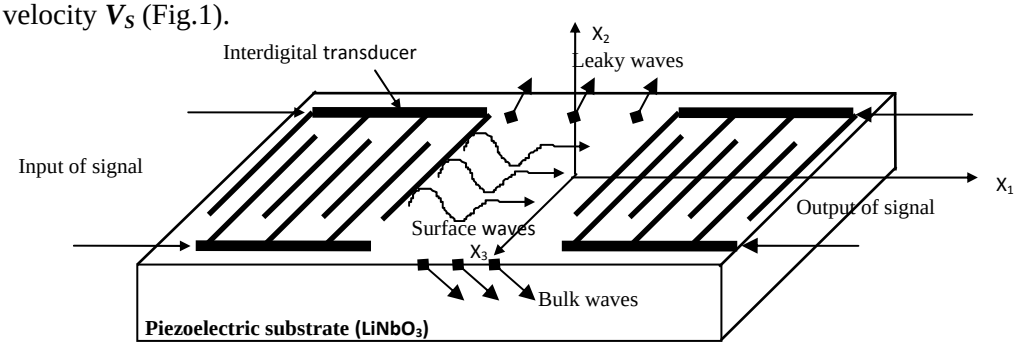

Fig.1: Niobate of Lithium ($LiNbO_3$) Crystal excited by transducer.

The propagation in this structure (Fig. 1) follows these piezoelectric tensorial equations:

$$C_{ijkl}\frac{\partial^2 U_k}{\partial X_i \partial X_l} + e_{kij}\frac{\partial^2 U_4}{\partial X_k \partial X_i} = \rho\frac{\partial^2 U_k}{\partial t^2} \tag{1}$$

$$e_{ikl}\frac{\partial^2 U_k}{\partial X_i \partial X_l} - \varepsilon_{ik}\frac{\partial^2 U_4}{\partial X_k \partial X_i} = 0 \qquad \textit{with i,j,k,l=1..3.} \tag{2}$$

Where C_{ijkl}, ε_{ik} and e_{lij} are the elastic, dielectric, and piezoelectric tensors respectively, ρ is the mass density of medium, U_i is the displacement amplitude and U_4 is the electric potential.

The main parameter in this study is the penetration coefficient given by:

$$\alpha_m = a_m + jb_m \qquad m=1..8 \tag{3}$$

The variation of the acoustic velocity $\boldsymbol{V_S}$ allows us to obtain $b_m = 0$ (imaginary part) and $\boldsymbol{U_i}$ is the function of propagation constant $\boldsymbol{k}$, given by:

$$U_i = u_i . exp - j\left[\omega.t - k.(X_1 + a_m X_2)\right] \tag{4}$$

The leaky waves (**L.W**) and bulk waves (**B.W**) depend on the sign of the real part of α_m *(for example m=4)*.

If $\boldsymbol{a_m}$ is positive, we have leaky waves (radiation out of the crystal (Fig.1 and 2)).
If $\boldsymbol{a_m}$ is negative, we have bulk waves (propagation into the crystal (Fig.1 and 2)).

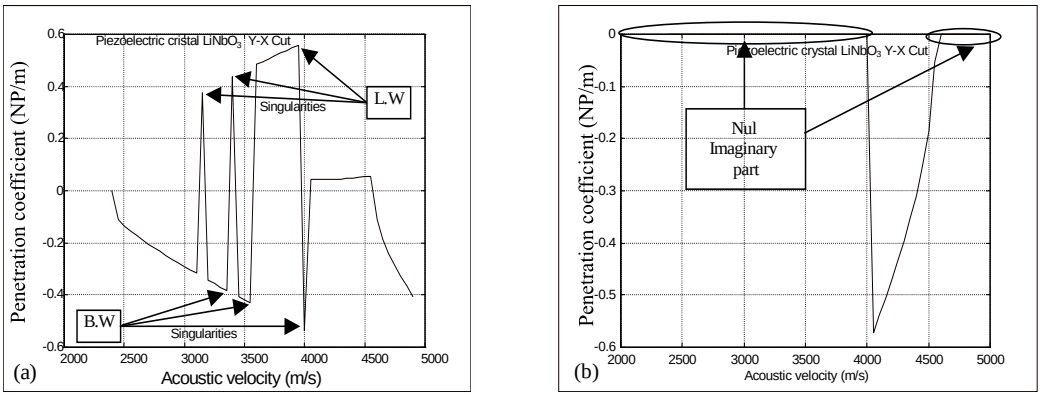

Fig.2: Penetration coefficient α_4. (a): Real part, (b): Imaginary part

This information can be useful for many applications such as the antenna (case of L.W) and the ultrasound ultrasonic devices (case of B.W).

References

1. Milson, R. F., N. H. C. Reilly and M. Redwood, "Analysis of generation and detection of surface and bulk acoustic waves by interdigital transducers," *IEEE Trans. Sonics and Ultrason*., Vol.24, No. 3, 147-166, 1977.
2. Yashiro, K. and N. Goto, "Analysis of generation of acoustic waves on the surface of a semi-ifinite piezoelectric solid," *IEEE Trans. Sonics and Ultrason*., Vol.25, No.3, 146-153, 1978.
3. Lightil, J.," Waves in fluid," *University Press,* Cambridge, 1978.
4. Fusero, Y., S. Ballandras, J. Desbois, J. M. Hodé and P. Ventura, "SSBW to PSAW Conversion in SAW Devices Using Heavy Mechanical Loading," *IEEE Trans. On ultrason., Ferroelectrics and frequency control*, Vol.49, No. 6, 805-814, 2002.
5. Martin, F., "Propagation characteristics of harmonic surface skimming bulk waves on ST," *Electron Lett*. Vol.38, pp. 941-942, 2002.
6. Benatia, D. and M. Benslama,"Identification of bulk microwaves and detection of Pseudo-singularities by wavelet technique in piezoelectric medium," *International Journal of Electronics*, Vol.93, No. 8, pp. 567-576, 2006.

Ultra-Wideband Waves Through Multilayer Planar and Cylindrical Models

S. Selim Seker[1*], Isil Alkocoglu[1], A. Yasin Citkaya[1]
[1]Bogazici University, Dept. of Electrical and Electronics Engineering, Istanbul, Turkey
[*]corresponding author: seker@boun.edu.tr

Abstract- This study consists of the propagation and simulation of an ultra-wideband (UWB) through-the- wall radar and its application for detecting an object (e.g. human) of interest. To reach this goal, first the object itself should be model using an appropriate method. In this work, multilayer planar and cylindrical model of typical wall and human body model are studied, which is essential to model the objects of interest using simpler approaches. The results of two different models for the same object (an average human body model) are compared.

Through-the-wall imaging technology is applied for making measurements at some distance without physical contact with the measured object. When a signal propagates in the same medium, the signal at the end of the medium is affected by the electromagnetic characteristics of the medium. For lossless case, the signal at the end of the medium is same as the starting signal. As for lossy medium, the signal is affected by the travelling distance, the attenuation constant and phase constant of the medium. When a signal is propagating from region one to region two, some of the incident signal is reflected back and some is transmitted to the next region.

The incident wave is taken as a Gaussian pulse since it is easy to analyze in both time and frequency domains. Also, the Gaussian function is continuous in time domain and it creates a single impulse-like pulse at its peak. The energy of the Gaussian function is uniformly distributed among its frequency spectrum and the second derivative is used as it has the largest bandwidth that has the most uniformly distributed energy [1, 2].

For cylindrical model, it was assumed that a electromagnetic wave(TM or TE) is incident on an multilayer-circular cylinder [3]. Each layer of the multilayer circular cylinder is homogeneous as seen in figure 1. The detail of theory and parameter of equations will be given in the full paper.

For planar model, an electromagnetic wave of TM or TE polarization was incidence with angle on a multilayer planar surface as seen in figure 2. The detail of theory and parameter of equations is given in the full paper [4]. The incident waves pass through a wall and then air before reaching the human body. It is expected for the received signal amplitude to decrease after each layer because of reflection and other loss effects. Using given equations, the EM fields in each layer are calculated numerically and then the results of planar and cylindrical models are plotted in a graph to compare them with each other.

For one layer of thickness 0.0014, permittivity 4.30 and the incident angle 0, the transmitted wave amplitude is obtained approximately 0.925. The calculated theoretical value with different approach from the literature and our result are very close to each other, and the code is working properly [1]. Instead of the transmitted amplitudes, if the reflected amplitudes between layers of the table are calculated, then how much of the wave is reflected back can be found. This is the main principle of RADAR systems, which can detect distance of object from the time delay between the incident wave and reflected wave [5].

Next, we simulated the transmitted wave with and without human beings behind the wall, at 9 GHz. It was

observed that without a human body model behind the wall (incidence angle=0), the received signal amplitude is 0.8006, while after passing through the human, the received amplitude reduced to 0.08843 for multilayer planar model. It was observed that without a human body model behind the wall (incidence angle=0), the received signal amplitude is 0.8279, while after passing through the human, the received amplitude reduced to 0.0897 for multilayer cylindrical model. As the next run, we simulated the same results with incidence angle as 60 degree. It was observed that without a human body model behind the wall, the received signal amplitude is 0.593, while after passing through the human, the received amplitude reduced to 0.05906 for multilayer planar model. It was observed that without a human body model behind the wall, the received signal amplitude is 0.6287, while after passing through the human, the received amplitude reduced to 0.0876 for multilayer cylindrical model.

For the frequency of 3 GHz, the new results are similar in shape as 9GHz case but amplitudes are bigger. The graphs which it will be in full paper, two different modeling techniques give similar but not completely matching results. The differences in the received amplitudes are due to different transfer functions in two different geometries. Since 3 GHz frequency has higher skin depth compared to 9 GHz frequency, the transmitted wave amplitude to the innermost layer (the bone tissue) is higher than 9GHz case. Comparison of the 9 GHz and 3 GHz cases for every incident angle that the transmitted wave amplitude is higher for 3 GHz frequency for both planar and cylindrical models. The amplitude of transmitted and reflected (RADAR) waves in the wall, in the layers of human beings for both models at different incidence angle will be given in the final paper.

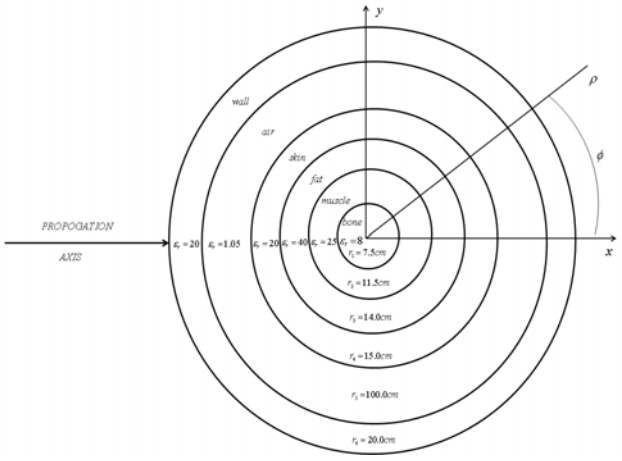

Figure 1. Circular cylindrical model of the human body

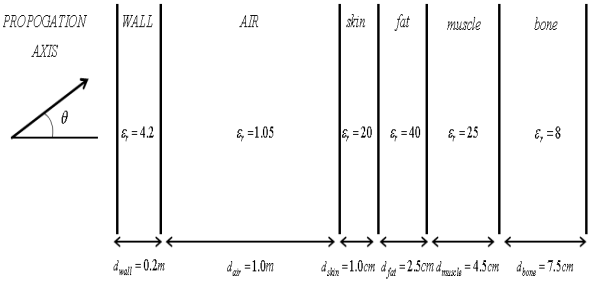

Figure 2. Planar model of the human body

Acknowledgements: This work is supported by Bogazici Univ. Research Foundation Project Code: 5698

REFERENCES

1. DARPA NETEX program: Ultra-wideband channel propagation measurements and channel modeling. Through-the-Wall Propagation and Material Characterization. Blacksburg, CA, 2002.
2. Yarovoy, A. G., L. P. Lighthart, J. Matuzas, and B. Levitas, “WB Radar for human detection”, *IEEE A&E Systems Magazine*, pp.10-14, March 2006.
3. Bussey, E. H. and J. H. Richmond, “Scattering by a lossy dielectric circular cylindrical multilayer, numerical values”, *IEEE Transactions on Antennas and Propagation*, Vol. 23, pp. 723-725, 1975.
4. Paris, T. D. and F. K. Hurd, *Basic Electromagnetic Theory*, McGraw-Hill Book Co., New York, 1969.

5. Eugene , S. A. M. and A. G. Tijhnis, “Pulsed EM fields in biological tissue”, *IEEE Eng. in Medicine and Biology Society*, Amsterdam, pp.1881-82, 1996.

EM Propagation Loss Model for Wireless Communication

S. Selim Seker[1*], Osman Cerezci[2], Fulya Kunter[3], A. Yasin Citkaya[1]
[1]Bogazici University, Dept. of Electrical and Electronics Engineering, Istanbul, Turkey
[2]Sakarya University, Dept. Electrical and Electronics Engineering, Sakarya, Turkey
[3]Marmara University, Dept. of Electrical and Electronics Engineering, Istanbul, Turkey
[*]corresponding author: seker@boun.edu.tr

Abstract-The main objective of this work is to simulate the attenuation in mobile communication, at frequencies used in Turkey such as 900, 1800 and 2270 MHz, due to environment like snow, rain and vegetation In this study the attenuation is obtained modeling snow rain and vegetation as a random medium using Discrete Propagation Model. In this work, spherical, oblate spheroid, plate and cylinder are used for modeling particles.

The capacity and coverage of cellular communication systems requires a deeper understanding of how the environment surrounding the base station influences radio propagation. Considerable attention has been given in the literature to the influence of buildings, the effect of trees, snow and rain [1, 2].

Oblate spheroid rain drop modeling produced results which are more compatible with ITU-R results especially at frequencies higher than 50 GHz. Moreover, attenuation of snow is simulated for different types using uniform distribution of snowflakes. The last, the attenuation of vegetation is simulated. It was found that snow attenuation is higher than rain attenuation specifically because of the differences in particle size [3].

In this work, we considered the problem of scattering of time harmonic electromagnetic wave from N discrete lossy dielectric scatterers, which have random positions and orientations in a volume V which represents a rain, snow or vegetation. Let identical scatterers have a volume V_p, a relative dielectric $\in_r$, radius R and a scatterer density which is taken as a constant value ρ for this study. The surrounding medium is considered to be free space. In this way, one can obtain a mean field equation from Maxwell's equations, assuming the incident field on each scatterer is in itself the mean field (Foldy approximation). By using this approximation along with an assumed sparse distribution of scatterers, which indicates the fractional volume $\delta=\rho V_p$ to be very small, the component of electric fields $E_{\alpha\beta}$ can be easily obtained,[2]

$$E_{\alpha\beta} = \mathbf{exp(}iK_{\alpha\beta}L\mathbf{)} \quad \alpha,\beta \in \mathbf{(}h,v\mathbf{)} \tag{1}$$

Here Kαβ is the effective propagation constant in the multi-component environment. It is given in terms of the forward-scattering amplitude of its individual components of medium as:

$$\text{Kpp}= k_0 + \frac{2\pi}{k_0}\{\rho_t \bar{f}_{pp}^{(t)} + \rho_b \bar{f}_{pp}^{(b)} + \rho_n \bar{f}_{pp}^{(n)} + \rho_l \bar{f}_{pp}^{(l)}\} \tag{2}$$

where k_0 is the wave number and $\bar{f}_{pp}^{(t)}, \bar{f}_{pp}^{(b)}, \bar{f}_{pp}^{(n)}$ and $\bar{f}_{pp}^{(l)}$ are the average forward scattering amplitudes for scatters model of thick cylinders(t), thin cylinders(b), needles(n), and disks(l) respectively.

The specific attenuation for the mean field can be obtained from above equations as

$$App = 8.686\,\lambda \mathrm{Im}\{\rho_t \bar{f}_{pp}^{(t)} + \rho_b \bar{f}_{pp}^{(b)} + \rho_n \bar{f}_{pp}^{(n)} + \rho_l \bar{f}_{pp}^{(l)}\},\ \mathrm{p}\{\mathrm{h,v}\} \quad (3)$$

For the simulation, the rain shape is sphere and the distribution is uniform. Comparisons with experimental results and ITU-R are very good but there are a few dB differences due to the fact that theoretical calculations use Rayleigh-Gans theory not Mie.

The snow attenuation is more severe than attenuation of rain due to its large snowflake size, and composition of water, ice and air molecules. For the snow modeling, certain ice crystal categories are chosen to be investigated. Needles, plates, and branches are the main three groups that are focused on and 13 different models are chosen as representing different snow particles. The elements in each group are chosen according to similar characteristics of the ice crystals. In total, there are 4 groups to be investigated since plate group is divided into two because of similarities. Moreover using literature, relative length is determined for each ice crystal model according to the structure of the model and length-diameter ratio. Simulations of snow, as the frequency increases, attenuation levels increase drastically. However, there is no linear relation between frequency and attenuation. When the frequency is doubled from 900MHz to 1800MHz, attenuation increases approximately by half of the initial value, as it was observed in the simulation of rain attenuation. Needle type crystals have the lowest attenuation due to its geometry. Column type and planes type were expected to have similar results which are higher than needle attenuation levels.

EM wave propagation through a park environment also studied by characterizing the vegetation as a collection of 13 discrete random scatters which they are representing needles, leaves, branches and trunks of vegetation or trees. For three cases, the realistic parameters from actual measurements are used and simulation results are compared with the literature. The simulation results and discussion of loss calculation for rain, snow and vegetation will be given in the full paper. The good results are obtained.

Simulation of Discrete Model has attempted to give a new approach to electromagnetic wave propagation through rain, snow and vegetation. In general, the losses are found to increase with frequency and to be dependent on the characteristics of the biomass. The microwave dielectric behavior of rain, snow and vegetation material as a function of water content, frequency and temperature plays a central role in the propagation characteristics of electromagnetic waves.

The rate of attenuation varies with the density of the scatterers and moisture content of region. This study shows that the difference between path losses at 2270, 1800 and 900 MHz such that the loss is higher for a higher frequency range.

Acknowledgements: This work is supported by Bogazici Univ. Research Foundation Project Code: 5698

REFERENCES

1. “Specific attenuation model for use in prediction method”, ITU-R recommendations 838, 1994 PN series Volume, Propagation in non-ionized media.
2. Seker, S. S., “Multicomponents discrete propagation model of forest,” *IEE Proceedings H.*, vol. 143(3), pp. 201-206, 1995.
3. R. M. Rasmussen, J. Vivekanandan, J. Cole, B. Myers, and C. Masters C., “The estimation of snowfall rate using visibility”, *Journal of Applied Meteorology*, vol. 38, pp. 1542-1563, 1999.

Gold nanoplots absorption and scattering cross section calculation

Nayla El-kork*[1, 2], Feiran Lei[3], Mohammad Ismail Elnaggar[1,3], Paul Moretti[2], Bernard jacquier[2]

.

[1]Khalifa University of Science, Technology and Research, Sharjah, UAE.
[2]Laboratoire de Physico Chimie des Matériaux Luminescents, Lyon, France.
[3]Ohio State University, Columbus, Ohio, U.S.A.

[*]corresponding author: nayla.elkork@kustar.ac.ae

Abstract- We study Local Surface Plasmon Resonance (LSPR) behavior of illuminated elliptical gold nanoplots. We present finite element simulations that show the repartition of the electric field on the surface of an excited gold plot, and corresponding absorption and extinction spectra. Results are in accordance with experiment.

I- Introduction

When a metallic object is placed in an electromagnetic field, the electric component of the last pushes the positively charged nuclei in one direction and the negatively charged electron cloud in the other[1]. A restoring Coulomb force results in their oscillation and the constituted oscillating dipole emits an electromagnetic wave whose oscillation magnitude is at maximum for a specific excitation frequency. This results in maximum light emission, or the formation of Local surface Plasmon[2] Resonance (LSPR) emission. LSPR has been recently used widely in different sensing applications[3]. In this paper, we investigate the formation of LSPR emission on nanosized structures used for biosensing application

II- Materials and methods

Electron Beam Lithography (EBL) was used for the fabrication of Au spheroid disc arrays. Each dot has a height of about 70 nm, a diameter of 140nm and is distant by 340nm from its neighbours. Near Field Optical Microscopy images were obtained for these nanoplots, when excited at 633nm

Finite Element Method calculations in the frequency domain were done using ANSYS HFSS[4], for the simulation of the electric field distribution of an illuminated nano rod, having the same dimensions as those fabricated by EBL. The excitation light is assumed to be linearly polarized and the electric field along the longitudinal axis of the nanostructure. Different simulations were repeated at different wavelengths so that corresponding absorption and emission spectra could be plotted. Optical spectra were calculated similarly to Chau et Al[4] and the Au permittivity data were obtained from Johnson and Christy[5] and fitted to the Drude model, with corrections to include the particle size effect [6.]

III- Results

Theoretical results agree well with experiment in addition to literature. Two distinctive hot spots are at the apex of gold plots in both FEM simulation and SNOM optical image. The absorption spectrum peaks at about 600nm, in accordance with the excitation wavelength used to illuminate the sample. Full width at half maximum is about 100nm, typical to that of a single nanorod spectrum.

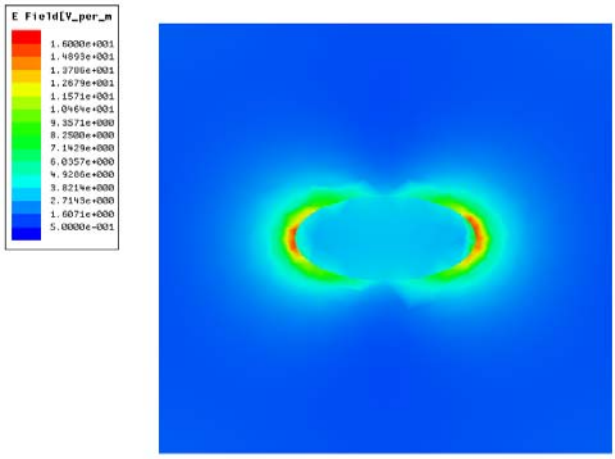

Figure 1: Gold nanoplot electric field simulation

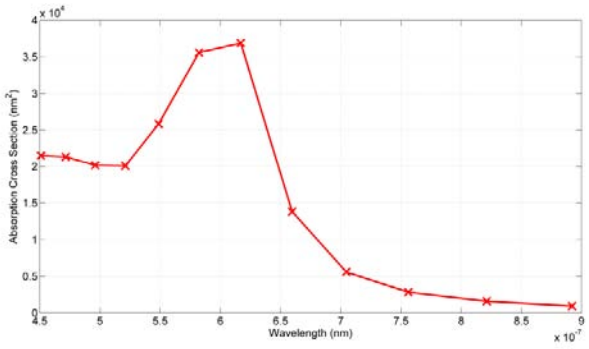

Figure2: Gold nanoplot calculated absorption spectrum

REFERENCES

1. K. Lance Kelly, E. Coronado, L. L. Zhao, G. C. Schatz "The optical properties of metal nanoparticles: The influence of size, shape and dielectric environment", P*roceedings Of The National Academy Of Sciences Of The United States Of America*," Vol. 107, no.3 ,pages 668-677, 2003.
2. E. Hutter et J. H. Fendler, "Exploitation of Localized Surface Plasmon Resonance", *Advanced Materials*, Vol. 16, no.19, pages 1685–1706, October, 2004.
3. C.M. Cobley, S.E. Skrabalak, D.J. Campbell, Y. Xia, "Shape-Controlled Synthesis of Silver Nanoparticles for Plasmonic and Sensing Applications" , *Plasmonics*, , Volume 4, no. 2, pages 171-179, June 2009.
4. http://www.ansys.com/
5. Y.F. Chau, M. W. Chen, and D. P. Tsai, "Three-dimensional Analysis of Surface Plasmon Resonance Modes on a Gold Nanorod.," *Applied Optics*, Vol. 48, no. 3, pages 617–22, January 20, 2009.
6. P. B. Johnson and R. W. Christy, "Optical Constants of the Noble Metals," *Physical Review B* 6, no. 12, pages 4370–4379, 1972.
7. S. Kawata, *Near-Field Optics and Surface Plasmon Polaritons*, vol. 81, Springer Berlin Heidelberg, 2001.

Scattering and inverse scattering

Scattering by chiral semi-elliptic-cylindrical boss on a ground plane

A-K. Hamid
University of Sharjah, ECE dept, Sharjah, United Arab Emirates
A-K. Hamid@sharjah.ac.ae.

Abstract- An exact solution is presented to the problem of scattering of a plane wave by a chiral semi-elliptic-cylindrical boss located on an infinite perfectly conducting ground plane. The problem is formulated by expressing the incident, reflected, scattered as well as the transmitted electromagnetic fields in terms of appropriate angular and radial Mathieu functions and sets of expansion coefficients. The unknown expansion coefficients can be determined by imposing the appropriate boundary conditions on the surface of the chiral semi elliptical cylinder. Numerical results are presented for echo pattern widths of semi-elliptic-cylindrical bosses of different chiral material, to show the effects of these on it.

A chiral medium is a reciprocal and isotropic medium characterized by different phase velocities for both right and left circularly polarized waves. In a lossless chiral medium, a linearly polarized wave undergoes a rotation of its polarization as it propagates. For chiral cylinders, these properties result in a coupling of the TM and TE polarizations. Analytic solutions describing elliptical cylinders with chiral media are given by [15-18].

The analysis and the software used for obtaining the results have been validated, by calculating the normalized backscattering widths for semi elliptical conducting cylinder, and showing that these results are in excellent agreement.

Consider a transverse magnetically (TM) polarized plane electromagnetic wave incident on an infinitely long chiral semi-elliptic-cylindrical boss located on an infinite perfectly conducting plane. The lengths of the semi-major and semi-minor axes of the ellipse that is forming the elliptical cross section are *a* and *b*, respectively, and the incident plane wave is assumed to make an angle φ_i with the x axis as shown in Fig. 1. For convenience, an elliptic coordinate system *u, v, z* with its origin at the centre of the elliptic face is defined. The *x* and *y* coordinates are related to *u* and *v* by $x=F\cosh(u)\cos(v)$, $y=F\sinh(u)\sin(v)$ with *F* being the semi-focal length of the ellipse. A time harmonic dependence of $\exp(j\omega t)$ is assumed, but suppressed for convenience.

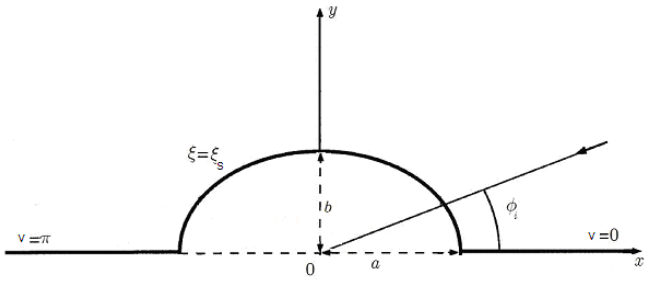

Fig. 1. Geometry of the problem.

The obtained numerical results are presented as normalized echo and backscattering pattern width for chiral semi elliptical boss for both TM polarization of the incident wave. We have selected $ka = 2.0$, axial ratio of 5, $\varepsilon_{rc} = 4.0$, $\mu_{rc} = 2.0$, $k\gamma = 0.15$ and $\varphi_i = 90^0$ [3]. To validate the analysis and the software used for calculating the results, we have computed the normalized echo pattern width for conducting semi elliptical cylinder, TM case. The results are in full agreement, verifying the accuracy of the analysis as well as the software used for obtaining the results [4].

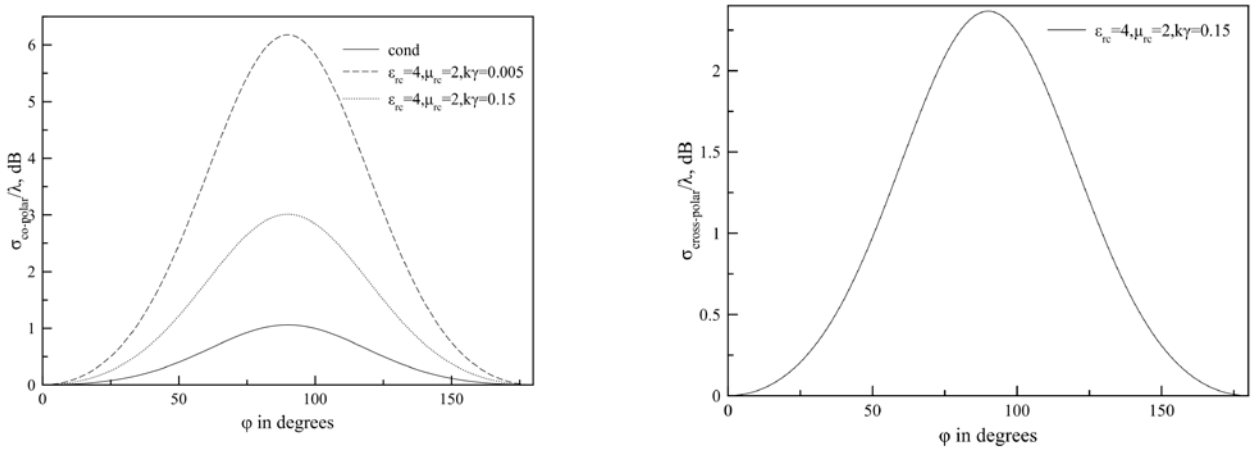

Fig. 2 Echo pattern width versus scattering angle for co and cross polarized chiral semi elliptical boss of ka=2.0, axial ratio of 5, and $\varphi_i = 90^o$, TM case.

Acknowledgements, Prof. A.-K. Hamid wishes to acknowledge the support he received from University of Sharjah, UAE, for conducting this research.

REFERENCES

1. N. Khatir, M. Al-Kanhal, and A. Sebak, "Electromagnetic wave scattering by elliptic chiral cylinder," Journal of Electromagnetic Waves and Applications, vol. 20, no. 10, pp. 1377–1390, 2006.
2. B. N. Khatir and A. R. Sebak, "Slot antenna on a conducting elliptic cylinder coated by chiral media," Electromagnetics, vol. 29, no. 7, pp. 522–540, 2009
3. A-K. Hamid, "Scattering by chiral lossy metamaterial elliptic cylinders", Accepted Applied Computational Electromagnetics Society (ACES) Journal, vol. 27, pp. 603-609, 2012.
4. A-K. Hamid and F.R. Cooray, "Exact Scattering by a Perfect Electromagnetic Conducting Semi-Elliptic-Cylindrical Boss on a Perfectly Conducting Ground Plane", International Journal of Electronics and Communications, AEUE, vol. 65, pp. 277-280, 2011.

Electromagnetic compatibility (EMc)

Design of Experiments for Factor Hierarchisation in Complex Structure Modelling

C. Kasmi[1, 2*], M. Hélier[2], M. Darces[2] and E. Prouff[1]

[1] Wireless and Hardware Security Lab. of the French Network and Information Security Agency, France

[2] UPMC Univ Paris 06, UR2, L2E, BC 252, 4 place Jussieu, 75005 Paris, France

[*]corresponding author: chaouki.kasmi@ssi.gouv.fr

Abstract- Modelling the distribution network is of fundamental interest to analyse the conducted propagation of unintentional and intentional electromagnetic interferences in the power-grid. The propagation is indeed highly influenced by channel behaviour. In this paper we investigate the effects of appliances and the position of cables in the network. First, the power-grid architecture is briefly described. Then, the principle of *Experimental Design* is described. Finally, the application of this well-founded methodology to power-grid modelling is discussed.

Many efforts are devoted to modelling the propagation of electromagnetic waves in a Low Voltage distribution network. Many input parameters of the models are not precisely defined. The uncertainties of those parameters may impact the accuracy of results. Hence, a stochastic approach is generally applied to generate a large number of random configurations. Estimating the effects of parameters variability should rely on a well-founded methodology. In this paper, we propose to hierarchize the input variables depending on their impact on the propagation of electromagnetic interferences [1]. Based on the results of the *Experimental Design* calculation, we also highlight the interaction between those parameters.

The Low Voltage distribution network can be characterized by the combination of several parameters. The power-grid in France is a 230 V power-supply at 50 Hz. Several cable cross-sections, from 0.6 to 300 mm², can be used depending on the maximal admissible current level. Moreover, different types of topologies (stars and chained topologies) can be used; a complex large power-grid can be represented by the combination of linear sub-networks. Finally, for safety requirements, several protections, such as fuses and breakers, may also be used. Their non-linear behaviour will not be considered.

In this paper, we propose to analyse the effects induced on the common mode output current level by the two main parameters, which are the cable topology and the connected appliances. To compare with realistic measurements, we have proposed a *de-embedding* method in [2] in order to characterize several appliances from 1 MHz to 100 MHz. Those measurements have been integrated into the CRIPTE Code [3] developed by the French Aerospace Laboratory (ONERA). Based on the *Electromagnetic Topology* and the resolution of the BLT Equation [4], we investigate both the effect of the cable positions, and those induced by the connected appliances, on the conducted interferences in the network. We have simulated the propagation of spurious compromising emanations generated by a computer, as depicted in Fig.1, with $V_{Source} = 1V$ and $Z_{Source}(f) = Z_{Computer}(f)$ where f is the working frequency. Based on physical considerations, it is assumed that the propagated mode in the network modelled as a Multiconductor Transmission Line is a quasi-TEM one.

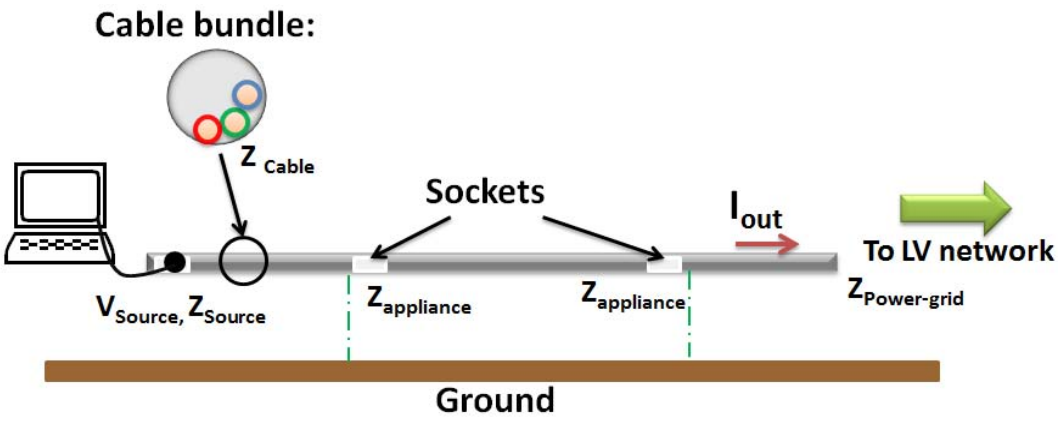

Figure 1: Modeled Low Voltage test network

The common mode end-current I_{out} is a function of several parameters as follows:

$$|I_{out}| = \alpha(V_{Source}, Z_{Source}, Z_{Cable}, Z_{Appliance}, Z_{Power\text{-}grid}, f)$$

where V_{Source} and Z_{Source} denote the electromagnetic noise generated by the computer, $Z_{Appliance}$ is the input impedance of the connected electronic equipment (printer, computer…), Z_{Cable} denotes the characteristic impedance of the equivalent Transmission Line. The latter variable is itself a function of the diameter of the cables, their height above ground, and their distance in the electric raceway. In order to simulate a realistic connection of the test network to a larger power-grid, the input impedance $Z_{Power\text{-}grid}$ has been measured.

The *Generalized Design of Experiments* aims at isolating the effects induced by each input variable, called factors, on the output current level; [5] is a good reference to start with this methodology. We introduce this formalism in order to highlight the effects of each factor and to point out the interaction between the appliances and the cable bundles. This is achieved by analysing the susceptibility of the end-current level to input parameters variability. The method is applied by using a stochastic simulation. We complete the analysis by showing the effects of the chosen working frequency band on the parameters effects and interactions. This leads to inferring the statistical distribution of the experimental design results.

Acknowledgements: This work is supported by the French Network and Information Security Agency (ANSSI); it emanates from a bilateral collaboration between University Pierre and Marie Curie (L2E) and ANSSI.

REFERENCES

1. D. V. Giri and F. M. Tesche, “Classification of Intentional Electromagnetics Environments (IEME)”, IEEE Transactions on Electromagnetic Compatibility, Vol. 4, pp. 322-328, August 2004.
2. C. Kasmi, M. Hélier and M. Darces, “High-frequency input impedance measurement of electronic devices based on a de-embedding technique”, Proceedings of EUROEM 2012, Toulouse, France.
3. J-P. Parmantier and S. Bertuol, “CRIPTE Training and Electromagnetic coupling on cable networks”, ONERA, Toulouse, France, 2011.
4. C.E. Baum, “Generalization of the BLT equation”, *Interaction Note*, Note 511, April 1995.
5. D. C. Montgomery, Design and Analysis of Experiments, ISBN-13 978-1118146927, Wiley, 2012.

Antenna theory and applications

Effect of superconducting patch on resonance characteristics of cylindrical microstrip antenna

D. Khedrouche[1], **and A. Benghalia**[2]
[1]Department d'Electronique, Université de M'sila, route Ichbilia, BP. 166, M'Sila, Algérie
[2]Department d'Electronique, Université de Constantine,25000 Constantine, Algérie
[*]corresponding author: dkhedrouche@yahoo.com

Abstract-A spectral moment method is applied to study the effect of superconducting patch on resonance characteristics of cylindrical-rectangular microstrip patch antenna. Numerical results of the resonant frequency and bandwidth versus the antenna parameters are presented. The obtained results show that the resonant frequency is affected significantly by the superconductivity property of the patch. Furthermore, the half-power bandwidth is considerably increased, which improves the narrow bandwidth characteristics of the microstrip structure.

Cylindrical microstrip structures have witnessed enormous growth in the past few years. Applications of cylindrical microstrip structures include high-speed aircrafts and spacecrafts, satellite and mobile communications, and radiators in biomedical applications [1]. A superconductivity of the patch is one of the parameters that have a great effect on the performance of microstrip antennas. Recently, several works concerning the effect of superconductivity of the patch on resonance and radiation characteristics of planar microstrip structures have been reported [2], [3]. But no or few works concerning the effects of this parameter on the performance of conformal microstrip structure have been reported in the open literature. In this paper, a spectral domain moment method is applied to study the effect of superconducting patch on resonance characteristics of cylindrical-rectangular microstrip patch antenna.

The relationship between the spectral tangential electric field at the air-substrate interface and the spectral electric surface current on the patch is given by [1]

$$\tilde{\tilde{E}}_v(k_z) = \bar{\bar{\tilde{G}}}_v(k_z) \cdot \tilde{\tilde{J}}_v(k_z) \tag{1}$$

$\bar{\bar{\tilde{G}}}_v(k_z)$ being the spectral dyadic Green's function of a single layer cylindrical microstrip structure.

The explicit component of $\bar{\bar{\tilde{G}}}_v(k_z)$ can be derived from [1, Equation (26)]. To include the superconductivity of the patch in the formulation, the surface electric field can be written as a superposition of an electric field in the patch and another out of the patch, this yield [2]

$$\tilde{\tilde{E}}_{vs} = \tilde{\tilde{E}}_{vs}^{in} + \tilde{\tilde{E}}_{vs}^{out} \tag{2}$$

Where the tangential electric field in the superconducting patch is given by

$$\tilde{\tilde{E}}_{vs}^{in} = Z_s \cdot \tilde{\tilde{J}}_v \tag{3}$$

with Z_s the surface impedance of superconducting patch and its expression is given, explicitly, in [3]

Now combining equations (1)-(3), we get

$$\tilde{\tilde{E}}_{vs}^{out} = \left(\bar{\bar{G}} - \bar{\bar{Z}}_s\right) \cdot \tilde{\tilde{J}}_v\left(k_z\right) \tag{4}$$

where

$$\bar{\bar{Z}}_s = diag(Z_s, Z_s) \tag{5}$$

and $\left(\bar{\bar{G}} - \bar{\bar{Z}}_s\right)$ represent the modified dyadic Green's function for the superconducting cylindrical-rectangular microstrip patch antenna. Then the Galerkin procedure of the moment method is applied to Equation (4) to obtain the resonant frequencies and the bandwidths of the considered structure.

Figure 1(a) shows that the resonant frequencies are shifted above when the superconducting patch of cylindrical microstrip antenna is used instead of the perfectly conducting one. The half-power bandwidth of a cylindrical microstrip antenna with a perfectly conducting and superconducting patches is shown in Figure 1(b).

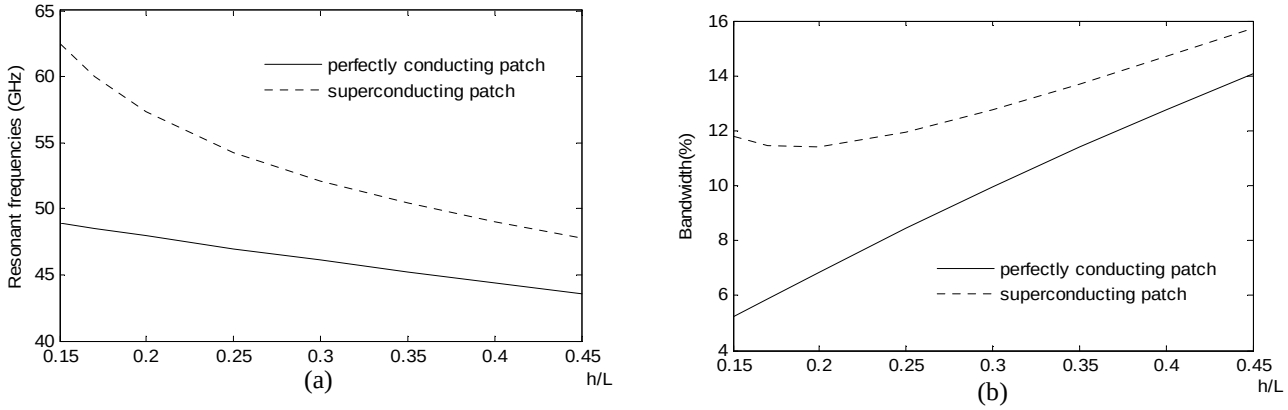

Figure 1: Resonant frequency and bandwidth of a perfectly conducting patch and a superconducting patch of cylindrical microstrip antenna versus the substrate thickness; a = 10 mm, L = 0.9 mm, w = 1.6 mm, σ_n = 210 S/mm, T/Tc = 0.5, λ_0 = 150 nm and e = 5 A^0.

The obtained results demonstrate a considerable increase in the half-power bandwidth; the improvement can reach 125 % for certain substrate thickness. This result allows us to overcome the problem of narrow bandwidth of the microstrip structures.

Acknowledgements, This work was supported by l'Agence Nationale pour le Développement de la Recherche Universitaire (ANDRU). via funding through the PNR-FONDAMENTAL program N° 8/u250/4235.

REFERENCES

1. Khedrouche, D., F. Bouttout, T. Fortaki, and A. Benghalia, " Spectral-domain analysis of multilayer cylindrical–rectangular microstrip antennas," *Engineering Analysis with Boundary Elements,* Vol.33, 930–939, 2009.
2. T. Fortaki, S. Benkouda1, M. Amir, and A. Benghalia, "Air gap tuning effect on the resonant frequency and half-power bandwidth of Superconducting microstrip Patch," *Piers online*, Vol. 5, No. 4, 350–354, 2009.
3. Barkat, O. ''Theoretical study of superconducting annular ring microstrip antenna with several dielectric layers," *Progress In Electromagnetics Research,* Vol. 127, 31-48, 2012.

Modified Corner Reflector Antenna fed by a Printed Dipole on a Quarter Cylinderical Substrate

Eqab Khleif, Dr.Hassan Ragheb, Dr.Sharif Iqbal
Department of Electrical Engineering
King Fahad University for Petroleum And Minerals
Dahran, Kingdom of Saudi Arabia
Email: g201003160@kfupm.edu.sa, h.ragheb@kfupm.edu.sa, sheikhsi@kfupm.edu.sa

***Abstract*—The paper presents a novel design of a corner reflector antenna which exhibits improved directivity and gain.**

The structure consisted of modified corner reflectors excited by printed dipole antennas on a quarter cylindrical substrate. The designed antenna is optimized using professional software (HFSS) to demonstrate improved antenna parameters. The proposed antenna can be used to improve the performance of 802.11 WiFi 2.4GHz devices. The simulation provided an impedance bandwidth 260 MHz at VSWR=2, and a gain of 7dB compared to isotropic radiation.

I. Introduction

Wireless communications are rapidly developing and geared by new applications demanding high bandwidth and need for high interference rejection, that imposes new demands and expectations to antenna system designers. Wireless system requires high directive antenna in order to cover the desirable area and reach critical customer location,while rejecting noise and interference. Antenna designers have used many techniques to achieve this objective. For instance V-shaped and the three-dimensional corner reflector antennas are some of these techniques that have greatly increases the directivities and gain. Reflector antennas, in one form or another, have been in use since the discovery of electromagnetic wave propagation in 1888 by Hertz.[1] Reflectors were wildly used to modify the radiation pattern of a radiating element.[2], by placings a plane sheet large enough at the back of the antenna to eliminate the backward radiated pattern. It was possible to introduce multiple lobes by controlling the distance from the apex, this is needed for beam forming and null introduction used for interference rejection. The development of reflector antennas was geared by the applications that requires high gains like, deep space communication, microwave point to point system , and satellite tracking systems. Naturally the reflector antenna takes different forms based on application, the most popular forms: planar reflector, corner reflector and curved(parabolic) reflector antennas.

The 90^o aperture corner reflector antenna was modified as shown in Fig(1), to be mounted on the quarter cylindrical substrate, and excited by a strip printed dipole. The reflecting sheets can be fixed in various aperture angle α , it can be π/N ,and the most common is the 90^o type. Microstrip line Printed dipoles are very popular due to ease of fabrication, low profile, low costs and conformable to non planar structures[4]. The

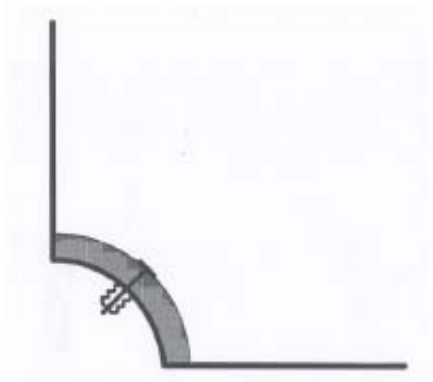

Fig. 1. Prototype for the Modified Corner Reflector with Printed Dipole on quarter cylinder substrate

cylindrical corner reflector is used in literature in an attempt to increase the gain and directivity of antenna [6], [7], the grid and conductive reflecting surface is used in the TV broadcasting and has shown a substantial improvement in the gain. Ordinary corner reflector antenna suffers from mechanical strength due to the feed supporting system. Also wind loading might affect the location if the feed which could degrade the antenna performance.The new design is rigid enough to avoid any mechanical displacement of the feed, more over making the feed as printed dipole on a fixed quarter cylinder never degrade antenna performance. The suggested structure use the cylindrical corner reflector with printed dipole. The cylindrical substrate has an influence on the resonance frequency based on the cylinder radius and reflecting sheets dimensions. In this complex structure, the reflector works as parasitic element that re radiates the impinged radiations either from or going to the radiating element, into free space, accordingly it has a direct relationship with the antenna gain. [7]

II. Antenna Design

The proposed antenna consist of three main parts, printed dipole, reflecting sheets, and the quarter cylinder substrate.

A. Strip Printed Dipole parameters And Design

Microstrip dipole of rectangular hatched or rectangular geometry as shown in figure can be designed for the lowest

resonant frequency using transmission line model [8]. The formula to calculate the value of , L, and W can be found in [8], [9]. The total dipole length is approximately given by:

$$L = 0.47\frac{v}{f} \tag{1}$$

where v is the actual propagation speed of wave in dielectric which is given by:

$$v = \frac{c}{\sqrt{\epsilon_{eff}}} \tag{2}$$

Where c is the free space light speed. Given the material dielectric ε_r , the substrate thickness h , and the resonance frequency f_r , the other antenna parameters can be found using the following steps:

- calculate the dipole antenna width W using :

$$W = \frac{1}{2f_r\sqrt{\mu_0\varepsilon_o}}\sqrt{\frac{2}{\varepsilon_r+1}} \tag{3}$$

  where ϵ_o and μ_o are the permitivity and permeability of free space.
- Calculate the effective dielectric constant ε_{eff} using the following equation for $\frac{W}{h} > 1$:

$$\varepsilon_{eff} = \frac{\varepsilon_r+1}{2} + \frac{\varepsilon_r-1}{2}(1+12\frac{h}{W})^{-1/2} \tag{4}$$

- Calculate the effective propagating wavelength is :

$$\lambda_{eff} = \frac{1}{2f_r\sqrt{\varepsilon_{eff}}\sqrt{\varepsilon_0\mu_0}} \tag{5}$$

- Calculating the input Impedance for the signal trace of width W and PCB thickness h with dielectric constant ϵ_r , the characteristic impedance is:

$$Z_c = \frac{120\pi}{\sqrt{\epsilon}[\frac{W}{h}+1.393+0.667Ln\frac{5.98h}{0.8W}]} \tag{6}$$

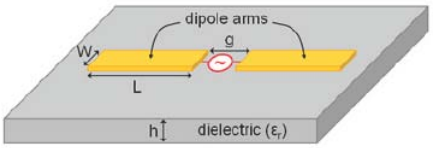

Fig. 2. Printed dipole on a planar substrate model

We have chosen the dielectric PCB for the substrate as Duroid(tm) with dielectric constant of 2.2 and thickness of 1.6mm. Dipole radials width can be found by equation 3 above and approximated to 4mm. The effective dielectric constant was found from equation (4) to be 1.827. Dipole radial length is found based on the effective wavelength of the propagating wave ($\lambda_{eff} = 92mm$) at 2.4GHz to be 23 mm. The reflectors dimensions are selected to be one wavelength for height and width. The cylindrical substrate has a radius of half wavelength as suggested by Balanis to get optimal radiation[1]. Optimized simulation found the radius of 0.7 wavelength as well as one wavelength. The effect of of different cylindrical radii on the antenna performance will be analyzed.

B. Cylindrical Corner Reflector

This part is based on design discussed in [6], [7], where the metallic cylinder sheet is replaced by dielectric substrate to be suitable for the printed dipole as the feed system. The figure below shows the structure, the feed will be replaced by the printed dipole with substrate.

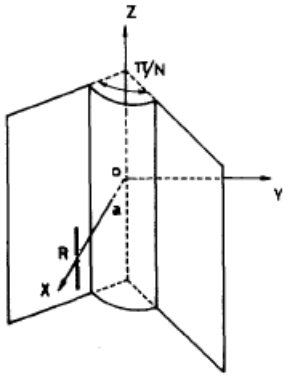

Fig. 3. Corner reflector with dipole feed.

Printed dipole on a substrate provides a more rigid structure that the wire dipole type feeding system offers. The reflectors are typically of HxL area dimensions.[6]

III. Simulation Results

Using HFSS we have build three antenna models The first that we will consider is a plane substrate with printed stip, dipole with dimensions illustrated in the previous section, and summarized in Table 1 above are used, the proceeding sections describes the deign and the results.

TABLE I
Antenna Dimentions

Designed Frequency	2.4 GHz
Dipole Radials Length	23 mm
Dipole Radials width	4 mm
Gap	1 mm
substrate height	1.6 mm
dielectric constant	2.2
Effective Wavelength	92 mm
Cylinder Radius	0.5λ
Cylinder Height	λ
Reflecting sheet HxL	$\lambda * \lambda$

A. Microstrip Printed Dipole on a Planar Substrate

Printed strip dipole geometry is constructed using HFSS Ansoft software. The EM solver was set to produce the

corresponding return loss for the range of frequencies from 0.1GHz to 4GHz. As one can see from Fig.4,the resonance occur at 2.4GHz with a dip at -22dB and an impedance bandwidth of 350MHz at VSWR=2. The far field radiation pattern is also illustrated in Fig.5 , which shows the normal dipole pattern.

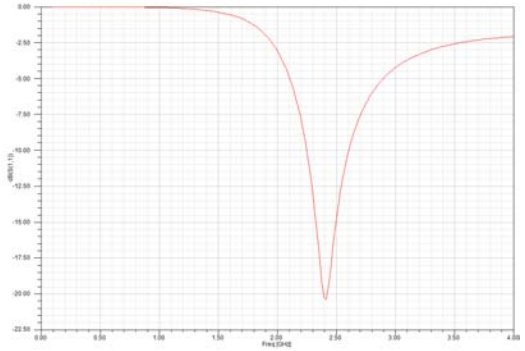

Fig. 4. Return loss of the Planar printed dipole antenna

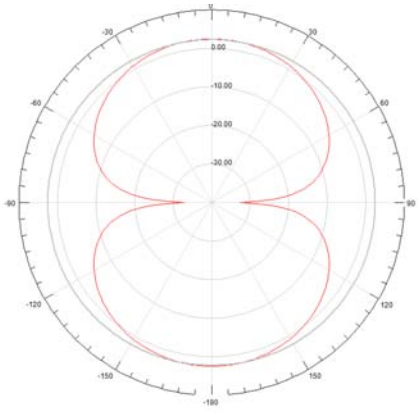

Fig. 5. Planar printed dipole radiation pattern

The results from simulations showed an agreement with the calculations obtained from the design section. The simulation shows that the input impedance is perfectly matched to 50 Ohm.

B. Microstrip Printed Dipole on the cylindrical substrate

The second step is to replace the planar substrate by a quarter cylindrical. It is part of a right circular cylinder along the z-direction. The coordinate system is rotated such that the radiation is directed to 90^o in the x-y plane. Compared to the planar structure, the results shows a similar radiation pattern and a slight reduction in the gain as shown in Fig 8 compared to results in Fig 5 using the planar substrate. In both cases the impedance was perfectly matched to 50 ohm.
The radiation pattern in the vertical plan is more directive than that of the planar strip dipole case. That was the effect of the curvature on the radiation pattern. In addition; there is a slight shift up in resonance frequency to 2.6 GHz with -18dB RL. It has a broader bandwidth of 420MHz as depicted in Fig 7.

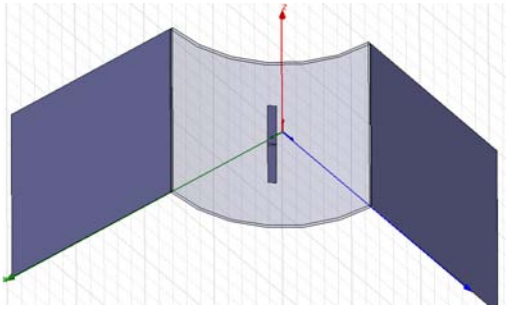

Fig. 6. Modified corner reflector with printed dipole-prototype

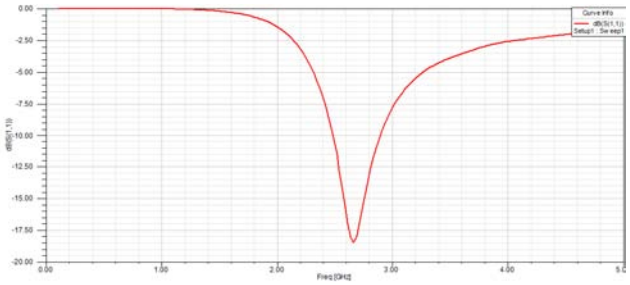

Fig. 7. S11 for cylindrical substrate printed dipole with no reflectors

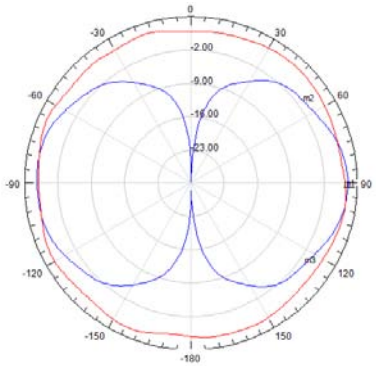

Fig. 8. Printed dipole Radiation pattern using cylindrical substrate

Fig. 8 above is showing the E-plane and H-plane field patterns which is very similar to the planar substrate field patterns obtained in section 1.

C. Final Antenna Structure with Reflectors added

Fig. 6 shows the prototype of the proposed antenna geometry using HFSS Ansoft Software. The Return loss graph is showing an impedance bandwidth 260 MHz at VSWR=2 around the resonance frequency of 2.3GHz with a dip of -23dB. Clearly the addition of reflectors has shifted down the resonance frequency and decreased the bandwidth of the antenna. The simulation is showing again of 9.3dB which is 7dB more than that of the model without the reflectors.

The antenna directivity and gain have increased in the direction of 45^o as designed with new bandwidth of 260MHz(13 percent of the operating frequency).

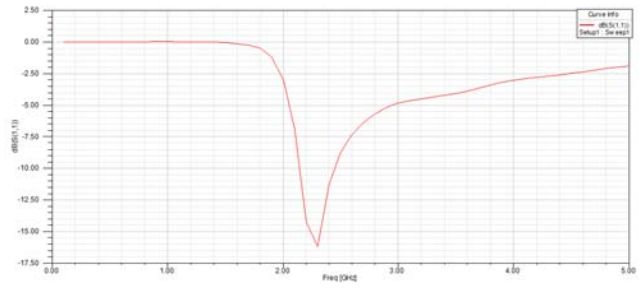

Fig. 9. Return loss of the antenna, BW= 260 MHz at VSWR=2 around the resonance frequency 2.3GHz.

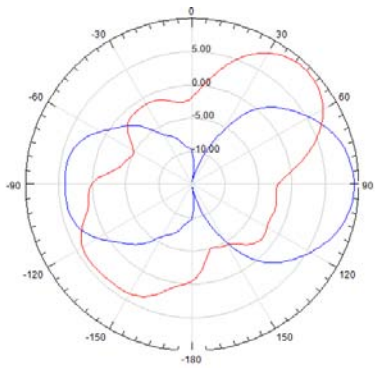

Fig. 10. Radiation patterns E plane , H plane .

The radiation efficiency is 86 percent, yet to be enhanced by doing more optimization to the structure. This will allow us to include more accurate simulation results at the conference in addition to the fabrication and measurements results.

IV. Conclusion

A low cost strip dipole antenna was used as a feed for the modified corner reflector operating at 2.4GHz for WLAN applications. Modified corner reflector has shown an improvement in gain and directivity by 7dB, with HPBW = 52^o, compared to isotropic radiation obtained from the strip printed dipole with no reflectors. The simulation indicates an impedance bandwidth of 260 MHz at VSWR=2. The quarter cylindrical substrate has minor influence on the radiation and the resonance frequency. Simulation results agrees with the theoretical design values,

V. Acknowledgments

Many thanks goes to King Fahad University for Petroleum and Minerals for providing the facility and resources for this research.

References

[1] Costantin A. Balanis,. *Antenna Theory, Analysis and Design, Chapter 14,15: Microstrip Patch*. John Willey And Sons, NY, 2nd edition (2008).

[2] John D Kraus,McGRAW HIll . *Antennas, Second Edition*. McGRAW HIll International Edition (1988).

[3] Girish Kumar,K.P. Ray. *Broad band Microstrip Antennas*. Artech House, INC(2003).

[4] JR James,PS Hall, *Handbook Of Microstrip Antennas*. Peter, Peregrinus Ltd(1989).

[5] Samir Dev Gupta *Design and Performance Analysis of Cylindrical Antenna and Array using Conformal Mapping Technique*. Samir Dev Gupta, Department of Electronics and Communication Engineering, JIIT, Noida, UP, India, samirdev.gupta@jiit.ac.in. MC Srivastava, Director, JIIT Sector-128, UP, India, mc.srivastava@jiit.ac.in. Amit Singh, Agilent Technologies, Manesar, Haryana, INDIA, amit.singhjiit@gmail.com.

[6] HASSAN M. ELKAMCHOUCHI *Cylindrical and Three-Dimensional Corner Reflector Antennas*. HASSAN M. ELKAMCHOUCHI, MEMBER, IEEE

[7] J. A. Romo, I. F. Am]nitzine, and J. Garate *Optimised Design of Cylindrical corner reflectors For Applications on TV Broadband Antennas*. Department of Elctronic and Telecommunications, University of Basque Country, AlamedaUrquilo s/n, Bilbao, Spain. juanantonio.romo@ehu.es; iggnacio.anitzine@ehu.es;jgarate001@ehu.es

[8] M.H.Jamaluddin, M.K. A. Rahim M. Z. A. Abd. Aziz, A. Asrokin *MICROSTRIP DIPOLE ANTENNA FOR WLAN APPLICATION*. Wireless Communication Center (WCC), Faculty of Electrical Engineering, Universiti Teknologi Malaysia, Email: haizal@fke.utm.my, mkamal@fke.utm.my , matjoin@yahoo.com, awi82@yahoo.com

[9] David, David M. Pozar *Microwaves Engineering*. John Willy and Sons, Inc, 1998

Resonant Frequency of Tunable Microstrip Ring Antenna Printed on Isotropic or Uniaxial Anisotropic substrate

A. Messai[1], S. Bedra[2*], M. Amir[2], and T. Fortaki[2]
[1] Electronics Department, University of Constantine, Algeria.
[2] Electronics Department, University of Batna, Algeria.
[*]corresponding author: bedra_sami@yahoo.fr

Abstract-In this study, the resonant frequency of annular ring microstrip resonator with uniaxial anisotropic substrate and air gap layer is analyzed. The cavity model for simple ring microstrip antenna is extended with some modifications for the tunable geometry taking into account the anisotropy in the layer. The theoretical resonant frequency results are in very good agreement with the experimental results reported elsewhere. The air gap tuning effect on the resonant characteristics is also investigated for fundamental and higher order modes.

1. Introduction

The cavity model has been chosen as a simple alternative to analyze and predict the behavior of microstrip ring antennas [1]. The aim of this work to perform an accurate and efficient analysis of annular-ring microstrip antennas on double layer substrate, as well as to perform the analyses for annular ring microstrip antennas on a single layer substrate and on a tunable substrate, as particular cases.

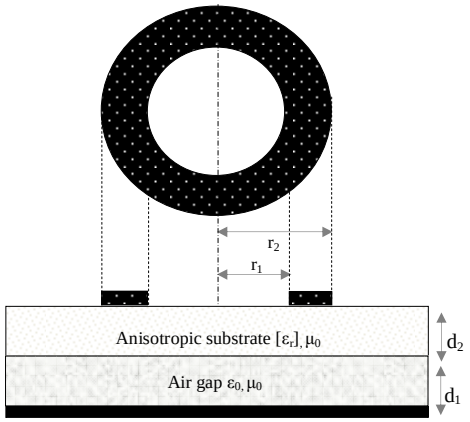

Figure 1. Geometry of a tunable microstrip ring antenna.

2. Outline of the numerical procedure

In order to calculate the resonant frequency, the original tow-layered structure (Fig.1) is reduced to a single layered one having an equivalent relative permittivity [2, 3]

$$f_{r,mn} = \frac{k\upsilon_0}{2a\sqrt{\varepsilon_{eq}}} \tag{1}$$

To account for the fact that small fraction of the field exists outside the dielectric; it is customary to use effective

permittivity ε_{eff} in place of ε_{req} [3]. If we want to take the substrate uniaxial anisotropy's into account, the relative dielectric permittivity ε_r will be replaced with the tensor $\varepsilon_r = diag(\varepsilon_x, \varepsilon_x, \varepsilon_z)$ [4], where ε_x and ε_z are the relative dielectric permittivity along x and z axis, respectively.

3. Results and discussion

In order to confirm the computation accuracy, our numerical results are compared with those obtained from [5, 6]. The comparison is done for different air separations with maximum deviation within 3%. Figure 2 depicts the influence of the air gap thickness on the resonant frequency of an annular ring microstrip patch for three anisotropic dielectric substrates. As it can be seen, the resonant frequency reduces considerably when the dielectric substrate changes from boron nitride to epsilam-10, and this is in contrast to what happens when the medium changes from epsilam-10 to sapphire.

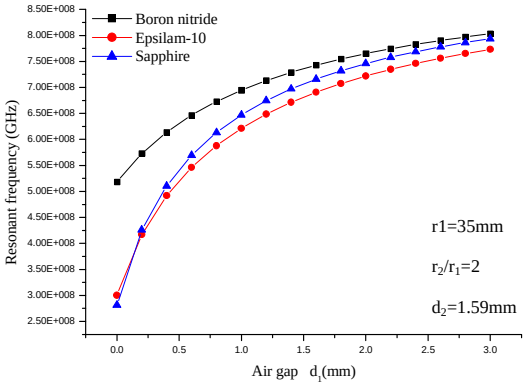

Figure 2. Resonant frequency versus air gap thickness.

4. Conclusion

The obtained results show that when the permittivity ε_z is changed and ε_x remains constant, the resonant frequency changes drastically, on the other hand, we found a slight shift in the resonant frequency when the permittivity ε_x is changed and ε_z remains constant. This means that important errors may arise in the computation of resonant frequencies of microstrip antennas with air gaps if substrate anisotropy is neglected.

REFERENCES

1. V. Sathi, Ghobadi. Ch and Nourinia, J., "Optimization of circular ring microstrip antenna using genetic algorithm", *Int J Infrared Milli Waves* 29:897–905, 2008.
2. I. J. Bahl, and Bhartia, P., "Microstrip Antennas, Chap. 3". *Artech House, Dedham, MA*, 1982.7
3. K. F. Lee, and Dahele, J. S., "Theory and experiment on the annular-ring microstrip antenna", *ANN.TÉLÉCOMMUN* 40, n°9-10, 1985.
4. Y. Tighilt, Bouttout, F., and Khellaf, A., "Modeling and Design of Printed Antennas Using Neural Networks", *Int J RF and Microwave CAE* 21:228–233, 2011.
5. K. F. Lee, and Dahele, J. S., "The two-layered annular ring microstrip antenna", *Int. J. Electron*., pp. 207-217, 1986.
6. J. Gomez-Tagle, and Christodoulou, C. G., "Extended cavity model analysis of stacked microstrip ring antenna", *IEEE Trans. Antennas Propagat*., Vol. 45, No. 11, Nov. 1997.

Resonance of superconducting microstrip antenna with aperture in the ground plane

S. Benkouda[1], **T. Fortaki**[1*], **M. Amir**[1], **and A. Benghalia**[2]
[1]Electronics Department, University of Batna, Algeria
[2]Electronics Department, University of Constantine, Algeria
[*]corresponding author: t_fortaki@yahoo.fr

Abstract-This paper presents a rigorous full-wave analysis of the high T_c superconducting rectangular microstrip antenna with a rectangular aperture in the ground plane. To include the effect of the superconductivity of the microstrip patch in the full-wave analysis, a complex surface impedance is considered. The proposed approach is validated by comparing the computed results with previously published data. Results showing the effect of the aperture on the resonance of the superconducting microstrip antenna are given.

Introduction: Rectangular microstrip patches can find application in microwave integrated circuit as planar resonators. Also, they can be used as resonant antennas. When a microstrip patch resonator acts as an antenna, the microstrip patch can be fed through an aperture cut into a microstrip line ground plane [1]. This feeding configuration has been found very advantageous for several reasons [2], [3]. Since ground-plane apertures can play a role in the design of microstrip patch antennas, the computer codes developed for the analysis of microstrip patch resonators should be able to account for the effect of possible apertures existing in the ground plane of the resonators. Setting aside the topic of microstrip patches over ground planes with apertures, recently there is some interest in the use of superconducting materials in microwave integrated circuits, which is due to their main characteristics, such as: very small losses, which means low-attenuation and low-noise, very small dispersion up to frequencies of several tens of GHz, smaller devices due to the lower losses, which leads to larger integration density and reduction in the time of propagation of the signals in the circuits. In this paper, we present a rigorous full-wave analysis of the high T_c superconducting rectangular microstrip antenna with a rectangular aperture in the ground plane.

Theory: The problem to be solved is illustrated in Figure 1. We have a high T_c superconducting rectangular microstrip patch of thickness e_1 over a ground plane with a rectangular aperture. The superconducting patch is characterized by a critical temperature T_c, a zero-temperature penetration depth λ_0 and a normal state conductivity σ_n. Let $\mathbf{J}_0(x, y)$ be the surface current density on the ground plane with rectangular aperture and let $\mathbf{J}(x, y)$ be the surface current density on the superconducting rectangular patch. Also, let $\mathbf{E}(x, y, 0)$ and $\mathbf{E}(x, y, d)$ are the values of the transverse electric field at the plane of the aperture and at the plane of the superconducting patch, respectively. Following a mathematical reasoning similar to that shown in [3], we can obtain a relation among $\mathbf{J}_0(x, y)$, $\mathbf{J}(x, y)$, $\mathbf{E}(x, y, 0)$ and $\mathbf{E}(x, y, d)$ in the vector Fourier transform domain given by

$$\mathbf{e}(\mathbf{k}_s, d) = \overline{\mathbf{G}}(\mathbf{k}_s) \cdot \mathbf{j}(\mathbf{k}_s) + \overline{\mathbf{\Gamma}}(\mathbf{k}_s) \cdot \mathbf{e}(\mathbf{k}_s, 0) \tag{1}$$

$$\mathbf{j}_0(\mathbf{k}_s) = -\overline{\mathbf{\Gamma}}(\mathbf{k}_s) \cdot \mathbf{j}(\mathbf{k}_s) + \overline{\mathbf{Y}}(\mathbf{k}_s) \cdot \mathbf{e}(\mathbf{k}_s, 0) \tag{2}$$

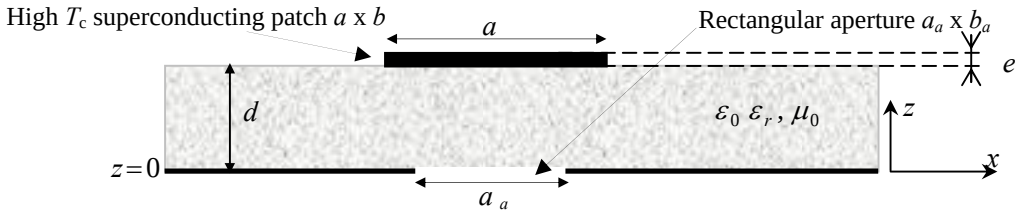

Figure 1. Superconducting rectangular microstrip antenna with rectangular aperture.

Table 1. Comparison of our calculated resonant frequencies with previously published data.

Relative permittivity (ε_r)	Resonant frequencies (GHz)		
	Cavity model [4]	Full-wave analysis [5]	Our results
11	41.638	41.041	41.585
16	35.300	34.856	34.816
23.81	28.937	28.671	28.764

Considering the superconducting effects, we need simply to modify equation (1) by replacing $\mathbf{G}(\mathbf{k}_s)$ par $\mathbf{G}(\mathbf{k}_s)$-Z_s . **I**, where **I** is the 2x2 unit matrix and Z_s is the surface impedance of the superconducting patch. It is determined by using London's equation and the Gorter-Casimir two-fluid model [4], [5].

Numerical results and discussion: In order to confirm the computation accuracy, our results are compared with the theoretical results of Richard *et al.* [4] and Silva *et al.* [5] when there is no aperture in the ground plane. The patch is fabricated with a YBCO superconducting thin film with parameters $\sigma_n = 10^6$ S/M, $T_c = 89$ K, $\lambda_0 = 140$ nm and $e = 350$ nm. The patch size is a x b = 1630 µm x 935 µm and the substrate has a thickness of d = 254 µm. The operating temperature is T = 50 K. Table 1 summarizes our computed resonant frequencies and those of [4] and [5] for three different materials and differences between these three results of less than 0.7% are obtained.

We have also obtained other numerical results (not given here) in order to study the effect of the aperture on the resonant frequency of the superconducting microstrip antenna. It has been found that the resonant frequencies of the superconducting patches over ground planes without apertures are larger than those obtained with apertures. This last result agrees with that discovered theoretically for perfectly conducting patches [3].

REFERENCES

1. Benkouda, T. and T. Fortaki, "Resonance of rectangular microstrip patch over ground plane with rectangular aperture in the presence of high-permittivity dielectric layer below the aperture," in *Proceedings of Progress In Electromagnetics Research Symposium*, Marrakech, Morocco, March 2011, 239–241.
2. Losada, V., R. R. Boix and M. Horno, "Resonance modes of circular microstrip patches over ground planes with circular apertures in multilayered substrates containing anisotropic and ferrite materials," *IEEE Trans. Microwave Theory Tech.*, Vol. 48, No. 10, 1756–1762, 2000.
3. Fortaki, T. and A. Benghalia, "Rigorous Full-wave analysis of rectangular microstrip patches over ground planes with rectangular apertures in multilayered substrates that contain isotropic and uniaxial anisotropic materials," *Microwave Opt. Technol. Lett.*, Vol. 41, No. 6, 496–500, 2004.
4. Richard, M. A., K. B. Bhasin and P. C. Claspy, "Superconducting microstrip antennas: an experimental comparison of two feeding methods," *IEEE Trans. Antennas Propagat.*, Vol. 41, No. 7, 967–974, 1993.
5. Silva, S. C., A. G. d'Assuncao and J. R. S. Oliveira, "Analysis of high T_c superconducting microstrip antenna and arrays," in *Proceedings of SBMO/IEEE MTT Symposium*, 1999, 243–243.

Resonance of high T_c superconducting microstrip patch in a substrate-superstrate configuration

S. Benkouda[1], **T. Fortaki**[1*], **M. Amir**[1], **and A. Benghalia**[2]
[1]Electronics Department, University of Batna, Algeria
[2]Electronics Department, University of Constantine, Algeria
[*]corresponding author: t_fortaki@yahoo.fr

Abstract-The effect of a protecting dielectric superstrate on the resonance of a high T_c superconducting microstrip patch is investigated. The analysis approach is based on the spectral-domain method of moments in conjunction with the complex resistive boundary condition. The complex surface impedance of the superconducting thin film is determined using London's equation and the two-fluid model of Gorter and Casimir. Numerical results show that the resonant frequency of the high T_c superconducting rectangular patch decreases monotonically with increasing superstrate thickness, the decrease being greater for high permittivity loading.

Introduction: Recently, there has been a growing interest in the use of superconducting materials in microwave integrated circuits, which is due to their main characteristics, such as: very small losses, which means low-attenuation and low-noise, very small dispersion up to frequencies of several tens, smaller devices due to the lower losses, which leads to larger integration density and reduction in the time of propagation of the signals in the circuits [1].

Superstrate dielectric layers are often used to protect printed circuit antennas from environmental hazards, or may be naturally firmed (e.g. ice layers) during flight or severe weather conditions. Theoretical researches on the effect of dielectric superstrate on the resonant frequency of a perfectly conducting patch are abundant [2]; however, there is no theoretical report on the effect of superstrate on the resonance of a high T_c superconducting rectangular microstrip antenna.

Formulation: The geometry under consideration is illustrated in Figure 1. A rectangular superconducting patch of thickness e is printed on a grounded dielectric slab of thickness d_1. The substrate is characterized by the free-space permeability μ_0 and a permittivity $\varepsilon_0\varepsilon_{r1}$. Above the radiating patch is the superstrate layer of thickness d_2 with permeability μ_0 and a permittivity $\varepsilon_0\varepsilon_{r2}$. The superconducting film is characterized by a critical temperature T_c, a zero-temperature penetration depth λ_0, and a normal state conductivity σ_n. Following a mathematical reasoning similar to that shown in [2] for obtaining a relation among the surface electric field at the plane of the superconducting patch and the surface current on the patch in the spectral domain given by

$$\begin{bmatrix} \tilde{E}_x \\ \tilde{E}_y \end{bmatrix} = \begin{bmatrix} Q_{xx} & Q_{xy} \\ Q_{yx} & Q_{yy} \end{bmatrix} \cdot \begin{bmatrix} \tilde{J}_x \\ \tilde{J}_y \end{bmatrix} \qquad (1)$$

Concerning the superconducting effects, we need simply to modify equation (1) by replacing Q_{xx} by Q_{xx} - Z_S and Q_{yy} by Q_{yy} - Z_S, where Z_S is the surface impedance of the superconducting patch. When the thickness of the superconducting patch is less than three times the zero-temperature penetration depth, the surface impedance

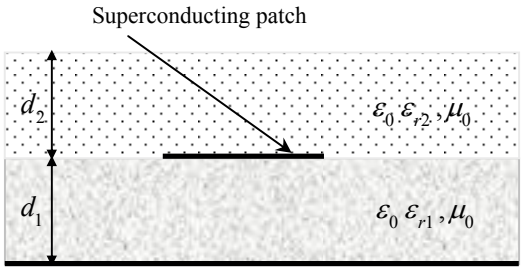

Figure 1. Structure of a high T_c superconducting patch in a substrate-superstrate configuration.

can be approximated as in [1]. Now, Galerkin method can be applied to equation (1) to obtain the resonant frequency of the superconducting patch in a substrate-superstrate configuration. Note that the resonant frequencies are defined as the real parts of the complex roots of the characteristic equation [3].

Influence of the superstrate on the resonant frequency: Now, we study the influence of the superstrate thickness on the resonant frequency. A rectangular patch having a length a = 8 mm and width b = 5 mm is printed on a substrate of oxide of magnesium (ε_{r1} = 9.6, d_1 =0.4 mm). For the superstrate we have considered three different materials. These materials are the arsenide of gallium (ε_{r2} = 6.6), the oxide of magnesium (ε_{r2} = 9.6) and the oxide of beryllium (ε_{r2} = 12.5). Figure 2 shows the resonant frequency versus the superstrate thickness. It is observed that when the superstrate thickness grows the resonant frequency decreases monotonically. The decrease being more important for superstrates with high relative permittivities.

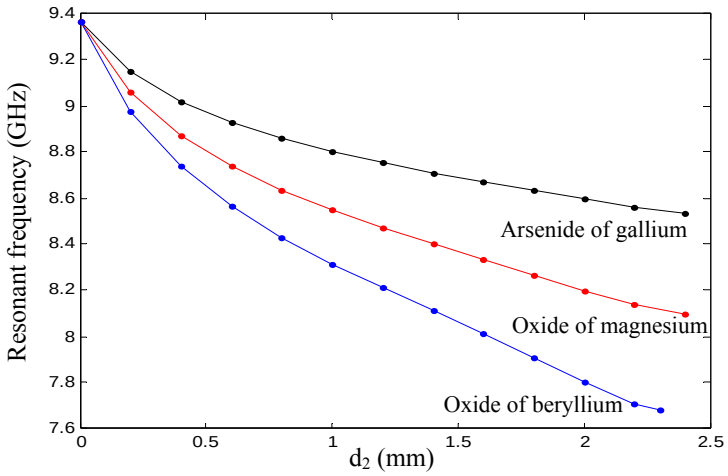

Figure 2. Resonant frequency of the superconducting patch versus the superstrate thickness. The characteristics of the superconducting film are $\sigma_n = 7.46.10^6$ S/m, T = 77 K, T_c = 89 K, λ_0 = 180 nm and e = 150 nm.

REFERENCES

1. Fortaki, T., M. Amir, S. Benkouda and A. Benghalia, "Study of a high T_c superconducting microstrip antenna," *PIERS Online*, Vol. 5, No. 4, 346–349, 2009.
2. Fortaki, T., L. Djouane, F. Chebbara and A. Benghalia, "Radiation of a rectangular microstrip patch antenna covered with a dielectric cover," *Int. J. Electronics*, Vol. 95, No. 9, 989–998, 2008.
3. Fortaki, T., L. Djouane, F. Chebbara and A. Benghalia, "On the dual-frequency behavior of stacked microstrip patches," *IEEE Antennas Wireless Propagat. Lett.*, Vol. 7, 310–313, 2008.

Multiport Antenna Systems for Space-Time Communications

E. Tsakalaki[*1], O. N. Alrabadi[1], M. Pelosi[1] and G. F. Pedersen[1]
[1]Antennas, Propagation & Radio Networking Section, Aalborg University, Denmark
[*]corresponding author: et@es.aau.dk

Abstract- The paper presents the concept of multiport antenna systems where multiple active and passive ports are deployed. The passive ports, implemented via tunable reactance-assisted (parasitic) antennas, can alter the far-field and near-field properties of the antenna system expressed by the antenna efficiency, electromagnetic coupling and spatial correlation. The system can be optimized in order to enhance the spatial multiplexing performance whereas the performance gains come at no significant additional cost and hardware complexity.

Multiple-antenna systems are in the forefront of wireless research due to their potential for improving the capacity of mobile services by offering remarkable diversity and spatial multiplexing gains. Such systems are conventionally implemented by a set of active antenna elements where each element is connected to a separate RF chain [1]. However, with the ongoing trend toward miniature, compact and highly integrated telecommunication devices, such systems suffer from high antenna correlation and decreased antenna efficiency due to the strong mutual coupling among the closely spaced antenna elements that alters the input impedance seen by the RF ports thus leading to a mismatch loss [2]. Techniques such as decoupling and matching (DMN) networks have been proposed but incur additional losses and complexity besides their negative impact on the bandwidth [3]. Uncoupled matching techniques such as the single-port matching may not hit the bandwidth but trade antenna efficiency for correlation maximizing the capacity only in the high SNR regime [1]. This paper addresses the limitations of multiple-active antennas by introducing hybrid array topologies of multiple-active and passive antenna architectures. The passive antenna ports are terminated with switched or tunable reactive loads that alter the boundary conditions of the antenna structure and, therefore, the propagation conditions. Firstly, this incurs advantages in terms of the antenna real-estate since the passive terminations are attached to low-cost switches / loads rather than to full RF chains. Furthermore, the antenna system is now able to alter the propagation channel by altering its radiation properties. This degree of freedom that does not exist in conventional antenna implementations permits us to treat the array configuration and its radiation properties as an additional component in the joint optimization of the system performance, thus allowing the system to approach its theoretical performance limits. The paper generalizes our prior work [2] (where theoretical models of dipoles/monopoles were used) to any kind of reconfigurable, switched, tunable or adaptive antenna structure.

To illustrate the concept of the general multiport network model, Figure 1 shows a 3-port system comprising a type of two-merged planar Inverted-F (PIFA) antenna structure whose feeding points constitute the two active ports (indexed as 1 and 2). The passive port (port 3) is placed at the end of the slot on top of the structure and is controlled via a variable reactive load. The structure is placed over a (55x110)mm^2 ground plane of typical modern smart phone dimensions and is modeled as lossless perfect electric conductor using the electromagnetic simulator CST MICROWAVE STUDIO®. Let $\hat{\mathbf{Z}}_{3x3}$ denote the 3x3 (standard) mutual impedance matrix with entries $\hat{Z}_{i,j}$, $i,j \in \{1,2,3\}$. The coupling model of such antenna system can be alternatively expressed by the 2x2 impedance matrix $\mathbf{Z}_{2x2}$ of the active ports expressed as a function of the reactive load $jX\ \Omega$ of the passive control

port. This matrix has entries

$$Z_{i,i}= \hat{Z}_{i,i}-Z_x \quad \text{and} \quad Z_{i,j}= \hat{Z}_{i,j}-Z_x, \quad \text{where} \quad i,j \in \{1,2\} \quad \text{and} \quad Z_x= (\hat{Z}_{1,2}\, \hat{Z}_{2,1}) /(\hat{Z}_{3,3}+ jX).$$

The equivalent impedance matrix expresses the fact the coupling and the input impedance of such antenna system is controlled indirectly, thanks to the mutual interactions among the antenna ports, via the passive load. Equivalently, the coupling model can be directly expressed by the collapsing the 3x3 scattering parameters matrix $\hat{\mathbf{S}}_{3x3}$ to an equivalent 2x2 scattering matrix $\mathbf{S}_{2x2}$ that is a function of the reactive load [4]. In our topology, the matrix $\mathbf{S}_{2x2}$ has entries $S_{1,1}=S_{2,2}$ and $S_{1,2}=S_{2,1}$ due to symmetry. The scattering parameters are illustrated in Figure 2 where the passive port has been appropriately tuned so that the active ports efficiently resonate at ~2GHz. It is noted that the impressive isolation level among the active ports has been attained within a type of *uncoupled simultaneous matching and decoupling* solution. Such method approaches the performance gains of conventional DMNs yet without any significant additional losses and hardware complexity. Since our interest is in the final spatial multiplexing performance, in the full version of the paper we shall explain how we can directly tune the variable control port in order to optimize the end system throughput that captures the individual antenna parameters (antenna efficiency, efficiency imbalance, and correlation) in arbitrary channel scenarios.

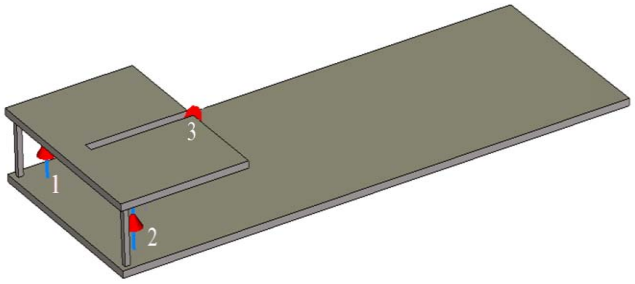

Figure 1 The multiport antenna system comprised of two active ports (ports 1 and 2) indirectly controlled via a passive port (port 3)

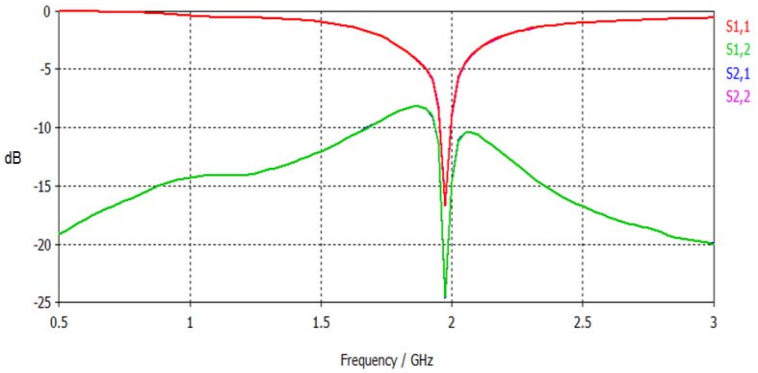

Figure 2 The frequency response of the scattering parameters of the proposed multiport antenna system.

REFERENCES

1. Lau B.K., Andersen J.B., Molisch A., Kristensson G., "Antenna matching for capacity maximization in compact MIMO systems," *3rd Int'l Symp. Wirel. Commun. Systems (ISWCS)*, pp. 254-257, 2006.
2. Tsakalaki, E., Alrabadi, O.N., Papadias C.P., Prasad, R. "Adaptive reactance-controlled antenna systems for MIMO applications," *IET Microwave Antennas & Propagation Journal*, Vol. 5, No. 8, pp. 975-984, 2011.
3. Lau B.K., Andersen J.B., Molisch A., "Impact of matching network on bandwidth of compact antenna arrays," *IEEE Trans. Antennas & Prop.*, Vol. 54, No., 11, pp. 3225-3238, 2006.
4. Alrabadi O.N, Pedersen G.F., "Antenna coupling in multi active multi passive port topologies," *6th European Conf. Antennas and Propag. (EUCAP)*, pp. 1063-1065, 2012.

Modified Ultrawideband Antipodal Tapered Slot Antenna With Improved Radiation Characteristics.

Muhammad. A. Ashraf [(1)], Khalid Jamil[(2)], Abdel Razik Sebak [(3)], Zeyad O. Al-Hekail[(1)], Majeed A. Alkanhal [(1)]
[1]Department of Electrical Engineering, King Saud University, Riyadh, 11421, Kingdom of Saudi Arabia
[2]PSATRI, King Saud University, Riyadh, 11421, Kingdom of Saudi Arabia
[3]Electrical and Computer Engineering Department, Concordia University, Montreal, Canada
mashraf@ksu.edu.sa

Abstract —This paper presents a modified antipodal tapered slot antenna with elliptical corrugations on its edges. The proposed elliptical shape is used to improve the antenna characteristics compared with traditional piece-wise linear corrugations. The proposed corrugated structure exhibits an ultrawideband performance (0.6 GHz to 10 GHz) with higher gain flatness, better front-to-back ratio and lower side lobe levels. The measured results show good agreement with simulations.

Introduction

The tapered slot antennas (TSA) or end-fire travelling wave antennas are good candidates for ultrawideband (UWB) systems, such as low profile radar, microwave imaging and short range communications, where robust antenna performance is required in order to transmit very narrow UWB pulses[1]. In this paper, merging the concept of antipodal tapered slot antenna (ATSA) and edge corrugation of elliptical shaped fins are used to improve the performance of original ATSA. Two different types (i) elliptical (ii) piecewise linear edge corrugations are designed to cover both lower and higher proposed frequency ranges (0.6 to 10 GHz). The different performance parameters such as return loss value, radiation pattern, front to back ratio and side lobe levels are improved by appropriate corrugation design. The results of both types of corrugations are summarized and compared with original ATSA performance.

Design and results

The configurations of traditional ATSA, piecewise linear corrugations (ATSA-LC) and elliptic corrugation (ATSA-EC) is shown in Fig. 1. The depth of the corrugation in both configurations is less than quarter wavelength of lowest frequency (0.6 GHz) exhibiting the inductive reactance to the passing wave [2].

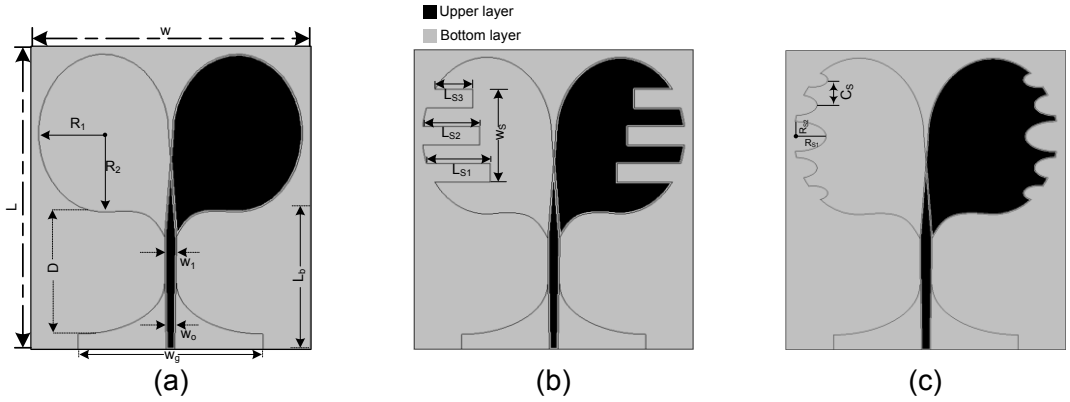

Fig.1 Geometry of proposed ATSA (a) Original ATSA (b) Modified ATSA with piece-wise linear corrugation (ATSA-LC) (c) Modified ATSA with elliptic corrugation (ATSA-EC)

The added inductance increases the electrical length of antennas. Therefore, the corrugated antennas have 9.8% shifts in lower resonance frequencies (from 0.6 to 0.55 GHz) as shown in Fig. 2(a). Moreover, the ATSA-EC has better gain flatness than the other two configurations (9 dB ± 1.2 dB) from 0.55 to 7.9 GHz, as shown in Fig. 2(b).

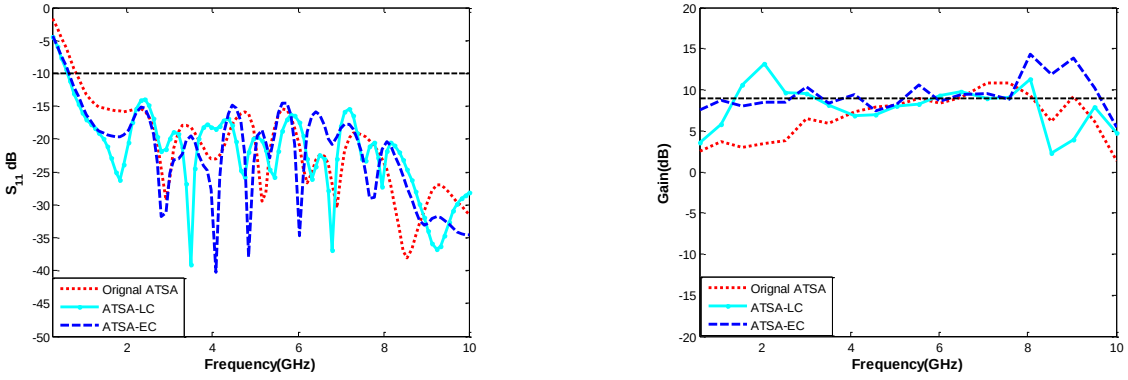

Fig. 2 Simulation results (a) Return loss characteristics (b) Gain characteristics.

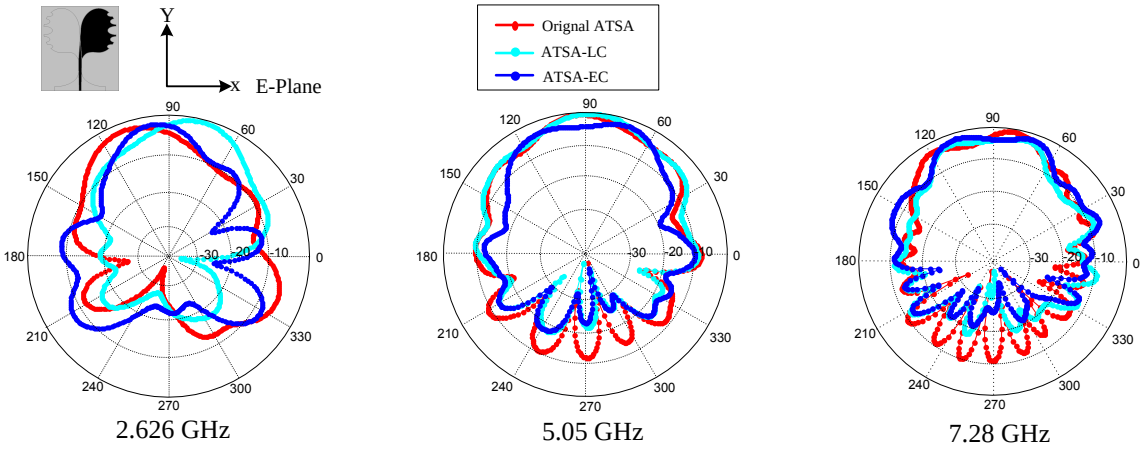

Fig. 3 Simulation results of E-plane radiation pattern at different frequencies.

The E-plane radiation patterns of proposed antennas for different operation frequencies are shown in Fig. 3. Both side lobe and back lobe levels are reduced. The performance of original ATSA and corresponding to corrugated configurations are listed in Table 1. Compared to the original ATSA [3], the 48% side lobe level is improved at 2.26 GH for ATSA-EC. Similarly significant improvements in lower frequencies' gain are up to 95% and 113% for ATSA-LC and ATSA-EC, respectively. Moreover, the front to back ratio values have also been improved, especially at higher frequencies, for both configurations. The proposed circuits are simulated by using full wave electromagnetic software HFSS v 13 [4].The original ATSA has been fabricated and tested and rest are under fabrication and testing.

Table 1. Simulation results of *E*-Plane pattern.

Frequency (GHz)		2.26	5.05	7.28
Design Parameters	Design Type			
3 dB beamwidth (degree)	Original ATSA	50.4	50.5	61.7
	ATSA-LC	50.9	76.7	64.4
	ATSA-EC	46.3	60.6	57.3
Side lobe level (dB)	Original ATSA	-10.2	-11.45	-11.39
	ATSA-LC	-13.6	-13.6	-12.96
	ATSA-EC	-15.15	-15.1	-11.68
Directivity Gain (dBi)	Original ATSA	4.5	8.18	10.28
	ATSA-LC	8.8	8.26	9.46
	ATSA-EC	9.6	8.05	9.08
Front to back ratio (dB)	Original ATSA	14	8.61	6.739
	ATSA-LC	16.92	16.0	14.42
	ATSA-EC	15.4	16.22	11.52

References:

[1] C. T. Rodenbeck, et al., "Ultra-wideband low-cost phased-array radars," Microwave Theory and Techniques, IEEE Transactions on, vol. 53, pp. 3697-3703, 2005.

[2] T. Milligan, *Modern Antenna Design*, 2nd ed. Piscataway, NJ: IEEE Press, 2005

[3] Siddiqui, J.Y.; Antar, Y.M.M.; Freundorfer, A.P.; Smith, E.C.; Morin, G.A.; Thayaparan, T.; , "Design of an Ultrawideband Antipodal Tapered Slot Antenna Using Elliptical Strip Conductors," Antennas and Wireless Propagation Letters, IEEE , vol.10, no., pp.251-254, 2011.

[4] HFSS, v13, Ansoft Corporation Software, Pittsburgh, PA, USA.

NOVEL KSA SIGN SHAPE MICROSTRIP ANTENNA ARRAY MUTUAL COUPLING REDUCTION

M. I. Ahmed[1,2*], E. A. Abdallah[1], A. A. Sebak[2], and H. M. Elhennawy[3]

[1] Electronics Research Institute, Cairo, Egypt

[2] Technology Innovation Center in RFTONICS, PSATRI, King Saud University, Riyadh, Saudi Arabia

[3]Ain Shams University, Cairo, Egypt

[*] miahmed@eri.sci.eg

Abstract- In this paper, a novel ksa sign shape microstrip antenna is presented. The single and two element antenna were designed and fabricated on a substrate with dielectric constant of 2.2, thickness of 1.5748 mm, and tan δ = 0.001. The measuring results were obtained using Anritsu 37297D VNA. The results show that a reduction in mutual coupling between array elements of 13.5 dB is achieved at 2.344 GHz with band (2.26 - 2.45) GHz. Also, a reduction in size of 70% is achieved. The microstrip array was studied by CST simulator and fabricated by proto laser machine with precision 25μm. The antenna can be used in the military or RFID applications.

Mutual coupling is a well-known effect in multi-element array antennas. Generally, mutual coupling is an unwanted phenomenon that distorts the behaviour of radiating elements in an antenna array. Every element in an antenna array affects every other element by radiating over the air or by propagating surface currents through the ground plane of microstrip antennas. Surface currents can be a bigger problem, especially when antenna elements are closely packed. Mutual coupling, which depends on inter element separation and relative orientation, causes undesirable effects on antenna characteristics [1].

Electromagnetic Band Gap structures (EBGs) are widely used in microwave circuit and antenna design because they produce band rejection characteristics [2]. Various configurations of EBG structures have been successfully applied in the patch antenna arrays to improve array characteristics, such as reduction of total size of the array and increasing radiation efficiency [3], [4].

This configuration is chosen because the ksa sign shape is the official page for any military application. So, this antenna may be used in soldier belts, any commodity for the military application, etc. The single and two element microstrip array are shown in Fig. 1 to study the mutual coupling and the effect of spacing between array elements. The EBG cells in the shape of small size ksa sign are inserted between the adjacent coupled elements in the array to suppress the pronounced surface waves. The comparison between the measured and simulated scattering parameters is shown in Fig. 2. The simulated gain and radiation efficiency for single element at f = 2.563 GHz are about 3.4 dBi and 89%, respectively. The radiation pattern for two elements without EBG is shown in Fig. 3(a). In this case the simulated gain and radiation efficiency at f = 2.512 GHz are 5.1 dBi and 91%, respectively. The radiation pattern for two elements array with EBG is shown in Fig. 3(b). The simulated gain and radiation efficiency at f = 2.542 GHz are 6.6 dBi and 92%, respectively. The measured results agree well with those obtained by the CST.

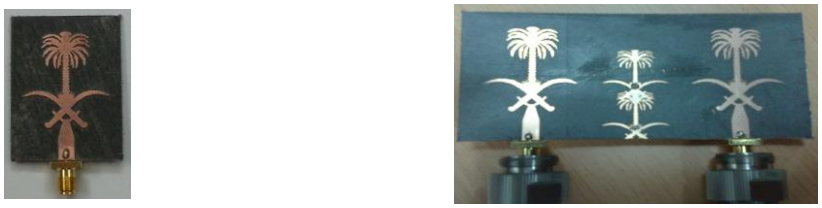

(a) (b)

Fig. 1: Fabricated novel KSA sign microstrip antenna (a) single element, and (b) 2 elements array with EBG.

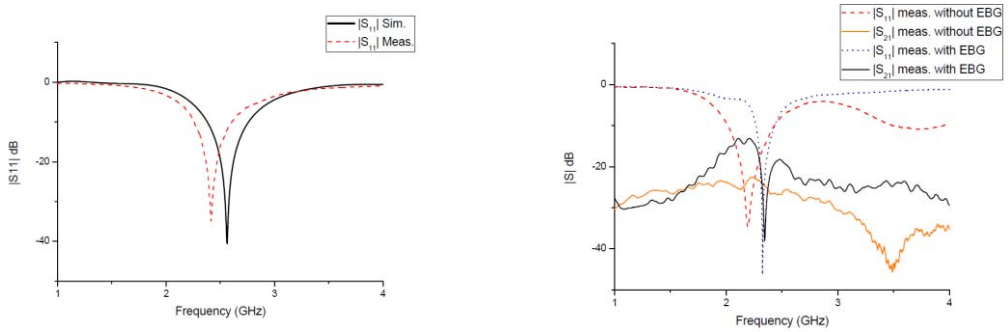

(a) (b)

Fig. 2: Comparison between simulation S-parameters and measurement of novel ksa sign shape microstrip antenna array (a) single element, and (b) 2 element array with and without EBG.

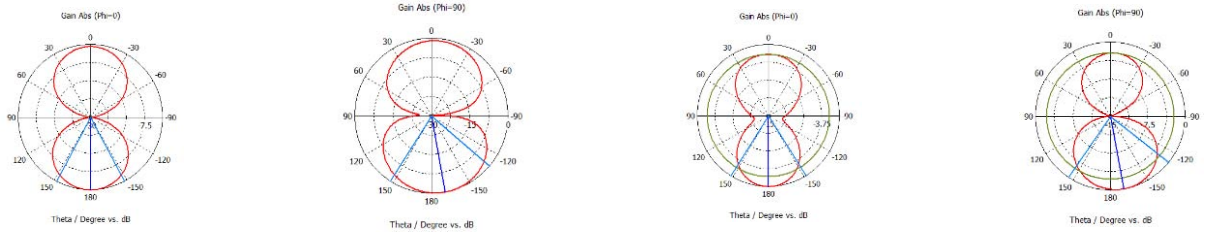

(a) (b)

Fig. 3: E-plane and H-plane radiation pattern of novel ksa sign shape microstrip antenna array without and with EBG at frequencies (a) 2.512GHz, and (b) 2.542GHz.

REFERENCES

1. Parthasarathy, K. V., *Mutual Coupling in Patch Antennas*, Lap Lambert Academic Publishing, Germany, 2011.
2. Assimonis, S.D., T. V. Yioultsis and C. S. Antonopoulos, "Design and Optimization of Uniplanar EBG Structures for Low Profile Antenna Applications and Mutual Coupling Reduction," *IEEE Transactions on Antennas and Propagation*, Vol. 60, No. 10, 4944 – 4949, Oct. 2012.
3. Exposito-Dominguez, G., J. M. Fernandez-Gonzalez, P. Padilla and M. Sierra-Castaner, "Mutual Coupling Reduction Using EBG in Steering Antennas," *IEEE Antennas and Wireless Propagation Letters*, Vol. 11, 1265 – 1268, 2012.
4. Hajilou, Y., H. R. Hassani and B. Rahmati, "Mutual Coupling Reduction Between Microstrip Patch Antennas," in *Proceedings of 6th European Conference on Antennas and Propagation (EUCAP)*, Prague, Czech Republic, March 2012, 1064–1067.

SUBSTRATE MAGNETIZATION EFFECTS ON RADIATION PROPERTIES OF RECTANGULAR MICROSTRIP ANTENNA

S. C. Raghavendra, [1]Karthik B. G. , [1]Iswaryan G. S, [1]Prashant M. T., [2]Revanasiddappa M.*

[1]Dept. of Electronics Engineering, Ruwais Colleges, P O Box No. 58855, HCT, Ruwais, Abu Dhabi, UAE

[1]Dept. of Electronics and Communication Engineering,

[2] Dept. of Chemistry,

P E S Institute of Technology (South Campus), Electronic City, Bangalore-5660100

Abstract-

Microstrip antennas are light weight, low profile antennas that are easy to fabricate. However, their applications are limited because of narrow impedance bandwidth (<2%) and low gain. In this work, we attempt to study the bandwidth parameters of a rectangular microstrip antenna by introducing magnetic loss tangent (tan δ_μ) and magnetic permeability (μ_r) in a commercially available substrate ADPIM-320 (manufactured by Arlon, $\varepsilon_r = 3.2$, tan $\delta = 3*10^{-3}$, h=1.575mm and copper height =35 μm). Simulation studies have been made by an electromagnetic simulation software tool, FEKO which uses Method of Moments (MoM) and other numerical techniques. The antennas simulation is carried out in the S band (2 to 4 GHz with 3GHz as centre frequency). The results of the simulations, show that for a particular set of magnetic parameters of the substrate, the impedance bandwidth of the rectangular microstrip antenna show an enhancement as high as 10% with single element basic rectangular radiating patch along with multiple resonant peaks. The results provide useful insight for practical design on this kind of structures when magnetic substrates are involved.

***** Author for Correspondence:

E-mail: sc.raghu@gmail.com

Abstract:

Antennas are becoming crucial in an increasingly growing number of vital applications namely with the emerging of the 3G, 4G and the 5G generations of communications. Of particular interest are the antennas designed to operate in point-to-multipoint configurations where efficiency, size, and cost play a decisive role. The common practice is to refer to the already existing antennas in the market for this sole purpose. Nonetheless, a major drawback of such solutions is that the aforementioned criteria are extremely hard to simultaneously optimize. The purpose of this paper is to present an innovative approach relying on the use of Slotted Waveguide Antennas, which are initially used in Radar applications, as an ultimate alternative that allows drastically enhancing the ratio of performance versus cost and size. Moreover, our antenna will be remodeled and designed to function as a Circularly Bent Rectangular Slotted Waveguide Antenna (CBRSWA). Simulation results were carried out at 2.4 GHz frequency and indubitably demonstrated high effectiveness in terms of directivity and high gain given a reduced cost, shape and size. A prototype will be assembled to carry out experimental results and compare them with simulation. It is still noteworthy to mention that these results are expected to match with an elevated accuracy since the pattern simulated under Autocad, Matlab and Feko is meshed and modeled to a far extent taking into account all non-ideal characteristics.

Analysis and Modeling of Annular Aperture Array Antenna Using Field Equivalence Principle

S. Khan[1*], M. J. Mughal[1], A. Noor[1] and M. M. Ali[1]
[1]GIK Institute of Engineering Sciences and Technology, Topi (23640), Pakistan
[*]corresponding author: safiullah.khan@hotmail.com

Abstract- In this paper a model based on field equivalence principle (extended huygens' principle) for annular aperture array antenna is proposed. The aperture is modeled as array of magnetic current loops. Far field expressions of array are obtained and antenna pattern has been plotted for different frequencies.

In order to achieve high directivity (large gain) and focused radiation pattern, either the dimension of the single antenna has to be increased or array of small elements be used. Arrays are preferred for high directivity, beam steering and controlled radiation pattern. Many researchers are working on annular array for different applications such as in biological sensing and lithography [1-2]. In this paper annular aperture array antenna is analyzed using field equivalence principle, i.e., the extended Huygens' Principle; a field over a closed surface can be modeled as equivalent electric and magnetic sources [3]. The radiation pattern of a single element antenna is wide and less directive (low gain). The apertures are modeled as constant magnetic current loops. The classical methods to compute the fields of an aperture are complex, whereas the proposed technique just requires integration over a closed surface. The first step is to select a perfect electric surface and then in second step place a thin dielectric film over it Fig. 1(a). The fields are generated by magnetic source $\mathbf{M_s}$ using electric vector potential **F** [4],

$$\vec{F} = \frac{\mu}{4\pi}\int_c \vec{I}_m(x', y', z')\frac{e^{-jkR}}{R}dl' \qquad \textbf{(1)}$$

The source coordinates are designated as primed (x', y', z'). R is the distance from any point on the magnetic current element antenna to the observation point and dl' is an infinitesimal section of the magnetic current element antenna Fig. 1(a). $\vec{I}_m$ is the magnetic source current, which is equal to,

$$\vec{I}_m = W.\vec{M}_s \qquad \textbf{(2)}$$

where $W = r_b - r_a$ and $.\vec{M}_s = -\hat{n}\times\vec{E}$.

The fields are computed by putting certain conditions in (1); once the fields are calculated for a single element antenna, we use [4],

$$\vec{E}_{\text{total}} = [\,\vec{E}\text{ (single element at reference point)}] \text{ x [array factor]} \qquad \textbf{(3)}$$

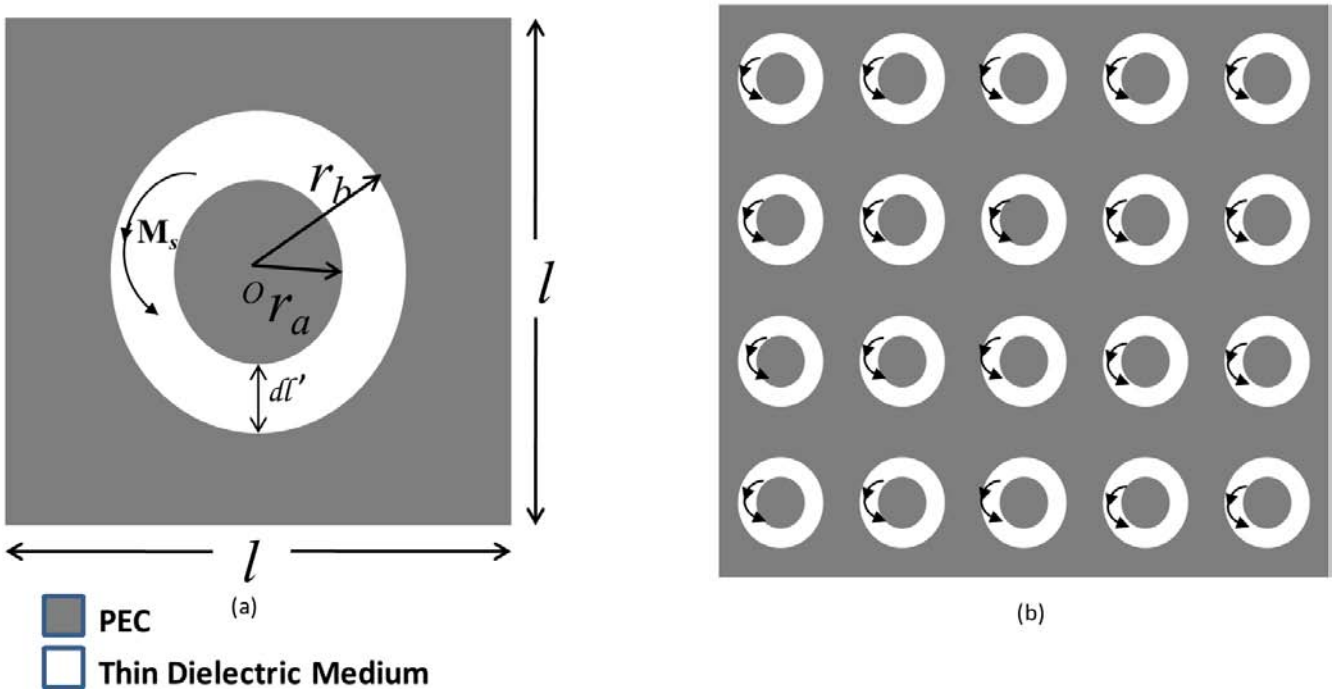

Fig. 1 (a) Single element of annular aperture (b) M x N array of annular aperture for M = 5 and N= 4.

This is used to find the magnetic current loop antenna array. The above equation is also referred to as pattern multiplication for arrays of identical elements [2].

The paper will also include the simulation results and plots made at different frequencies. Fig. 1 shows the single and multiple elements of array antenna. The aperture is equivalent to horizontal magnetic current loop over a perfect electric conductor i.e. $\mathbf{M}_s \neq 0$ and $\mathbf{J}_s = 0$. The final expressions present the relation between the voltage and fields.

REFERENCES

1. Kim, H., J. Cho, J. Park, S. Han, and S. Seo, "Generation of midfield concentrated beam arrays using periodic metal annular apertures," Appl. Opt. Vol. 51, 1076-1085, 2012.
2. Tan, Q., M. Roussey, A. Cosentino, and H. P. Herzig, "In-plane illuminated metallic annular aperture array for sensing application," Opt. Lett. Vol. 37, 635-637, 2012.
3. Kraus, J. D. and Carver, K.R., *Electromagnetics* (2nd edition), McGraw-Hill, New York, 1973.
4. Balanis, C. A., *Antenna Theory* (3rd edition), John Wiley & Sons. Inc. 2005.

Patch Antenna on Ferrite Substrate Controlled by External Magnetic Field

Hedi SAKLI[1*], **Dhaou BOUCHOUICHA**[1], **and Taoufik AGUILI**[1]
[1]Ecole Nationale d'Ingénieurs de Tunis (Labo SYS'COM), B.P :37, Le Belvédère, 1002 Tunis, Tunisia
[*]corresponding author: saklihedi12@gmail.com

Abstract-In this paper, the ferrite patch antenna is presented. We can control externally the resonant frequency by the tensor permeability which is a function of the magnetization of ferrite substrate. The wavelength in the ferrite becomes shorter as the magnetization becomes stronger. This antenna has become broadband.

In the high frequency communication, ferrite is one of the important magnetic materials which are very useful in microwave antenna applications. The reason for using ferrite material in microstrip structures is that the applied magnetic field changes the permeability and thus the electrical properties of material, which in turn changes the antenna properties. The significance of this is that it is possible to change the antenna characteristics through the DC magnetic field applied externally [1,2].

In the present paper, the concept of tunable antenna has been developed by rectangular patch printed on Magnesium Spinels (ferrite TT1-414 of Trans-Tech) substrate in the S band. The geometry of antenna is shown in fig. 1. The patch of length L and width W printed on ferrite substrate of thickness h. The dielectric constant ε_r and saturation magnetization $4\pi M_S$ of substrate are 11.3 and 750 Gauss respectively, with dielectric loss tangent $\tan(\delta) = 10^{-4}$.

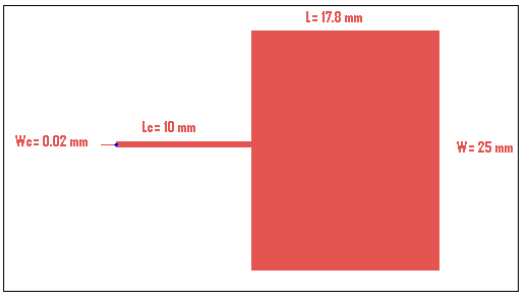

Figure 1. Geometry of microstrip rectangular patch antenna

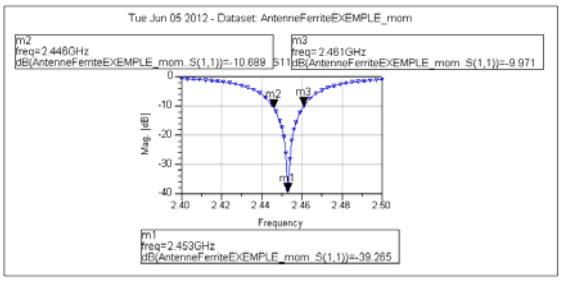

Figure 2. Return loss S_{11} of the microstrip patch antenna with demagnetized Ferrite substrate, f = 2.45 GHz.

Consider a ferrite substrate with a DC magnetic field $\vec{H}_0$ applied longitudinally. The permeability of the ferrite magnetized longitudinally (z-direction) is expressed by [3].

$$\overline{\overline{\mu}} = \mu_0 \cdot \begin{pmatrix} \mu & -j\kappa & 0 \\ j\kappa & \mu & 0 \\ 0 & 0 & \mu_{rz} \end{pmatrix} \quad (1)$$

For a partial magnetization of the ferrites, Green [4] and Shloeman [5] give the empirical expressions of μ, κ and μ_{rz}. When the magnetization is equal to zero, $\kappa = 0$ and $\mu = \mu_{rz} \approx 1$. The ferrite becomes then an isotropic dielectric [6]. Where μ, κ and μ_{rz} are real quantities which depend of the magnetization $4\pi M$, the saturation magnetization $4\pi M_S$ and the frequency f. The dimension of patch is calculated by following equations

$$W = \frac{C}{2f\sqrt{\varepsilon_{r.eff}}} \quad (7)$$

$$L = \frac{C}{2f\sqrt{\frac{(\varepsilon_{r.eff}+1)}{2}}} - 2\Delta L \tag{8}$$

where

$$\varepsilon_{r.eff} = \frac{\varepsilon_r + 1}{2} + \frac{\varepsilon_r - 1}{2}\left(1 + 12\frac{h}{W}\right)^{-\frac{1}{2}} \tag{9}$$

$$\Delta L = 0.412h\frac{(\varepsilon_r + 0.3)\left(\frac{W}{h} + 0.264\right)}{(\varepsilon_r - 0.258)\left(\frac{W}{h} + 0.8\right)} \tag{10}$$

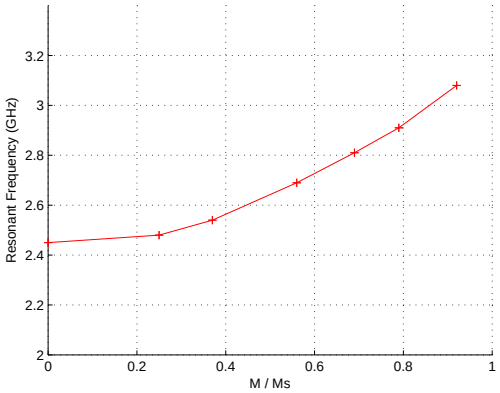

Figure 3. Numerical result of the resonance frequency according magnetization M/M_S.

The above equations are based on the transmission line model [7]. The dimensions of the patch antenna operating at 2.45 GHz, with a ferrite demagnetized, are: W= 2.5 cm and L= 1.78 cm, with h= 1.6 cm (see fig. 1). This ferrite antenna without magnetization has a bandwidth of 13 MHz (see fig. 2) and a gain of 5 dB. By increasing the magnetization M of 0 to $0.9M_S$, the frequency increases from 2.45 GHz to 3.08 GHz as shown in figure 3. Our antenna has become so broadband (bandwidth = 600 MHz). This is an external antenna control.

REFERENCES

1. Brown, A. D., J. L. Volakis, L. C. Kempel and Y. Y. Botros, "Patch antennas on ferromagnetic substrates," *IEEE, Transactions on Antennas and Propagation*, Vol. 47, No. 1, 26-32, 1999.
2. Pozar D. M., "RCS reduction for a microstrip antenna using a normally biased ferrite substrate," *IEEE Microwave Guided Wave Letters,* Vol. 2, 196-198, 1992.
3. Polder D., "On the theory of ferromagnetic resonance," *Philosophers' Magazine,* 40, 99-115, 1949.
4. Green J. J. and F. Sandy, "Microwave characterization of partially magnetized ferrites," *IEEE Trans-MTT*, Vol.22, 641-645, June 1974.
5. Schloemann E., "Microwave behavior of partially magnetized ferrites," *J. Appl. Phys*., Vol. 1, p.1204, June 1970.
6. Sakli H., H. Benzina, T. Aguili and J. W. Tao, "A Rigorous study of some planar structures with longitudinally magnetized ferrite by a modified LSBR method," *IJMOT, International Journal of Microwave and Optical Technology,* Vol. 4, No. 6, pp. 358-367.
7. Balanis C. A., *Antenna Theory Analysis and Design*, Harper & Row Publisher, New York, 1982.

High Resolution Direction Finding using multi-band antenna arrays for Passive Bistatic Radar systems

K. Jamil[1], M. A. Hadi[1, 2*], M. Alam[2], M. Alkanhal[2] and Z. O. Alhekail[1]
[1]Prince Sultan Advanced Technology Research Institute, King Saud University, Saudi Arabia
[2]Department of Electrical Engineering, King Saud University, Saudi Arabia
[*]corresponding author: hadi@ksu.edu.sa

Abstract- Passive radars have many advantages as they utilize signals from existing RF radiation in the environment. A reconfigurable software defined radio (SDR) technology was used to build a fully-synchronized multi-channel passive radar receiver systems that can operate with flexible bands and bandwidths for signals up to 6 GHz. Implementation of the associated antenna arrays and digital beamforming techniques are described here that enabled locating targets anywhere in the space while using high resolution direction finding of incoming signals.

Introduction: Passive bistatic radar utilizes existing free-to-air RF transmissions (e.g. TV, FM radio, digital broadcasts etc) to acquire reflections from targets in order to perform detection and localization. This avoidance of a dedicated transmitter makes this type of radar inexpensive as well as covert [1]. In the bistatic-range measurement, one transmitter and receiver pair provides an elliptical trajectory for the target, and the foci represent the transmitter and the receiver. In this case, it is essential to estimate the direction of arrival (DOA) precisely and find the target location estimating the intersection of the DOA line with the bistatic ellipse.

Research methodology: A software defined passive radar receiver system enabled us to utilize plethora of broadcast or wireless communication transmissions. This paper gives accounts of a multiband high resolution direction finding system to be used in a multiband bistatic passive radar system. The design and development steps for the overall system and processing algorithms are described here in brief.

- **Implementing Wideband smart antenna arrays:** The antenna of a passive radar should be able to steer 360 degrees to receive clean direct signal and target echo signals separately with minimum interference from other directions. To satisfy these requirements, various wideband antenna arrays were designed (e.g. figure (1)), implemented and utilized for digital beamforming for incorporation with a multiband operation using the SDR based passive radar prototype, as reported in [2].
- **Antenna switching unit and GUI development:** Customized software-controlled antenna switching unit (ASU) and GUI based control software were developed to help the acquisition and recording multi-channel real-time data synchronously from appropriate antenna array. The micro-controller based ASU was needed to facilitate the switching between different sets of antenna arrays and calibration signals on-the-fly.
- **Receiver system synchronization:** For the passive radar system, the array data has to be completely synchronized in terms of amplitude and phase for any meaningful results. Each channel was made capable to phase synchronize using external reference signals from a GPS-disciplined source. Also specific phase-calibrating signal was injected down the RF port to phase-align each channel in

digital domain by correcting phase-offset error between the channels.

Figure 1: An eight element circular antenna array for VHF radio signals.

- **Array calibration and digital beamforming:** Extensive calibrations were performed to overcome errors from mutual coupling between array elements, spatial mismatch of element positions, electrical length mismatches of cables, impedance mismatches of different connections. The array data was pre-processed to remove these distortions using a full system calibration approach [3] to take care of the above errors. A special training signal was transmitted at known angles around the circular or linear array. The errors in each channel were measured compared to an ideal case and was calibrated out using multi-variable optimization against an objective function. The calibrated data was then used to estimate the DOA (direction of the arrival) of the incoming signal. The beamforming was implemented to separate the desired signals in spatial domain forming the direct transmitted signal as well as the weak target echo signals to be cross-correlated for passive bistatic detection. For effective extraction of the signal in certain spatial direction, we forced the side-lobes to be at the minimum level possible enabling spatial removal of other interferences.

Conclusion: Implementation of the antenna arrays and digital beamforming techniques for software defined passive bistatic radar are described here. These techniques enabled locating targets using the passive bistatic radar anywhere in the space along with direction finding of incoming signals. The results from these array signal processing will be detailed in the full-length paper.

REFERENCES

1. Griffiths, H. and C. Baker, “Passive coherent location radar systems. Part 1: Performance prediction,” *IEE Proceedings of Radar, Sonar and Navigation*, Vol. 152, No. 3, 153-159, 2005.
2. Jamil K., M. Alam, M. A. Hadi, and Z. O. Alhekail, “A multi-band multi-beam software-defined passive radar part I: system design,” in *IET International Conference on Radar Systems*, UK, 2012.
3. Malanowski M., and K. Kulpa, "Digital beamforming for Passive Coherent Location radar," IEEE Radar Conference (RADAR ’08), 1-6, 2008

Experimental Characterization of Various Digital Beamforming Algorithms for Ultra Wideband Signals

S. Tahir[*†], **M. Elnamaky**[*], **M. A. Ashraf** [**] **and K. Jamil**[*]
[*]Prince Sultan Advanced Technologies Research Institute (PSATRI)
[**]Department of Electrical Engineering
King Saud University, Saudi Arabia
[†]corresponding author: stahir@ksu.edu.sa

Abstract- This paper presents a first attempt of its kind in experimental characterization of different Digital Beamforming (DBF) algorithms namely, FIR filters structure, direct two dimensional Discrete Fourier Transform (2D-DFT) and sub-band processing, for Ultra Wideband (UWB) signals. A 1 GHz wide UWB signal is generated by a high speed arbitrary waveform generator (AWG) operating at 12 GS/s. The output of AWG was transmitted by the Antipodal Tapered Slot Antenna (ATSA). At the receiver side, a four channel synchronous receiver, built with a uniform linear array of 4 ATSAs, is employed with each channel operating at 4GS/s. Different beamforming algorithms were then applied to the digitized data to compare their performance in a real time experimental setup. The frequency band of interest was set to be 1-2 GHz with a center frequency of 1.5GHz.

Ultra-wideband digital beam-forming has been a topic of intense research because of its significant advantages over the existing analogue beam forming architectures [1]. The digital nature of the signaling makes UWB DBF an attractive candidate for a number of applications including radars, remote sensing, broadband electronic warfare, microwave imaging and cognitive radios [2]. However a number of different challenges have resisted UWB digital beamforming to be implemented practically, with the major one being the extremely high sampling rate which requires very high speed analogue to digital converters (ADCs). With the advent of digital signal processing technology, high speed ADCs are now becoming commercially available and the hardware realization of UWB digital beamforming is turning into reality. The authors have previously taken some first steps towards such a hardware implementation of a beamformer in a real UWB channel complete with real UWB antennas by employing a digital FIR filter bank structure [3].The following work is an extension to their previous effort.

This aim of this paper is to compare the main types of digital beamforming algorithms for UWB signals in a real time hardware setup. Three different approaches are often cited in literature for digital beamforming which includes FIR filters structure, direct two dimensional Discrete Fourier Transform (2D-DFT) and sub-band processing:

(1) In FIR filter structure, on each branch of the array, a bank of filters is appended to allow each element to have a phase response that varies with frequency. By the temporal signal processing, the phase shifts due to higher and lower frequencies get equalized [4].
(2) In the 2D-DFT approach, the Fourier transform relationship between temporal and spatial parameters of array and its beam pattern is exploited to produce frequency invariant beam pattern [5]
(3) In the sub-band technique, the wide band signal is decomposed into several narrowband signals and narrowband beam forming techniques are applied to each sub band. By summing up the outputs of each band, wideband beamformer is achieved [6].

All the above mentioned approaches are however limited to simulations only and have not been implemented practically. It is the aim of this paper to experimentally demonstrate and compare these major beam forming techniques. The major work of this paper can be outlined as follows:

1. Simulation, Fabrication and Measurements of a four-element linear ATSA array

2. Real time hardware implementation of UWB DBF array in transmit and receive mode with high speed analog-to-digital and digital-to-analog converters with FPGA processing power.
3. Experimental characterization of the major UWB digital beamforming techniques.

Fig. 1 shows our experimental setup and Fig. 2 shows the ATSA array fabricated in the lab. The physical dimensions of antenna was shown in Fig 3 with $\varepsilon_r = 2.2$, $W_g = 60$ mm, $W_o = 4.65$ mm, $W_1 = 5.95$ mm, D= 67.75 mm and $L_b = 72.75$ mm. The overall dimension of ATSA is 16 cm × 14 cm excluding the coaxial connector. The designed ATSA element has lower return loss value from 0.6-10 GHz as shown in Fig. 4. Measured results are compared to the simulation results obtained using a commercial full wave electromagnetic simulator HFSS v 13.

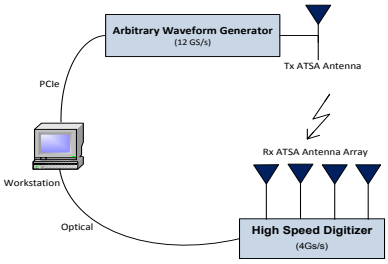

Fig. 1 Experimental Setup

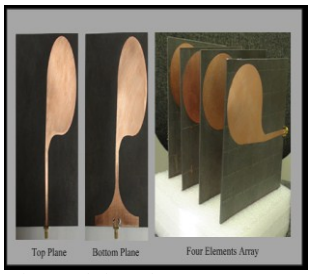

Fig. 2 Fabricated ATSA Array

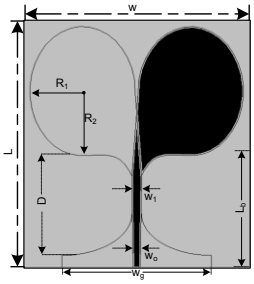

Fig. 3 Geometry of ATSA Element

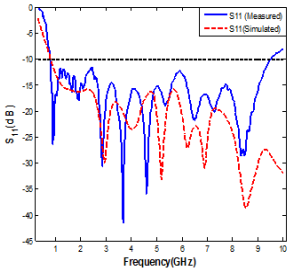

Fig.4 Return Loss for ATSA

For demonstration purpose, the results for the first approach for beamforming (FIR Filter Structure), obtained from the experimental setup, has been shown. The technique of optimizing the coefficients of FIR filter is used to achieve a frequency invariant wideband beamformer. Interested readers could find more details in [4]. A train of second derivative Gaussian pulses was transmitted by the AWG via ATSA, with each pulse having a waveform described by: $y(t) = A\left(1 - 4\pi\left(\frac{t}{\tau}\right)^2\right)\exp\left[-2\pi\left(\frac{t}{\tau}\right)^2\right]$, where, A stands for the maximum amplitude and τ for the pulse width of the Gaussian pulse. The corresponding time and spectral density representations of the pulses transmitted from the antenna were shown in Fig. 5 and Fig.6 respectively. These transmitted signals were received by a synchronous four element ATSA array, with each element connected to a separate channel of high speed digitizer. We assumed that our desired beam pattern was the response of a narrow band signal with a frequency of 1.5 GHz and that response is calculated by using Taylor weights [7] for -30dB side-lobes. After optimization of FIR Filter coefficients, the achieved beam former response is shown in Fig. 8, along with the desired response for comparison purpose. The beam pattern matches the desired beam pattern approximately and the side lobe levels were below -30dB as required.

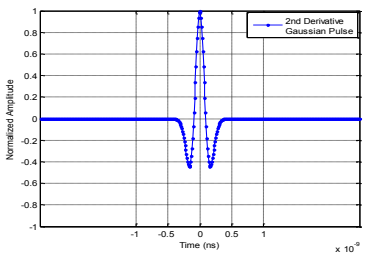

Fig. 5 Transmitted Pulse (Time Domain)

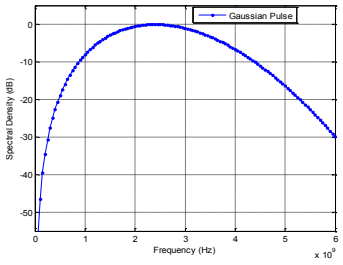

Fig. 6 Spectrum of Transmitted Pulse

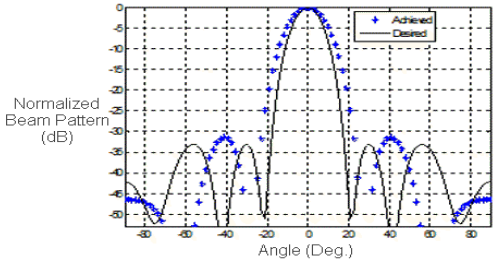

Fig. 7 Achieved vs Desired Beam Patterns of Gaussian Pulses

References

[1] Hum S. V., H. L. P. A. Madanayake, and L. T. Bruton, "UWB beamforming using 2-D beam digital fillters" IEEE Trans. Antennas Propag., 2009.

[2] Kondapalli S., A. Madanayake and L. Bruton, "Digital Architectures for UWB Beamforming Using 2D IIR Spatio-Temporal Frequency-Planar Filters", Int. Journal of Antenn. and Prop., Volume 2012.

[3] Tahir S., M. Elnamaky, M. A. Ashraf and K. Jamil, "Hardware Implementation of Digital Beamforming Network for Ultra Wide Band Signals using Uniform Linear Arrays", 2nd IEEE-APS Middle East Conference on Antennas and Propagation, December 2012.

[4] Weicheng Z. and C. Zengping, "Design of Frequency Invariant Wideband Beamformer with Real and Symmetric FIR Filters,'' Defence Science Journal, Vol. 62, No. 4, July 2012.

[5] Liu W. and S. Weiss, "Design of frequency invariant beamformers for broadband arrays," IEEE Trans. Signal Processing, 2008.

[6] Liu W. and R. J. Langley, "An adaptive wideband beamforming structure with combined subband decomposition," IEEE Trans. Antenna Propagation, 2009.

[7] Taylor T., "Design of Line-Source antennas for narrow beamwidths and low sidelobes," IRE Trans. Antenn. Propagation, 1955.

High permittivity dielectric resonator antenna based on TiZrO

E. E. C. Oliveira[1], A. G. D'Assunção[2*], J. B. L. Oliveira[2], A. M. Cabral[2] and P. C. Assis Jr[1]
[1]State University of Paraíba, Brazil
[2]Federal University of Rio Grande do Norte, Brazil
[*]corresponding author: adaildo@ymail.com.br

Abstract-A cylindrical dielectric resonator antenna (DRA) with high dielectric constant is proposed for wireless communication systems. A microstrip line is used to feed the dielectric resonator. Simulated and measured results for the antenna return loss are presented and discussed, as well as measured results for the antenna input impedance. Simulated results are obtained using Ansoft HFSS software based on the finite element method.

Dielectric resonator antennas (DRA) are being investigated by many researchers due to their high Q and low loss characteristics that make them suitable for several applications at the microwave and millimeter wave bands. Some of these applications are in the development of antennas and filters [1].

Usually high dielectric constant materials are used in the development of dielectric resonator (DR) antennas. In this work we propose a DR antenna with cylindrical geometry, low profile based on a chemical compound zirconium titanate ($Ti_{0.75}Zr_{0.25}O_2$) produced by Pechini method in a reaction at high temperature. The antenna is fed by a microstrip line with high impedance. Simulated and measured results are presented. The antenna main characteristics are low loss, broadband performance and good impedance matching condition.

The DR is mounted on a microstrip with a FR-4 substrate with height equal to 1.5 mm and dielectric constant equal 4.4. The proposed geometry is shown in Fig. 1 and its resonant frequency is given by [2]:

$$F_r = \frac{c}{2\pi a\sqrt{\varepsilon_r}}\sqrt{\chi_{11}^2 + \left(\frac{\pi a}{2d}\right)^2} \tag{1}$$

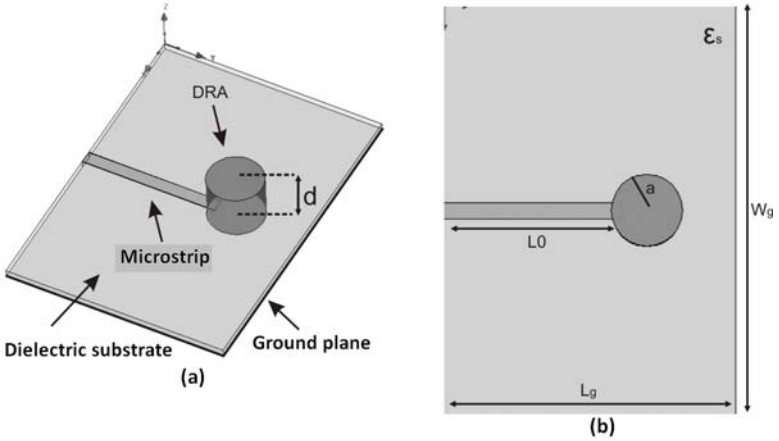

Figure 1 - Proposed DRA: (a) geometry and (b) top view.

where c is the speed of light and χ_{11} is 1.841. The DRA dimensions and parameters are given in Table I.

The DRA properties were investigated using Ansoft HFSS software. Prototypes were built and measured

using a vector network analyzer (model R&S ZVB14). Simulated and measured return loss results are shown in Fig. 2(a) and input impedance measured results are presented in Fig. 2(b). A broadband performance was obtained for the DR antenna. Agreement was obtained between simulated and measured results. The estimated resonant frequency error is 7.5% (at 8.15 GHz). Also a measured bandwidth of 600 MHz was obtained. The antenna dimensions and results are given in Tables I and II respectively.

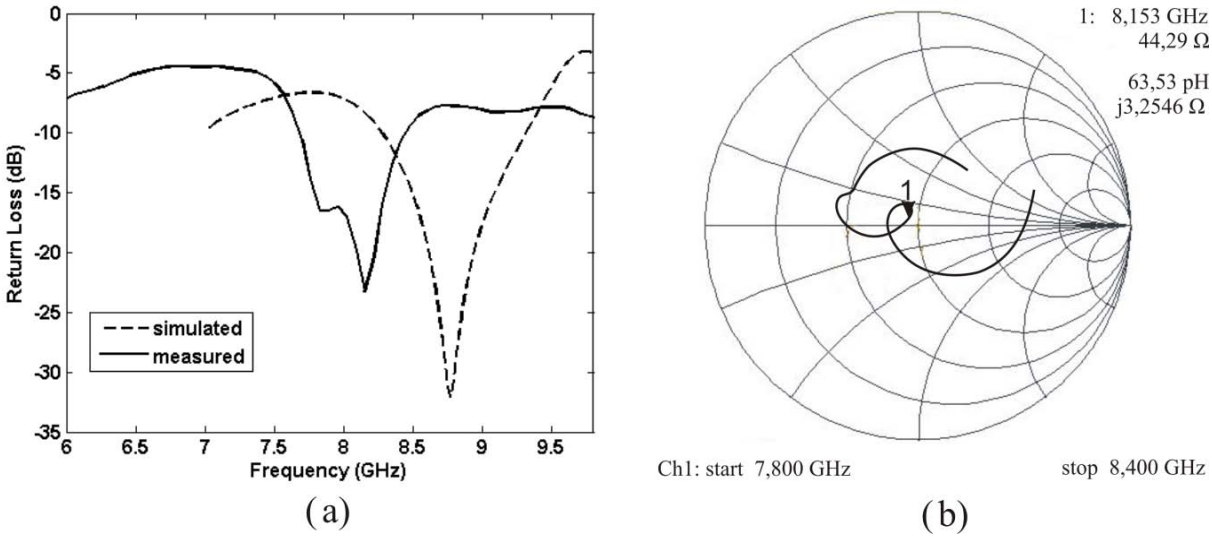

Figure 2. (a) Simulated and measured return loss results and (b) measured input impedance behavior.

Table I. DRA structural parameters.

Relative dielectric permittivity (ε_r)	35.0
Relative magnetic permeability (μ_r)	1
Electric loss tangent (tan δ_e)	0.0002
A, L_0, W_g, L_g, d (mm)	6.13; 30.5; 80.0; 70.0; 10.21

Table II. Measured DRA resonant frequency and bandwidth results.

Resonant frequency	8.153 GHz
Bandwidth	600 MHz
Bandwidth (%)	7.4%

A compact dielectric resonator antenna (DRA) with a high permittivity value was proposed for microwave application. Low return loss value at the resonant frequency and a broadband feature were achieved.

REFERENCES

1. Aoutoul, M., O. El-Mrabet, M. Essaaidi and A. El Moussaoui, "A compact rectangular dielectric resonator antenna for UWB wireless communication systems," *Microw. Opt. Technol. Lett.*, Vol. 51, No. 10, 2281-2286, 2009.
2. Oliveira, E. E. C., A. G. D'Assunção, J. B. L. Oliveira and A. M. Cabral, "Small size dual-band rectangular dielectric resonator antenna based on calcium titanate ($CaTiO_3$)," *Microw. Opt. Technol. Lett.*, Vol. 54, No. 4, 976-979, 2012.

Small antenna analysis using convex optimization

Mats Gustafsson

Lund University, Sweden
mats.gustafsson@eit.lth.se

Abstract— The performance of small antennas is constrained by the electrical size of the antenna structure. Here, convex optimization is used to analyze small antennas. It is shown that stored electric and magnetic energies, radiated power, and radiated field expressed in the current density can by combined to form convex optimization problems for many interesting antenna cases. The solution of the optimization problem determines physical bounds on the antenna performance.

Fundamental limitations on small antennas were first studied more than 60 years ago by Wheeler [14] and Chu [2], see also [9, 13]. The approach by Chu is based on mode expansions of the fields outside the smallest circumscribing sphere [2] and explicit calculations of the stored electric and magnetic energies and the radiated power to determine the Q-factor. This approach has dominated the research but is unfortunately restricted to canonical geometries such as spheres. The analysis was generalized to arbitrarily shaped antennas by a reformulation of the antenna problem into a scattering problem and utilizing the forward scattering sum rule [4, 5], see also [6, 10, 12, 15] for alternative approaches.

In this presentation, the analysis is generalized to many new and important antenna problems using convex optimization [1, 8]. The results are based on formulations of the antenna problems as convex optimizations problems, where we use that the stored electric and magnetic energies, and radiated power are positive semi-definite quadratic forms in the current density. We use the explicit expressions by Vanderbosch [11] for the stored energies, see also [7] for an alternative derivation and interpretation. Moreover, the presented results are for current densities in free space.

Following the notation in [8] and expand the current density, $\boldsymbol{J}$, in local basis functions as in the method of moments (MoM), and let

$$\begin{cases} W_{\mathrm{e}} \approx \mathbf{J}^{\mathrm{H}}\mathbf{X}_{\mathrm{e}}\mathbf{J} & \text{stored electric energy} \\ W_{\mathrm{m}} \approx \mathbf{J}^{\mathrm{H}}\mathbf{X}_{\mathrm{m}}\mathbf{J} & \text{stored magnetic energy} \\ P_{\mathrm{r}} \approx \mathbf{J}^{\mathrm{H}}\mathbf{R}_{\mathrm{r}}\mathbf{J} & \text{radiated power} \\ \hat{\boldsymbol{e}}^* \cdot \boldsymbol{F}(\hat{\boldsymbol{k}}) \approx \mathbf{F}^{\mathrm{H}}\mathbf{J} & \text{far field in the } \hat{\boldsymbol{k}} \text{ direction and the } \hat{\boldsymbol{e}} \text{ polarization,} \end{cases} \tag{1}$$

where $\mathbf{J}$ is a column matrix with the expansion coefficients for $\boldsymbol{J}$ and the superscripts * and $^{\mathrm{H}}$ denote the complex conjugate and Hermitian transpose, respectively. The quality factor is defined as a weighted quotient between the stored energy and the radiated power [2, 9, 13]

$$Q = \frac{2\omega \max\{W_{\mathrm{e}}, W_{\mathrm{m}}\}}{P_{\mathrm{r}}} \approx \frac{2\omega \max\{\mathbf{J}^{\mathrm{H}}\mathbf{X}_{\mathrm{e}}\mathbf{J}, \mathbf{J}^{\mathrm{H}}\mathbf{X}_{\mathrm{m}}\mathbf{J}\}}{\mathbf{J}^{\mathrm{H}}\mathbf{R}_{\mathrm{r}}\mathbf{J}}. \tag{2}$$

Similarly, the partial directivity is a weighted quotient between the radiation intensity in the direction $\hat{\boldsymbol{k}}$ and polarization $\hat{\boldsymbol{e}}$ and the radiated power, *i.e.*,

$$D(\hat{\boldsymbol{k}}, \hat{\boldsymbol{e}}) = \frac{\beta|\hat{\boldsymbol{e}}^* \cdot \boldsymbol{F}(\hat{\boldsymbol{k}})|^2}{P_{\mathrm{r}}} \approx \frac{\beta|\mathbf{F}^{\mathrm{H}}\mathbf{J}|^2}{\mathbf{J}^{\mathrm{H}}\mathbf{R}_{\mathrm{r}}\mathbf{J}}, \tag{3}$$

where β is a normalization constant. To form convex optimization problems, we first consider the partial directivity Q-factor quotient

$$\frac{D(\hat{\boldsymbol{k}}, \hat{\boldsymbol{e}})}{Q} \leq \max_{\boldsymbol{J}} \frac{D(\hat{\boldsymbol{k}}, \hat{\boldsymbol{e}})}{Q} = \max_{\boldsymbol{J}} \frac{\beta|\hat{\boldsymbol{e}}^* \cdot \boldsymbol{F}(\hat{\boldsymbol{k}})|^2}{2\omega \max\{W_{\mathrm{e}}, W_{\mathrm{m}}\}} \approx \max_{\boldsymbol{J}} \frac{\beta|\mathbf{F}^{\mathrm{H}}\mathbf{J}|^2}{2\omega \max\{\mathbf{J}^{\mathrm{H}}\mathbf{X}_{\mathrm{e}}\mathbf{J}, \mathbf{J}^{\mathrm{H}}\mathbf{X}_{\mathrm{m}}\mathbf{J}\}}. \tag{4}$$

The quotient is invariant for a multiplicative scaling $\boldsymbol{J} \to \alpha \boldsymbol{J}$ showing that it is sufficient to consider $|\mathbf{F}^{\mathrm{H}}\mathbf{J}|^2 = 1$ or $\mathrm{Re}\{\mathbf{F}^{\mathrm{H}}\mathbf{J}\} = 1$, see [6]. This gives the convex optimization problem

$$\begin{aligned} &\text{minimize} && \max\{\mathbf{J}^{\mathrm{H}}\mathbf{X}_{\mathrm{e}}\mathbf{J}, \mathbf{J}^{\mathrm{H}}\mathbf{X}_{\mathrm{m}}\mathbf{J}\} \\ &\text{subject to} && \mathrm{Re}\{\mathbf{F}^{\mathrm{H}}\mathbf{J}\} = 1 \end{aligned} \tag{5}$$

where the constant 1 is used for simplicity. Convex optimization problems can be solved with *e.g.*, the matlab toolbox `CVX` [3], see [8]. The main advantage with the formulation as a convex optimization problem is that we can easily extend the D/Q problem (5) to other problems. By *e.g.*, adding a constraint on the radiated power P_{r}, we get the convex optimization problem

$$\begin{aligned} &\text{minimize} && \max\{\mathbf{J}^{\mathrm{H}}\mathbf{X}_{\mathrm{e}}\mathbf{J}, \mathbf{J}^{\mathrm{H}}\mathbf{X}_{\mathrm{m}}\mathbf{J}\} \\ &\text{subject to} && \mathrm{Re}\{\mathbf{F}^{\mathrm{H}}\mathbf{J}\} = 1 \\ & && \mathbf{J}^{\mathrm{H}}\mathbf{R}_{\mathrm{r}}\mathbf{J} \leq \beta D_0^{-1}, \end{aligned} \tag{6}$$

that can be interpreted as a constraint on the partial directivity $D(\hat{\boldsymbol{k}}, \hat{\boldsymbol{e}}) \geq D_0$. The formulation (6) can be used to analyze the minimum Q for superdirective antennas. We can also add other constraints that determines bounds on antennas that have a specified radiated field or are integrated in passive (metallic and/or dielectric) structures [8].

REFERENCES

1. S. P. Boyd and L. Vandenberghe. *Convex optimization*. Cambridge Univ Pr, 2004.
2. L. J. Chu. Physical limitations of omni-directional antennas. *J. Appl. Phys.*, **19**, 1163–1175, 1948.
3. M. Grant and S. Boyd. CVX: Matlab software for disciplined convex programming, version 1.21. cvxr.com/cvx, April 2011.
4. M. Gustafsson, C. Sohl, and G. Kristensson. Physical limitations on antennas of arbitrary shape. *Proc. R. Soc. A*, **463**, 2589–2607, 2007.
5. M. Gustafsson, C. Sohl, and G. Kristensson. Illustrations of new physical bounds on linearly polarized antennas. *IEEE Trans. Antennas Propagat.*, **57**(5), 1319–1327, May 2009.
6. M. Gustafsson, M. Cismasu, and B. L. G. Jonsson. Physical bounds and optimal currents on antennas. *IEEE Trans. Antennas Propagat.*, **60**(6), 2672–2681, 2012.
7. M. Gustafsson and B. Jonsson. Stored electromagnetic energy and antenna Q. Technical Report LUTEDX/(TEAT-7222)/1–25/(2012), Lund University, Department of Electrical and Information Technology, P.O. Box 118, S-221 00 Lund, Sweden, 2012. http://www.eit.lth.se.
8. M. Gustafsson and S. Nordebo. Antenna currents for optimal Q, superdirectivity, and radiation patterns using convex optimization. *IEEE Trans. Antennas Propagat.*, 2013. (in press).
9. R. C. Hansen and R. E. Collin. *Small Antenna Handbook*. Wiley, 2011.
10. H. Thal. Q bounds for arbitrary small antennas: A circuit approach. *IEEE Trans. Antennas Propagat.*, **60**(7), 3120–3128, 2012.
11. G. A. E. Vandenbosch. Reactive energies, impedance, and Q factor of radiating structures. *IEEE Trans. Antennas Propagat.*, **58**(4), 1112–1127, 2010.
12. G. A. E. Vandenbosch. Simple procedure to derive lower bounds for radiation Q of electrically small devices of arbitrary topology. *IEEE Trans. Antennas Propagat.*, **59**(6), 2217–2225, 2011.
13. J. Volakis, C. C. Chen, and K. Fujimoto. *Small Antennas: Miniaturization Techniques & Applications*. McGraw-Hill, New York, 2010.
14. H. A. Wheeler. Fundamental limitations of small antennas. *Proc. IRE*, **35**(12), 1479–1484, 1947.
15. A. D. Yaghjian and H. R. Stuart. Lower bounds on the Q of electrically small dipole antennas. *IEEE Trans. Antennas Propagat.*, **58**(10), 3114–3121, 2010.

NOVEL FLAG SHAPE MICROSTRIP ANTENNA ARRAY MUTUAL COUPLING REDUCTION

M. I. Ahmed[1,2*], **E. A. Abdallah**[1], **A. A. Sebak**[2], **and H. M. Elhennawy**[3]

[1] Electronics Research Institute, Cairo, Egypt

[2] Technology Innovation Center in RFTONICS, PSATRI, King Saud University, Riyadh, Saudi Arabia

[3]Ain Shams University, Cairo, Egypt

[*] miahmed@eri.sci.eg

Abstract- In this paper, a novel flag shape microstrip antenna is presented. The single and two element antenna were designed and fabricated on a substrate with dielectric constant of 2.2, thickness of 1.5748 mm, and tan δ = 0.001. The measuring results were obtained using Anritsu 37297D VNA. The results show that a reduction in mutual coupling of 36 dB is achieved at first band (1.68 - 2.65) GHz and 22.1 dB at second band (6.5 – 8.86) GHz. Also, a reduction in size of 80% is achieved. The microstrip array was studied by CST simulator and fabricated by proto laser machine with precision 25μm. The antenna can be used in the military or RFID applications.

Mutual coupling is a well-known effect in multi-element array antennas. Generally, mutual coupling is an unwanted phenomenon that distorts the behaviour of radiating elements in an antenna array. Every element in an antenna array affects every other element by radiating over the air or by propagating surface currents through the ground plane of microstrip antennas. Surface currents can be a bigger problem, especially when antenna elements are closely packed. Mutual coupling, which depends on inter element separation and relative orientation, causes undesirable effects on antenna characteristics [1].

Electromagnetic Band Gap structures (EBGs) are widely used in microwave circuit and antenna design because they produce band rejection characteristics [2]. Various configurations of EBG structures have been successfully applied in the patch antenna arrays to improve array characteristics, such as reduction of total size of the array and increasing radiation efficiency [3], [4].

This configuration is chosen because the ksa sign shape is the official page for any military application. So, this antenna may be used in soldier belts, any commodity for the military application, etc. The single and two element microstrip array are shown in Fig. 1 to study the mutual coupling and the effect of spacing between array elements. The EBG cells in the shape of small size ksa sign are inserted between the adjacent coupled elements in the array to suppress the pronounced surface waves. The comparison between the measured and simulated results is shown in Fig. 2. The simulated gain and radiation efficiency for single element at f = 2.413 GHz are about 2.28 dBi and 89%, respectively, while at f = 7.867 GHz they are 3.151 dBi and 94%, respectively. In two elements without EBG case the simulated gain and radiation efficiency at f = 2.359 GHz are 4 dBi and 95%, respectively, while at f = 9.55 GHz they are 6.23 dBi and 93%, respectively. The radiation pattern for two elements without EBG is shown in Fig. 3. The simulated gain and radiation efficiency for two elements with EBG at f = 2.152 GHz are 3.1 dBi and 96%, respectively, while at f = 9.433 GHz they are 4.953 dBi and 95%, respectively. The measured results agree well with those obtained by the CST.

(a) (b)

Fig. 1: Fabricated novel flag shape microstrip antenna array (a) single element, and (b) 2 elements array with EBG.

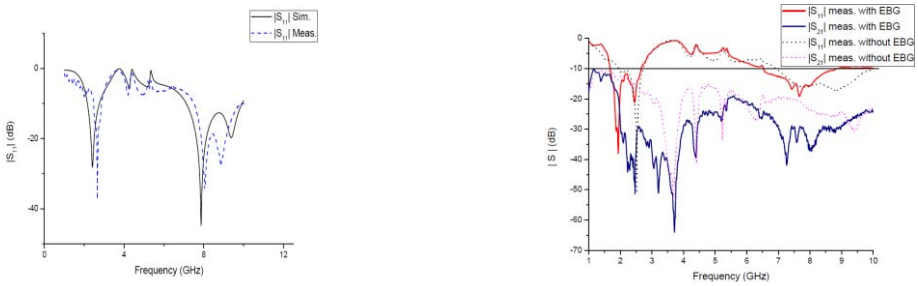

(a) (b)

Fig. 2: Comparison between simulation and measurement of novel flag shape microstrip antenna array (a) single element, and (b) 2 element array with and without EBG.

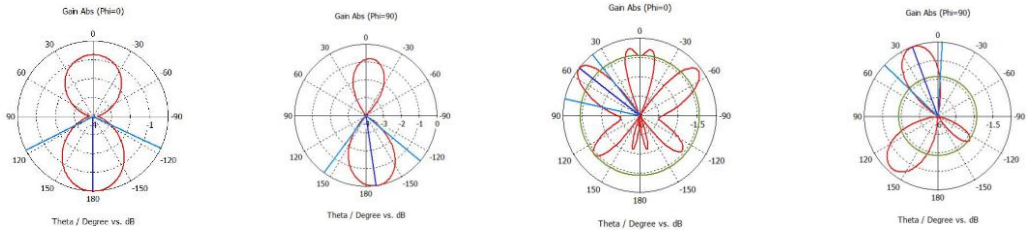

(a) (b)

Fig. 3: E-plane and H-plane radiation pattern of novel flag shape microstrip antenna array with EBG at frequencies (a) 2.152GHz, and (b) 9.433GHz.

REFERENCES

1. Parthasarathy, K. V., *Mutual Coupling in Patch Antennas*, Lap Lambert Academic Publishing, Germany, 2011.
2. Assimonis, S.D., T. V. Yioultsis and C. S. Antonopoulos, "Design and Optimization of Uniplanar EBG Structures for Low Profile Antenna Applications and Mutual Coupling Reduction," *IEEE Transactions on Antennas and Propagation*, Vol. 60, No. 10, 4944 – 4949, Oct. 2012.
3. Exposito-Dominguez, G., J. M. Fernandez-Gonzalez, P. Padilla and M. Sierra-Castaner, "Mutual Coupling Reduction Using EBG in Steering Antennas," *IEEE Antennas and Wireless Propagation Letters*, Vol. 11, 1265 – 1268, 2012.
4. Hajilou, Y., H. R. Hassani and B. Rahmati, "Mutual Coupling Reduction Between Microstrip Patch Antennas," in *Proceedings of 6th European Conference on Antennas and Propagation (EUCAP)*, Prague, Czech Republic, March 2012, 1064–1067.

Performances Improvement of printed antennas, by the use of electromagnetic bandgaps dielectric substrate

Mouloud. BOUZOUAD, Mourad REGGAB
Telecommunications, Signals and Systems Laboratory
University of Laghouat: BP 37G, Ghardaïa's Highway, 03000 Laghouat, Algeria.

Abstract— In this work we develop a technique to reduce the surface waves excited in the substrate of a micro strip antenna by means of planar structures with electromagnetic bandgaps (2D-PEBG). To highlight the contribution of this type of substrate in the suppression of surface waves, we conceived and carried out a set of printed antennas. Two of them use the 2D-PEBG substrate and the other two, use a standard substrate. They serve as references. For each type of substrate we chose two different thicknesses. One which is weak for which the surface waves are less excited in the substrate, the other more significant supporting their excitation. For the antennas printed on the thick substrates one expects that those using the 2D-PEBG substrate would be more powerful. Whereas those using the low thickness substrates (of the two types), should have comparable performances.

1 Introduction

Nowadays, one of the major problems in the design of printed antennas remains the energy transferred to the surface modes. This energy constitutes a significant part of the losses in the energy balance. According to the thickness and permittivity of the substrate, the part of power transferred to the surface modes can reach significant proportions, thus reducing the gain of the antenna.

These surfaces waves come completely out of phase to be added to the principal field radiated by the antenna causing a degradation of its radiation diagram. Indeed, when arrived at the limit of the ground plane of finite size, they are diffracted in space and disturb the clean radiation of the antenna.

The principal idea of this work is to use the concept of photonic/electromagnetic crystals with bandgaps (PBI or EBI) to remove or reduce to the maximum the propagation surface waves in the substrate, so that the antenna can transform the totality of the power received into radiated waves.

Indeed, during these two last decades, the structures with photonic bandgaps were the center of interest of a great number of studies of around the world. Re-launched by the proposal according to which: "tow- or tri-dimensional periodic dielectric structures could present frequency bands where the electromagnetic waves cannot propagate within the structure for all incidence angle and polarization of the wave" [1], [2]. The absence of propagating modes in such structures, in a band of frequencies, is then described as photonic/electromagnetic bandgap. In the range of microwave frequencies, these structures were proposed, for the first time in micro strip technology, towards the end of the Nineties. They are planar periodic artificial structures with two dimensions (2D-PEBG), based on transmission lines with periodic modulations in the wave impedance [3]. This impedance modulation can be obtained by carrying out adequate periodic patterns: perforated in the substrate [4], fabricated in the ground plate [5], by changing the geometry of the microstrip line [6], or by combining the former solutions.

This possibility of controlling the electromagnetic wave propagation in the three directions of space makes it possible to use these structures successfully in many applications, amongst which, the realization of: frequency selective surfaces [7], very directive antennas [8], antennas reflectors and radoms [9] and to remove the surface waves in the substrates of the printed antennas [10].

2 Determination and measurement of the BIEs' diagrams of the 2D-PEBG substrate.

The 2D-PEBG substrate (fig. 1-b) which we will use to produce our patch antennas consists of a set of holes of radius *r* pierced in a substrate host of permittivity ε_r, and thickness *h* and whose lower face is covered with a ground plane. The holes are laid out according to a periodic latticeof period *a*. The design of this substrate, starts from that of an infinite 2D-BIE material (fig. 1-a). The gaps must appear at the points *M* and K of the 1st Brillouin zone (fig. 1-c).

To determine the scatter chart of such a structure 2D-PEBG, it suffices that the wave vector traverses the contour of the triangle ΓMK of the 1st Brillouin zone [11]. But it is shown that it suffices to consider only the two directions of high symmetry ΓK and ΓM along whose the extremas of the bands are located [12].

An infinite 2D-BIE material consists of a lattice of a dielectric cylinder of radius r, separated by a period a and drowned in another dielectric. Several types of arrangements in the plan can be used. Only the triangular lattice is expected to present complete bandgaps for all directions in the plan (Kz = 0) and for all polarizations (which one will call thereafter a "2D- Band") [13]. This is due to the very high degree of symmetry of the Brillouin zone associated to it. In the case of small values of the ratio *r/a* the central frequencies of the bandgaps in the directions ΓK and ΓM can be estimated from the constants of propagation of the non-disturbed structure. Whereas for high values of the ratio r/a the recourse to the concept of the equivalent dielectric permittivity of substrate 2D-PEBG, makes it possible to obtain an approximation of these frequencies, to determine the lattice constants of the $a_{\Gamma K}$ and $a_{\Gamma M}$ and to obtain the bandgaps in the directions ΓK and ΓM. For a triangular lattice of air cylinders ($\varepsilon_{r1} = 1$) in a dielectric matrix (ε_{r2}), the equivalent dielectric permittivity is given by [11]:

$$\varepsilon_{req} = \varepsilon_{r2}\left(1 - 2\pi r^2 / \sqrt{3}a^2\right) \quad (1)$$

The propagation constant k is:

$$k = 2\pi\left(\lambda_0 \Big/ \sqrt{\varepsilon_{req}}\right) \qquad (2)$$

The lattice periods, for propagations along ΓK and ΓM are given by:

$$a_{\Gamma K} = 4\pi/3k \quad \text{and} \quad a_{\Gamma M} = 2\pi/\sqrt{3}k \qquad (3)$$

To obtain a 2D bandgap, it would be necessary to adopt for the period a an intermediate value between $a_{\Gamma K}$ and $a_{\Gamma M}$. On another side, the more significant is the disturbance, the more significant is the bandgap [11]. Thus, strong values of the ratio r/a are necessary to carry out EBG substrates presenting broad 2D-bandgaps for all polarizations. In the same way, the more contrast between the permittivity of the two used materials (ε_{r1} and ε_{r2}) is significant the larger is the bandgap [14].

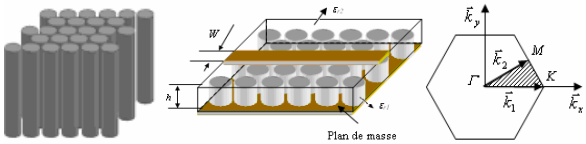

(a) (b) (c)

Fig.1. Infinite structure 2D-BIE (a), line substrate 2D-PEBG (b), 1st Brillouin Zone (c).

It is well-known that the presence of a disturbance in the periodic lattice, which is also known as "defect", produces a located mode within the bandgap [15]. The defect in our structure is consisted of the central chip of the substrate on which the antenna will be printed. The central hole of the substrate is no more filled with air but with another material of dielectric permittivity ε_{rd}.

2.1 Determination and measurement of the BIE diagrams of substrate 2D-PEBG

We use the transmission lines method to determine the 2D-bandgaps of the 2D-PEBG substrate (fig. 2) [10]. The formulation used makes it possible to take account of the geometry modulation of the microstrip line, of the dielectric material permittivity as it also takes account of the frequency response of the line parameters. Figure 3 shows a comparison of the S_{21} parameter of a microstrip line printed on the 2D-PEBG substrate. Note the good agreement between the calculated and experimental results.

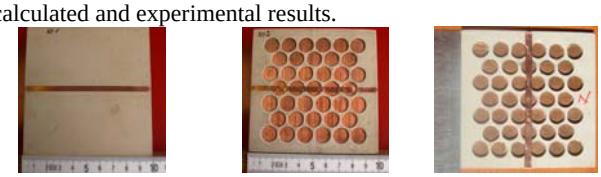

(a) (b) (c)

Fig. 2. Photographs of the microstrip lines carried out on a substrate: standard (a), 2D-PEBG directed according to ΓK (b), according to ΓM (c).

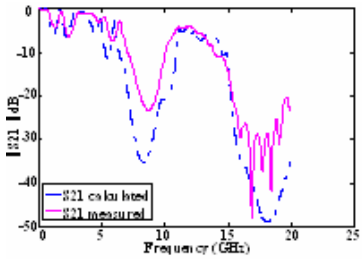

(a

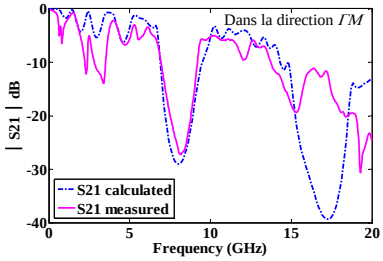

(b)

Fig. 3. Measured and calculated S parameters of a microstrip line printed on a substrate 2D-PEBG: directed in the direction ΓK (a), and in the direction ΓM *(b)*

2.2 The 2D omnidirectional bands diagram

The omni directional 2d bandgaps charts of a substrate 2D-PEBG, are obtained by the intersection of the charts of the given unidirectional bands for the two high symmetry directions ΓK and ΓM (fig. 3) [16]. Figure 4 shows the comparison between the charts of the omni directional bandgaps of an infinite structure 2D-BIE and that of substrate 2D-PEBG, of thickness h made up of air filled cylinders of diameter 12.7 mm, in a dielectric host of permittivity $\varepsilon_r = 10.2$. These charts are calculated by the method of the plane waves for the first structure and the method of transmission lines for the second. In spite of the simplicity of the method of transmission lines, the obtained results are in good concord with those of the method of plane waves mainly for the first band (Fig. 4) [10].

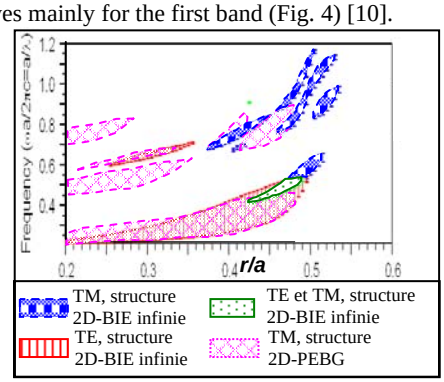

Fig. 4. Charts of the bandgaps of 2D-PEBG substrate and 2D-BIE infinite structure .

3 Design of the microstrip antenna on the 2D-PEBG substrate

3.1 The surface waves

The purpose of an antenna is naturally to radiate waves in free space. But, there are also other types of excited waves in a printed antenna which are, in general, undesirable. The most significant ones are the surface waves, which are generally harmful for the performances of the antennas. We always desire to avoid or reduce to the maximum their excitation.

The analytical solution for these wave modes was given by R. E. Collin [17]. They are transverse magnetic (TM) and electric (TE) modes which propagate in the substrate out of the area where the patch is. These modes are associated to the waveguide formed by the substrate, of thickness h, and the ground plane. They propagate in the substrate in slightly tilted directions to the bottom of the patch, with an elevation angle Θ such as: $\pi/2 \le \theta \le \pi - \arcsin\left(1/\sqrt{\varepsilon_r}\right)$. When the waves reach the ground plane they are reflected to the top and by reaching the dielectric-air interface they are again reflected to the bottom, and so on. The phase velocity of these surface waves strongly depends on the dielectric permittivity ε_r and the thickness h of

the substrate. The surface waves power decreases only to $1/r$ with the distance. The cut-off frequencies of these surface modes are given by [18]: $f_{cn} = nc \Big/ \left(4h\sqrt{\varepsilon_r - 1}\right)$ (5)

where c is the speed of light in the vacuum, n = 1, 3, 5,…for the modes TE_n and n = 0, 2, 4, 6, ... for the TM_n modes. Note that the mode TM_0 has a null cut-off frequency, so that it is always excited, even in the thin substrates of low permittivity. The more is the the substrate electrically thick, the more excited are the surface waves. James and Hendreson studied the excitation of the mode TM_0 They showed that the excitation of the surface waves becomes significant when $h/\lambda_0 > 0.09$ for $\varepsilon_r \approx 2.3$ and $h/\lambda_0 > 0.03$ for $\varepsilon_r \approx 10$ [19]. The TE_0 mode is mainly excited at the discontinuities of the microstrip line geometry. It has a non null cut-off frequency beyond which there is an "optimal" possibility of coupling with the propagated modes. Thus in general, if we observe the above constraints in the choice of the substrate for a particular application, no significant difficulty of excitation of surface wave should arise. However, in our study we want to precisely support the excitation of the surface waves, to highlight the role of substrate 2D-PEBG in their suppression.

3.2 Design of the rectangular Patch antenna

We will simulate and fabricate four antennas (Fig. 6). The two first are printed on a 2D-PEBG substrate and the two others, which will be used as reference, on a standard substrate. For the two types of substrate, we will use two different thicknesses h = 1.27 mm and h = 1.9 mm. With the first value of h we are at the limits of the conditions supporting the excitation of the TM_0 mode of the surface waves ($h/\lambda_0 = 0.036$) [20], and the performances of the produced antennas on the two types of substrate should be comparable. On the other hand, for the second value we are under conditions very favorable to the excitation of the surface waves ($h/\lambda_0 = 0.054$) and we expect that the antennas produced on the 2D-PEBG substrate, should present better performances. The 2D-PEBG substrate, which we would like to conceive, to produce our patch antennas, must present a bandgap centered around f_0 = 9 GHz [12]. Obtaining a broad bandgap requires a strong contrast between the permittivities of the used materials. The holes being air-filled ($\varepsilon_{r1} = 1$), we chose for the host dielectric a high value of the permittivity $\varepsilon_r = 10.2$. A value of the ratio r/a of 0.46 is sufficient, to be sure of the opening of the bandgaps. The equivalent permittivity of the 2D-PEBG substrate is equal to 2.37 and the periods of the lattice $a_{\Gamma K}$ and $a_{\Gamma M}$ are respectively 14.44 mm and 12.5 mm. By adopting for a an intermediate value equal to 13.8 mm, and with a ratio r/a = 0.46 we obtain for the air cylinders a radius r = 6.35 mm. Finally our 2D-PEBG substrate consists of a set of holes, of diameters r pierced in a host substrate of permittivity ε_r The holes are laid out according to a triangular periodic lattice of period a. This 2D-PEBG substrate has a broad omnidirectional bandgap (41.5 %) extending from f_{c1} = 5.6 GHz to f_{c2} = 9 GHz and centered at f_0 = 8.16 GHz (Table 1). As we can see it on figure 5, the presence of the central chip which supports the patch creates a mode of defect inside the bandgap at the frequency f_{md}. Thus, The truly usable bandgaps lie between the frequency of the defect mode and one of the two cut-off frequencies of the omnidirectional band, according to whether we use the lower or higher mini band.

The operating frequency of our antennas is fixed at f_0 = 8.5 GHz. It was selected to be inside the rejection band of the 2D-PEBG substrate which extends from 7.3 GHz with 9 GHz. With this operating frequency, and for the chosen dielectric substrate thicknesses, the first higher surface wave mode TE_1 of cut-off frequency 12.98 GHz, cannot be excited. Consequently, the only possible improvements, of the antenna performances , will be due to the suppression of the only TM_0 mode With a permittivity of 10.2, if we wanted to excite the first surface mode TE_1 in the 5-10 GHz frequency band , we would need a substrate thickness of 2.54 mm. Unfortunately, with this thickness, and considering dimensions of the patch (of the order of 5 mm) and of the excitation coaxial probe (Φ_{probe} = 1.28 mm), it would be impossible to adapt the antenna to the value of 50 Ω the inductive component introduced by the probe would be too significant. For this reason, we chose for our realizations substrates of thickness 1.27 mm and 1.9 mm.

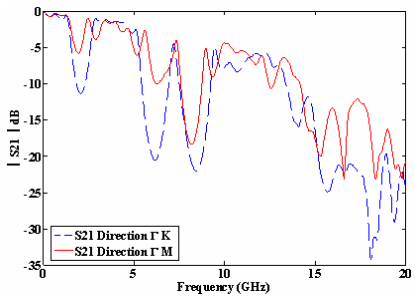

Fig. 5. Measured and calculated S_{11}, parameters of a transmission ligne on a 2D-PEBG substrate with defect.

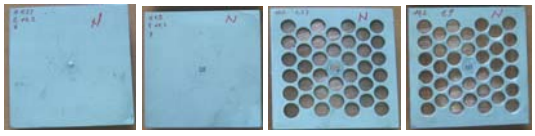

(a) (b)

Fig. 6. Manufactured antennas prototypes on: standard substrate (a) and 2D-PEBG (b).

TABLE 1: THE BANDS STRUCTURE OF 2D-PEBG SUBSTRATE WHERE THE FREQUENCIES ARE IN GHZ

Direction	f_{c1}	f_{dm}	f_{c2}	Δf_1	f_{01}	Δf_2	f_{02}
ΓK	5.1	7.2	9.5	2.1	6.1	2.3	8.3
ΓM	5.6	7.3	9.0	1.8	6.5	1.6	8.2
2D	5.6	7.3	9.0	1.8	6.5	1.6	8.2

3.3 Patch antennas dimensions

Once the operating frequency and the parameters of the substrate are fixed, the dimensions of the patch antennas can be determined [10]. Table 2 presents dimensions of our antennas obtained by simulation with the ***HFSS*** software. Since polarization is linear, a simple excitation by coaxial probe is used. The adaptation to 50 Ω is ensured by the choice of X_p (position of the probe) on the patch's axis of symmetry.

TABLE 2 : DIMENSIONS OF THE PATCH ANTENNAS (

Antenna	L (mm)	W (mm)	X_p (mm)	f_0 (GHz)
Uni-1d27	4.58	6.38	0.87	8.52
Bie-1d27	4.58	6.38	0.84	8.51
Uni-1d9	4.00	5.56	0.90	8.47
Bie-1d9	4.00	5.56	0.82	8.38

RESULTS AND DISCUSSION

Table 3 presents a comparison between the HFSS simulations results and the experimental ones. The suffixes "-s" and "-m" in the names of the antennas refer to the simulation results, and

measurements ones respectively. We notice first of all a rather good concordance, especially concerning the resonance frequencies where the difference does not exceed 2 %. Concerning the input resistances of the antennas (R_{in} , we observe variations, between the theoretical and experimental values, varying between 5 % (for the Bie-1d27 antenna) and 15 % (for the antenna Uni-1d27). These variations are due to two factors related to the excitation of the antennas. The first relates to the dimensions of the excitation probe, compared to those of the antennas. The latter (L and W of the four antennas) are lower than 5 mm, whereas the probe has a diameter Φ_S = 1.28 mm ($L/\Phi_S = 3.5$). The second factor relates to the positioning of the excitation point (table 3). For the four antennas, the probes are located at less than 1 mm from the center of the patch, whereas Φ_S = 1.28 mm. In this area, the variation of R_{in} according to X_p is very fast. For example, for the Bie-1d9 antenna, a variation of X_p of 0.05 mm, around the optimal value 0.82 mm, change the real part of the input impedance R_{in} of 5 Ω. Considering the value of Φ_S it is difficult, to position the probe at distance X_p with a precision of the order of the tenth of a millimetre. Such a variation on Xp can produce a significant variation of R_{in}.

TABLE 3 : PATCH ANTENNAS CARACTÉRISTIQUES

Antenna	X_p (mm)	f_0 (GHz)	R_{in} (Ω)	B (%)	G (dB)
Uni-1d27-s	0,82	8,50	44.3	2.7	5.1
	0.92	8.53	51.5	3.0	5.1
Uni-1d27-m	0.87	8.42	53.7	2.9	
Bie-1d27-s	0.79	8.49	43.8	2.5	5.5
	0.89	8.53	54.5	2.8	5.5
Bie-1d27-m	0.85	8.48	46.6	2.8	
Uni-1d9-s	0.85	8.46	43.5	5.6	4.4
	0.95	8.47	53.3	6.4	4.4
Uni-1d9-m	0.90	8.39	43.5	8.2	
Bie-1d9-s	0.77	8.46	42.1	4.5	5.7
	0.87	8.46	52.8	5.0	6.6
Bie-1d9-m	0.82	8.53	31.8	5.0	

3.4 Pass Bande

The examination of table 3 shows first of all certain deviations between the theoretical and measured values of the passband widths. These variations caused by the impedance mismatching of the manufactured and measured antennas due to the positioning of the excitation probe. Nevertheless, the results obtained remain coherently conform to the Chu criterion [21]. We observe moreover, that the antennas, manufactured on the of 1.9 mm thick substrates (standard and BIE), present much more significant band-widths than those of the antennas, realized on the 1.27 mm thick substrates. This increase of the substrate thickness is cause a gain reduction in the case of Uni-1d9 antenna compared to the reference antenna (Uni-1d27), and a clear degradation of its radiation diagram (fig. 9). On the other hand, we note that the Bie-1d9 antenna, presents a gain higher than that of the reference antenna and a comparable radiation diagram. Its bandwidth is as significant as that of the Uni - 1d9 antenna (Table 3 and fig. 10).

3.5 Surface waves Suppression

Figure 7 shows the electric field charts, for two different frequencies, in the two substrate types (standard and 2D-PEBG) and for the two thicknesses. We notice that for the two types of less thick substrates (h = 1.27 mm), the intensity of the electric field is almost identical. The frequencies used are too much lower than the cut-off frequency of the first surface mode TE_1 equal to 19.5 GHz at this thickness. Whereas in the thick substrates (h = 1.9 mm), we note that the intensity, of the electric field on the surface of the standard substrate, is appreciable starting from the frequency of 8.5 GHz, because for this thickness the cut-off frequency of the first surface mode is 12.98 GHz. On the other hand, for 2D-PEBG substrate the intensity of the electric field on the surface of the substrate is clearly reduced even at the frequency of 12 GHz. For the two frequencies, the density of the electric field on the surface of the standard substrates is clearly more significant than on the surface of 2D-PEBG substrates. The higher the frequency and the thickness, of the substrate, are the more significant is the intensity of the excited surface waves in the standard substrate and the more appreciable becomes the effect of 2D-PEBG substrate .

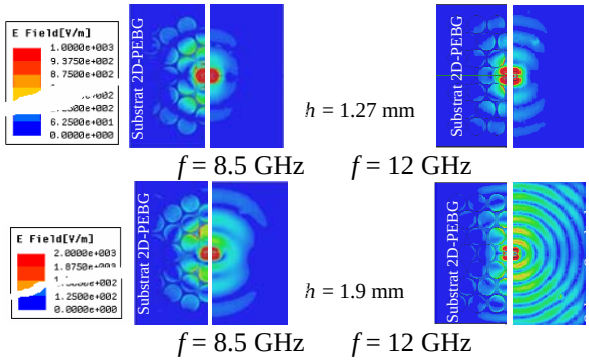

Fig. 7. Chart of the electric field on the surface of the standard substrates and 2-DBIEP.

The comparison of the radiation diagrams of the four antennas (fig. 9 and 10), confirms the previous observations and highlights the suppression of the surface waves by 2D-PEBG substrate. Indeed, when the surfaces waves are only less excited in the radiating structure, case of the substrates thickness 1.27 mm, the use of substrate 2D-PEBG does not make a great improvement to the diagram of radiation.

3.6Patch antennas gain

In figure 8 are presented the gains of the four antennas. We notice, that the increase in thickness of the standard substrate results in a reduction in the gain of about 16 %, compared to that of the antenna Uni - 1d27. The antenna Uni - 1d9 presents the weakest gain. This observation is in conformity with the predictions because this structure offers the best excitation conditions of the surface waves.

Whereas the use of substrate 2D-PEBG makes it possible to increase the gain approximately 10 % compared to the antenna Uni - 1d27 and 27 % compared to the antenna Uni-1d9. This performance is due to the suppression of the surface waves by this type of substrate. On the other hand, for the substrates of thickness 1.27 mm, the gain of the antennas on standard substrate and 2D-PEBG do not differ much, since for this thickness the surface waves are less excited.

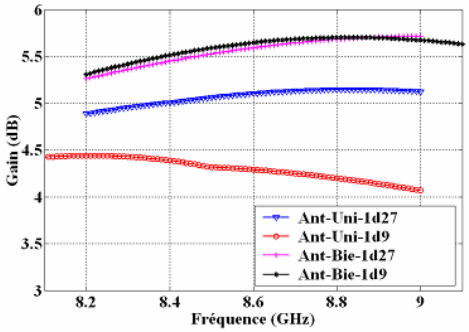

Fig. 8. Antennas gains according to the frequency .

3.7 Radiation Diagram

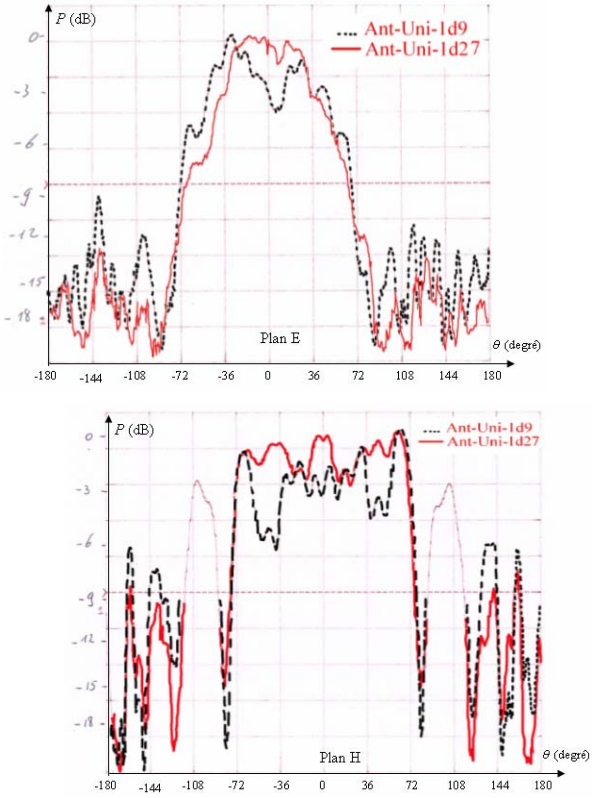

Fig. 9. Radiation diagrams of the antennas with standard substrate (H = 1.90 mm and H = 1.27 mm).

Figures 9 and 10 show the measured radiation diagrams of the various produced antennas. We notice that the increase in thickness of the standard substrate supports the excitation of the surface waves, which are responsible for the degradation of the radiation diagram of the antenna. On the other hand, the same increase in thickness of 2D-PEBG substrate does not affect the radiation diagram. This performance is due to the property which the substrates have with electromagnetic bandgaps to prevent the electromagnetic wave propagation whose frequencies are located inside the bandgap. This property enables us to use thicker substrates without being disturbed by the appearance of surface waves. In other words, an increase in thickness of the standard substrate of 0.63 mm causes an increase in the side lobes level of approximately 4 dB in the E plan (3 dB in the H plan). This degradation is due primarily to the excitation of the surface waves in the substrate. The use of 2D-PEBG substrate, enables us to exploit its bandgaps to reduce the effects of surface waves. Indeed, the examination of figures 9, 10 and of table 3 makes it possible to highlight the role of 2D-PEBG substrate in the improvement of the radiation diagram of the Bie-1d9 antenna compared to the Uni-1d9 antenna.

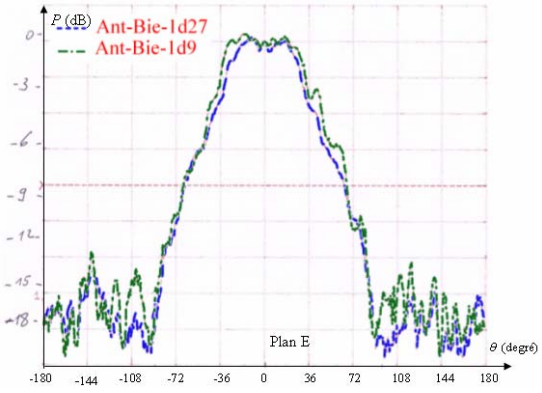

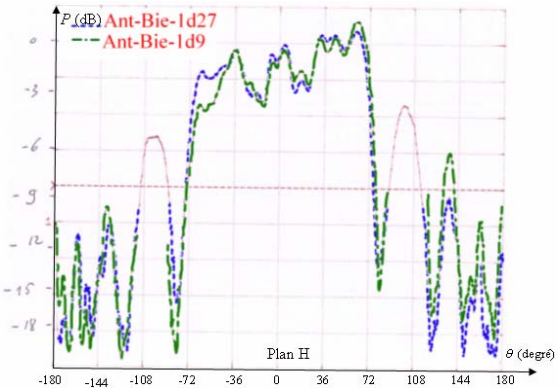

Fig. 10. Radiation diagrams of the antennas with 2D-PEBG substrate (H = 1.90 mm and H = 1.27 mm)

4 Conclusion

The method of transmission lines, used to determine the structures of bands of a 2D-PEBG substrate, is very simple to implement. It gives good results and constitutes a very efficient analytical tool for the determination of the bandgaps charts of this type of structures. The latter offer a very interesting filtering effect of which can be used to minimize the effect of the surface waves excited in the substrates of microstrip antennas.

The comparison of the gains and the radiation diagrams of the various studied antennas make it possible to highlight the improvements of the performances brought to the antennas by the use of 2D-BIE substrates. An increase of 49 % in thickness of the substrate makes it possible to double the band-width. In against part, with a standard substrate, it causes a real degradation of the radiation diagrams of the antenna. On the other hand, with a thick substrate 2D-PEBG, allowing reducing the surfaces waves, in addition to the increase in the band-width, we obtain an increase in the gain without deterioration of the radiation diagram

REFERENCES

[1] E. Yablonovitch, 'Inhibited Spontaneous Emission in Solid-State Physics and Electronics', Phy. Rev. Lett., Vol. 58, 1987, pp. 2059.

[2] S. John, 'Strong localization of photons in certain disordred dielectric superlattices', Phys. Rev. Lett. 1987, 58, 2486

[3] A. Görür, C. Karpuz and M. Alkan, 'Characteristics of Periodically Loaded CPW Structures', IEEE Microwave Guided Wave Lett No 8 1998, pp 278-280.

[4] Y. Qian, V. Radisic, and T. Itho, 'Simulation and experiment of photonic band-gap structures for microstrip circuits', Asia Pacific Microwave Conf. Proc., Hong Kong, Dec. 1997, pp 585-58.

[5] T. Lopetegi, M.A. G. Laso, M. J. Erro, D. Benito, M. J. Garde, F. Falcone, and M. Sorolla, ' Novel Photonic Bandgap Microstrip Structures Using Network Topology', Microwe and optical Technology letters Vol. 25, 2000, pp 33-36

[6] A. Saib, R. Platteborze, and I. Huynen, 'Experimental demonstration of the origin of photonic bandgap creation and associated defect modes in microwave circuits,' Microwave and Optical Technology Letters, vol. 41, 2004, pp. 5–9.

[7] S. Maci, M. Caiazzo, A. Cucini, and M. Casaletti, 'A Pole-Zero Matching Method for EBG Surfaces Composed of a Dipole FSS Printed on a Grounded Dielectric Slab', IEEE Trans. On Antennas And Propagation, VOL. 53, 2005, NO. 1.

[8] J. Danglot, T. Akalin, O. Vanbésien, D Lippens, "effet d'autocollimation pour des sources hyperfréquences a cavité a bande interdite photonique', 12èmes Journées Nationales Microondes, Poitier, mai 2001.

[9] G. Poilasne, J. Lenormand, P. Poiliguen, K. Mahdjoubi, C. Terret, Ph. Gelin, 'Theoretical Study Of Interactions Between Antennas And Metallic Photonic Bandgap Materials', Microwave and Optical Techn. Lett. Vol. 15, No. 6, August 1997.

[10] M. Bouzouad, Thèse de doctorat d'état, Dec. 2007, ENP, Algérie.

[11] R. Cocciioli, T. Itoh, 'Design of photonic band-gap substrates for surface waves duppression', IEEE MTT-S Digst. 1998.

[12] K. Agi, M. Mojahedi, B. Minhas, E. Schamiloglu, and K. J. Malloy, 'The effects of an electromagnetic crystal substrate on a microstrip patch antenna ', IEEE Trans. AP, Vol. 50, 2002, pp.451-456.
[13] R. Cocciioli, T. Itoh, 'Design of photonic band-gap substrates for surface waves duppression', IEEE MTT-S Digst. 1998
[14] M.Bouzouad, A. Saib, R. Platteborze, I. Huynen, R. Aksas, 'Defect Modes in Microstrip lines on Electromagnetic Bandgap Substrates of Finite Extent', Microwave and Optical Technology Letters, Vol. 48, No. 1, 2006, pp. 144-150.
[15] D. R. Smith, S. Schultz, S; L. McCall, and P. M. Platzmann, 'Defect studies in a Two-dimensional periodic Photonic Lattice', Journal of modern Optics, vol. 41, No. 2, 1994, pp. 395-404.
[16] M. Bouzouad, A. Benabdelkrim, R. Aksas, 'Détermination expérimentale des bandes interdites des matériaux diélectriques périodiques artificiels en technologie microstrip', 1st International Symposium on Electromagnetism, Satellites and Cryptography, June, 19-21, 2005, Jijel, Algeria.
[17] Collin, R. E. Field Theory of Guided waves, McGraw-Hill Book Co. N. Y., 1960, pp 470, 474.
[18] D. Pozar, 'Consideration for millimeter wave printed antennas', IEEE Trans Ant. Propagat., Vol. 31, No 5, 1983, pp. 740–747.
[19] J. R. James, and A. Hendreson, 'Hight-Frequency Behavior of Microstrip Open-Circuit Terminations', IEE J Microwaves Optics and Acoustics, Vol. 3, 1979, pp. 205-218.
[20] I. J. Bahl and P. Bhartia, 'Microstrip Antenna', Artech House, 1980.
[21] L. J. Chu, 'Physical limitations in omnidirectional antennas', J Appl. Phys, 19, 1948, pp. 1163–1175.

Mobile antennas; Smart skin antennas

An Agile and Efficient MIMO System for Small Terminals

O. N. Alrabadi[*1], E. P. Tsakalaki[1], M. Pelosi[1] and G. F. Pedersen[1]
[1]Antennas, Propagation & Radio Networking Section, Aalborg University, Denmark
[*]corresponding author: ona@es.aau.dk

Abstract- A novel multiple-input-multiple-output (MIMO) system for the high LTE bands is proposed. The system is comprised of four small loop antennas, each having one communication and one control port. The antennas exhibit impressive frequency agility and a good level of inherent isolation over the different frequency bands. The performance of the MIMO system is evaluated by the spectral efficiency versus frequency and by the newly defined information bandwidth metric.

Future generations of mobile devices rely on MIMO technology to deliver on the promises of boosted data rates and higher system performance. In this work we propose a novel MIMO architecture where four loop antennas are placed at the four corners of the ground plane (GP) thus maintaining a sufficient bandwidth. We focus on the free-space scenario while user coupling scenarios are left as a future work. Each loop has two ports: an RF communication port and a control port for tuning the antenna. The antenna system shown in Figure 1 (with dimensions in millimeters, mm) is comprised of four loop antennas over a (55x110)mm^2 GP representing the typical dimensions of a modern smart phone. Each loop antenna occupies an area of (15x4)mm^2. The MIMO structure made of annealed copper was simulated using the transient time domain solver from CST MICROWAVE STUDIO®. The MIMO system can be expressed as a four (active) port network with the 4x4 scattering matrix $\boldsymbol{S}$ whereas the symmetries in its entries $S_{ii}=S_{jj}$, $S_{ij}=S_{ji}$, $\{i,j\}\in\{1,\ldots,4\}$ are due to using identical antenna elements with equal capacitance at their control ports, over a symmetric topology.

Figure 2 shows the frequency response of the MIMO antenna system at the center frequencies f=1600MHz, 1800MHz, 2200MHz and 2400MHz. The control port was tuned between a minimum capacitance of 0.01pF and a maximum capacitance of 1pF. By integrating the active pattern over a sphere, a total efficiency that accounts for the Ohmic losses in the copper of -0.5dB has been obtained across all bands. The coupling mechanism among the MIMO antennas can be observed from the logarithmic contour map of the surface currents shown in Figure 3. The figure shows the surface currents magnitude (in dB) when exciting the first loop antenna with a unit voltage signal while terminating the other ports with their matching impedances (same procedure for obtaining the active element response). The figure clearly shows that the antennas cross-coupling mainly happens through the edges of the GP as is already expected. On the other hand, the performance of the MIMO system not only depends on the self-matching and cross-coupling among the four loop antennas, but also on the spatial correlation. All the antenna parameters can be taken into consideration by observing the system spectral efficiency versus frequency as explained in [1]. A tight bound on the spectral efficiency of the proposed system assuming a uniform three-dimensional (3D) environment is given by

$$\eta_{\mathrm{UB}} = \log_2\left|\left(1+\frac{\mathrm{SNR}}{4}\right)\mathbf{I}_4 - \frac{\mathrm{SNR}}{4}\boldsymbol{S}^{\mathrm{H}}\boldsymbol{S}\right|,$$

where $\mathbf{I}_4$ is an identity matrix of a fourth dimension, |X| returns the determinant of X, and $(\,.\,)^{\mathrm{H}}$ is the conjugate

transpose operator. Figure 4 shows the spectral efficiency versus frequency for the proposed MIMO system (the four loop antennas) as well as the spectral efficiency of three and four ideal MIMO antennas. The figure clearly illustrates the multiplexing potential of the proposed MIMO system. For example, the proposed MIMO system can be said to have an information bandwidth of 420MHz (2180MHz-2600MHz) which is the bandwidth over which the system provides a better MIMO performance than three ideal MIMO antennas. The MIMO performance of the antenna system is ranked 'good' in view that no decoupling & matching networks or GP modifications have been used.

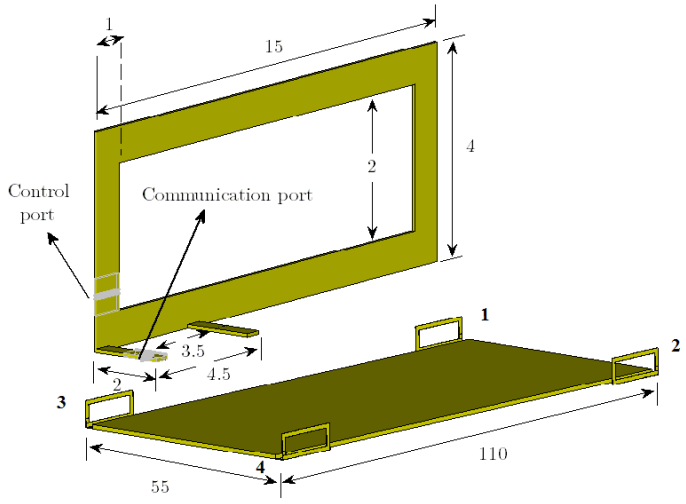

Figure 1 The numerical model of the antenna system comprised of 4 loop antennas (antenna dimensions in mm)

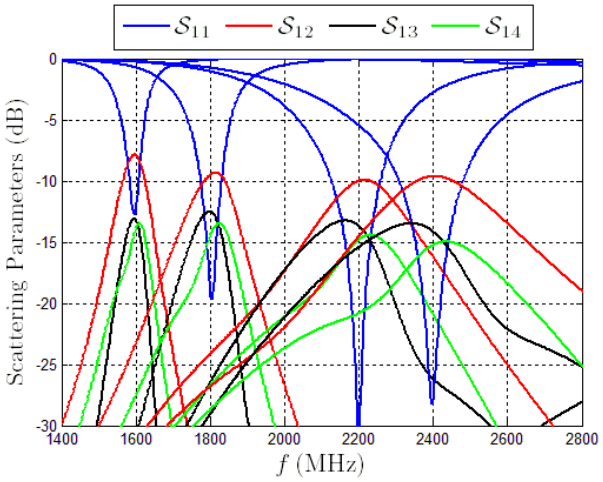

Figure 2 The frequency response of the proposed MIMO system at f = {1600, 1800, 2200, 2400}MHz

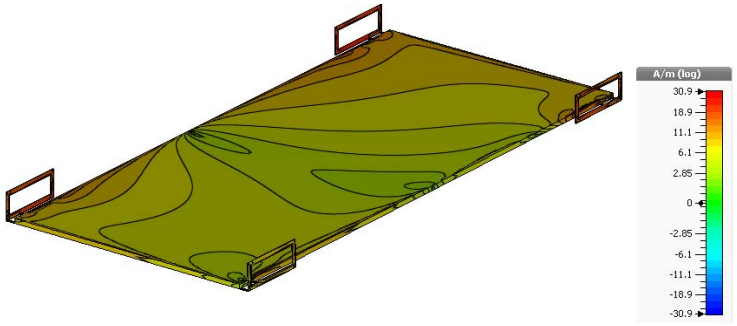

Figure 3 A logarithmic contour map of the (active) surface currents of the first loop antenna at f = 2000MHz

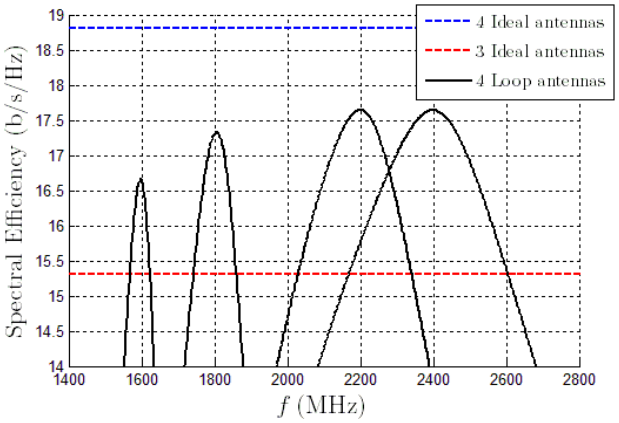

Figure 4 The spectral efficiency of the proposed MIMO system at SNR=20 dB, f = {1600, 1800, 2200, 2400}MHz

REFERENCES

1. Tsakalaki, E., Alrabadi O.N., Pelosi M., Pedersen G.F., "Multiplexing Index and MIMO Band Index: Two Novel Metrics for MIMO Antenna Evaluation," *Submitted to IEEE AWPL.*
2. Pelosi, M., Knudsen, M.B., Pedersen G.F., "Multiple antenna systems with inherently decoupled radiators," *IEEE Trans. on Ant. and Prop.*, Vol. 60, pp. 503-515, 2012.

A Review of Design Considerations for Capacitive Coupling Elements in Small Terminals

M. Pelosi, O. N. Alrabadi, E. Tsakalaki, G.F. Pedersen

(APNet), Department of Electronic Systems, Faculty of Engineering and Science, Aalborg University

Aalborg, Denmark.

Abstract-In this paper a methodological review of Capacitive Coupling Elements (CCEs) for small terminals is presented, comparing a series of configurations representing the radiating structures commonly reported in literature. It was found that very simple CCEs still provide the best average bandwidth potential, avoiding the use of complex structures and simplifying design. CCEs do not benefit from being enlarged electrically if their overall volume remains constant, as they do not follow the same behavior of self-resonant antenna elements.

Introduction

CCEs were introduced for the first time in [1], which presented a framework describing the interaction between a radiating element and the chassis in the form of a system of coupled resonators. The underlying concept is that the chassis itself contributes significantly to radiation, especially at lower frequencies, where the dipole fundamental mode depends on its dimensions with respect to the operating wavelength. Over time several studies have accumulated in literature [1-5], lacking however a holistic approach which would highlight the core design guidelines for CCEs. At this purpose, we gathered all the proposed solutions throughout literature, grouping them according to their features in 14 root structures as displayed in figure 1. Each individual configuration then is modified to accommodate the subsequent removal of CCE walls, in such a way to study the impact of each topological modification on the radiating mechanism (the procedure is omitted here for brevity).

Simulation Setup

The PCB dimensions were always kept constant, having a width of 50mm and a length of 120mm, representing the typical dimensions of a contemporary smartphone. The height and width of the CCE were both set to 10mm, while its length was equal to 50mm. The chassis and the CCE were both modeled as lossless Perfect Electric Conductors (PECs), using CST Microwave Studio for the electromagnetic simulation itself and post-processing results in Matlab. In order to compare different simulations in a concise way, we devised a new metric called hereinafter Average Bandwidth Potential ABP, which is the average of the bandwidth potential over a particular range of frequencies (500MHz-2500MHz).

Simulation Results

After obtaining the bandwidth potential for each simulated CCE, for each configuration we picked the combination exhibiting the highest ABP, as can be seen in figure 2. From a design perspective, it is obvious that an optimum choice would require picking that particular solution which provides the highest ABP, paying also attention at the volume occupation and the complexity of the structure. Simulation A0 exhibits the highest ABP as represents the largest CCE and can be thought as a reference. In B35, we find that it is beneficial to L-bend the CCE around the chassis, while simulations C45, D45, and E45 display a similar behavior.

Simulations F55, G55, H55 all degenerate in the same radiating element, showing that even a single plate is sufficient to constitute an efficient CCE. Similarly, the triad I60, L60, M60 also degenerate in a single planar element together with the triad N60, O60, P60. The findings are consistent with the existing literature, proving in a systematic way which structures are preferable depending on the particular chassis-CCE configuration. It is demonstrated that it is not relevant to bend the lateral walls of the CCE hoping to electrically enlarge the radiating structure, as CCEs do not behave as conventional self-resonating elements.

Conclusion

In this paper design guidelines for CCEs have been reviewed and assessed by means of electromagnetic simulations, comparing different solutions by looking at their ABP. It was found that it is not necessary to rely on complicated CCEs, as their inherent non-self-resonant coupling mechanism accommodates for the use of simple plates L-bent over the chassis. Moreover, the best configurations are at the same time the simplest, making it possible to accommodate CCEs of various shapes depending on the design needs.

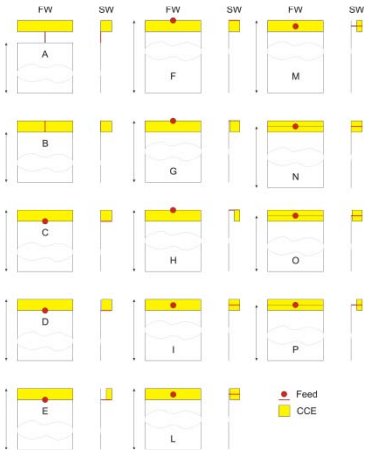

Fig. 1. CCEs A-P in Front View (FW) and Side View (SW).

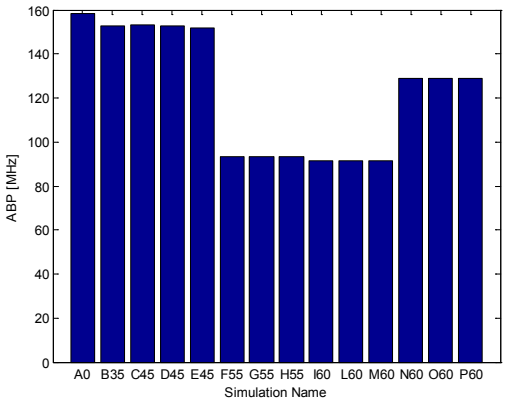

Fig. 2. Average Bandwidth Potential for the best CCEs.

References

[1] Vainikainen, P.; Ollikainen, J.; Kivekas, O.; Kelander, K.; , "Resonator-based analysis of the combination of mobile handset antenna and chassis," Antennas and Propagation, IEEE Transactions on , vol.50, no.10, pp. 1433- 1444, Oct 2002.

[2] Villanen, J.; Ollikainen, J.; Kivekas, O.; Vainikainen, P.; , "Compact antenna structures for mobile handsets," Vehicular Technology Conference, 2003. VTC 2003-Fall. 2003 IEEE 58th , vol.1, no., pp. 40- 44 Vol.1, 6-9 Oct. 2003.

[3] Villanen, J.; Ollikainen, J.; Kivekas, O.; Vainikainen, P.; , "Coupling element based mobile terminal antenna structures," Antennas and Propagation, IEEE Transactions on , vol.54, no.7, pp. 2142- 2153, July 2006.

[4] R. Valkonen, J. Holopainen, C. Icheln, and P. Vainikainen, "Minimization of power loss and distortion in a tuning circuit for a mobile terminal antenna," in Proc. International Symposium on Antennas and Propagation (ISAP 2008), 27-30 October 2008, Taipei, Taiwan, pp. 449-452.

[5] Vainikainen, P.; Villanen, J.; Holopainen, J.; Icheln, C.; , "Development trends of small antennas for mobile terminals," Antennas and Propagation Society International Symposium, 2007 IEEE , vol., no., pp.2837-2840, 9-15 June 2007.

Electrically Small Superdirective Arrays of Metamaterial-Inspired Antennas

B. Sentucq, A. Sharaiha, S. Collardey
Institute of Electronics and Telecommunications of Rennes (IETR)
University of Rennes 1, Rennes, France
Bruno.sentucq@univ-rennes1.fr, Ala.sharaiha@univ-rennes1.fr, Sylvain.collardey@univ-rennes1.fr

Abstract-A new electrically small antenna design based on a metamaterial-inspired structure driven by an electrically small monopole antenna is presented. This antenna of $\lambda_0/19x\lambda_0/19$ size works in the UHF band and offers a simulated maximum gain of 0.86dB and a directivity of 2.12dB in the matched bandwidth of 5.2MHz. The two driven elements compact array and the parasitic array are then compared. The design details, simulated and measured radiation characteristics of the antenna system and antenna arrays are reported.

Introduction

For several applications, a high directivity with electrically small antennas is required. Since the miniaturization of antennas implies a decrease in directivity, electrically small antennas have to be used in an array in order to narrow the beam width. We know that the directivity of an array of N isotropic radiators can approach the value of N^2 when the distance between radiating elements approaches zero [1] and it has been shown that an array of two monopole elements over a large ground plane can reach such a super-directivity, whether the two antennas are driven or only one is fed, the other one being a parasitic element [2].

In this paper, we present in a first time an electrically small antenna inspired from metamaterial [3]. Then, we compare the performance of the two driven elements array and those of the parasitic array.

Antenna design

The antenna will be integrated on a small printed circuit board which is here replaced by a ground plane with dimension of 50x50mm². The geometry of the elementary antenna and the antenna array is presented in Fig.1. It consists in a short circuited two-dimensional capacitively loaded quarter-loop near field resonant parasitic element electrically coupled to an electrically small monopole antenna [4]. The NFRP structure and the ground plane are on one side of the substrate, and the electrically small monopole antenna on the other side. The antenna is matched at its resonant frequency of 919.1MHz and its maximum gain is then of 0.86dB with a directivity of 2.12dB and an efficiency η = 74.9%. The antenna size is $\lambda_0/19x\lambda_0/19$, where λ_0 is the resonant wavelength, thus ka = 0.248.

The first two elements array investigated has two feedings, as shown in Fig.1. Two identical NFRP antennas are stacked along the Z axis, with different spacing. For each elements spacing, the excitation phase of the two elements is chosen to obtain the maximum directivity. It can be noticed that the maximum directivity is obtained when the two excitations are out-of-phase. The array resonant frequency is slightly shifted to a higher frequency than the elementary antenna and depends on the distance between the two elements. The maximum directivity obtained for different spacing, which is plotted in Fig.2 in wavelength, is always around 4.2dB.

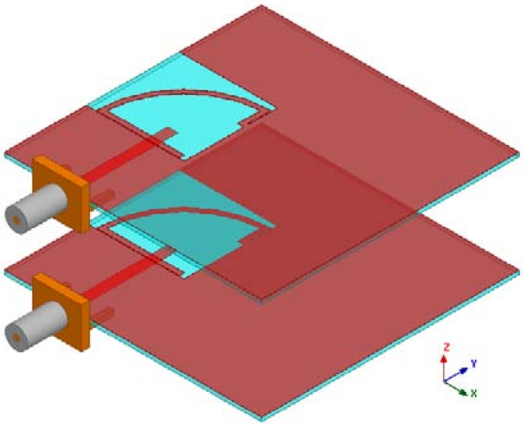

Figure 1. Antenna array geometry

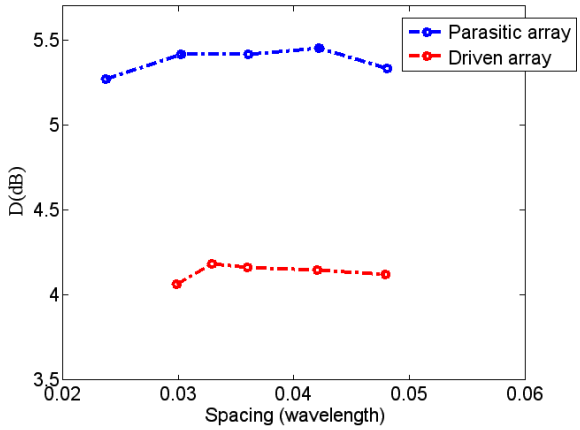

Figure 2. Arrays directivity versus elements spacing

The performance of the array presented in Fig.1 are then computed with only the top element driven. This parasitic array has two resonant frequencies, one higher and one lower than the single element resonant frequency. The directivity at the lower resonant frequency is around 2dB, whereas it is greater than 5dB at the higher resonant frequency, as plotted in Fig.2. The surface current distributions on the two elements are different at the two resonant frequencies: while they are in-phase at the lower frequency, the surface currents are out-of-phase at the higher frequency. This phase opposition is the condition for a two driven elements array to obtain super-directivity and can thus be reached with a parasitic array, leading to a high directivity using a simpler feeding network.

Conclusion

An electrically small antenna printed on a PCB has been introduced in this paper. This antenna was then used to design two arrays of two elements, a driven and a parasitic array. It has been shown that the parasitic array can produce directivity higher than a driven array

The performance of the antenna and the arrays computed using ANSYS HFSS, as well as measurement results, will be presented in the final paper.

Acknwoledgment

This work has been done with the funding of the French National Research Agency for the “Socrate” project and the support of the “Images et Réseaux” cluster of the Brittany region, France.

REFERENCES

1. A.I. Uzkov, “An Approach to the Problem of Optimum Directive Antennae Design”, *Comptes Rendus (Doklady) de l’Academie des Sciences de l’URSS*, Vol.53, 35–38, 1946.
2. T.H. O’Donnell, A.D. Yaghjian, “Electrically Small Superdirective Arrays Using Parasitic Elements”, *IEEE Antennas and Propagation Society International Symposium 2006*, 3111–3114, 2006.
3. C.-C. Lin, P. Jin and R.W. Ziolkowski, “Multi-Functional, Magnetically-Coupled, Electrically Small, Near-Field Resonant Parasitic Wire Antennas”, *IEEE Transactions on Antennas and Propagation*, Vol.59, No.3, 714–724, March 2011.
4. B. Sentucq, A. Sharaiha, S. Collardey, “Metamaterial-Inspired Electrically Small Antenna for UHF Applications”, *15th International Symposium on Antenna Technology and Applied Electromagnetics (ANTEM)*, June 2012.

RF and wireless communication

BER Performance of TH-PPM Low-Complexity Ultra Wideband RAKE Receivers in Underground Tunnels in Coal Mine Channels

M. Abou El-Nasr[1], **H. A. Shaban**[1], **and M. El-Sayed**[1]

[1]Arab Academy for Science, Technology & Maritime Transport (AASTMT), Alex., Egypt
hshaban@vt.edu

Abstract— This paper evaluates the bit-error-rate (BER) performance of ultra-wideband (UWB) time-hopping communication system with pulse position modulation (TH-PPM) with low-complexity RAKE reception in underground tunnels in mine channels. The studied receivers are partial-RAKE (P-RAKE) and selective-RAKE (S-RAKE), and are compared to optimal All-RAKE (A-RAKE) receivers. Numerical results show that TH-PPM UWB systems with low-complexity RAKE receivers are good candidates for communications in mine coal tunnels

1. INTRODUCTION

In safety monitoring of coal mines, such as in tunnels, wireless communications can overcome the problem of applying and maintaining wired systems. However, coal mine channels are very challenging, where they is characterized by being flammable environments. Thus, high transmit powers are very dangerous [1].

Ultra wideband (UWB) communication systems are characterized by their robust performance in harsh and dense multipath channels. This is due to the ultra short pulses of UWB systems, typically on the order of few nanoseconds. Moreover, UWB systems are characterized by their high data rates, low-complexity, low-cost, and low-transmit power, which make them a promising solution to the key issues of transmit power restriction and complex nature of mine channels [1].

This paper studies the BER performance of low-complexity UWB RAKE receivers, namely partial-RAKE (P-RAKE) and selective-RAKE (S-RAKE), in mine coal tunnels. The assumed modulation scheme is time-hopping pulse-position modulation (TH-PPM) scheme. Moreover, the performance of the studied receivers is compared to the optimal ALL-RAKE (A-RAKE) receiver.

2. SYSTEM AND CHANNEL MODELS

We assume that the transmitted pulse is the Gaussian pulse. The basic Gaussian pulse defined in terms of pulse-width T_p and $\tau_p = 0.5 * T_p$ is defined as [2]:

$$\omega_0(t) = exp\left(-2\pi\left(t^2/\tau_p^2\right)\right) \tag{1}$$

The n-th order Gaussian pulse is given by [3]:

$$\omega_n(t) = \frac{d^{(n)}}{dt^n}\left(\frac{1}{\sqrt{2\pi\sigma^2}}e^{\frac{-t^2}{2\sigma^2}}\right) \tag{2}$$

where $\sigma^2 = T_p/2\pi$. Assuming TH-PPM modulation, the typical modulated signal is defined by [1]:

$$s(t) = \sum_j \sqrt{(E_\omega)}\omega\left(t - jT_f - c_jT_c - \delta d_{[j/N_s]}\right) \tag{3}$$

where, E_ω is the pulse energy, j is the number of transmit pulses, c_j is the time hopping sequence, T_c is the chip duration, and d_j is the pulse spacing of PPM sequence [1].

In coal mine tunnels, the channel changes slowly compared to symbol transmission rate. The channel impulse response is expressed as [1]:

$$h(t) = \sum_{k=0}^{L-1} \alpha_k \delta\left(t - k\Delta\right) \tag{4}$$

where α_k is the amplitude of the path response, L is the number of paths, and Δ is the channel resolution. Coal mine tunnel channel parameters are summarized in Table 1.

Table 1: Coal mine tunnel channel parameters [1].

Parameter	Value
Λ (1/ns)	0.0667
λ (1/ns)	5
Γ	14
γ	8
σ_1 and σ_2 (dB)	3.3941
σ_x (dB)	1

The optimal receiver in multipath channels is the A-RAKE receiver. However, this receiver structure requires a very large number of fingers to capture the available multipath components. On the other hand, low-complexity RAKE structures are available, such as P-RAKE and S-RAKE receivers. In these structures, low-complexity is traded for degradation in BER performance [4]. This paper investigates the BER performance of these structures, and compare it to the performance of A-RAKE in mine coal tunnels.

3. NUMERICAL RESULTS AND CONCLUSIONS

The BER performance of P-RAKE, S-RAKE, and A-RAKE receivers is simulated and compared in coal mine tunnels based on the parameters defined in the previous section using MATLAB. Figure 1 shows a comparison of the performance of the aforementioned receivers for different number of RAKE fingers. As can be seen from figure, A-RAKE receiver outperforms S-RAKE with five fingers by only $\approx$ 2 dB at BER = 1e-2. On the other hand, P-RAKE receiver with five fingers achieves an approaching performance to S-RAKE with two fingers with a performance degradation of $\approx$ 5 dB compared to A-RAKE receiver. This relatively small degradation is compared to considerable high reduction in receiver complexity, and consequently in power consumption. Thus, low-complexity TH-PPM UWB-based RAKE receivers are good candidates for communications in coal mine tunnels.

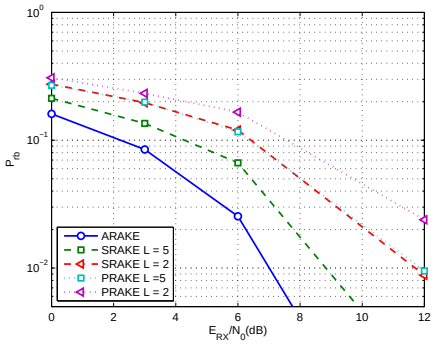

Figure 1: BER performance of TH-PPM in coal mine tunnels for different types of rake receivers.

REFERENCES

1. Li, P. and L.Xue, "Wireless channel model of UWB for underground tunnels in coal mine ," in *Proceedings of 5th International Conference on Wireless communications, Networking and Mobile Computing (WiCom)*, Beijing, China, Sept. 2009, 1-4.
2. Dardari, D., C.-C. Chong, and M. Z. Win, "Improved lower bounds on time-of-arrival estimation error in realistic UWB channels," in *Proceedings of 2006 IEEE International Conference on Ultra-Wideband*, Waltham, MA, Sept. 2006 531–537.
3. L. Sangyoub, "Design and analysis of ultra-wide bandwidth impulse radio receiver," *Ph.D. dissertation*, Southern California University, 2002.
4. Quek, T., and M. Win, "Analysis of UWB transmitted-reference communication systems in dense multipath channels" *IEEE Journal on Selected Areas in Communications*, Vol. 23, No. 9, 1863-1874, 2005.

Microwave and millimeter wave circuits and devices

Cascaded frequency selective surfaces using helical patch elements for stop-band spatial filter X-band applications

J. I. A. Trindade[1], A. G. D'Assunção[1*], and P. H. da F. Silva[2]

[1]Federal University of Rio Grande do Norte, Caixa Postal 1655, CEP: 59078-970, Natal, RN, Brazil

[2]Federal Institute of Education, Science and Technology of Paraíba, João Pessoa, PB, Brazil

[*]corresponding author: adaildo@ct.ufrn.br

Abstract-This work presents an analysis of cascaded frequency selective surfaces (FSSs). Each FSS is composed of metal helical elements printed on a dielectric substrate. A parametric analysis is performed in terms of the thickness of the air gap layer between the FSSs and of the particular type of the helical patch element. FSS structures are proposed to behave like stop-band spatial filters and exhibit interesting features to be used in the design of compact FSSs for X-band applications.

Recently, the configuration of multilayer FSS has attracted the attention of researchers from various fields. For this case, the electromagnetic behavior of the structure is observed by cascading two or more structures. It can act as spatial filters, which in turn can be used in radomes, dichroic subreflectors, and microwave absorbers [1]. The electromagnetic behavior of these structures is determined by the type of the element that is used in 2-D periodic array. The types of elements that compose the arrangement can take various forms, including square, rectangular and circular. In [2], the miniaturized element frequency selective surface has been studied as building blocks of multiband FSSs. In [3], a new type of element is presented, the multiperiodicity combined element (MPCE) is used to achieve a response resonance in a wide band. The electromagnetic performance of the MPCEs shows that the MPCEs FSS have much weaker grating lobes than the traditional FSSs.

In this work the proposed FSS structures consist of periodic arrays of helical patch elements (Fig. 1) mounted on fiberglass (FR-4) substrates, with dielectric thickness and constant equal to 1.5 mm and 4.4, respectively. In addition *p* is the FSS periodicity and *d* is the patch element diameter. The patch elements were designed based on helical elements that are generated experimentally with squares in the centers of the circles. In this work, the side of these squares, *l*, is varied from 0 to 5 mm. The quadrants of the circles are attached to the sides of the central square, generating a helix. Then that same propeller makes a 90 degree rotation and shapes the propeller used as part of the FSS. For the square with $l = 0$ mm, H0 element is generated. Similarly for the square with $l = 1$ mm, H1 element is generated, and so on until $l = 5$ mm, for the H5 element generation (Fig. 1). The cascaded FSS geometry is shown in Fig. 2.

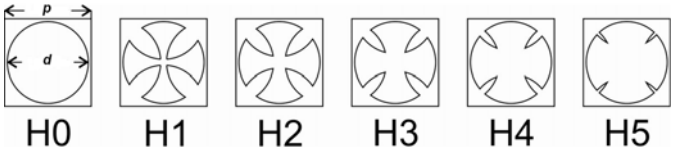

Figure 1. Helical patch elements of the proposed FSS structures.

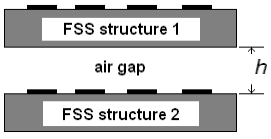

Figure 2. FSS cascaded structure.

Figure 3 shows simulated results for single FSS structures with H0, H1, H2, H3, H4, and H5 elements, for the range from 1 GHz to 13 GHz. The FSS periodicity, *p*, is 15 mm and the patch element external diameter, *d*, is 14 mm. Six resonant frequencies were obtained in the range from 5 GHz to 13 GHz, one for each FSS structure. Considering the resonant frequency values shown in Fig. 3 and the possible use in the X band, we decided to cascade FSS with H0 and H4 elements.

Therefore two single FSS structures, one with H0 elements (FSS 1 in Fig. 2) and the other one with H4 elements (FSS 2 in Fig. 2) were broadside coupled through a dielectric layer filled with air (air gap) resulting in a cascaded FSS structure. Then a parametric analysis was performed to investigate the effect of the air gap thickness, *h*, on the cascaded FSS performance. Variations from 5 mm to 10 mm, with step equal to 1.0 mm, were considered.

Figure 4 shows the simulated results for the cascaded FSS structure (Fig. 2), with H0 (FSS 1) and H4 (FSS 2) elements, for the range from 5 GHz to 14 GHz. The FSS periodicity, *p*, is 15 mm and the patch element external diameter, *d*, is 14 mm.

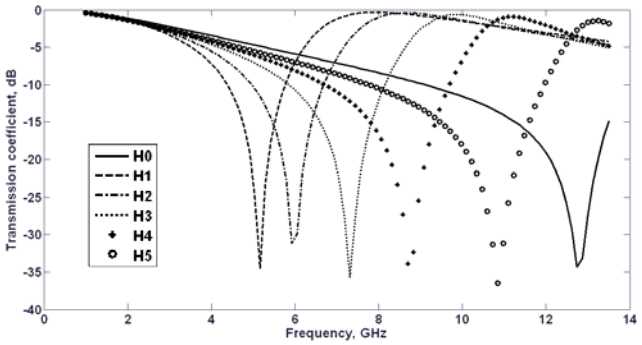

Figure 3. Simulated results with *p*=15 mm and *d*=14 mm for H0, H1, H2, H3, H4, and H5 FSS structures.

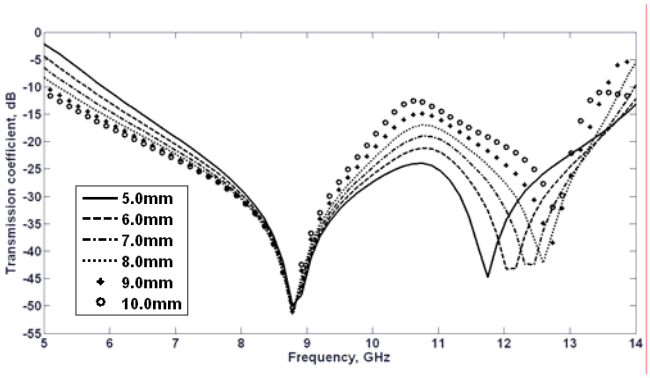

Figure 4. Parametric results for the cascaded FSS structure with H0 (FSS 1) and H4 (FSS 2) elements.

In Fig. 4, considering a -20 dB insertion loss reference, a band reject bandwidth of about 6 GHz is achieved for air gap thickness, *h*, values equal to 5 mm and 6 mm. Therefore the proposed cascaded FSS structure has shown the ability of providing wide bandwidth rejecting the entire X-band (8 GHz to 12 GHz). Observe that a dual band performance is achieved with the proposed cascaded FSS structure for higher values of the air gap thickness (h > 7 mm).

Finally helical patch elements were used to design FSS stop-band filters. Firstly six FSS structures were simulated. Then two of these FSS structures with particular elements (H0, for FSS 1, and H4, for FSS 2) were cascaded and used to generate stop-band characteristics. Potential applications in the development of X-Band (8 GHz to 12 GHz) stop-band spatial filters were shown.

REFERENCES

1. Munk, B. A., *Frequency Selective Surfaces: Theory and Design*, John Wiley & Sons, New York, 2000.
2. Bayatpur, F. and K. Sarabandi, "Multi-layer miniaturized-element frequency selective surfaces," *Proceedings of IEEE International Symposium on Antennas and Propagation*, San Diego, USA, July 2008.
3. Huang, M., M. Lv, J. Huang and Z. Wu, "A new type of combined element multiband frequency selective surface", *IEEE Trans. Ant. Propag.*, Vol. 57, No. 6, 1798-1803, 2009.

High frequency properties of ferrite for microwave devices

G. N. Sabri[1]

[1]Bechar university, N°417, street Kenad, Bechar, Algeria

*corresponding author: sabri_nm@yahooo.fr

Abstract-The purpose of the paper is the study of high frequencies properties and application possibilities of magnetic materials. Another aspect involved in the paper is the integration of many passive components on chips and the knowledge of electromagnetic properties of the ferrite, which is important to show their influence on the development of modern technology connected with miniaturization of devices in telecommunication field.

The current microwave ferrite devices must to evolve significantly to meet the requirements of public telecommunications market and the new microwave electronic technology challenges require integration of many passive components on chips. Among them, isolators and circulators are nonreciprocal passive devices which contain magnetic materials. Hence, the knowledge of electromagnetic properties of magnetic materials, such as the ferrite, is important for microwave passive component design.

Our objective is then to study the particular behavior of ferrites in hyperfrequencies when they are polarized by a static magnetic field is translates in particular into the phenomenon of non-reciprocity. To better understand these physical phenomena occurring in the microwave structures we take the example of a coplanar line on a ferrite layer is the case junction circulators Y.

In a medium consisting of ferrite magnetized vertically, the wave (RF magnetic field) is elliptically polarized left and rotates in the same direction as the precession gyromagnetic causing a strong interaction of the electromagnetic wave with the ferrite. And when the magnetic field rotates in the opposite direction of the gyromagnetic precession, it produces a weak interaction with the material. Gyromagnetic resonance is one of important phenomena which are operated in the range of high frequency electromagnetic spectrum, wherein the ferrites are used.

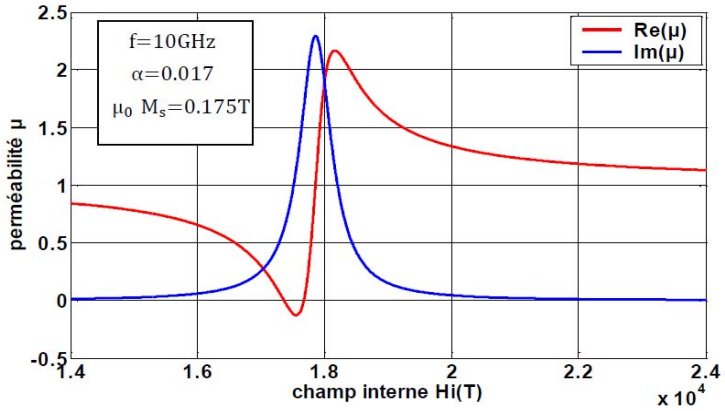

Figure1: Evolution of the magnetic permeability of the material as a function of internal field (according to the model Polder)

It gives the material its ability to respond differently to an electromagnetic wave according to its polarization. In addition, it allows separate devices into two distinct classes: those who work at resonance (isolators, filters ...), and those who work outside the resonance (circulators. ..). Therefore the cyclotron resonance is related to the movement of precession of the magnetic moment of the electron spin around the direction of the internal magnetic field.

The resolution of such an equation of motion leads to a permeability modeling using the Polder model given by:

$$\bar{\bar{\mu}}_r = \mu_0 \begin{pmatrix} \mu_r & -j\kappa & 0 \\ +j\kappa & \mu_r & 0 \\ 0 & 0 & 1 \end{pmatrix} \quad (1)$$

Where

$$\mu_r = \mu' - j\mu'' = 1 + \frac{(\omega_r + j\alpha\omega)\omega_M}{(\omega_r + j\alpha\omega)^2 - \omega^2} \quad (2)$$

$$\kappa = \kappa' - j\kappa'' = \frac{\omega\omega_M}{(\omega_r + j\alpha\omega)^2 - \omega^2} \quad (3)$$

$$\omega_M = \gamma\mu_0 M_s \quad (4)$$

$$\omega_r = \gamma\mu_0 H_i \quad (5)$$

The real and imaginary part of permeability is shown on the figure 1 for saturated materials with polarization along the z axis.

Ferrimagnets having low RF loss are used in passive microwave components and miniature antennas operating in a wide range of frequencies (1–100 GHz) and as magnetic recording media owing to their novel physical properties.

REFERENCES

1. Pardavi-Horvath, M. "Journal of Magnetism and Magnetic Materials," *Microwave of soft ferrites*, Vol. 34, No. 10, 215–216, 2000 (171-183).
2. Dobrzański, L. A., Drak, M. and B. Ziębowicz, "Journal of Achievements in Materials and Manufacturing Engineering," *Journal of Achievements in Materials and Manufacturing Engineering*, Vol. 17, No. 1-2, 37– 40, 2006.
3. Murthy, S. R., "Bull. Mater. Sci., Indian Academy of Sciences ", Development of low-power loss Mn–Zn ferrites using microwave sintering method , Vol. 26, No. 5, August 2003, pp. 499–503.
4. Capraroa.S, Chatelona, J.P. , Le Berreb, M. and Al., Journal of Magnetism and Magnetic Materials, Barium ferrite thick films for microwave applications, 272–276 (2004) e1805–e1806.

Optics and photonics

Wavelength dependent enhancement of photoluminescence from silicon nitride by localized surface plasmons

Feng Wang[1], Dongsheng Li[1*], Peihong Cheng[2], Deren Yang[1], and Duanlin Que[1]

[1] State Key Laboratory of Silicon Materials and Department of Materials Science and Engineering, Zhejiang University, Hangzhou 310027, China

[2] School of Electronic and Information Engineering, Ningbo University of Technology, Ningbo 315016, China

[*]Corresponding author: mselds@zju.edu.cn

Abstract-The interaction between localized surface plasmons (LSPs) and excitons is demonstrated theoretically and experimentally. From the finite differential time domain (FDTD) simulations, we obtained that the out-radiated electromagnetic fields are strongly wavelength dependent. This evolution of the out-radiated electromagnetic fields with the incident wavelength of plane wave makes the enhancement factor of photoluminescence intensity of silicon nitride matrix via the addition of silver nanostructures wavelength dependent.

During the last decades, the localized surface plasmons (LSPs, the collective oscillation of confined conduction electrons within metallic nanostructures excited by the external radiation) have received extensive attentions as an effective approach to overcome the diffraction limit of classical optics originated from the mismatch of energy and momentum between electrons and photons [1,2]. The excitons within luminescence matrix would transfer their energies to the LSP modes if the energy of excitons was close to the electron vibration energy of LSPs. This process can enhance the radiative recombination rates of excitons by the Purcell factor [3]. After that, the energy from the LSP modes will be partially out-coupled to radiated photons. The enhancement or degeneration of the luminescence intensity by the addition of metal nanostructures is strongly dependent on these two processes, which is dependent on the energy of excitons as well as the luminescence wavelength of the active matrix. The investigation of this wavelength dependent interaction between LSPs and excitons is particularly valuable for optimizing the luminescence properties of active matrix. Therefore, we demonstrate this wavelength dependent interaction theoretically and experimentally in this paper.

Figure 1 represents the finite differential time domain (FDTD) simulations of electromagnetic fields surrounding 100 nm sized Ag nanostructures under the different central wavelength of incident plane wave ($\lambda_{inc.}$). For the $\lambda_{inc.}$=410 nm, the confinement of the electromagnetic fields is extremely serious, where little of them could be out-radiated (not shown here). This confinement is weakened significantly with the increase of $\lambda_{inc.}$ from 410 nm to 500 nm, where the resonance coupling between LSPs and excitons takes place and the intensity of the out-radiated electromagnetic fields achieves maximal, as shown in Fig. 1(a). By further increasing the incident wavelength ($\lambda_{inc.}$>500 nm), the confinement of the electromagnetic fields becomes more and more serious and the out-radiated electromagnetic fields become more and more weak, as shown in Figs. 1(b)-1(c). The wavelength of the maximal out-radiated electromagnetic fields intensity might be red-shifted due to the larger dielectric constant of SiN_x films than that of air we used for FDTD simulations, as shown in the inset of Fig. 2.

For the determination of this wavelength dependent confinement of the electromagnetic fields on the

luminescence properties of silicon nitride (SiN_x), a promising material for the application of silicon-based light sources with promising luminescence efficiency [4-6], the photoluminescence (PL) spectra of the SiN_x films with and without Ag nanostructures were measured, as shown in Fig. 2. By dividing the PL intensity of the sample with Ag to that of the reference one, we obtained that the maximal enhancement factor of PL by the addition of Ag nanostructures is located at ~520 nm, as shown in the inset of Fig. 2 (the left axis), which is close to the wavelength of the maximal electromagnetic fields intensity. This wavelength is far smaller than that of the dipolar resonance peak (~580 nm, the right axis in the inset of Fig. 2), which contributes to the peak of PL enhancement factor at ~600 nm.

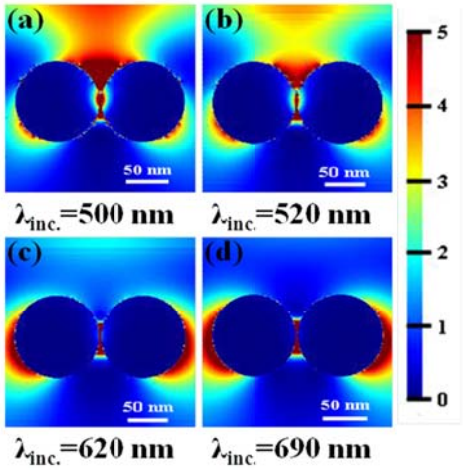

Fig. 1: The finite differential time domain (FDTD) simulations of electromagnetic fields surrounding 100 nm sized Ag nanostructures under the different central wavelength of incident plane wave ($\lambda_{inc.}$).

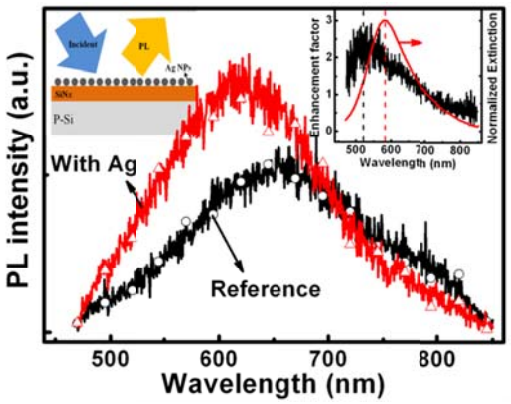

Fig. 2: The PL spectra of SiN_x films with and without 100 nm sized Ag nanostructures. Inset is the PL enhancement factor by dividing the PL intensity of SiN_x films with Ag to that without Ag. The extinction spectra of Ag/SiN_x/quartz structure are also provided in the inset (the red line).

In conclusion, the wavelength dependent interaction between LSPs and excitons is demonstrated theoretically and experimentally. Both the wavelength dependent out-radiated efficiency and the LSPs resonance coupling efficiency by the addition of metal nanostructures should be considered for the optimization of the luminescence performance of active matrix.

Acknowledgements We thank the 863 Program (Grant No. 2011AA050517) for financial support.

REFERENCES

1. Barnes, W. L., "Surface plasmon subwavelength optics," *Nature*, Vol. 424, No. 6950, 824-830, 2003.
2. Ozbay, E., "Plasmonics: merging photonics and electronics at nanoscale dimensions," *Science*, Vol. 311, No. 5758, 189-193, 2006.
3. Purcell, M., "Spontaneous emission probabilities at radio frequencies," *Phys. Rev.*, Vol. 69, No. 11-12, 681, 1946.
4. Wang, M., Li, D., Yuan, Z., Yang, D., and Que, D., "Photoluminescence of Si-rich silicon nitride: Defect-related states and silicon nanoclusters," *Appl. Phys. Lett.*, Vol. 90, No. 13, 131903, 2007.
5. Wang, F., Li, D., Yang, D., Que, D., "Enhancement of light-extraction efficiency of SiN_x light emitting devices through a rough Ag island film," *Appl. Phys. Lett.*, Vol. 100, No. 3, 031113, 2012.
6. Li, D., Wang, F., Yang, D., Que, D., "Electrically tunable electroluminescence from SiN_x-based light-emitting devices," *Opt. Express*, Vol. 20, No. 16, 17359-17366, 2012.

Photonic band structure of a dynamic medium whose permittivity and permeability are modulated periodically in time

P. Halevi* **and O. M. Becerra-Fuentes**
Instituto Nacional de Astrofisica, Optica y Electronica, Puebla, Mexico
*halevi@inaoep.mx

Abstract - We have studied a bulk dynamic medium whose permittivity $\varepsilon(t)$ and permeability $\mu(t)$ are both periodic functions of time, modulated at the same frequency, however with an arbitrary phase difference. The dispersion relation turns out to be a band structure with forbidden bands for the propagation vector. We show that, the same behavior can be obtained in the microwave regime by means of a dynamic "low pass" transmission line whose dynamic capacitance $C(t)$ and inductance $L(t)$ per unit length are given, respectively, by $\varepsilon(t)$ and $\mu(t)$.

Recently, Zurita et al [1] have explored the idea of a "temporal photonic crystal (TPC)", namely, a uniform medium whose permittivity $\varepsilon(t)$ is a periodic function of time. This resulted in a band structure that is periodic in frequency and exhibits band gaps in the propagation vector. Subsequent investigation by Zurita and Halevi [2] showed that a slab of such a dynamic-periodic medium gives rise to resonant reflection and transmission under appropriate conditions for the slab thickness and the modulation frequency. Further, Halevi et al [3] demonstrated that such a TPC can be realized in practice in the microwave regime by means of a "low pass" transmission line whose capacitors are replaced by varactors with periodically modulated capacitance $C(t)$. In the present study we generalize ref. [1] to the case that the permeability $\mu(t)$ of the medium, as well as its permittivity $\varepsilon(t)$ are being modulated in time at the same frequency, however not necessarily in phase.

We consider a bulk, uniform and isotropic medium with (real) relative permittivity $\varepsilon_r(t)$ and a relative permeability $\mu_r(t)$. Being periodic, both functions can be expanded in Fourier series as $\varepsilon_r(t) = \sum_l \varepsilon_l \exp(il\Omega t)$ and $\mu_r(t) = \sum_m \mu_m \exp(im\Omega t)$. The wave equation for the electric field has plane wave solutions of the form $E(x,t) = E(t)\exp(i(kx - \omega t))$ with the amplitude $E(t)$ given by the Floquet theorem *in time*, namely $E(t) = \sum_n e_n(\omega)\exp(in\Omega t)$ is periodic with the same period $2\pi/\Omega$ as $\varepsilon(t)$ and $\mu(t)$. This leads to the following eigenvalue equation for the $e_n(\omega)$:

$$\sum_n \sum_m \left[\mu_{l-m}\varepsilon_{m-n}(\omega - m\Omega)(\omega - l\Omega) - k^2c^2\delta_{l,n}\delta_{m,0}\right]e_n(\omega) = 0, \qquad l,m,n = 0,\pm1,\pm2,..., \qquad (1)$$

where $\delta_{l,n}$ and $\delta_{m,0}$ are the Kronecker-delta functions and c is the speed of light in vacuum. Equating to zero the determinant of the expression in the square brackets, we obtain the eigenvalues $k(\omega)$ in the form of a band structure. This is shown in Fig.1, assuming the harmonic variations $\varepsilon_r(t) = \bar{\varepsilon}_r\left[1 + M_\varepsilon \sin(\Omega t)\right]$ and $\mu_r(t) = \bar{\mu}_r\left[1 + M_\mu \sin(\Omega t + \theta)\right]$ where $M_{\varepsilon,\mu}$ are modulation strengths and θ is a phase difference. The frequency

and wave vector have been normalized as $\hat{\omega} = \omega/\Omega$ and $\hat{k} = kc\Big/\left(\Omega\sqrt{\bar{\varepsilon}_r\bar{\mu}_r}\right)$.

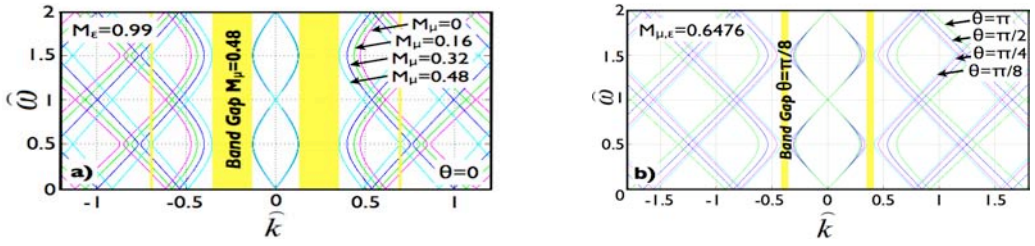

Fig.1. Band structures for (a) $M_\varepsilon = 0.9904$ with different M_μ and (b) $M_\mu = M_\varepsilon = 0.6476$ with different θ

Fig.1a shows that, the larger the difference between the modulations, the wider the forbidden gap is for $\theta = 0$. On the other hand, Fig.1b demonstrates that, for a given modulation strength, the larger the phase difference, the wider the forbidden gap is.

Next we confirm that the TPC studied above can be actually realized by means of a low-pass transmission line (TL) whose (static) capacitors and inductors have been replaced, respectively, by dynamic capacitors (varactors) and inductors. This is true in the long wavelength limit ($ka << 1$) provided that $C(t) = \varepsilon(t)a$ and $L(t) = \mu(t)a$, where "a" is the spatial period of the TL. Fig. 2a shows the dynamic TL and Fig. 2b is the corresponding dispersion relation for $L(t)$ out of phase with $C(t)$ ($\theta = \pi$) and equally strong modulations $M = 0.6476$. Three values of the parameter $\hat{\Omega} = \Omega\sqrt{\bar{L}\bar{C}}$ are considered and the dispersion curves are compared with results for effective medium (as in Fig.1).

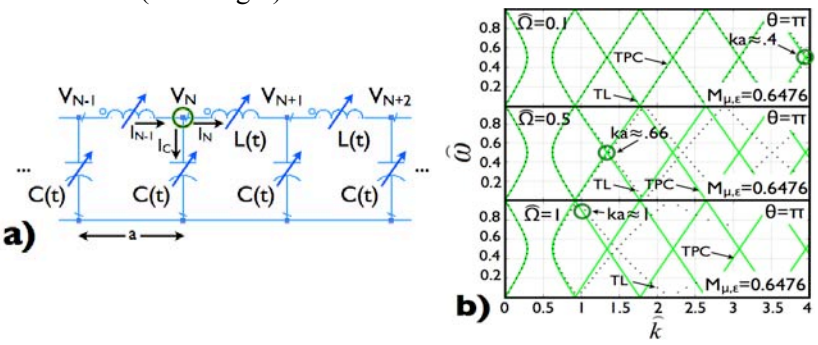

Fig.2. (a) Ideal dynamic transmission line and (b) band structure for $\hat{\Omega}$ = 0.1, 0.5 and 1 when ka<<1.

It is seen that the fits are excellent provided that both $\hat{\Omega}$ and $\hat{k}$ are sufficiently small. Not surprisingly, this actually corresponds to the long-wavelength limit as $\hat{k}\hat{\Omega} = ka$. We have thus shown that, for $ka << 1$, a TL whose capacitance and inductance both vary periodically in time can be considered as a TPC!.

This research has been supported by the CONACyT project 103644-F.

REFERENCES

1. Zurita-Sánchez, J. R., P. Halevi and J. C. Cervantes-Gonzalez, "Reflection and transmission of a wave incident on a slab with time-periodic dielectric function ε(t)", *Phys. Rev. A* **79**, 053821, 2009.
2. Zurita-Sánchez, J. R. and P. Halevi, "Resonances in the optical response of a slab with time-periodic dielectric function ε(t)", *Phys. Rev. A* **81**, 053834, 2010.
3. Halevi, P., U. Algredo-Badillo and J. R. Zurita-Sánchez, "Optical response of a slab with time-periodic dielectric function ε(t): Towards a dynamic metamaterial" in *Proc. SPIE 8095*, 809501 San Diego, USA, 2011.

Nanophotonics; THz technology

Design Considerations for Near Field Enhancement in Nano-Antennas

M.N.Gadalla[1], and A.Shamim[2]

[1,2]King Abdullah University for science and technology, Saudi Arabia

[*]corresponding author: mena.gadalla@kaust.edu.sa

Abstract

Optical antennas are very similar to their microwave counterparts, however there is no established theory for optical antenna design. When visible or infrared light incident on an antenna's surface it excites surface palsmon oscillations and drive current towards the feed point of the antenna creating a hot spot at which the field intensity is enhanced. In this paper we investigate the response of different antenna shapes and the geometrical effects of the antenna on the intensity enhancement of the localized fields.

Optical or Nano antennas have many applications such as Nano scale imaging and spectroscopy [1], improving solar cell efficiency [2, 3] and coherent control [4]. Optical antennas are made of noble metals that are highly dispersive in THz frequencies, consequently over the past 15 years researchers investigated optical properties of metallic Nano particles [5, 6]. Even though the Drude model can be used to model metals' optical or electronic properties, metal characterization using spectroscopy is highly recommended to avoid Drude's model major drawback of ignoring absorption due to inter-band transition. In this piece of research we used Lide's modeling for gold [7] to compare the performance of four shapes of Nano antennas. Ansoft HFSS was used to model a problem of Nano bowtie, rod, torus, and sphere dipole with a gap of 1nm as shown in figure 1. After the frequency dependent optical properties were imported to HFSS Electric Field was computed at the midpoint of the gap for a 1v/m incident field with polarization parallel to the antenna's axis and 1nm surface meshing.

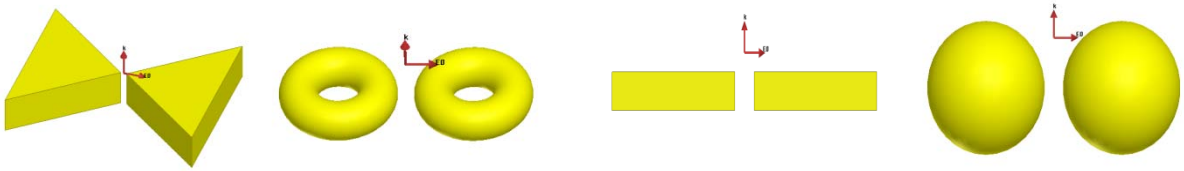

Figure 1: Four types of Nano antennas.

Nano structures and very small separations require very fine meshing, further more frequency dependent dielectric function substantially increases the computational matrix size. In order to overcome computational resources limitations, electric and magnetic symmetry planes were used to simulate only one fourth of the problem. As shown in figure 1 the bowtie antenna has the highest ability to enhance the electric field at a point, this can be explained by the coupling of free propagating modes in the air to traveling surface plasmon modes that are localized at the interface between the antenna and free space. Moreover, Both group and phase velocity of these propagating surface waves decrease along propagation until they reach zero at the tapered end [8], as a result energy is accumulated at the tip. In order to find the geometrical effects on the near field enhancement, we studied the effect of different bow angle, gap size and angle of incidence on the field localization due to a bowtie antenna for mid infrared spectrum. Figure 2 shows that the increase of gap size will decrease the intensity enhancement due to the evanescent nature of the induced field which is localized to the bowtie tip. For example, the difference between the electric field intensity for a gap of 10nm and 100nm is three orders of magnitude whilst the resonance wavelength stays relatively constant.

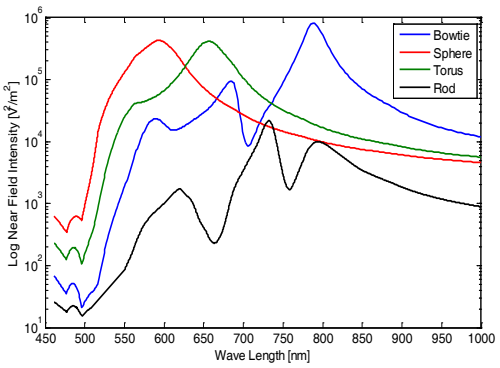

Figure 2: Comparison of near field intensity for different Nano antennas.

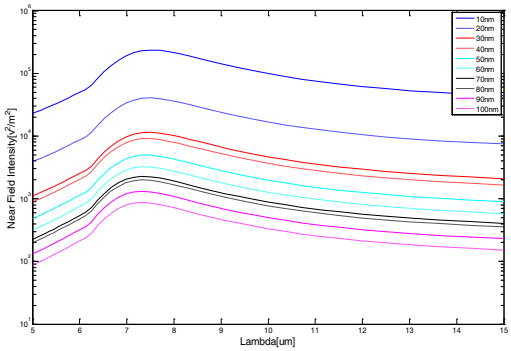

Figure 3: Variation of near field intensity with gap size.

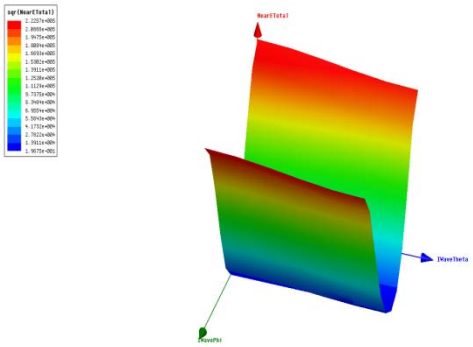

Figure 4: Variation of near field intensity with angle of incidence.

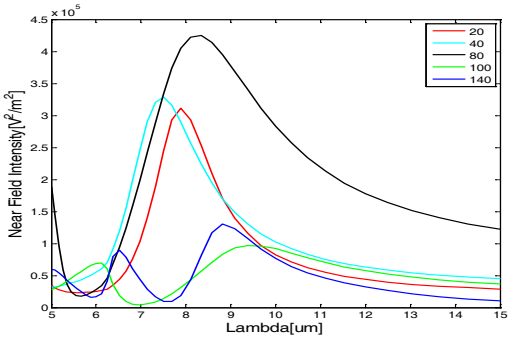

Figure 5: Variation of near field intensity with bow angle.

Like microwave antenna theory maximum field enhancement occurs when the electric filed polarization is parallel to the antenna axis and no enhancement when it is normal to antenna axis. The optimum bow angle is 80° which resulted in relative intensity enhancement of 5 orders of magnitude for 10nm gap.

References

[1] L. Novotny and S. J. Stranick, "Near-field optical microscopy and spectroscopy with pointed probes*," *Annu. Rev. Phys. Chem.,* vol. 57, pp. 303-331, 2006.

[2] C. Hagglund, M. Zach, G. Petersson, and B. Kasemo, "Electromagnetic coupling of light into a silicon solar cell by nanodisk plasmons," *Applied Physics Letters,* vol. 92, pp. 053110-053110-3, 2008.

[3] A. J. Morfa, K. L. Rowlen, T. H. Reilly, M. J. Romero, and J. van de Lagemaat, "Plasmon-enhanced solar energy conversion in organic bulk heterojunction photovoltaics," *Applied Physics Letters,* vol. 92, pp. 013504-013504-3, 2008.

[4] M. I. Stockman, D. J. Bergman, and T. Kobayashi, "Coherent control of nanoscale localization of ultrafast optical excitation in nanosystems," *Physical Review B,* vol. 69, p. 054202, 2004.

[5] W. Gotschy, K. Vonmetz, A. Leitner, and F. Aussenegg, "Optical dichroism of lithographically designed silver nanoparticle films," *Optics letters,* vol. 21, pp. 1099-1101, 1996.

[6] I. Puscasu, B. Monacelli, and G. Boreman, "Plasmon dispersion relation of Au and Ag nanowires," *PHYSICAL REVIEW B Phys Rev B,* vol. 68, p. 155427, 2003.

[7] D. R. Lide, *CRC Handbook of chemistry and physics*. Boca Raton, FL [u.a.]: CRC, 2006.

[8] M. I. Stockman, "Nanofocusing of optical energy in tapered plasmonic waveguides," *Physical review letters,* vol. 93, p. 137404, 2004.

Experimental characterization techniques

Evolution of Solitons in Nonlinear Photonic Cristal Fiber with High Order of Dispersion

L. Cherbi*, N. Lamhene, F. Boukhelkhal and A. Bellil
[1] Laboratory of instrumentation (LINS), USTHB, Algeria
* corresponding author: cherbi_lynda@hotmail.com

Abstract- In this work, we investigated the creation and the propagation of solitons in a Nonlinear 'PCF' by varying the dispersion and the nonlinear parameters such as the self phase modulation and the Stimulated Raman Scattering. Given that the third order dispersion plays an important role in the propagation of solitons in PCF when the pulse wavelength is in the vicinity of the zero dispersion wavelength, we also simulated its impact on the evolution of the fundamental soliton in this fiber.

The propagation of a light pulse through the optical fiber is governed by the Generalized Nonlinear Schrödinger Equation (NLSE) [1]. We can get a pulse that does not vary during its propagation in the case of anomalous dispersion (β_2<0) with a balance between the chromatic dispersion (GVD) and the input power such that : $\frac{\gamma P_0 T_0^2}{|\beta_2|} = \frac{L_d}{L_{NL}} = N^2$ where T_0 is the pulse width, γ the Nonlinear coefficient, β_2 the GVD parameter, L_d the dispersion length, L_{Nl} the nonlinear length and P_0 is the input peak power.

First, we generated a fundamental soliton (N = 1) by a compromise between the dispersive effects (GVD) and the SPM in a nonlinear PCF working at λ = 1064 nm and characterized by: Zero dispersion wavelength = 1040 ± 10 nm, γ at 1060 nm = 11 $(W\cdot km)^{-1}$, Attenuation at 1040nm < 3 dB/km, Mode Field Diameter = 4.0 ± 0.2µm, NA at 1060nm = 0.20 ± 0.05. By using the Split Step Fourier Method (SSFM)[1][2], we solved the NLSE to simulate the propagation of the fundamental soliton in the PCF by choosing the following parameters: " P_0=1500W, $L_{d=}$ 6.060 cm, L=980 mm =16xL_d, β_2 = -13.2380 ps^2/Km , γ= 11 $Km^{-1}W^{-1}$, $L_{Nl=}$ 6.060 cm". Figures 1 and 2 attest the physical aspect of the generated fundamental soliton in the PCF respectively in temporal and spectral domain without any change up to a length of 100m despite the high amplitude of the injected power. However, starting from a length of 110 m, the soliton undergoes small perturbations in the output spectrum during its propagation, with the appearance of some additional harmonics compared to the input spectrum (see Fig. 3); these disturbances will increase further beyond this length. Thereafter, we were able to generate higher order solitons (N> 1) which can be used in optical pulse compression [3][4] and supercontinuum generation[5]. In this precise case of solitons, the light pulse returns to its original shape periodically with a spatial period defined by:

$$z_0 = \frac{\pi L_d}{2} = \frac{\pi T_0^2}{2|\beta_2|}$$

We have noticed that for generating higher order solitons in the same PCF, we ought to amplify the nonlinear effects by increasing the injected power up to P0 = 6000 W for the second order of solitons (N = 2) and P0 = 13500 W for the third order of soliton (N = 3). Figures 4 and 5 show respectively the temporal evolution of the second and third order of solitons.

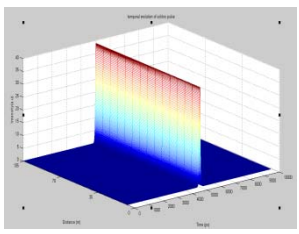

Fig.1. Temporal evolution of fundamental soliton in PCF for P_0 =1.5kw

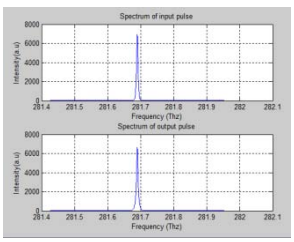

Fig.2. Spectrum evolution of fundamental soliton in PCF for P_0 =1.5kw

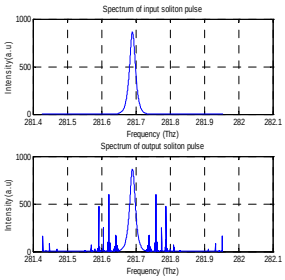

Fig.3. Input and Output soliton Spectrum for PCF length of 110m.

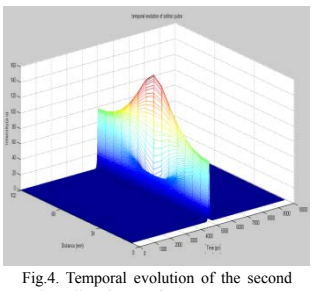

Fig.4. Temporal evolution of the second order soliton in PCF for Z_0 = 95.705 mm

Afterward, we simulated the effect of Stimulated Raman Scattering (SRS) on the fundamental soliton propagated in the same PCF of 100cm length by using SSFM to solve the Nonlinear Schrödinger Equation (NLSE). Fig 6.a shows the temporal evolution of the fundamental soliton under SRS where we don't notice any large variation

compared to the input pulse, but just a slight temporal drift. On the other hand, we note a gradual frequency shift in the spectrum of the fundamental soliton toward the lower frequencies (fig.6.b), the spectrum is split into two major distinct peaks (Fig. 7). We also notice the widening of the spectrum which could be made use in the generation of supercontinuum.

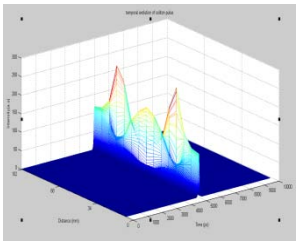

Fig.5. Temporal evolution of the third order soliton in PCF for Z_0 = 95.705 mm

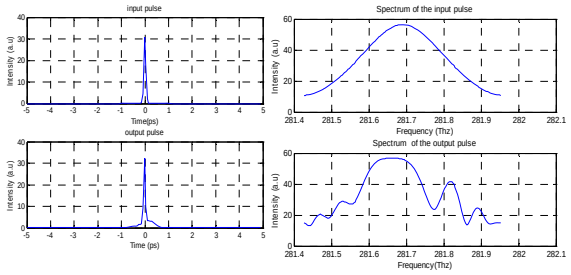

(a) **(b)**

Fig.6. Evolution of soliton pulse in the PCF under SRS (a) Temporal domain (b) Spectral domain.

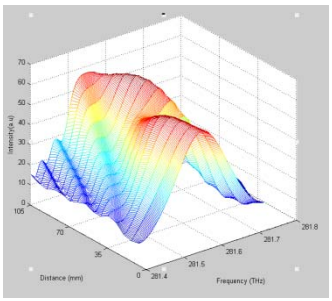

Fig.7. Spectrum of soliton at the input and the output of PCF under SRS

The propagation of light along the fiber as a function of the dispersion is described by the propagation constant which is developed in a Taylor series in the frequency domain [1]. The higher order dispersive effects play an important role in the propagation of solitons in the PCF when the central wavelength pulse matches with the zero dispersion wavelength inducing asymmetric widening of the pulse along with oscillations. We simulated the impact of Third Order of Dispersion "TOD" on the propagated fundamental soliton in a PCF in both temporal and spectral domains by solving NLSE.

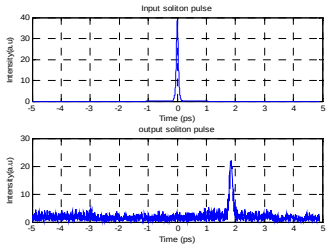

Fig.8. Temporal evoultion of soliton at input and output of PCF under TOD

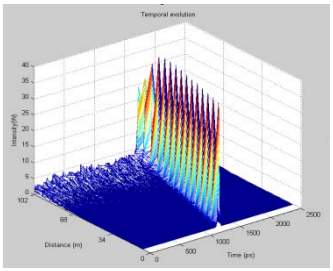

Fig.9. Temporal evolution of soliton according to the length of PCF under TOD

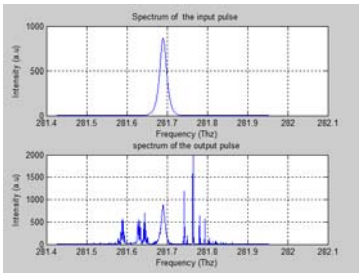

Fig.10. Spectrum of the soliton at input and output of PCF under TOD

We simulated the impact of β3 on the propagation of fundamental soliton in the PCF using the following parameters: P_0 = 1500 W, T_0 = 28.4 fs, γ = 11 $Km^{-1}W^{-1,}$ β_2 = -13.2380 ps^2/km, β_3 = 0.11 ps^3/Km, L = 100m, L_d = 0.06092 m, L_{Nl} = 0.060606 m, L_{d3}=0.2082m. From Fig.8, we note that the TOD shifts the soliton from its initial position and induces temporal oscillations (perturbations) that change side depending on the sign of β_3. The peak of the soliton is delayed by an amount that increases linearly with the distance (fig.9). Fig.10 shows the spectrum of the soliton at input and output of PCF under the effect of TOD where we detect a disturbance with several frequency peaks.

References

1. Govind.P.Agrawell, Non Linear Fiber optics, Academic press, (third edition), 2001
2. Apithy, H.; Bouslimani, Y.; Hamam, Overview and Advantages of the Split step Method, Proceedings of SCI, Orlando, FL, 2004.
3. S. O. Iakushev1, I. A. Sukhoivanov2, O. V. Shulika1, Nonlinear Pulse Reshaping in Optical Fibers, Laser Systems for Applications, InTech, 2011
4. M.Yihong Chen, H.Subbaraman and R.Chen, One stage pulse compression at 1554nm through highly anomalous dispersive photonic crystal fiber, Optical Society of America, 2011
5. Dudley, J. M. Genty , G. Coen, Supercontinuum generation in photonic crystal fiber. *Rev. Mod. Phys.,* Vol. 78, No. 4, pp. 1135-1184 (2006).

Experimental study for detection of ductile fracture in weldments

Moussa Zaoui[1] , **Chami Noureddine**[2]
Department of Mechanical Engineering, University of M'sila, 28000, M'sila, Algeria
m_zaouidz@yahoo.fr

Abstract
Welded joints are always preferred areas for the occurrence of defects and the requirement in terms of security for such facilities, thus making it essential to study their fracture. Comprehensive approaches such as the J integral of Rice, are used to analyze the harmfulness of defects in welds. This work has explored the various parameters involved at the same time, to explain the phenomena of ductile tearing in a welded joint in order to develop an analytical method suitable for this type of junction. the mechanical properties of the base metal has a pervasive effect on the overall behavior of such structures and the growth rate of cavities R/R0 is sensitive to changes in the fields of stress and strain at the bottom of the crack .

Keywords: Ductile fracture, A48 steel, local approach.

REFERENCES

- WILSIUS .J, Experimental and numerical study of ductile tearing Approaches based on local fracture mechanics. *PhD Thesis, University of Science and Technology of Lille,* (1995)
- Vincent Gaffard,. Experimental study and modelling of high temperature creep flow and damage behaviour of 9Cr1Mo-NbV steel weldments, *ENSEEG of Paris*, (2004)
- Quentin AUZOUX,. Cracking in relieving of the austenitic stainless steels influences work hardening on intergranular damage, *ENSM of Paris.* (2004)
- N. P. O'Dowd, K. M. Nikbin and F. R. Biglari, Creep crack initiation in a weld steel: effects of residual stress, *proceedings of ASME Pressure Vessels and Piping Division Conference, Denver, Colorado, USA.* (2005)
- Bilat, Anne-Sophie. Estimating the risk of brittle fracture of welds of pipelines in high-grade steels: characterization and modeling, *ENSMP of Paris,* (2007)
- Zuheir Barsoum, Sweden. Residual Stress Analysis and Fatigue Assessment of Welded Steel Structures, *School of Engineering Sciences, Stockholm, Sweden.* (2008).

Optical communications

A New Compact Optical Switch Based on 2D Photonic Crystal and Magneto-Optical Cavity

Victor Dmitriev, Marcelo N. Kawakatsu and Gianni Portela

Department of Electrical Engineering, Federal University of Para, Av. Augusto Correa 01, Belem, Para, Brazil

In this paper we will show theoretically a possibility to design a switch based on a MO cavity. The magneto-optical cavity of the switch operates with a dipole mode. The cavity is coupled to two parallel and misaligned PhC waveguides. The switching from the state *off* to the state *on* is fulfilled by a dc magnetic field applied normally to the PhC. The state *off* corresponds to the high reflection of the electromagnetic wave from the resonator.

An idealized scheme showing the principle of the switch functioning is given in Fig.1. The device consists of a resonator with a magnetic medium which can be magnetized by a dc magnetic field $\mathbf{H}_0$ normal to the PhC plane (Fig.1b). The input waveguide 1 and the output waveguide 2 which are parallel but misaligned are connected to the resonator. The resonator on Fig. 1 is bounded by the big circles which define the resonator region. The two small circles in these figures represent schematically the distribution of the ac magnetic field H_z showing the standing waves (idealized dipole modes) in the resonator.

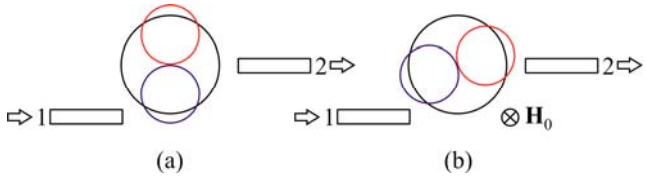

Fig. 1. Optical switch schemes in the *off* (a) and *on* (b) states with dipole mode in MO cavity.

Without external magnetic field $\mathbf{H}_0$ the cavity supports two degenerate right- and left-rotating modes with the frequencies ω- and ω^+ which are equal, i.e. $\omega- = \omega^+$. Their superposition gives a standing dipole mode with a node in the output waveguide (Fig.1a). This means that the wave incident in port 1 cannot pass to the port 2 and it will be reflected from the resonator. This corresponds to the switch state *off*.

A dc magnetic field $\mathbf{H}_0$ produces a splitting of the frequencies ω- and ω^+ of modes rotating in the opposite directions. By choosing the parameters of the magnetized MO resonator, the field pattern of the resulting standing wave can be rotated by the angle $\alpha \approx \mathbf{60}^0$, forming the required distribution of ac electromagnetic fields with equal amplitudes in the input and output ports. This permits propagation of the incident wave from port 1 to port 2, i.e. defines the state *on* of the switch.

The proposed device was simulated using the software COMSOL [1]. The switch is based on a two dimensional PhC with the lattice constant a in the plane x0y. The crystal is a triangular lattice of air holes of radius 0.3a in a MO material. The geometry of the resonator is similar to that discussed in [2].

In the *off* state, the material of the resonator is described by the scalar relative permittivity $\varepsilon_r = 6.25$ and the scalar permeability μ_0. In the *on* state, the MO material of the resonator is characterized by the following expression for the permittivity tensor with magnetization along the axis z:

$$\varepsilon = \varepsilon_0 \begin{bmatrix} \varepsilon_r & ig & 0 \\ -ig & \varepsilon_r & 0 \\ 0 & 0 & \varepsilon_r \end{bmatrix} \qquad (1)$$

where $\varepsilon_r = 6.25$ and $g = 0.3$ [3] (the Voigt parameter is $g/\varepsilon_r = 0.048$).

The frequency responses for power transmission of the switch in the *on* and the *off* states are given in Fig. 2 for excitation at port 1 and at port 2. In this curves, the waveguide losses were removed in order to show only the MO cavity losses, which are $P_{on} = -2$ dB and $P_{off} = -20$ dB for the frequency $\omega a/2\pi c = 0.3031$. The calculated switch *on* and *off* ratio $P_{off}(dB)/P_{on}(dB)$ at the peak of transmission ($\omega a/2\pi c = 0.3031$) is about 18. The frequency band at the level -15dB of the resonant curve for the *off* state is about 180 GHz. This band is defined by resonant nature of the switch.

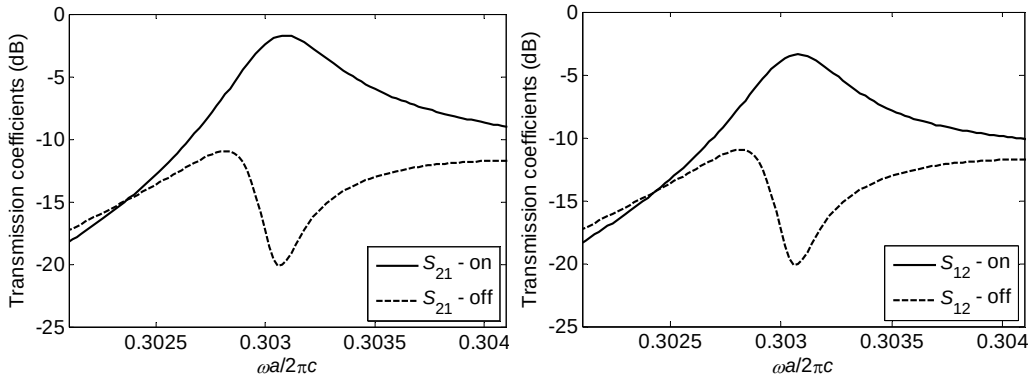

Fig. 2. Optical switch frequency responses of power transmission in *on* and *off* states for excitation at port 1 (left), and at port 2 (right).

We show in Fig.3 the normal component of the ac magnetic field H_z distribution for excitation at port 1 at the frequency of $\omega a/2\pi c = 0.3031$. As it can be observed, the field amplitude is greatly increased in the MO cavity and the orientations of the standing dipole mode are in accordance with the schemes of Fig. 1.

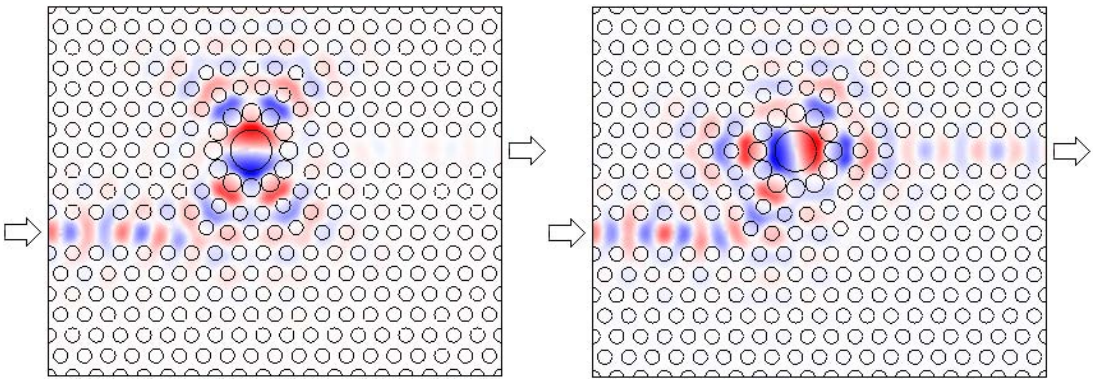

Fig. 3. Distribution of normal component H_z of ac magnetic field in optical switch excited at port 1 in *off* state (left), in *on* state (right).

References

[1] www.comsol.com
[2] V. Dmitriev, M. Kawakatsu, F. J. M. de Souza, "Compact three-port optical 2D photonic crystal-based circulator of W-format", Optics Letters, **37**, 3192-3194, 2012.
[3] Hiroyuki Takeda and Sajeev John, "Compact optical one-way waveguide isolators for photonic-band-gap microchips", Phys. Rev. A, **78**, 023804, 2008.

Fiber-to-the-home services based on OCDMA technique

Tawfig Eltaif[1*], Hesham A. Bakarman[2*], Abdulrahman Khonji[1], and B. A. Hamida[3]

[1]Faculty of Engineering & technology (FET); Multimedia University,
Jalan Ayer Keroh Lama, 75450; Bukit Beruang, Melaka, Malaysia

[2]PTL, Institute of Microengineering and Nanoelectronics;
National University of Malaysia (UKM), Bangi, 43600, Selangor, Malaysia

[3]Optoelectronics Laboratory, Faculty of Engineering, International Islamic
University Malaysia (IIUM), 53100 Gombak, Kuala Lumpur, Malaysia

[*]corresponding author: tefosat@ieee.org; hesham@vlsi.eng.ukm.my

Abstract- Application of optical code division multiple access (OCDMA) in the passive optical network (PON) architecture is introduced. Fiber to the home based on direct detection OCDMA-PON architecture supporting multi optical network units is implemented by using modified quadratic congruence code (MQC) sequences as the address code to identify all users in the optical domain. Each PON comprises many users encoded by MQC codes for the upstream signals. The results have indicated that low error rate transmission at high data rate for distances up to 20 km.

Summary: Indeed, the era of Fiber to the Home (FTTH) has arrived, and with the advantages of optical fiber such as high bandwidth over long distances, immunity to electromagnetic interference, data security and ease of installation, the optical fiber is capable of delivering bandwidth-intensive, integrated voice, data and video services at distances beyond 20 km in the subscriber access network. The passive optical network (PON) is a technology viewed by many as an attractive solution to the first-mile problem [1-5]. The PON network consist of 3 items, an optical line terminal (OLT) at the central office is connected via optical fiber to many optical network units (ONU) at remote nodes through one or multiple 1: N optical splitters. Since the network between the OLT and the ONU is passive, i.e. it does not need any power supply, the PON technology which has been viewed by many researchers as an attractive solution to the first-mile problem is being given more attention by the telecommunication industry as the first-mile solution because of its advantages for local access networks [2, 5]. The advantages that make it replaced the other techniques can be found in [2]. A PON can operate at distances up to 20 km using only one single fiber and only one port per PON is required in the central office. PON is enable the system to support higher bandwidth compared to the standard PON, and this make it the ultimate goal of fiber reaching all the way to the customer premises fiber-to-the-home (FTTH) may be the most economical deployment today. Moreover, it's easy to upgrade the PON network to higher bit rates.

OCDMA technique [2-4] is a point-to-multipoint technology where each end-user matches its own communication from the transmitted signal. The code division format offers excellent resistance to signal interference (i.e., in optical communication, light interference). Correspondingly, PON architecture design is also considered as a point to- multipoint access technology with passive components, such as splitters, couplers, fiber- optics etc., where potentially the cost is reduced. The first-mile is a network with a central office (CO) which serves multiple users.

The aim of this article is to introduce multi upstream passive optical network based on coding technique.

OCDMA technique is considered the next-generation optical access network. The OCDMA link is apparent to the input channel's data procedure with security. It maintains burst secure traffic and random access protocols. Hence, incorporating this technique with PON will enable the system to support higher bandwidth compared to the standard PON. The architectures of transmitter, receiver, optical network unit (ONU) and optical line terminal (OLT) as part of the OCDMA-PON are clarified in this paper. A multi PON access network using direct detection encoder scheme, each PON comprises 9 user encoded by modified quadratic congruence (MQC) codes at the C band for the upstream signal with channel spacing 50 GHz is simulated. In this article low error rate transmission at high data rate for distances up to 20 km is demonstrated. Variation in the results was studied when fiber length and data rate were varied and different transmission power was applied. The results have indicated that the proposed PON based on direct detection OCDMA can be capable to support local area networks as an application FTTH.

REFERENCES

1. Lin, Ch. Broadband, Optical Access Networks and Fiber-to-the-Home Systems Technologies and Deployment Strategies. (John Wiley & Sons Ltd, 1th edition. 2006)
2. Ghafouri-Shiraz, H. and Karbassian, M. M. optical CDMA networks principles, analysis and applications. (John Wiley & Sons Ltd, 1th edition .2012)
3. P. R. Prucnal, Optical Code Division Multiple Accesses: Fundamentals and Applications (Taylor & Francis, 2005).
4. K.-I. Kitayama, X. Wang, and N. Wada, "OCDMA over WDM PON - solution path to gigabit-symmetric FTTH," J. Lightwave Technol. 24(4), 1654–1662. 2006.
5. Kramer, G. (2005) Ethernet passive optical network. McGraw-Hill, New York, USA.

Broadband services to the end users

Tawfig Eltaif[1*], Ahmed ba haretha[1], Anitha Mohan[1], Abdulrahman Khonji[1], B. A. Hamida[2], and Hesham A. Bakarman[3]

[1]Faculty of Engineering & technology (FET); Multimedia University,
Jalan Ayer Keroh Lama, 75450; Bukit Beruang, Melaka, Malaysia
[2]Optoelectronics Laboratory, Faculty of Engineering, International Islamic University Malaysia (IIUM), 53100 Gombak, Kuala Lumpur, Malaysia
[3]PTL, Institute of Microengineering and Nanoelectronics;
National University of Malaysia (UKM), Bangi, 43600, Selangor, Malaysia
[*]corresponding author: tefosat@ieee.org

Abstract- This article introduces a study on wavelength division multiplexed passive optical network (WDM-PON). First, we simulated downstream transmission signals for long reach WDM-PON architecture taking into account the effect of four-wave mixing (FWM), and then we simulated downstream broadband signals. The focus in this work was set on data rate based optical transmission systems with a varying number of channels in order to investigate the potential of 0.64 Tb/s technologies for the implementation in the next generation optical transmission networks. Simulation results show that error-free operation can be achieved in long reach transmission.

Summary: In recent years, the network providers start deploying optical fiber in the access network to accommodate the bandwidth demand. Due to the number of features wavelength division multiplexed passive optical networks (WDM-PONs) have, including wide bandwidth, large split ratio, extended transmission reach; WDM-PON considered as a promising candidate to provide broadband access for the next generation networks. PON was invented at British Telecom in the late 1980s [1], and the Electronics and Telecommunications Research Institute in Korea has had since 1982 a series of pilot studies and field tests of fiber to the curb (FTTC) and fiber to the home (FTTH), either passive point to point (P2P) or point to multi point (P2MP) or active [2]. But the big yearly event that KT (former Korea Telecom) had was in early 90s; when the company was set a plan to meet the explosive communication demands in the country [1]. The first step of FTTH was taken from there, but officially FTTH was first introduced in 1999 in Japan, and as of September 2007 10.5 million FTTH connections are reported in Japan [3] making it leads the world in number of subscribers served by FTTH [2]. After a decades Malaysia has launched Unifi broadband services based on optical transmission networks. As of Jun 2011, Telekom Malaysia ™ has offered this service to more than 100,000 customers.

The passive optical network (PON) is a technology that does not require active components along the fiber infrastructure. PON which has been viewed by many researchers, and it considered as an attractive solution to the first-mile problem [1-7] consist of 3 items, an optical line terminal (OLT) at the central office is connected via optical fiber to many optical network units (ONU) at remote nodes through one or multiple 1: N optical splitters. The ONU is the customer's gateway to the optical network, and is responsible for creating all the services for which the subscriber pays. A PON is the ultimate technology that can operate at distances up to 20 km using only one single fiber, and in order to accommodate the huge traffic from the broadband access networks, an incorporation wavelength division multiplexing (WDM) in PON network enables the system to

support high bandwidth to the customer premises compared to the standard PON. Moreover, it's easy to upgrade the PON network to higher bit rates [7].

The aim of this article is divided in two sections, first to introduce a simulation study on downstream transmission signals for long reach WDM-PON architecture taking into account the effect of four-wave mixing (FWM), and simulation study on downstream broadband signals. The focus in this work was set on data rate based optical transmission systems with a varying number of channels in order to investigate the potential of 0.64 Tb/s technologies for the implementation in the next generation optical transmission networks. The C band has been selected with channel spacing 50GHz and 25GHz, because of the law attention. The transmission length between the ONU to the CO is over 80 km, the attenuation and dispersion of single mode fiber (SMF) at 1550nm are about 0.25dB/km and 17ps/km/nm, respectively. In the second section, we introduce a simulated downstream broadband signals using a C band. Using none return to zero format (NRZ), WDM-PON system for many-downstream signals was designed and variation in the results is studied when fiber length and data rate are varied and different transmission power is applied. The system shows good results in terms of the bit error rate (BER) at 10 Gb/s.

REFERENCES

1. Lin, Ch. Broadband, *Optical Access Networks and Fiber-to-the-Home Systems Technologies and Deployment Strategies*. John Wiley & Sons Ltd, 1th edition, England. 2006
2. Paul E. Green Jr, *Fiber to the Home: The New Empowerment*. John Wiley & Sons Ltd, 1th edition, New Jersey. 2006
3. Press Release, Telecommunications Bureau, Ministry of Internal Affairs and Communications (MIC), 18 December 2007.
4. Josep Prat, *Next-Generation FTTH Passive Optical Networks: Research Towards Unlimited Bandwidth Access*. Springer, 1th edition. 2008
5. Effenberger F J, Ichibangase H, Yamashita H. "Advances in broadband passive optical networking technologies," *IEEE Communications Magazine,* 2001; 39(12): 118–124.
6. A. Banerjee, Y. Park, F. Clarke, H. Song, S. Yang, G. Kramer, K. Kim , and B. Mukherjee, "Wavelength-division-multiplexed passive optical network (WDM-PON) technologies for broadband access: a review [Invited]," J. Optical Networking, vol. 4, No. 11, pp. 737-758, 1998.
7. Ton Koonen, "Fiber to the Home/Fiber to the Premises: What, Where, and When?," Proceedings of the IEEE. vol. 94, No. 5, May 2006.

Bioeffects of EM fields

Exposure to Extremely Low Frequency Electromagnetic Fields and its Attributable Health Risks

H. M. Elmehdi
Applied Physics Department, University of Sharjah, UAE
[2]Author Affiliation, Country
[*]Corresponding author: hmelmehdi@sharjah.ac.ae

Abstract- Numerous studies have linked extremely low frequency electromagnetic fields (ELEMF) to possible adverse heath effects, the most prominent of which is childhood leukaemia. In our research we have conduct a pooled study in which we have examined research over the past ten years to review possible association between exposure to ELEMF and risk of childhood leukaemia. The collected data covered wide range of countries and field ranging from <0.1 μT and up to fields of ≥ 0.4 μT. The results show the existence weak association between ELEMF exposure and childhood leukaemia at high magnetic fields.

The energy quanta carried by non-ionizing radiation is not strong enough to break the chemical bonds in genetic molecules to be considered carcinogenic to humans. However, it is well established that there are biophysical mechanisms that can lead to adverse health effects as result of sufficiently strong exposure. For low frequency the mechanism is described as stimulation of the nerve and muscle cells due to induced currents. For higher frequencies tissue heating is the mechanism. With the advances we are experiencing in our modern world where we are continuously exposed to electromagnetic fields from casual use of various home appliances and electronic devices, the concept of *zero exposure* does not exist. Children who spend most of their time at home are exposed the most. Due to these facts, a number of researches have carried out research to measure exposure rates and examine the possible links to adverse effects such as leukaemia among young children. The findings of some of the early work have prompted international organizations such as the International Commission on Radiation Protection (ICRP) and world health organization (WHO) to list ELF as carcinogenic to children. This encouraged these agencies to issue exposure limits below which the risk becomes minimal even at long exposure times. For example, the ICRP limits are published as a function of frequency. For example, the limits are set at 5000 μT /*f* for frequencies lower than 800Hz and 0.2 μT for frequencies up to 300GHz.

Over thirty (30) studies were reviewed over the period from 1999 to 2010 for magnetic fields in the ranges from <0.1 μT and up to fields of ≥ 0.4 μT. The collected results are summarizes in Figures 1 and 2. It should be noted that the collected studies cover wide range of courtiers from around the world including Europe, North America, South America, Australia and Asia.

In the studies examined, the investigated sites were classified in accordance to exposure to electromagnetic fields arising from electrical wiring and/or transformers in that site. Areas were designated as high current configuration (HCC) and low current configuration (LCC). An odds ration (OR) was defined as follows:

$$\text{Odds Ratio (OR)} = \frac{\text{HCC cases}}{\text{HCC controls}} \times \frac{\text{LCC controls}}{\text{LCC cases}} \quad \ldots\ldots\ldots (1)$$

The OR is taken an indication of the increase in risk from exposure to ELEM. OR's were calculated for both birth and death addresses as well as for children who had lived at the same address throughout their life. In previous pooled and met analyses, restrictions such as the number of cases/control, area, magnetic field strength, and research methodology, were imposed on the included studies. In an attempt to get an overall assessment of the risk, we included all available studies. Our aim of this study is to be able to conduct a similar study in the United Arab Emirates and compare the risk to the existing data.

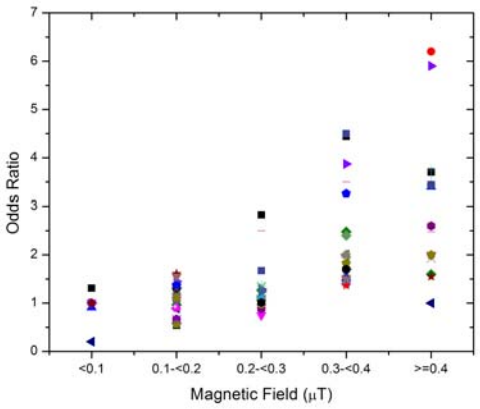

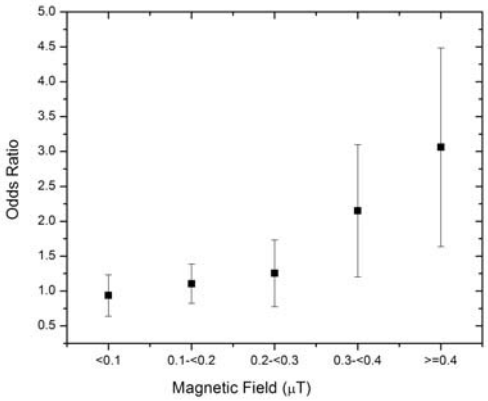

It should be noted that almost all reported studies have concentrated on the association of magnetic fields with increased risk of childhood leukaemia. From Figures 1 and 2, its is clear that there an increased risk associated with the top percentiles of exposure levels. However, this group of studies (high magnetic fields) noticeably involved a small number of exposed cases. When compared to other studies such as the selective pooled analyses by Ahlbom et al, (2000) and Greenland et al, (2000), our findings is consistent in that there is an epidemiological association exists between residential exposure to magnetic fields and the increased risk of childhood leukaemia. Similar results were obtained by Schuz et al (2007) and Kheifets (2010).

Acknowledgements: The author is grateful to the College of Sciences, University of Sharjah for partial funding for this project.

REFERENCES[*] *(due to the limited space of 2 pages, we will only include a 5 out of the 43 references used in the research).*

1. Ahlbom A, Day N, Feychting M, Roman E, Skinner J, Dockerty J, Linet M, McBride M, Michaelis J, Tynes T, Verkasalo PK. A pooled analysis of magnetic fields and childhood leukaemia. *Br J Cancer* 83(5): 692 – 698, 2000.
2. Greenland S, Sheppard AR, Kaune WT, Poole C, Kelsh MA. A pooled analysis of magnetic fields, wire codes, and childhood leukemia. Childhood Leukemia-EMF Study Group. Epidemiology 11(6): 624–634, 2000.
3. Schuz J, Ahlbom A Exposure to electromagnetic fields and the risk of childhood leukaemia: a review. Radiat Prot Dosimetry 132(2): 202–211, 2008.
4. World Health Organization Environmental Health Criteria (WHO EHC). Extremely Low Frequency Fields, *Vol 238. WHO*: Spain, 2007.

Effects of Mobile-phone Base-Stations Radiation on Albino Rats' Body Growth and Blood

A. M. Ahmed [1], A. K. Sabir Ali [2], S. T. Kafi [1], and Aida A. Salama[3]

(1) Department of Medical Physics and Biophysics, Faculty of Science and Technology, Al-Neelain University, Khartoum, Sudan.

(2) Department of Biology and Environmental Sciences, Faculty of Science and Technology, Al-Neelain University Khartoum, Sudan.

(3)Department of Biophysics, Al- Azhar university, Cairo, Egypt

Corresponding author: Email abdophysics@gmail.com

Abstract: The present work was proposed to study the effects of RF/MW radiation emitted from a mobile -phone base- station on albino rats' blood. Two groups of albino rats were exposed to 10.5μW/cm^2 and 0.5μW/ cm^2 radiation intensity and a third control group received no radiation. The results showed clear changes in the body growth and the physical and chemical characteristics of blood of the exposed rats. Symptoms of anxiety, aggressiveness, thirst and frequent urination were evident on the irradiated rats.

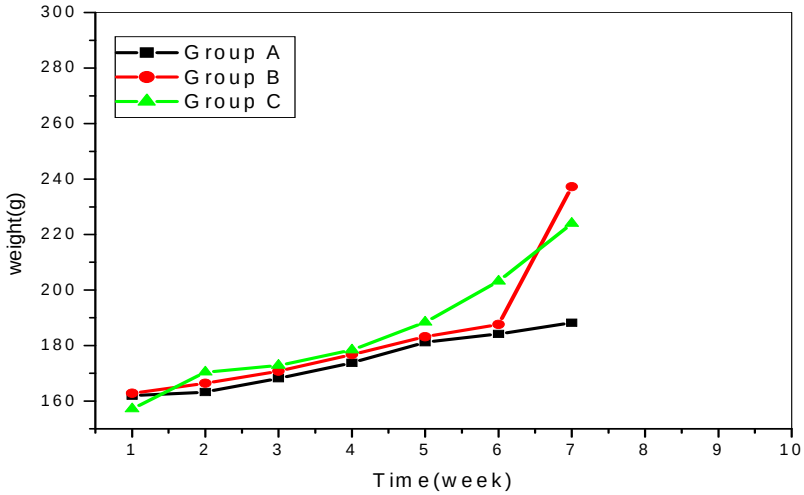

Fig (1): Effects of radiation on body growth
(**A:** control **B:** 10.5μW/cm^2 **C:** 0.5μW/ cm^2)

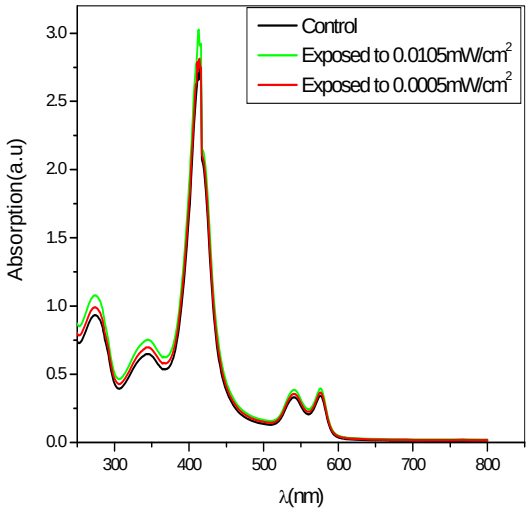

Fig (2): Absorption spectra after 6 weeks exposure

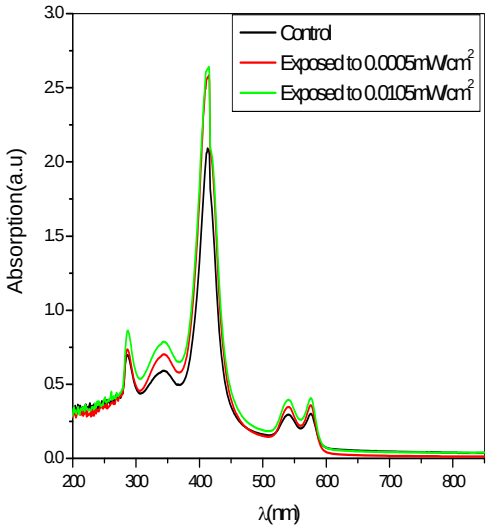

Fig (3): Absorption spectra after 12 weeks exposure

Acknowledgements

We would like to thank the Egyptian Research Institute and The Department of Biophysics in Cairo and Al Azhar Universities and the staff of Biochemistry and Microbiology Departments at Al Neelain University.

References

1. John Moulder, Mobile Phone (Cell Phone) Base Stations and Human Health, Medical College of Wisconsin, Milwaukee, Wisc, U.S.A, version No 7.7.5**.** 13 Aug 2006.
2. S. Gabriel, R. W. Lau, and C. Gabriel, "The dielectric properties of biological tissues: II. Measurement in the frequency range 10 Hz to 20 GHz," Phys. Med. Biol., vol. 41, no. 11, pp. 2251–2269, 1996.
3. Mikhail.N, Shehata.M, and Attia.M.M, Effect of Exposure of Rats to Low Frequency Electromagnetic Field(E.M.F) on RBC, Heart, Kidney , and Liver . j.Med. Res. Insttitute . 1998.
4. 'Inzeo, G., et. al, Microwave effects on acetycholine-induced channels in cultured chick myotubes. Bioelectromagnetics 9; 363-372. 1988.
5. Mann, K., et. al., 1996. Effects of pulsed high-frequency electromagnetic fields on human sleep. Neuropsychobiology;33:41-7. 1996.
6. Neil Cherry, Criticism of the health assessment in the ICNIRP guidelines for radiofrequency and microwave radiation (100KHz- 300GHz), Lincoln University.2000.

Effects of RF/MW Exposure from Mobile-phone Base-Stations on the Growth of Green Mint Plant using *Chl* a Fluorescence Emission

S. T. Kafi [1,4*], A. M. Ahmed [1], M. K. Sabah-Alkhair[2], D. A. Mohamed [3], R. S. Ahmed[3], and Z. O. Hassaan[3]

(1) Department of Medical Physics and Biophysics, Faculty of Science and Technology, Al-Neelain University, Khartoum, Sudan.

(2) Department of Biochemistry, Faculty of Science and Technology, Al-Neelain University Khartoum, Sudan.

(3) Laser Department, Faculty of Science and Technology, Al-Neelain University, Khartoum, Sudan.

(4) Department of Physics, Faculty of Science, Al-Baha University, Kingdom Saudi Arabia

***Correspondent author** : e-mail stawer.kafi@gmail.com

Abstract: This work was proposed to study the effects of RF/MW radiation emitted from mobile-phone base-stations on the growth of green mint plant using spectroscopic and vegetative parameters. Green mint plants divided into several groups, were exposed to different levels of radiation intensities (i.e. between 0.5μW/cm^2 and 10.5μW/cm^2), while one group was set free of radiation exposure to serve as control. A USB2000 spectrophotometer of resolution 1.34 nm bandwidth from ocean optics company (USA) was used to collect the fluorescence signals from intact leaves of plant. Results showed symptoms of radiation damage on all groups subjected to exposure. Retarding radiation effects were evident also on some morphological characters e.g. height of plants, leaf length and width, fresh and dry weights. Vegetative data were consistent with spectroscopic data.

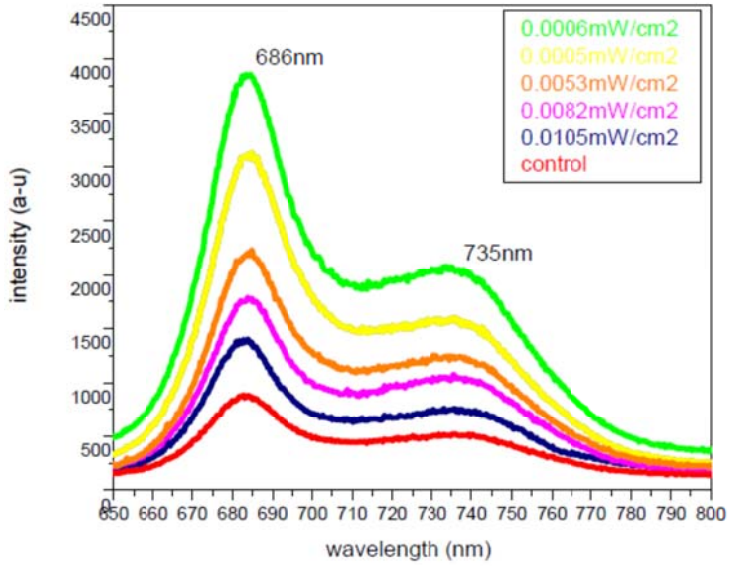

Fig (1): Fluorescence spectra from intact leaves of Green Mint plant obtained by LED excitation source with 450 nm wavelength and 60 μW output power.

References

(1) S. T. Kafi, I. M. K. Medani, A. M. Ahmed and A. K. Sabir Ali, Monitoring the Development of Cotton (*Gossypium barbadense* L.) using Emission Spectra of Chlorophyll Fluorescence, *Jordan Journal of Physics* , Vol 2, Number 2, 2009. pp. 103-111.
(2) R. Gopul , K . B .Mishra , M .Zeeshan, S. M Prasad and M. M Joshi. Laser-induced chlorophyll fluorescence of mung plants growing under nickel stress, *Current Science*, 83 (7). 2002.
(3) Kwan-Hoong, N. G. (2003). Non-Ionizing Radiations – Sources and exposure: Biological Effects, *Proceedings of the International Conference on Non-Ionizing Radiation* at UNITEN ICNIR 2003
(4) Pozar, David M. (1993*). Microwave Engineering* Addison-Wesley Publishing Company. ISBN 0-201-50418-9

Medical electromagnetics

A Novel Microwave Coaxial Slot Antenna Using EBG Structures for Liver Tumor Ablation

H. Açıkgöz*, A. Yılmaz*, I. Türer
*KTO Karatay University, Turkey
Corresponding author: hulusi.acikgoz@karatay.edu.tr

Abstract- This paper deals with the use of electromagnetic band-gap (EBG) structure to enhance the capability of the microwave coaxial slot antenna (MCA) in the treatment of liver cancer. The MCA is composed of an interstitial coaxial line that is enclosed in a catheter. The EBG structure used in this study is a 1D periodic T-ring shape structure wrapped on the outer conductor of the MCA. Thanks to the EBG structure, the backward heating problem appearing in many antennas is reduced.

I. Introduction

According to [1], the number of liver cancers diagnosed throughout the world is increasing at an alarming rate. Also this rate is estimated to increase over the next few decades. Among other possible treatments (surgical operation, chemotherapy, *etc.*) microwave ablation (MWA) is a promising alternative to eradicate cancerous tissue without damaging surrounding healthy tissue. Most of studies are based on the use of microwave coaxial antenna (MCA) and focused on SAR distribution and heating effect caused in the vicinity of the antenna [2]. An important type of MCA is a single slot antenna that achieves localized SAR distribution near the distal tip of the antenna. However, the major drawback of coaxial slot antenna [3] is to have backward heating that is represented in many SAR patterns as a 'tail' along the coaxial feedline. This paper presents a novel approach to include the EBG structure in the coaxial antenna design. The EBG structure (1D periodic T-ring shape structure) combined with the coaxial slot antenna seems to address the problem cited above and achieves a highly localized SAR pattern.

II. Design of the antenna

The EBG structure is derived from 2D mushroom-like structure [4] (Fig. 1a) where the periodicity in one direction is released (Fig. 1b). The 1D periodic structure is depicted in Fig.1b.

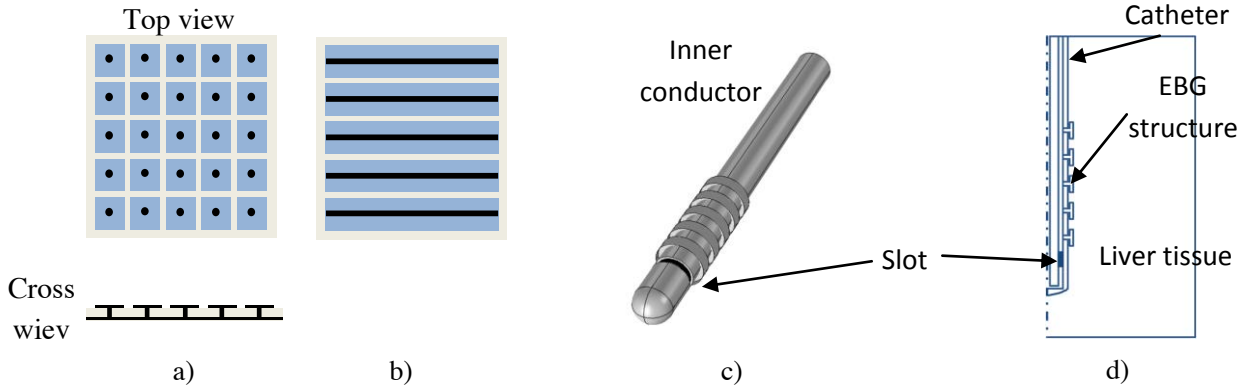

Fig.1 a) 2D mushroom-like structure, b) 1D periodic structure, c) coaxial slot antenna with EBG structure (without the catheter), d) 2D EBG coaxial slot antenna model within the liver tissue

The overall antenna is composed of a coaxial slot antenna around which the 1D periodic EBG structure is wrapped (Fig. 1c). The periodic structure is electrically connected to the outer conductor. Because of hygienic needs, a catheter layer of polytetrafluorethylene (PTFE) is deposited on the outer conductor of the antenna. The new coaxial antenna in the liver tissue is shown in Fig.1d.

III. Results

The SAR (Specific Absorption Rate) and the temperature at a distance 2.5 mm along the antenna are obtained using 2D axially symmetrical finite element model. The model is first solved for the electromagnetic wave distribution and then for the temperature distribution that is induced by the electromagnetic heating. The analysis of the heat transfer in the liver tissue is performed using the Pennes' bioheat equation. The SAR and temperature distribution along the antenna are presented in Fig.2. One can observe that at the slot position (62.5 mm) the SAR value is much higher for the new MCA. Similarly, the temperature in the liver tissue is also higher at that slot position. Another important result is that, with the introduction of the EBG structure, the backward heating problem along the MCA is reduced compared to the unmodified single slot antenna especially after 20 mm of insertion depth.

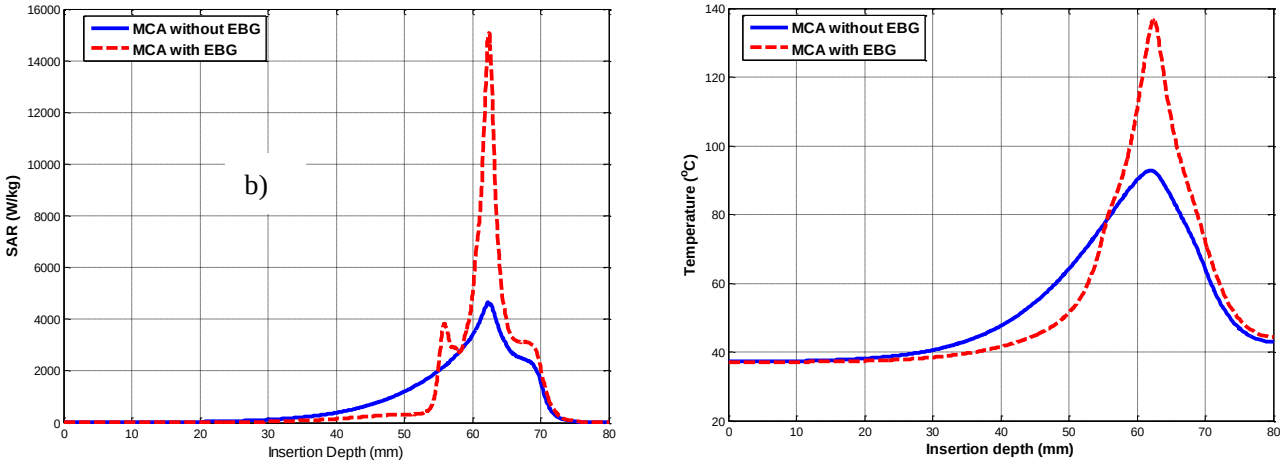

Fig.2 a) SAR distribution in the liver tissue at a distance 2.5 mm along the antenna, b) Temperature of the liver tissue at 2.5 mm along the antenna.

IV. Conclusion

The new MCA with EBG structure seems to achieve higher localized SAR distribution at the slot position than the classical one. The backward heating problem is also improved by the new antenna. However, more studies are required to optimize the antenna. In the full paper version more details and results are to be presented.

REFERENCES

1. John Hopkins Pathology Liver Cancer website, http://pathology.jhu.edu/liver/index.cfm.
2. Keangin P., Rattanadecho P., Wessapan T., "An analysis of heat transfer in liver tissue during microwave ablation using single slot antenna", International Communication in Heat and Mass Transfer, Vol. 38, 757-766, 2011.
3. Deshan Y., Bertram J.M., Converse M.C., O'Rourke A.P., Webster J.G., Hagness S.C., Will J.A., Mahvi D.M., "A floating Sleeve Antenna Yields Localized Hepatic Microwave Ablation", IEEE Transaction on Biomedical Engineering, Vol. 53, No. 3, March 2006.
4. Yang F., Rahmat-Samii Y., "Electromagnetic Band Gap Structures in Antenna Engineering", Cambridge University Press, 2009

Biological media; composite media; Random & structured materials

Static and dynamic analysis of piezoelectric multilayered plates under active actuation

M. Ajdour[1] and L. Azrar[23]

[1]Modeling and Simulation of Mechanical Systems, Modeling and Systems Analysis Laboratory, Faculty of Sciences of Tetouan, AbdelMalek Essaadi University; Tetouan; Morocco

[2]Mathematical Modeling and Control, Faculty of Sciences and Techniques of Tangier, AbdelMalek Essaadi University; Tangier; Morocco

[3]Faculty of Engineering, King Abdulaziz University; Jeddah; Saudi Arabia

[*]corresponding author: majdour@hotmail.fr; azrarlahcen@yahoo.fr

Abstract-

In a attempt to develop an efficient approach for the electromechanical analysis of laminated piezoelectric structures, an exact transfer matrix methodology is presented. The related equations for a three dimensional piezoelectric and elastic lamina are developed based on the Stroh formalism [1,2]. Solution for the vibrations of linear piezoelectric laminated plates is obtained by extending the Stroh formalism to the generalized plane strain vibrations of piezoelectric materials [3,4]. The laminated plate consists of homogeneous orthotropic electro-elastic three layered rectangular plate with horizontal dimensions L_x and L_y and with arbitrary thickness (figure 1).

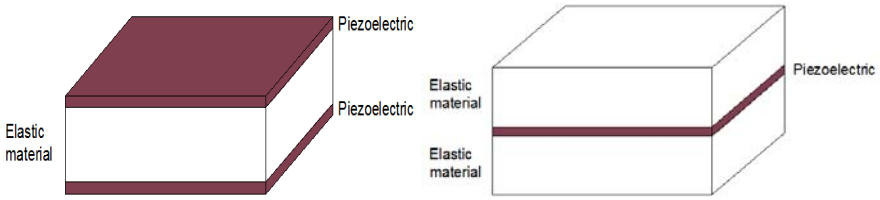

Figure1: Multilayered plates of piezoelectric and elastic material

The constitutive equation for an electro-elastic solid is expressed as

$$\begin{aligned} \sigma_i &= C_{ik}\gamma_k - e_{ki}E_k \\ D_i &= e_{ik}\gamma_k + \varepsilon_{ki}E_k \end{aligned} \qquad (1)$$

where σ_i and D_i are the stress and electric displacement, γ_k and E_k are the strain and electric field, C_{ik}, ε_{ik} and e_{ik} are elastic, dielectric and piezoelectric coefficients respectively. The components of electric field are expressed by electric potential Φi as follows:

$$E_i = -\Phi_i \qquad (2)$$

The equilibrium equations can be written as:

$$\begin{aligned} \sigma_{ij,j} + f_i &= 0 \\ D_{j,j} + f_e &= 0 \end{aligned} \qquad (3)$$

where f_i and f_e are the body force and the electric charge density respectively.

Our aim is to solve this partial differential system for a given boundary condition. The main focus is the prediction of stresses, displacements and electrical displacements in the thickness direction for various load types (mechanical and electrical load).

Numerical illustrations for static and dynamic analysis of simply supported rectangular electro-elastic plates under different active actuation will be analyzed and presented.

REFERENCES

1. Stroh, A.N. “Philos. Mag”, 625-646, 1958.
2. Ting, T.C.T, “Oxford University Press”, 1996.
3. Vel, S, Mewer, R.C, Batra, R.C “International Journal of Solids and Structures”, Vol. 41, 1625-1643, 2004.
4. Vel, S, Batra, R.C “International Journal of Solids and Structures”, Vol. 37, 715-733, 2000.

gnetic materials: Metamaterials; Plasmonics; Photonic crystals; chiral a

HPEM Crucial Parameters

L. Palisek
VOP CZ, s.p., Czech Republic
palisek.l@vop.cz

Abstract- High Power Electromagnetics (HPEM) environment is shortly introduced at the beginning of this paper. The main part of this paper is focused on overview of electromagnetic immunity of electronic equipment with HPEM parameters considerations. Results from experimental measurements as well as from simulations are used for this purpose. Important HPEM parameters as crucial ones regarding to electromagnetic susceptibility of electronic equipment are assessed and discussed.

Pulse power electromagnetic fields like NEMP (Nuclear Electromagnetic Pulse), HPM (High Power Microwave) and UWB (Ultra-wide Band) are considered as a possible threat for sensitive electronic equipment [1]. While NEMP is considered as a typical single pulse threat, HPM and UWB are often considered as signals with possibility of repetition rates according to state of the art technologies [2]. Moreover frequency as well as pulse width can be changed for HPM and UWB technologies. All these parameters are taken in to account in this paper.

Overview of measurements related to electromagnetic immunity to HPM and UWB signals carried out at VOP CZ, s.p. considering influence of repetition rate is mentioned. Transfer function measurements are used to support considerations regarding to frequency influence.

Due to very low possibilities to change parameters of available testing technologies it was very useful to prepare simulation model with possibility to change relevant parameters arbitrarily. It is known the most vulnerable parts of electronic are semiconductors. Due to this fact the area of interest was focused on semiconductor junction. The principle mechanisms by which a semiconductor junction may fail are surface breakdown and internal breakdown through the junction within the body of the device [3], [4]. Main problem within the junction is an internal breakdown where destruct mechanism results from changes in the junction parameters due to the high temperatures locally within the junction area. Very high temperatures of junction lead to melting or even evaporation of the junction (~1000 °C). For this consideration suitable temperature model of the junction was created. Electro-thermal analogy was used for the purpose to simulate rep-rate influence as well as pulse width within the semiconductor junction. This analogy can be explained by next equations:

$$T_M(t) = T_M(0) + \int \frac{P}{M} dt \tag{1}$$

$$V_C(t) = V_C(0) + \int \frac{i}{C} dt \tag{2}$$

where:
TM is temperature of thermal mass, °C
P is power input to thermal mass, W

M is thermal mass (thermal capacitance), J/°C
VC is voltage on capacitance, V
i is current input to capacitance, A
C is value of capacitance, F

Comparing the equations (1) and (2) we find that temperature corresponds to voltage, power (thermal) corresponds to current and thermal mass (thermal capacitance) corresponds to electrical capacitance. Since current is the analog of power (thermal) then an electrical current source can be analog of heat power source. A resistor in an electrical circuit corresponds to thermal resistance.

Finally it will be possible to assess and to discuss crucial parameters of HPEM environment with results from experimental measurements supported with results from simulations.

REFERENCES

1. Taylor, C. D. and D. V. Giri, *High-Power Microwave Systems and Effects*, Taylor and Francis, Washington, 1994.
2. EC 61000-2-13, First edition, 2005-03, Electromagnetic compatibility (EMC) – Part 2-13: Environment – High-power electromagnetic (HPEM) environments – Radiated and conducted.
3. Wunsch, D. C. and R. R. Bell, "Determination of threshold failure levels of semiconductor diodes and transistors due to pulse voltage," *IEEE Trans. Nuc. Sci*. NS-15, 244-259, Dec. 1968.
4. Tasca, D. M., "Pulse power failure modes in semiconductors," *IEEE Trans. Nuc. Sci*. NS-17, 364-372, 1970.

Tuneable metamaterials containing soft ferromagnetic wires

M. Ipatov[1*], L. V. Panina[2,3], V. Zhukova[1] and A. Zhukov[1,4]

[1]Dpto. Física de Materiales, Universidad del País Vasco, San Sebastián, Spain
[2]Institute for Design Problems in Microelectronics RAS, Moscow, Russia
[3]School of Computing & Mathematics, University of Plymouth, UK
[4]IKERBASQUE, Basque Foundation for Science, 48011 Bilbao, Spain
[*]corresponding author: arkadi.joukov@ehu.es

Abstract- We present studies of metamaterials consisting of soft magnetic wires embedded in a polymeric matrix. The combination of two effects, namely, a strong dispersion of the effective permittivity in metallic wire composites (resonance or plasmonic type) and giant magnetoimpedance effect in wires results in unusual behavior of the developed metamaterials that is dependence of an effective dielectric response on the wire magnetization which can be changed with different external stimuli. We used Free-space method to investigate the magnetic field tuneabilty of composites containing Co-rich soft magnetic amorphous wires.

It is worth mentioning, that studies of magnetic properties of amorphous glass coated microwires recently attracted considerable attention mainly due to a number of unusual magnetic properties and their potential applications in sensors [1-3] and multifunctional composites [4,5].

The composites with embedded arrays of metallic wires may demonstrate a strong dispersion of the effective permittivity ε_{ef} in the microwave range. It is known that the impedance of magnetically soft microwires can be very sensitive to external stimuli as magnetic field and mechanical load. These effects known as giant magneto-impedance (GMI) and stress impedance (SI) can be applied for engineering artificial dielectrics with tuneable electromagnetic properties. A possibility to control or monitor the electromagnetic parameters (and therefore scattering and absorption) of composite metamaterials is of great interest for different application such as remote non-destructive testing, remote stress and temperature monitoring, microwave tunable coatings and absorbers. On the other

hand the dispersion of the effective permittivity ε_{ef} is determined by the geometry of wire medium and the frequency dependence of wire impedance.

Here we present our recent results on the dependence of the effective permittivity in metamaterials prepared from short-cut Co-based amorphous microwires with different length on the external magnetic field applied along the wires. We measured S-parameters in free space in the frequency band of 0.9-17 GHz from which the effective permittivity was deduced. Fig.1 shows the experimental dependences of transmission spectra for cut-wires composites with different length of microwires. Fig. 1 shows the real and imaginary parts of the effective permittivity.The effective permittivity spectra were deduced from reflection and transmission measurements. In present case it is confirmed that the effective permittivity has resonance type dispersion due to the dipole resonance in wires at half wavelength condition. The application of the field broadens the resonance and shifts it towards the higher frequencies. We can conclude that both types of wire composites possess a strong dependence of the effective permittivity on the external magnetic field and are suitable for large scale applications as tunable microwave materials.

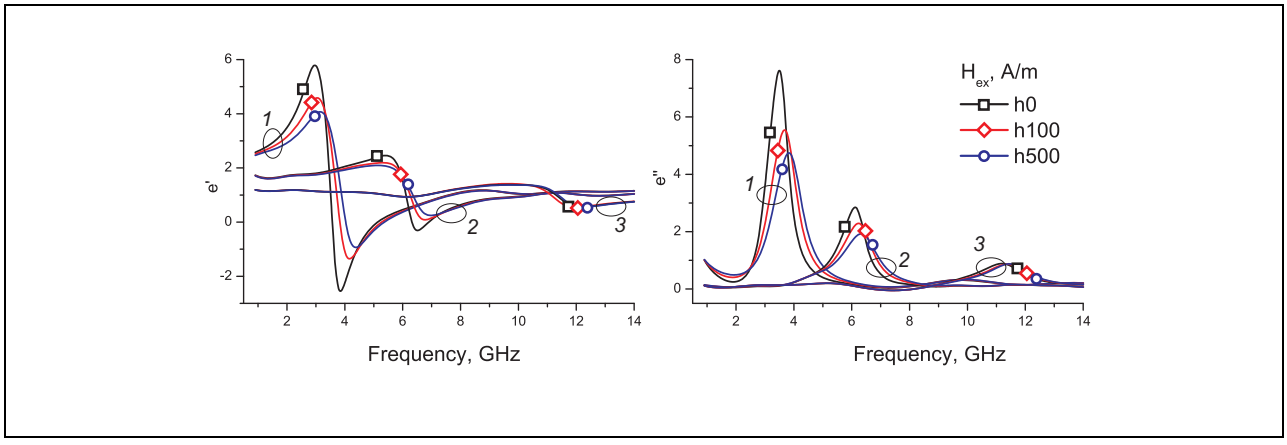

Fig. 1. Effective permittivity spectra for composites with cut wires of length 40 (1), 20 (2) and 10 (3)mm with the field as a parameter

The experimental results are well explained considering scattering from a single wire and assuming that the wires in the diluted composite interact weakly. The magnetic properties of wires affect scattering via impedance boundary conditions.

The potential applications for composite based on microwires with large and sensitive magneto-impedance effect can be related with the control the composite's electromagnetic characteristics. The application of a magnetic field or other stimuli will cause change in reflection, transmission and absorption in the composite material. For example, an "active microwave window" can be realized, the state of which can be changed from transparent (open) to opaque (close) for the microwaves. Other applications are transmission signal modulation, deferent frequency selective surfaces and reconfigurable absorbers.

Acknowledgements, This work was supported by EU ERA-NET programme under project DEVMAGMIWIRTEC (MANUNET-2007-Basque-3), by Spanish MICINN under Projects MAT2010-18914 by the Basque Government under Saiotek 09 MICMAGN (S-PE09UN38) and MEMFOMAG (S-PE12UN139) projects and by federal target program "Scientific and scientific-pedagogical personnel of innovative Russia", state contract no 14.A18.21.0783.

REFERENCES

1. Zhukova, V; Ipatov, M. & Zhukov A., Thin Magnetically Soft Wires for Magnetic Microsensors. *Sensors* Vol. 9, No. 11, pp. 9216-9240, 2009
2. Vazquez, M.; Chiriac, H.; Zhukov, A; Panina, L. & Uchiyama T., On the state-of-the-art in magnetic microwires and expected trends for scientific and technological studies. *Phys. Status Solidi A*, Vol. 208, No. 3, pp. 493–501, 2011
3. Honkura, Y. Development of amorphous wire type MI sensors for automobile use. *J. Magn. Magn. Mater.* Vol. 249, No. 1-2, pp. 375-381, 2002
4. Panina L., Ipatov M., Zhukova V., Gonzalez J. and Zhukov A., Tuneable composites containing magnetic microwires, Book: Metal, ceramic and polymeric composites for various usesEdited by John Cuppoletti, ISBN: 978-953-307-353-8 (ISBN 978-953-307-1098-3) , chapter 22, pp.431-460, InTech - Open Access Publisher (www.intechweb.org), Janeza Trdine, 9, 51000 Rijeka, Croatia

Short Pulse Antennas with Applications

Dr. D. V. Giri
Pro-Tech, 11-C Orchard Court, Alamo, CA 94507-1541 USA,
Dept. of ECE, University of New Mexico, Albuquerque, NM 87131 USA
Giri@DVGiri.com, www.dvgiri.com

Abstract-We start this presentation with a four-band classification of high-power electromagnetic (HPEM) waveforms [1] based on bandwidth that has been proposed and formalized. An antenna system that radiates impulse-like waveforms making use of reflectors has been called the impulse radiating antenna (IRA). This paper presents such antennas along with some representative applications.

1. HYPERBAND SYSTEMS (*band ratio* > 10)

Since it was the first proposed by Baum [2], paraboloidal reflectors fed by TEM transmission lines have received a lot of attention, owing to their main attractive property of extremely wide bandwidth, without the adverse effects of dispersion. They have been called the impulse radiating antennas (IRAs) and a photograph of an example, the prototype IRA can be seen in Figure 1.

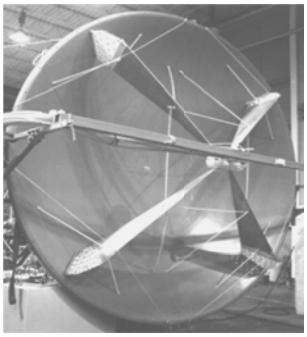

Figure 1. Prototype Impulse Radiating Antenna (3.7m diameter reflector)

The bandwidth associated with time-domain antennas is to be distinguished from the approximately 10 to 1 bandwidth of the so called frequency independent antennas such as the log-periodic antenna, which is highly dispersive since the phase center of the antenna is not fixed. Different CW frequencies applied to a log-periodic antenna get radiated from different portions of the antenna, which makes it dispersive, if all of the frequencies are applied at the same time as in a pulsed application. Reflector IRAs overcome this problem and even have equivalent electric and magnetic dipole moments characterizing the low-frequency performance. Even the dipolar radiation at low frequencies is along the optical axis of the reflector. Many optimal reflector IRAs has been designed, fabricated and tested.

2 . ILLUSTRATIVE APPLICATIONS

Hyperband systems can be built in many forms such as reflector IRAs described above [3], or TEM horns, and lens IRAs. They have useful applications such as:

- **Disrupter** (**D**isrupting **I**ntegrated **S**ystem, **R**eleasing **U**ltra-**P**ower **T**ransient **E**lectromagnetic **R**adiation)
- Buried target detection such as demining
- Hostile target detection and identification
- Space debris detection
- Periscope detection
- Source for vulnerability studies via transfer functions
- High-power, hyper-wideband jammers
- Law-enforcement applications such as “seeing through walls”
- Electrical characterization of materials (e.g., wave propagation measurements in materials such as rock, concrete)
- Industrial applications (detection of leaky or defective pipes)
- Searching for victims of natural disasters such as earth quake rubble and avalanche

These antennas can be designed to operate from 10’s of MHz to several GHz. This is an extremely wideband spectrum where critical military and civilian operations take place in the field of radar and communication engineering. We will briefly discuss some of the above mentioned applications.

REFERENCES

1. Giri, D. V. and Tesche, F. M., *Classification of Intentional Electromagnetic Environments (IEME),* IEEE Transactions on Electromagnetic Compatibility, Volume 26, Number 3, pp 322-328, August 2004.

2. Baum, C. E., *Radiation of Impulse-Like Transient Fields*, Sensor and Simulation Note 321, November 1989. Can be downloaded from http://www.ece.unm.edu/summa/notes

3. Giri, D. V., *High-Power Electromagnetic Radiators: Nonlethal Weapons and Other Applications,* Harvard University Press, 2004, Cambridge, MA, USA.2004.

RF DEW Scenarios

R. L. Gardner[1*]
[1]Consultant, Alexandria, VA, USA
[*]Robert.L.Gardner@verizon.net

Abstract- High power microwave weapons interact with their targets in complex ways. That interaction can best be described as a sequence of transfer functions describing the HPM source, antenna, propagation to the target, external target response, penetration into the target and finally the response of the target circuitry. Prediction of the actual target is response is usually done empirically and publicly available data are used to quantitatively estimate range to effect for various scenarios. The paper concludes with three scenarios across seven sources and broad estimates are given for the effectiveness of the candidate sources.

Applications of high-power microwave weapons can only be described in complete tactical scenarios (Ref 1). Estimates of that effectiveness involves a sequence of transfer functions as show in Fig. 1 (Ref. 2). All of the transfer functions are frequency dependent and, in some cases, may be nonlinear.

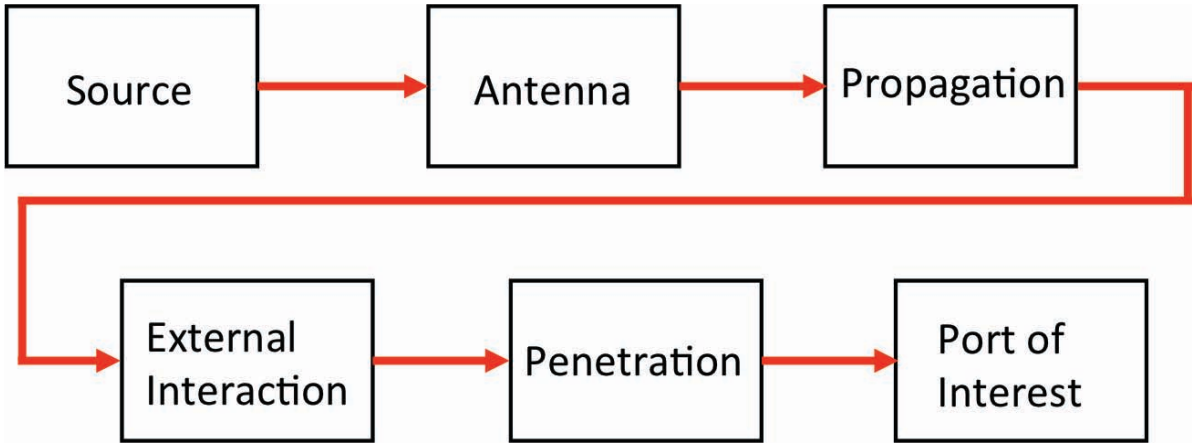

Figure 1: Transfer Functions From Source to Effect

The source produces the desired fields and the antenna shapes the fields. The propagation transfer function represents the attenuation of the fields from distance and sometimes from the atmosphere (exponential attenuation). Different frequencies react with the target surface differently and best coupling is achieved using the appropriate resonant frequencies. To get to the interior electronics the fields (and currents) must penetrate into the system and that transfer function(s) also depends strongly on frequency and local resonances. Finally the fields and currents enter the target electronics and interact with the target.

HPM effects on electronics are often established empirically but there are many variables (knobs) in the test design – driving the cost of complete testing to high levels. A complete model of the effectiveness of a source in a particular tactical scenario has eluded the HPM community so we must rely on simple estimates. Further,

many organizations and countries consider HPM effects data sensitive so the span of data sets available to us is very limited. In the effects section of this paper we will derive our effects relations from some of the open literature papers available (e.g., Ref. 3).

We conclude this paper with estimates of three example tactical scenarios using seven sources from the literature to draw some conclusions about the effectiveness of those sources in a tactical environment. Because of the limited effects data, the errors in our conclusions will be large but useful in explaining the process.

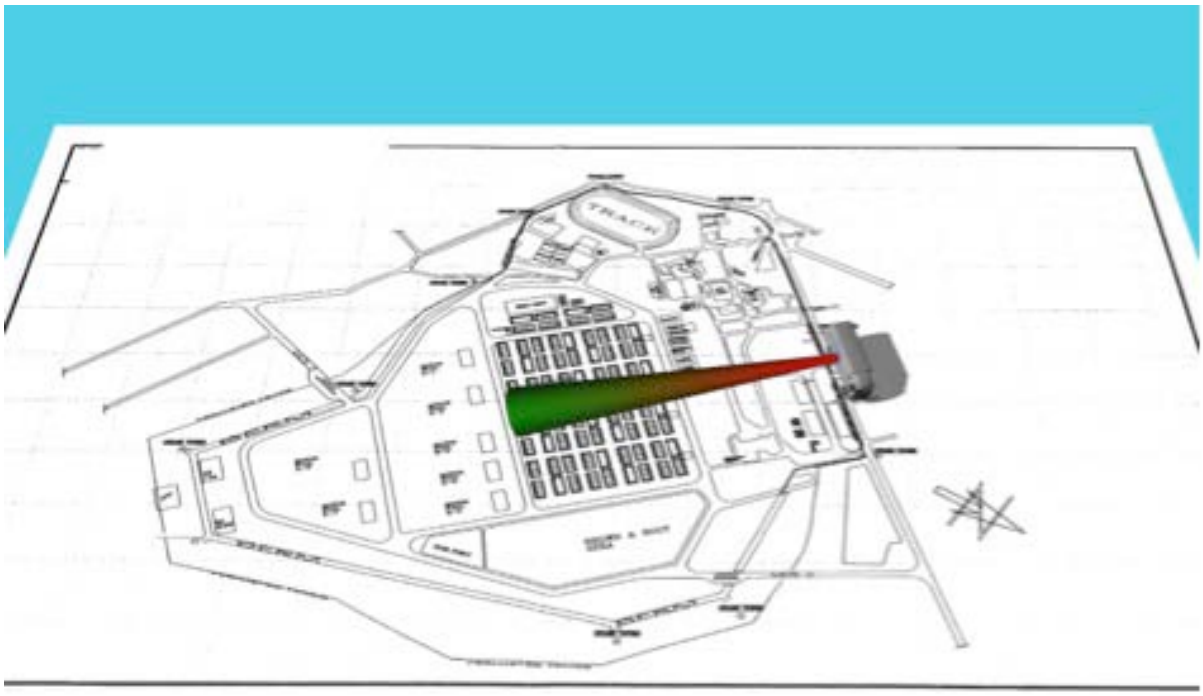

Figure 2: Truck Mounted HPM Scenario

REFERENCES

1. Benford, J., J. A. Swegle and E. Schamiloglu, *High Power Microwaves, 2nd ed.,* Taylor and Francis, 2007. *Book Title*, Wiley-Interscience, New York, 1986.
2. Lee, K.S. H., ed., *EMP Interaction: Principles, Techniques and Reference Data*, Hemisphere, 1986.
3. Nitsch, J. and F. Sabath, "Equipment Susceptibility", Plenary Lecture, American Electromagnetics Meeting, Albuquerque, NM USA, 2006.

Metamaterials Technology to Improve Microwave Devices for Electromagnetic Compatibility Test

H. X. Araujo[1,2]**, and L. C. Kretly**[2]
[1]Federal University of Sao Joao Del Rei, Brazil
[2]University of Campinas, State of Sao Paulo, Brazil
hxaraujo@ufsj.edu.br

Abstract - In this work, three metamaterial structures are applied to a GTEM – *Gigahertz Transverse Electromagnetic Chamber* to improve and give flexibility to its frequency response. The main goal is to achieve a better frequency resonance regardless the dimensions of the original chamber. Therefore, a comparison between the CLL – *Capacitively Loaded Loop*, Fractal and Jerusalem – Cross – Pair metamaterial technology for these purposes, is done. Experimental results are compared to the simulated ones.

The concept of the metamaterial technology, was approached in the late 90's with a work about macroscopic composites with synthetic and periodic cellular architecture. However, the first attempt to explore the concept of "artificial" materials was in 1898 with Jagadis Chunder Bose by his experiment about twisted structures [1]. Later, in 1914, the work about artificial chiral media was done by Lindman [2]. After these, in the past 20 years, the interest on metamaterial technology had strong increased, with researches on superlens and telecommunication environment, including transmission lines and antennas applications [3], and now to improve the performance of microwave devices for electromagnetic compatibility [4].

Actually, metamaterial is a macroscopic composite of periodic or non-periodic structure, whose function is due to both the cellular architecture and the chemical composition [5]. Therefore, the behavior of a material, in the presence of an electric field, is determined by the macroscopic parameters, permittivity ε and permeability μ.

In this context, to improve a performance of the GTEM chamber designed in [6], in terms of frequency response or to tune the chamber in a frequency range of interest, in order to obtain more realistic results, the metamaterial cells were applied to the internal conductor. The basic structures are composed by the RR – *Ring Resonator* or CLL – *Capacitively Loaded Loop*, fractal cells, and the *Jerusalem-Cross-Pair* topology. The current surface distribution of the three applied structures can be seen in Fig. 1. Moreover, periodic structures as *Ring Slot Resonators* can be considered as reconfigurable antennas when properly arranged [5]. It is important to emphasize that when the metamaterials standards are applied in metals or metallic structures, the cells are not additive layers, as when applied in dielectric materials. In this case, the metamaterial cells are holes printed on the metallic layer. Simulated and experimental results are compared to demonstrate the potential of this new approach. In Fig. 2 is shown some preliminary results.

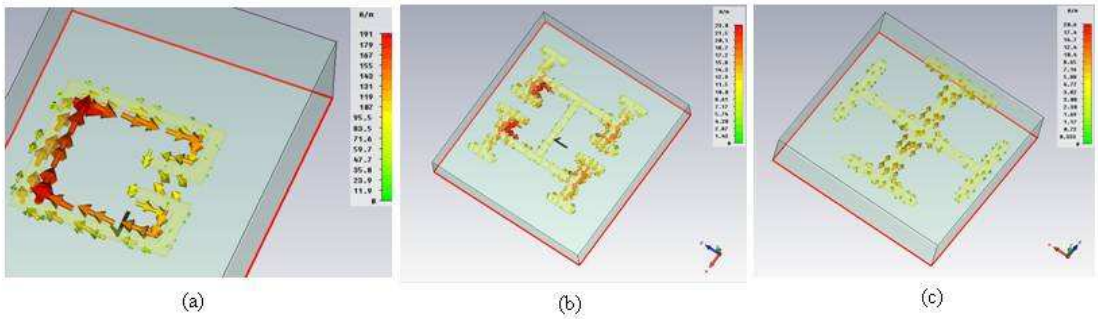

Figure 1. Surface Current distribution of an unitary metamaterial cell: (a) CLL cell; (b) Fractal cell; (c) Jerusalem cross pair cell.

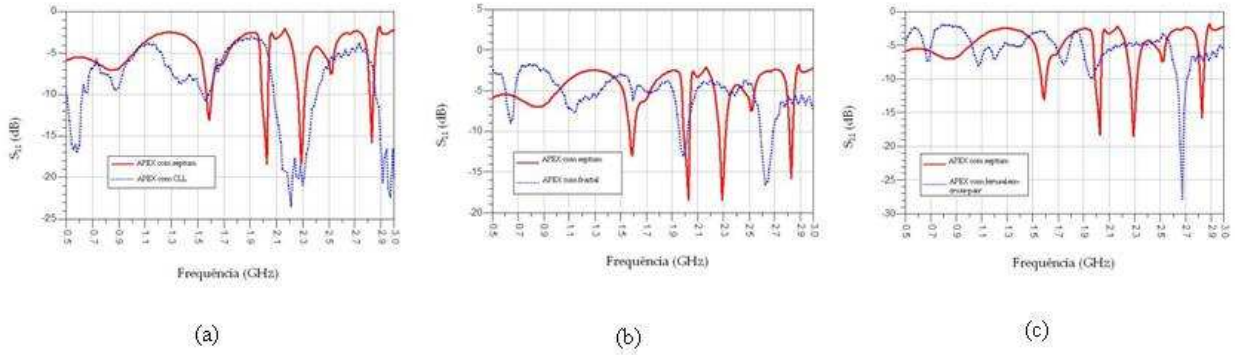

Figure 2. Return loss parameter: (a) CLL cell; (b) Fractal cell; (c) Jerusalem–Cross–Pair cell.

REFERENCES

1. Bose, J. C.. "On the rotation of plane of polarization of electric waves by a twisted structure," *Proc. Roy. Soc*., vol. 63, pp. 146-152, 1898.
2. Lindell, I. V., A. H. Sihvola and J. Kurkijarvi, "Karl F. Lindman: The last Hertzian, and a Harbinger of electromagnetic chirality," *IEEE Antennas Propag. Mag*., vol. 34, n. 3, pp. 24-30, 1992.
3. Cui, T. J., "Electromagnetic Metamaterials: Recent advances on the theory, experiments, and applications," *IEEE Antennas Propag. Mag*., 2008.
4. H. X. Araujo and L. C. Kretly, "The Effect of Metamaterial Patterning to Improve the Septum GTEM Chamber Performance", 29th Progress in Electromagnetics Research Symposium, Marrakesh, Morooco, 2011.
5. Cui, T. J., D. V. Smith and R. Liu, *Metamaterials:Theory, Design and Applications*, Springer, New York, 2010.
6. H. X. Araujo and L. C. Kretly, "An EM Simulation and Design a GTEM Chamber for EMC Pre-Compliance Tests on Electronic Board and ICs in 500 MHz – 18 GHz Range", Momag 2010, Vila Velha, Brazil, August, 2010.
7. Erentok, A, P. Luljak and R. W. Ziolkowski (editors), "Antenna performance near a volumetric metamaterial realization of an artificial magnetic conductor," *IEEE Trans. Antennas Propagat.*, Vol. 53, 160–172, 2005.
8. H. X. Araujo and L. C. Kretly, "Metamaterial Patterning to Improve the Septum of a GTEM Chamber Performance: Ring Resonator Cells Stamped and Tested on the APEX", IEEE Symposium on Product Compliance Engineering, San Diego ,USA, 2011.

Development of A Bounded-wave EMP Simulator and Applications

Yan-zhao XIE, Jun GUO, Xu KONG, Ke-jie LI
State Key Laboratory of Electrical Insulation and Power Equipment
School of Electrical Engineering, Xi'an Jiaotong University
yanzhao.xie@gmail.com

Abstract- An asymmetrical bounded-wave EMP simulator has been constructed. The design and the main parameters of this simulator are presented and discussed. The measured E-field waveform showed that this simulator may provide good uniform field inside the working volume for the calibration of transient E-field sensor and the validation of transmission line model

Depending upon different purposes, e.g. EMP effects experiments, calibration of the sensor or validation of transmission line model, etc, there exists many ways to simulate transient E-field. For the purpose of calibration and validation, we need a transient E-field with uniform working volume as a standard. Generally speaking, transverse electromagnetic (TEM) Cell or Gigahertz Transverse Electromagnetic (GTEM) Cell is capable of producing uniform electromagnetic field. However it is a little bit more difficult than other ways to produce EMP field with very large field intensity (at least 50kV/m) due to the limited insulation distance at the input port. Therefore, the bounded-wave simulator, which has the advantages of providing a more uniform and precisely controllable environment compared to the radiating-wave simulator, was selected to fulfill this requirement.

More recently, an asymmetrical flat-plate bounded-wave EMP simulator with distributed terminators was designed and constructed in Xi'an Jiaotong University. Fig.1 shows a photograph of this simulator, which can simulate transient waveforms of IEC61000-2-9 [1], Bell Laboratory and some other double exponential waveforms to simulate the discharges in gas insulated substation (GIS) when being energized by corresponding transient pulse source.

Fig.1 Photograph of EMP simulator in Xi'an Jiaotong University

The volume between two plates is 3m (long)×2m (wide)×1m (high). The performance of the simulator was optimized by the ways of extending the length of front transition section, widening the bottom plate to adjust the characteristic impedance and employing the distributed terminator, etc. These improvements allowed obtaining a good E-field shape and uniformity inside the working volume. The distributed terminator consists of 6 parallel resistor strings. Each resistive chain has three non-inductive resistors with a total value of 600Ω, connected with the corresponding taper of the top and the bottom plate. The width of each taper was calculated according to the approach presented in [2]. Each width is different so that it can carry equal current.

This simulator could produce the uniform E-field for the calibration of transient E-field sensor. The transient

E-field sensor consists of a monopole, matching circuit, laser modulated circuit and fiber-optic link, etc. Fig.2 shows the photograph of the sensor.

Fig. 2 Photograph of the transient E-field sensor

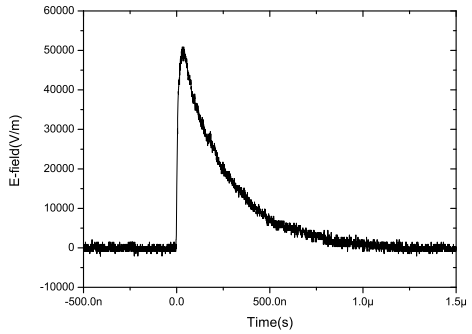

Fig. 3 The measured EMP waveform inside the EMP simulator

Fig.3 shows the measured EMP waveform with the rise time of 3ns, which shows that the newly fabricated EMP simulator could produce very uniform E-field and the transient E-field sensor works very well. The sensitivity, the dynamic range and the linearity of the measurement system could be calibrated by this EMP simulator.

This work is supported by State Key Laboratory of Electrical Insulation and Power Equipment (EIPE 11110) and National Natural Science Foundation of China (51277148).

REFERENCES

1. IEC 61000-2-9, Electromagnetic compatibility (EMC) – Part 2-9: Environment –*Description of HEMP environment - Radiated disturbance*
2. D. V. Giri, Design Guidelines for Flat-Plate Conical Guided-Wave EMP Simulators With Distributed Terminators, Sensor and Simulation Notes, Note 402, 1996

Enhancement of solar cell efficiency using 1D photonic crystal

Asma Ouanoughi[1], **Abdesselam Hocini**[2*]

[1]Laboratoire d'Analyse des Signaux et Systèmes BP.166, Route Ichebilia, Université de M'sila, M'sila 28000, Algeria

[2] Département d'Electronique BP.166, Route Ichebilia, Université de M'sila, M'sila 28000, Algeria

[*]corresponding author: hocini74@yahoo.fr

Abstract-In this work, we design via numerical simulation the geometry of solar cell made by 1D photonic crystal in order to enhance the absorption. We investigated the performance of the considered structure and determined the geometrical parameters (lattice and filling factor) that allow a better absorption. The obtained results show that the absorption in the patterned structure is increased considerably compared to the unpatterned layer.

One of the main challenges for a thin film solar cell is how to confine the incident light into such thin layers of semiconductor, such as amorphous-, poly- and mono-crystalline Si. Photonic Crystals (PCs)[1]. Design and simulation become very important before fabrication; in order to design a thin film solar cell, the first step was to investigate the absorption characteristics due to its geometry. Based on others previous works [1-3] for designing a-Si:H photonic devices, the software Rsoft based on FDTD method [4], has been used to study the influence of the geometrical parameters for the 1D photonic crystal on the absorption. The filling factor was fixed at 59%, the thickness at 100nm and a series of simulations for different values of period L=0.320µm, L=0.335µm and L=0.350µm are studied to determine the absorption, and we also calculate the absorption in the unpatterned layer with the same thickness.

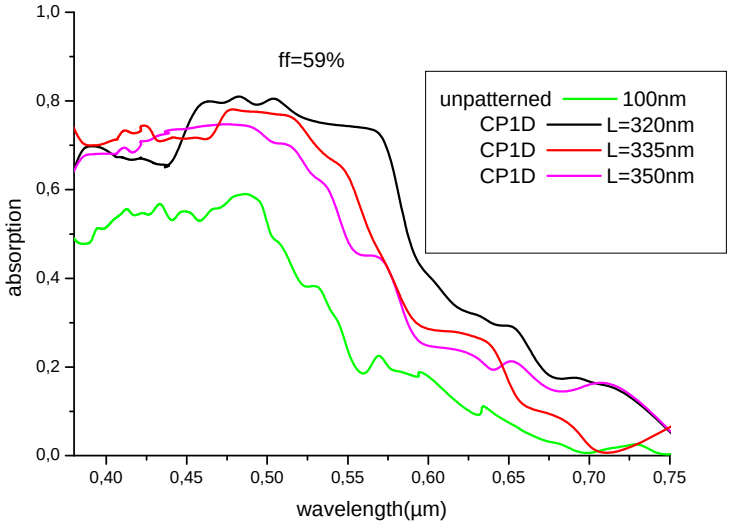

Figure 1: Absorption spectra of the 1D PPC structure , with a fixed filling factor of 59% and for different values of period L=0.320µm, L=0.335µm, L=0.350µm and an unpatterned layer with the same thickness.

Figure 1 shows the absorption as a function of wavelength on the front surface for the different values of period L. It is clear that as the value of period (L) increases, the absorption spectra decreases. In the other hand we can observe that the 1D PC structures absorb the incident light better than unpatterned layer.

REFERENCES

1. Meng, Xianqin; Depauw, Valerie; Gomard, Guillaume; El Daif, Ounsi; Trompoukis, Christos; Drouard, Emmanuel; Jamois, Cécile; Fave, Alain; Dross, Frederic; Gordon, Ivan; Seassal, Christian "Absorbing photonic crystals for mono-crystalline silicon thin film solar cells"SPIE, Volume 8425, pp. 84250R-84250R-9, 2012.
2. Ounsi El Daif1, Emmanuel Drouard, Guillaume Gomard, Anne Kaminski, Alain Fave, Mustapha Lemiti, Sungmo Ahn, Sihan Kim, Pere Roca i Cabarrocas, Heonsu Jeon, Christian Seassa, 'Absorbing one-dimensional planar photonic crystal for amorphous silicon solar cell' Optics Express, Vol. 18, Issue S3, pp. A293-A299, 2010.
3. Guillaume Gomard, Emmanuel Drouard, Xavier Letartre, Xianqin Meng, Anne Kaminski,Alain Fave, Mustapha Lemiti, Enric Garcia-Caurel,3and Christian Seassal''tow-dimensional photonic crystal for absorption enhancement in hydrogenated amorphous silicon thin film solar cells'', J. Appl. Phys. 108, 123102, 2010.
4. RSoft Design Group, FullWAVE, Inc. 200 Executive Blvd. Ossining, NY 10562.

Finite element formulation for dispersion analysis of metamaterials

D. A. Ketzaki, E. E. Kriezis, and T. V. Yioultsis*

Dept. of Electrical and Computer Engineering, Aristotle University of Thessaloniki, Greece

*corresponding author: traianos@auth.gr

Abstract-A finite element formulation for the dispersion analysis and parameter characterization of metamaterials is presented. The computational procedure is based on a reformulation of the eigenvalue problem that is capable of dealing with lossy materials and the computation of evanescent modes, resulting in a linear eigensolver and a rigorous metamaterial parameter extraction, based entirely on the dispersion diagram.

The numerical simulation of electromagnetic fields in periodic structures, such as metamaterials or photonic crystals, has drawn significant attention over the last years. Among several methods which have been suggested towards this direction, dispersion analysis has been a useful tool for understanding the main features of these periodic formations. The conventional analysis of determining the eigemodes of such structures has been reformulated and expanded to include evanescent or, in general, complex modes, on the basis of a linear eigensolver approach [1]. Following this rationale, the eigenmodes are calculated by specifying frequency (k_0) and solving the dispersion equation for its complex solutions of the propagation vector ($\gamma=\alpha+i\beta$). In this way, both band diagrams (k-β) and attenuation diagrams (k-α) can be obtained enabling a thorough investigation of the periodic structure.

In this work, the Finite Element Method (FEM) is used, with a procedure similar to [2], [3], in order to simulate several metamaterial configurations and compute their eigenmodes. This complex propagation vector calculation could comprise the basis of a characterization procedure for the periodic structures relevant to their constitutive parameters, which would be a challenging perspective for the case of metamaterial or photonic crystal structures. Proper extensions to correctly identify the modes of the structure, including backpropagating waves, associated to negative-index equivalent material parameters are introduced. The overall parameter retrieval is, then, based entirely on the dispersion relations that fully capture the metamaterial's behavior, being able to include and characterize anisotropic properties.

Validation of the proposed approach is performed by analyzing a repeated pattern of two infinite layers of known materials (Fig. 1) showing a perfect match of the eigenvalue computation to the analytical solution.

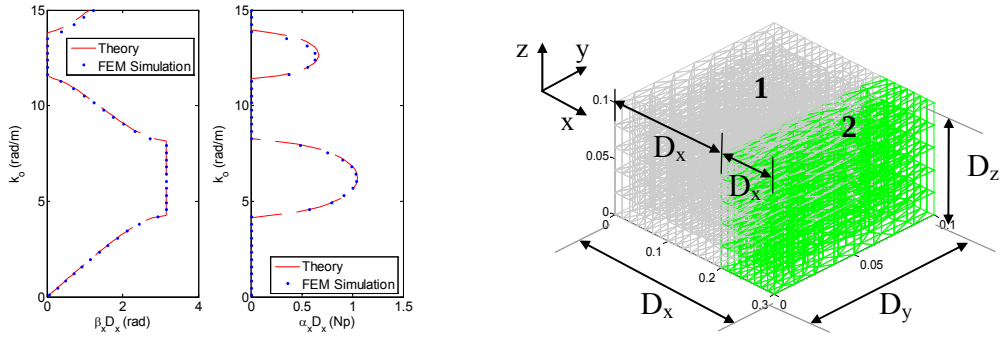

(a) (b)

Figure 1. Complex propagation constant (a) Imaginary and real part. (b) Configuration structure: Repeated pattern of two infinite layers.

Next, a similar process has been followed to analyze a periodic array of infinitely long metal rods, forming the basis of a negative-epsilon metamaterial (Fig.2) and also a periodic array of metal cubes (Fig. 3). Periodic (continuity or Floquet) boundary conditions are properly imposed. Eigenmodes have been calculated for both configurations, signifying their ability to support both propagating (including backward) and evanescent modes.

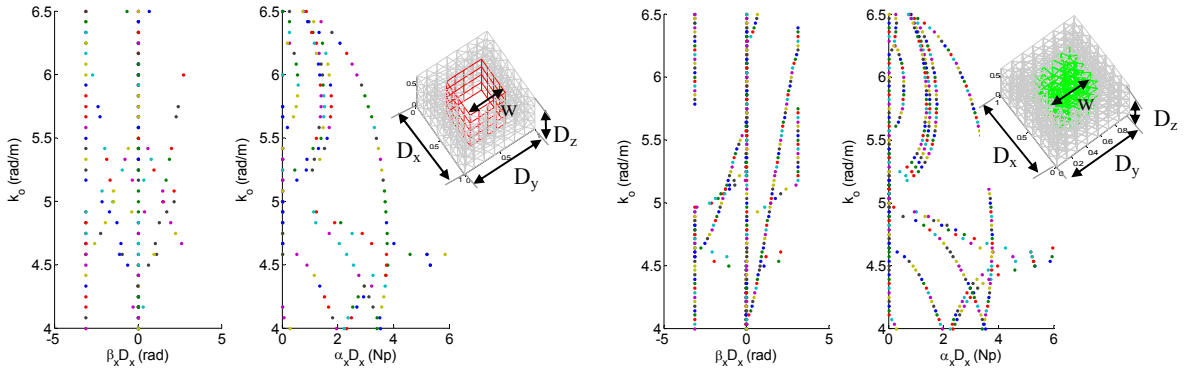

(c) (d)

Figure 2. Imaginary and real part of complex propagation constant for (a) perfectly conducting metal rods. (b) lossy material metal rods.

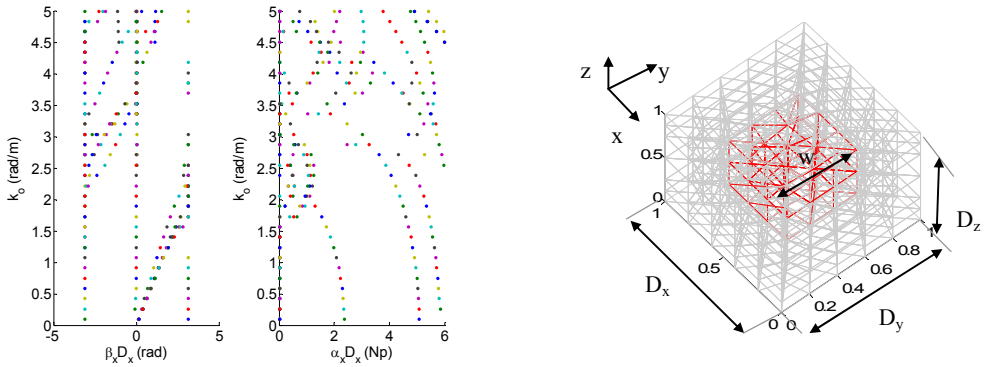

(a) (b)

Figure 3. Complex propagation constant (a) Imaginary and real part. (b) Configuration structure: Lossy material metal cubes.

Acknowledgement: This research has been co-financed by the European Union (European Social Fund - ESF) and Greek national funds through the Operational Program ”Education and Lifelong Learning” of the National Strategic Reference Framework (NSRF) - Research Funding Program: THALES: Reinforcement of the interdisciplinary and/or inter-institutional research and innovation (Project ANEMOS).

REFERENCES

1. Tavallaee, A. A. and Webb J. P.,“Finite-Element Modeling of Evanescent Modes in the Stopband of Periodic Structures,” *IEEE Trans. Magnetics*, Vol. 44, No. 6, 1358–1361, 2008.
2. Bostani, A. and Webb J. P., “A Sparse Finite-Element Method for Modeling Evanescent Modes in the Stopband of Periodic Structures,” *IEEE Trans. Magnetics*, Vol. 47, No. 5, 1186–1189, 2011.
3. Bostani, A. and. Webb J. P, “Finite-Element Eigenvalue Analysis of Propagating and Evanescent Modes in 3-D Periodic Structures Using Model-Order Reduction,” *IEEE Trans. Microw. Theory Tech.*, Vol. 60, No. 9, 2677–2683, 2012.

Wearable and Flexible Antennas, By A. Shamim

Inkjet-printed Flexible RFID Tag for Wearable Applications

Sangkil Kim[1*], **Benjamin Cook**[1], **and Manos M. Tentzeris**[1]
[1]Georgia Institute of Technology, USA
[*] ksangkil3@gatech.edu

Abstract- In this paper, an inkjet-printed UHF RFID tag for wearable applications is demonstrated on a new flexible synthetic and environmentally friendly Teslin paper substrate. First, the RF characteristics of the Teslin substrate are investigated by using the microstrip ring resonator in order to characterize the relative permittivity (ε_r) and loss tangent ($\tan\delta$) of the substrate from L band to C band (0.9 GHz ~ 6.3 GHz). A flexible UHF RFID tag is then designed with the inkjet-printing technology and its flexibility is investigated.

I. Introduction

Inkjet-printed wearable electronics on flexible substrates such as a paper have been investigated by many researchers [1-3]. However, standard cellulose paper is not compatible with high temperature sintering processes used for annealing silver nano-particles which results loss of flexibility and cracking [3]. In this paper, the electrical properties of flexible synthetic Teslin paper are going to be characterized and a flexible RFID tag utilizing the new substrate is demonstrated.

II. Substrate Characterization

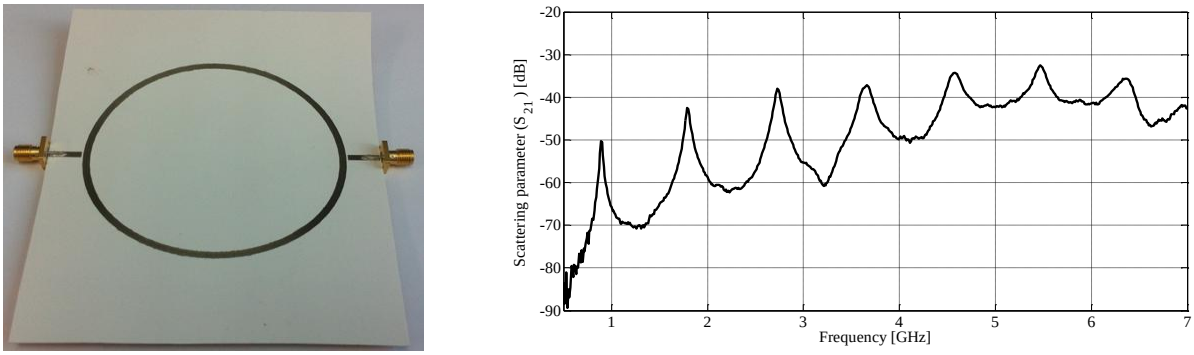

(a) (b)

Figure 1. (a) Fabricated ring resonator and (b) measured S_{21}

Teslin, is a flexible and waterproof printing medium for inkjet, laser, and aerosol jet printing. This material is an excellent substrate for wearable RF applications since it is petroleum-free meaning non-toxic, recyclable, and environmentally friendly [4]. It is widely used in the production of ID and security cards, however, its high frequency characteristic have yet to be characterized. An inkjet-printed ring resonator is fabricated on a Teslin substrate (figure 1(a)), and its RF properties including relative dielectric constant (ε_r) and loss tangent ($\tan\delta$) are derived from the scattering parameter (S_{21}) as shown in figure 1(b).

III. RFID Tag Design

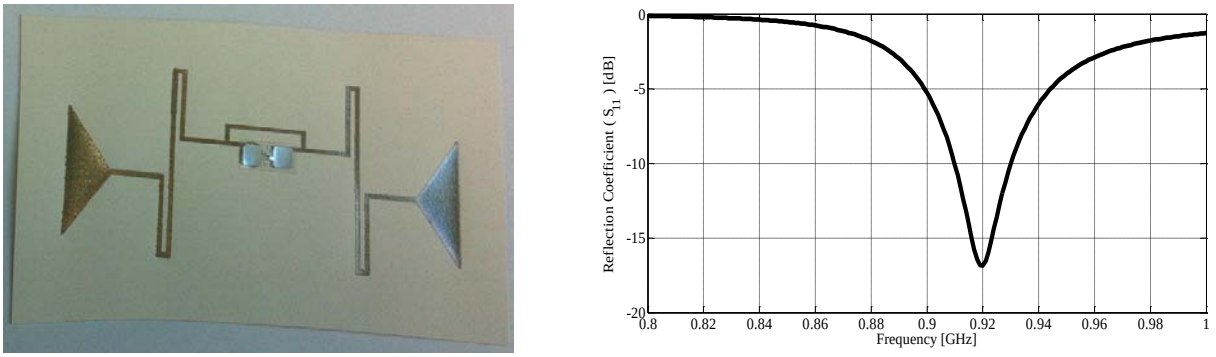

(a) (b)

Figure 2. (a) Fabricated RFID tag and (b) simulated reflection coefficient (S_{11})

Based on the measured electrical properties of the Teslin, a bowtie RFID tag for UHF band is designed and fabricated as shown in figure 2(a). The demand for flexible RFID tags has rapidly increased due to the current trends in inventory management and bio-medical monitoring [5]. The flexibility is an especially important factor for wearable applications when printed conductors are involved, and the reduction of cracking due to deformation will be investigated. The simulated reflection coefficient (S_{11}) is shown in figure 2(b) and required power for RFID chip excitation will be presented according to curvature of the RFID tag.

IV. Conclusion

The electrical characteristics of a synthetic paper, Teslin, are going to be investigated by the ring resonator method in the wide frequency band (0.9 GHz ~ 6.3 GHz) using inkjet printing technology. A flexible inkjet-printed RFID tag has been designed and its frequency response and structural properties will be investigated according to bending radius.

Acknowledgements

This work was supported by SRC/IFC and NSF-ECS-0801798.

REFERENCES

1. Cook. B., and Shmim, A, “Inkjet Printing of Novel Wideband and High Gain Antennas on Low-Cost Paper Substrate,” *IEEE Trans. Ant. Prop.*, 2012, 60, p4148-4156
2. Basiricò, L., P. Cosseddu, B. Fraboni, and A. Bonfiglio, “Inkjet printing of transparent, flexible, organic transistors,” *Thin Solid Films*, 2011, 520, (4), pp. 1291-1294
3. Yang, L., A. Rida, R. Vyas, and M.M. Tentzeris, "RFID Tag and RF Structures on a Paper Substrate Using Inkjet-Printing Technology," *IEEE Trans. Microw. Theory Tech*, vol.55, no.12, pp.2894-2901, Dec. 2007.
4. [Online] Available: https://www.duracard.com/LearningCenter/cards-made-of.aspx
5. Yang, L., S. Basat, A. Rida, and M. M. Tentzeris, “Design and development of novel miniaturized UHF RFID tags on ultra-low-cost paper-based substrates,” in Proc. Asia–Pacific Microw. Conf., Yokohama, Japan, Dec. 2006, pp. 1493–1496.

A Novel Wideband Inkjet Printed Antenna for Future Flexible Devices

Hattan F. Abutarboush[1], **and Atif Shamim**[1]

Department of Computer, Electrical and Mathematical Sciences and Engineering (CEMSE), King Abdullah University of Science and Technology (KAUST), Thuwal 23955-6900, Saudi Arabia.

Hattan.Abutarboush@ieee.org

Abstract- A low cost inkjet printed multiband monopole antenna is presented. The antenna shows a planar structure with a total size of 40 x 40 mm^2 making it especially suitable for small devices. In addition, since the antenna is built on a paper substrate, it can be flexed with different curves. The antenna is suitable for future flexible mobile phone devices serving the Personal Communication System (PCS), Digital Communication Systems (DCS), Global System for Mobile Communications (GSM1800) and (GSM 1900), Universal Mobile Telecommunications System (UMTS), Wireless Local Area Networks (2.4, 5.2 GHz WLAN), and Worldwide Interoperability for Microwave Access (WiMAX) band I, band II and band III

I. Introduction

Recently, there has been much interest in developing a system with the ability to integrate more than one communication standard for enhancing performances. One interesting candidate is the inkjet printed planar antenna. The cost, size and weight of the antenna are important for the antenna to be practical. These characteristics can be achieved by using cheap organic substrates such as paper or polymers and by employing low cost fabrication methods such as inkjet printing [1]. Inkjet printing can be used on different substrates by depositing almost any material that can be put into liquid form. Inkjet-printing is a direct-write technology where the layout of the structure is printed directly on the paper or the substrate whereas the other fabrication methods require expensive masks and etching processes. Inkjet printing on substrates such as paper can be run reel to reel or roll to roll making the fabrication more cost effective for mass production as compared to wafer by wafer processing. Different inkjet printed antennas have been reported recently for Tri-Band [2] and UWB [3].

II. Design layout

The structure of the proposed antenna consists of branch lines, a 50-Ω microstrip feedline and a ground plane with L slots as shown in Fig. 1. It is designed on a paper substrate with an overall area of 30 × 40 mm^2, a thickness of 0.44mm, a dielectric constant of 3.2 and a loss tangent of 0.05 [1]. The branched lines are designed to generate two low frequency bands and one high frequency band while the L slots are cut on the ground plane to create another current path to excite three narrow bands. The design of the antenna is optimised using the high-frequency simulation software (HFSS).

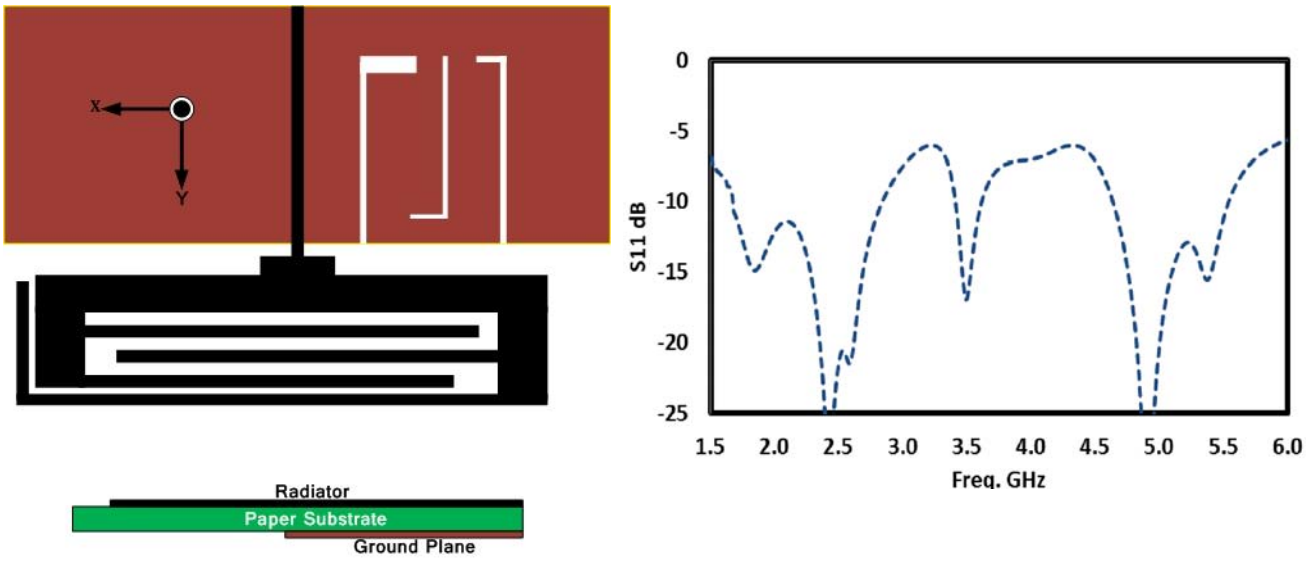

(a) (b)

Figure 1: (a) Layout of proposed antenna and (b) S11 of proposed antenna

III. Results

A prototype of the final designed antenna, Antenna #4, has been constructed and tested. The simulated and measured S_{11} are shown in Fig. 1(b). Six measured distinct resonant modes at 1.95, 2.4, 2.7, 3.5, 4.7 and 5.2 GHz are excited. The first three bands at 1.95, 2.4 and 2.7 are formed a wide bandwidth and another narrow band at 3.5 GHz. The last two bands at 4.7 and 5.2 GHz are formed as a wide bandwidth. The simulated bandwidths of the antenna are 25% (1.7 – 2.8 GHZ), 23% (3.4 – 3.6 GHz) and 55% (4.6 – 5.8 GHz). Thus, the proposed antenna is suitable for Personal Communication System (PCS), Digital Communication Systems (DCS), Global System for Mobile Communications (GSM1800) and (GSM 1900), Universal Mobile Telecommunications System (UMTS), Wireless Local Area Networks (2.4, 5.2 GHz WLAN), and Worldwide Interoperability for Microwave Access (WiMAX) band I, band II and band III.

REFERENCES

1. B. Cook and A. Shamim, “Inkjet printing of novel wideband and high gain antennas on low-cost paper substrate,” IEEE Transaction Antennas Propagations, vol. 60, no. 9, pp. 4148–4156, Sep. 2012.
2. H. F. Abutarboush, A. Shamim, "Paper-Based Inkjet Printed Tri-Band U-Slot Monopole Antenna for Wireless Applications," IEEE Antennas and Wireless Propagation Letters (AWPL), accepted, September 2012
3. A. R. Maza, B. S. Cook, J. Ghassan, A. Shamim, “Paper-Based Inkjet Printed UWB Fractal Antennas,” IET Microwaves Antennas and Propagation, Vol. 6, no. 12, pp.1366–1373, October 2012.

Design of LCP based Flexible Patch Antenna Array

A. A. Hamdoun[1], F. A. Ghaffar[2*], A. Shamim[2] and L. Roy[1]
[1]Department of Electronics, Carleton University, Canada
[2]Electrical Engineering Program, KAUST, Saudi Arabia
[*]corresponding author: farhan.ghaffar@kaust.edu.sa

Abstract- A fully characterized 38 GHz flexible two element patch antenna array realized on LCP is presented. A single LCP layer is used to maximize flexibility, allowing wrapping in the E and H planes. Measured and simulated results show relatively small degradation of the gain and radiation performance with wrapping, and a clear advantage of H plane plane bending versus E plane bending. The design is highly suitable for wearable and flexible applications.

Introduction –Flexible antennas have gathered significant attention in the past decade [1]. With the advent of commercial products such as smart tags and flexible displays, there has been considerable progress in this field [2]. Such products require low loss and flexible substrates to maintain their functional capabilities. One flexible substrate is Liquid Crystal Polymer (LCP), which has been used by several designers to demonstrate high performance and efficient antennas. A tapered slot antenna has been studied in [3] to show its potential for conformal applications. In [4], we have demonstrated the concept of a two element patch antenna array with simulated results for wrapping of the array in its two principal planes. This work furthers [4], by presenting the measured results of the design and explaining the shift observed in the center frequency of the patch antenna when flexed.

Two Element Array Design:

Design and Simulation: A single layer of LCP is inherently flexible and can be used for designing high performance passive microwave circuits. However, increasing the number of layers can significantly limit elasticity. In this work the same single layer LCP patch antenna design has been pursued as reported in [4]. However here we report the measured results of the design.

The array is then bent in the H and E planes to study the effect on gain and impedance. It is observed that bending the antenna in the E plane causes its center frequency to shift by 3.5 GHz, as opposed to a shift of merely 400 MHz for H plane bending. To understand this behavior, surface currents on the patch are plotted using HFSS as shown in Fig. 1. The different current distributions reveal why the antenna is more affected in one case than the other. With H plane wrapping (Fig. 1(a)) the currents remain essentially longitudinally directed, as for a conventional planar patch. With E plane wrapping (Fig. 1(b)), the currents have significant transverse components due to a longer effective patch length and greater perturbation of the original resonance condition. Despite the shift in frequency the gain performance of the design is consistent in all three cases as can be observed in table I.

Fabrication and Measurement: The array has been fabricated using in-house facilities. Due to technical limitations, some dimensional discrepancies existed compared to the original design. However these changes did not affect the antenna performance significantly. The fabricated array is shown in Fig. 1(c) and 1(d). For the planar case, impedance measurements could be done using both Ground Signal Ground (GSG) probe and SMA connector; however, to allow array wrapping and radiation pattern measurements, a 3.5 mm SMA connector (rated only up to 26.5 GHz) was used to characterize the antenna. The measurement results generally agree well with simulations. The measured shifts in frequency are similar to the simulated shifts. However the measured gains are considerably lower

than the simulated values. This difference can be attributed to the connector loss at 38 GHz. Indeed, as verified by impedance measurements, the return loss never goes below 5 dB showing the inefficient performance of the connector at such high frequencies. The measured impedance performance of the array is shown in Fig. 2.

TABLE I. Two Element Antenna Array Performance

Design	Simulated Results (no connector)			Measured Results (with connector)		
	Frequency (GHz)	Gain (dB)	Bandwidth (MHz)	Frequency (GHz)	Gain (dB)	Bandwidth (MHz)
Planar Array	38	8.5	710	37.4	5.0	580
Wrapped around E Plane	34.5	7.4	850	34.7	3.9	710
Wrapped around H Plane	37.6	7.1	1050	37.3	4.1	800

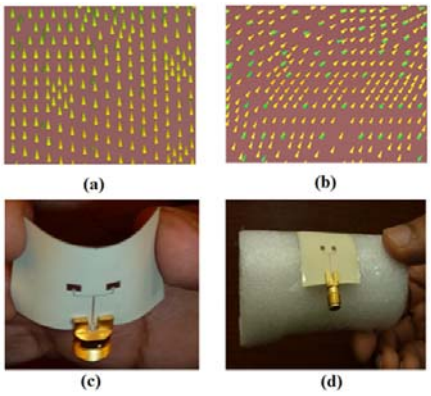

Figure 1: Top - Current distribution for (a) H Plane bending and (b) E Plane Bending . Bottom - Fabricated Array (c) wrapped in H plane and (d) wrapped in E plane.

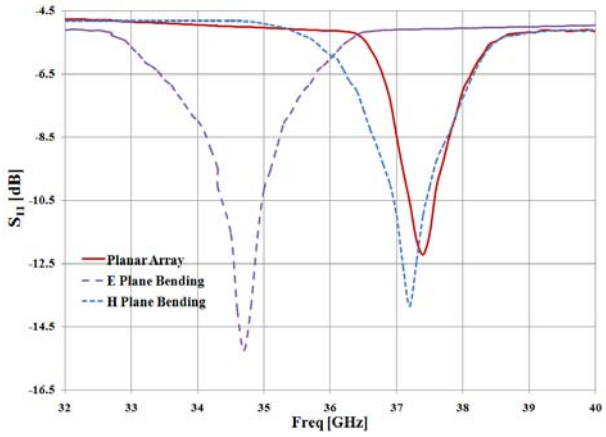

Figure 2: Measured Impedance Performance of the antenna array

Four Element Array Design: The results above demonstrate efficient performance of LCP as a substrate for flexible antenna designs. Further enhancements in antenna performance (gain, bandwidth, tolerance to bending) can be obtained by increasing the number of array elements. To this end, the authors have designed a four element array with an impedance bandwidth of 2.6 % and a gain of 10.1 dB. The antenna is under study for its performance when wrapped around a cylinder in its two principal planes.

Conclusion: The paper reports the performance of a LCP based patch antenna array when flexed in its principal planes. The study shows that wrapping in the H plane induces a smaller center frequency shift compared to wrapping in the E plane. Overall, the results demonstrate that LCP is highly suitable for flexible antenna designs.

REFERENCES

1. G. DeJean, et. al., “Liquid Crystal Polymer (LCP): A new organic material for the development of multilayer dual frequency/dual polarization flexible antenna arrays”, IEEE Antennas and Wireless Propagation Letters, vol. 4, 2005.
2. C. P. Lin, et. al., “Development of a flexible SU-8/PDMS based antenna”, IEEE Antennas and Wireless Propagation Letters, vol. 10, 2011.
3. S. Nikolaou, et. al., “Conformal Double Exponentially Tapered Slot Antenna (DETSA) on LCP for UWB Applications”, IEEE Transactions on Antennas and Propagation, vol.54, no. 6, pp. 1663-1669, 2006.
4. F. A Ghaffar, et. al., "Study of LCP based flexible patch antenna array", IEEE International Symposium on *Antennas and Propagation Society (APSURSI), 2012.*

Inkjet Printed Circularly Polarized Monopole Antenna on Paper for GPS Applications

M. F. Farooqui[1*], and A. Shamim[1]
[1]King Abdullah University of Science and Technology, Saudi Arabia
[*]corresponding author: muhammad.farooqui@kaust.edu.sa

Abstract-A novel inkjet printed monopole antenna on paper substrate is presented for GPS applications. Circular polarization is achieved by introducing an L-shaped slit in the rectangle monopole structure. The simulation results show a maximum gain of 1.2 dBi at 1.575 GHz with 3dB axial ratio bandwidth of 2%. The overall dimensions of the antenna are 67 mm x 60 mm x 0.9 mm.

The applications of global position system (GPS) are expanding with smart phones, automobiles, wrist watches etc. being increasingly equipped with GPS. GPS signals are right hand circularly polarized (RHCP). Circularly polarized (CP) waves are immune to antenna misalignment errors and are more robust to adverse weather conditions compared to linearly polarized waves, hence they are used in radars and satellites including GPS. Circular polarization is achieved by exciting two orthogonal field components having equal magnitude and 90 degrees phase difference. The two orthogonal components are usually excited by introducing a perturbation or asymmetry in the antenna structure. Few CP monopole antenna designs have been reported including an asymmetric fed monopole [1], circular patch monopole with orthogonal slits [2] and asymmetric y-shaped monopole [3]. Monopole design is attractive for organic substrates such as paper as the antenna performance is not affected much by the lossy substrate.

In this paper, a novel circularly polarized monopole antenna for GPS applications is proposed. Circular polarization is achieved by introducing L-shaped slit in the rectangle patch monopole structure. The antennas are inkjet printed on a four layer thick paper substrate with thickness of 880 μm and dielectric constant of 3.2 using Dimatix® 2831 materials printer. Inkjet printing offers advantage over conventional fabrication techniques like

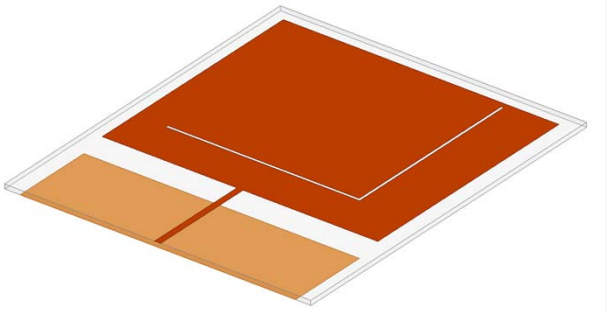

Figure 1. Proposed GPS antenna model.

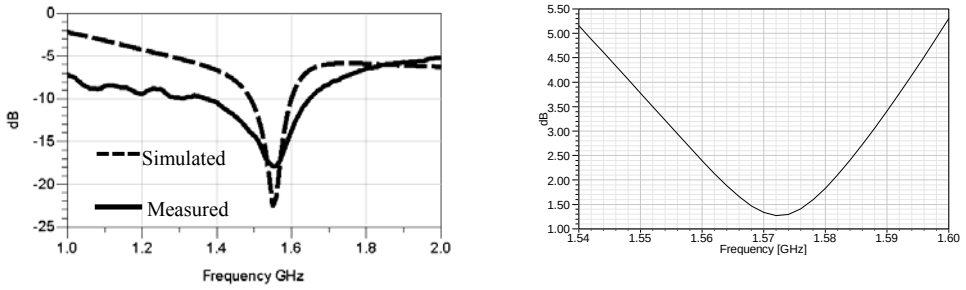

(a) (b)

Figure 2. (a) Simulated and measured return loss and (b) simulated axial ratio.

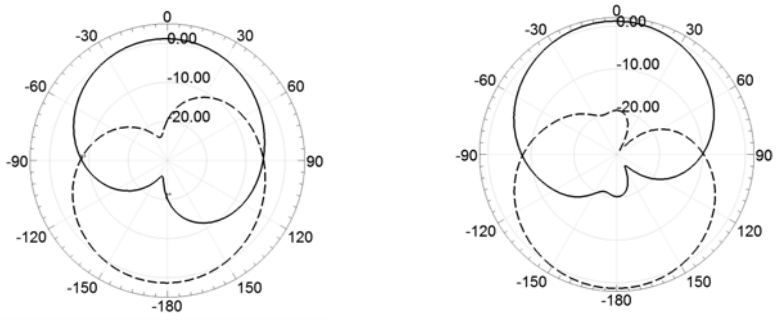

(a) (b)

Figure 3. Simulated radiation pattern. RHCP(solid) and LHCP(dashed). (a) xz- plane (b) yz-plane.

lithography and milling with low cost roll-to-roll mass fabrication and ability to fabricate on variety of flexible substrates like paper and polymers for wearable applications

The proposed antenna model is shown in fig. 1. The simulated and measured antenna return loss is shown in fig. 2 along with the simulated axial ratio. The 3dB axial ratio bandwidth is around 2%. The simulated radiation pattern is shown in fig. 3. The maximum gain of the antenna is 1.2 dBi.

REFERENCES

1. J.-W. Wu, J.-Y. Ke, C.F. Jou, and C.-J. Wang, "Microstrip-fed broadband circularly polarized monopole antenna," *IET Microw. Antennas Propag.*, vol.4, iss. 4, 2012, pp. 518-525.
2. S. A. Rezaeieh, "Dual band dual sense circularly polarized monopole antenna for GPS and WLAN applications," *Electronics Letters*, vol. 47, no. 22, 2011.
3. A. Ghobadi, and M. Dehmollaian, "A printed circularly polarized Y-shaped monopole antenna", *IEEE Antennas Wireless Propag. Lett.*, vol. 11, 2012, pp. 22-25.

Electroactive and magnetoactive materials

Structure and nonlinear properties of PZT ferroelectric multilayer heterostructures

K. Vorotilov[1,2], A. Sigov[1], D. Seregin[1,2], and O. Zhigalina[1]
[1]Moscow State Technical University of Radioengineering, Electronics and Automation (MIREA), Russia
[2]JSC Technological Center, Russia
vorotilov@mirea.ru

Abstract-An effect of crystallization temperature on the microstructure and electrical properties of PZT films prepared by chemical solution deposition on platinized silicon substrates is studied. The films are annealed at temperatures from 550 to 900°C. Structure of the films is studied by TEM and XRD, electrical properties are characterized by capacitance-voltage and current-voltage techniques.

Thin lead zirconate titanate (PZT) films and heterostructures are prominent materials for ferroelectric random access memory (FRAM), MEMS and other integrated ferroelectric devices, see e.g [1, 2].

Chemical solution deposition (including sol-gel techniques) is widely used for formation of thin films of multicomponent oxides due to good stoichiometric control and a relatively low temperature of oxide phase formation, see e.g. [3, 4]. The sol-gel method involves the initial deposition of amorphous layer and its subsequent crystallization during heat treatment. High diffusion rate of individual components of the film and metallization layers during high temperature annealing leads to formation of undesirable phases in multilayer heterostructure, see e.g. [5]. In this regard, the main strategy of annealing procedure during the formation of ferroelectric film is to achieve good crystalline structure and electrical properties at a minimum temperature of the heat treatment.

In this work we have tried to establish main regular trends in formation of crystalline structure during crystallization of thin sol-gel ferroelectric films and its effect on electrical properties of the films. For this purpose we studied microstructural and electrical properties of $PbZr_{0.48}Ti_{0.52}O_3/Pt/TiO_2/SiO_2/Si$ multilayer heterostructures prepared at annealing temperatures in the rather wide range (from 550 to 900 °C). Perovskite (Pe) grain nucleation in PZT films occurs at about 550 °C: rounded (111) grains grows on platinum surface with the same (111) orientation in this case. The height of Pe grains comprises a half of the film thickness. Disordered Pe grains (on the order of smaller size) and pyrochlore (Py) grains (2 ...15 nm) are formed in the bulk of the film as well. At annealing temperature 600 °C the Pe grains grows through the whole film thickness, the amount of Py phase is significantly reduced and practically disappears when the annealing temperature rises up to 700 °C. At the same time an amount of (100) oriented Pe grains increases and dominates over (111) oriented ones after annealing at 900 °C. The reason is activation of diffusion processes in the layers of heterostructure that leads in particular to formation of TiO_2 inclusions on the Pt surface. Dielectric hysteresis, permittivity, capacitance-voltage and current voltage dependences are studied to establish correlation between crystalline structure and main electrical phenomena in the films. Different components of crystalline structure have different effect on polarization switching, permitivitty and charge transport phenomena. For example, the maximum value of remanent polarization is observed after annealing at 600 °C, at the same time permittivity of the films increases up to annealing temperature of 750 °C.

Table. Structure of the sol-gel PZT films prepared at annealing temperature from 550 to 900 ° C

T,° C	Phase composition	Morphology and grain size		Texture	Composition profile
		Pe	Py		
550	Pe+Py	Round shape grains growing from Pt interface with average size of 90 nm. Small grains of 10 – 20 nm.	2 - 15 nm	Pt (111); Pe (111) + Pe (100)	Homogeneous
600	Pe+Py	Column grains, average size of 100 nm.	2 - 15 nm	Pt (111); Pe (111) + Pe (100)	Homogeneous
650	Pe+Py	Column grains, average size of 120 nm.	3 - 10 nm (low)	Pt (111); Pe (111) + Pe (100)	Pb and Ti increase with the distance from the surface in some areas
700	Pe	Column grains, average size of 135 nm.	No	Pt (111); Pe (111) + Pe (100) (100) enhancement	Pb and Ti increase with the distance from the film surface
750	Pe	Column grains, average size of 140 nm.	No	Pt (111); Pe (100) + Pe (111) (100) enhancement	Pb and Ti increase with the distance from the surface. Diffusion of Si into Pt and PZT.
900	Pe	Column grains, average size of 150 - 160 nm. Partial recrystallization, the disappearance of columnar grains in some areas.	No	Pt (111) + Pt (220). Pe (100) + Pe (111) (100) enhancement	Pb and Ti increase with the distance from the surface. High content of Si, Pb and Ti in Pt.

Acknowledgements, This work is partially supported by RFBR grant N 12-02-01363-a.

REFERENCES

1. Kawashima, S.and Cross, J.S., *FeRAM* , in *Embedded Memories for Nano-Scale VLSIs*, K. Zhang, ed., Springer Science+Business Media Inc, NY, 2009, 279–328.
2. Vorotilov, K.A., Muchortov, V.M., and Sigov A.S., *Integrated ferroelectric devices*, Energoatomizdat, Moscow, 2011.
3. Brinker, C.J., and Scherer, G.W., *Sol-gel science: the physics and chemistry of sol-gel processing*, Academic Press, N.Y, 1990.
4. Vorotilov, K.A., Yanovskaya, M.I., Turevskaya, E.P., and Sigov, A.S., Sol-gel derived ferroelectric thin films: avenues for control of microstructural and electric properties, *J. Sol-Gel Science and Technology*, Vol. 16, 109-118, 1999.
5. Zhigalina, O.M., Burmistrova, P.V., Vasiliev, A.L., Roddatis, V.V., Sigov, A.S., and Vorotilov, K.A., Microstructure of PZT capacitor structures, *Ferroelectrics*. Vol. 286, 311-320, 2003).

Mechanisms of charge transport in thin ferroelectric films

A. Sigov[1], Yu. Podgorny[1], K. Vorotilov[1,2], D. Seregin[1,2]
[1]Moscow State Technical University of Radioengineering, Electronics and Automation (MIREA), Russia
[2]JSC Technological Center, Russia
rector@mirea.ru

Abstract-An effect of crystallization temperature on the microstructure and electrical properties of PZT films prepared by chemical solution deposition on platinized silicon substrates is studied. The films are annealed at temperatures from 550 to 900°C. Structure of the films is studied by TEM and XRD, electrical properties are characterized by capacitance-voltage and current-voltage techniques.

Ferroelectrics are used in the capacitor structures of memory devices; therefore, leakage currents and electrical breakdown represent potential problems, which should be solved to provide the required operating characteristics. The study of the current–voltage (I–V) characteristics permits to obtain information on charge transport mechanisms in ferroelectric lead zirconate titanate (PZT) films and interfaces with electrodes.

The possible conduction mechanisms in ferroelectric films (dielectrics) are the Schottky and Poole–Frenkel emissions, the Fowler–Nordheim tunneling, the ohmic, space–charge–limited, hopping conductivity and conductivity on the grain boundaries [1–4].

The objective of this research is to study the conduction mechanisms in the PZT ferroelectric thin films prepared by the sol–gel method on silicon substrates with platinum bottom electrode for the different exposure times and strengths of electric fields. Long–term (tens of minutes) depolarization processes in the metal–ferroelectric–metal (MFM) structure are studied as well.

The samples were prepared by the sol-gel method. Preparation of film-forming solutions of $Pb_{(1+x)}(Zr_yTi_{1-y})O_3$) is performed by dissolving estimated amounts of the components in 2-methoxyethanol with $x = 0.15$ and $y = 0.48$. Lead acetate $Pb(CH_3COO)_2$ is used as Pb - containing component. Zr is introduced as solution of crystalline zirconium isopropoxide monosolvate $Zr(O^iPr)_4 \cdot HO^iPr$ in 2-methoxyethanol. Ti is introduced as titanium tetraisopropoxide $Ti(O^iPr)_4$. Film-forming solution is deposited by layer-by-layer procedure (5 layers with intermediate drying at 180 ºC and pyrolysis at 400 ºC). The substrates are 200 mm silicon wafers with the structure Pt (150 nm) - TiO_2 (10 nm) - SiO_2 (300 nm) - Si. After deposition the samples are subjected to annealing (crystallization) at the temperatures of 550 - 700 °C during 20 min. The final thickness of the prepared PZT films is approximately 150 nm.

Four specific regions are determined in I–V dependencies:

1) The region of very low fields (< 10 kV/cm) is characterized by the fact that the current having some finite value in the absence of the external electric field, first decreases to zero, and only after that increases with further increase of the external bias. This part of the I-V dependence may be represented as the sum of two components directed to meet each other, namely, the current due to external voltage and the depolarization current.

2) In the low fields region (from 10 to 70-90 kV/cm) I-V demonstrates a close-to-linear dependence. Leakage current in this region decreases with increasing delay time. The main leakage current components in this region are ohmic and displacement currents. Sometimes the space charge limited current which has quadratic voltage dependence is observed.

3) Next region (from 80 up to ~ 130 kV/cm) presents a transition between the low and high field regions. A relaxing jump current increase is observed, which is caused by the breakdown of the reverse bias Schottky barrier.

4) The next region is the high field one (≥ 110-130 kV/cm), where the current has more pronounced dependence on the electric field. In this region leakage current increases with the rise of the delay time in contrast to the low field region. Approximation of experimental data in the high field region gives the best results for the Pool-Frenkel model.

The experimental study of long-term (tens of minutes) depolarization process of sol-gel PZT thin films is performed. Short-circuit I-t dependences have a decaying exponential form and can be approximated by the sum of exponents with different relaxation times. Typically two exponents approximation gives appropriate results. Analysis of the experimental data leads to a conclusion that two different relaxation mechanisms exist. One of them has 5 - 6 times shorter relaxation times and 2 - 3 times smaller depolarization values than the second one.

Comparison of sol-gel films prepared at different crystallization temperatures shows that both absolute and relative values of the depolarization increase with the increase of annealing temperature as a result of film-substrate interface distortion.

Acknowledgements, This work is partially supported by RFBR grant N 12-02-01363-a.

REFERENCES

1. Sze, S., and Kwok, K.Ng., *Physics of Semiconductor Devices*, John Wiley & Sons, Inc., Hoboken, New Jersey, 2007.
2. Chen, H.–M., Tsaur, S.–W., and Lee, J.Y.–M., Leakage Current Characteristics of Lead–Zirconate–Titanate Thin Film Capacitors for Memory Device Applications, *Jpn. J. Appl. Phys*. Vol. 37, 4056–4060, 1998.
3. Dawber, M., Rabe, K.M., and Scott, J.F., Physics of thin–film ferroelectric oxides, *Rev. Mod. Phys*. Vol. 77, 1083–1130, 2005.
4. Waser, R., and Klee, M., Theory of conduction and breakdown in perovskite thin films, *Integated Ferroelectrics,* Vol. 2, 23–40, 1992.

Active materials and Structures, by L. Daniel & Y. Bernard

An Alternative Technique for Analyzing Frequency Selective Surfaces

M. W. B. Silva[1], L. C. Kretly[1], and A. L. P. S. Campos[2]
[1]University of Campinas, Brazil
[2]Federal University of Rio Grande do Norte, Brazil
mauweber@dmo.fee.unicamp.br, kretly@dmo.fee.unicamp.br, and antonio.luiz@pq.cnpq.br

Abstract-A simple and representative technique for analyzing Frequency Selective Surfaces (FSSs), which can be applied to periodic array of arbitrary structures for normal and oblique incidence, is described. Since the structure is periodic, was applied Floquet theorem to reduce analysis. The method, valid up to the frequency where high propagating Floquet mode occurs, is based on a circuital approach and takes into account the response of the FSS elements which can be represented for either series or parallel LC circuits.

Frequency selective surfaces (FSSs) are periodic arrangements comprised of metallic patch or aperture elements, which could exhibit total reflection or transmission. This kind of the structure finds numerous applications in microwave/millimeter wave and optical wave regime of the electromagnetic spectrum, such as radomes, electromagnetic shielding, absorbers and antennas [1].

For analyzing the electromagnetic behavior of frequency selective surfaces, several classical numerical techniques have been used. Among them, the Finite Difference Time Domain technique (FDTD), the Finite Element Method (FEM), and the Integral Equation Method (IEM) are the most popular [2,3]. The FDTD method and the FEM are enables the analysis of any type element, but typically are quite slow and requires a great computational effort. The IEM is very efficient if used with entire domain basis functions, however, is usually limited to a few shapes [4,5]. This work investigates a technique for analyzing frequency selective surfaces through a circuital approach. The structure is analyzed by a transmission line model and accounts the parallel connection between real structure and a lumped-LC-network. The proposed model approximates the response of FSS while computing the inductance and capacitance values. Therefore, it is possible to compute the answer to any proposed structures with different parameters without large computational time spent in full-wave simulations.

The structure to be considered in this analysis is the patch array. In Fig. 1 the comparison between FSS patch impedance obtained by employing the MoM code and lumped model is shown. For the analyzed FSS geometry, for normal incidence and in the freestanding configuration the optimal values of the lumped components were L = 0.6701 nH, C = 44.45 fF. Thus, it is possible to compute the L and C parameters representing a given FSS element and compare the results.

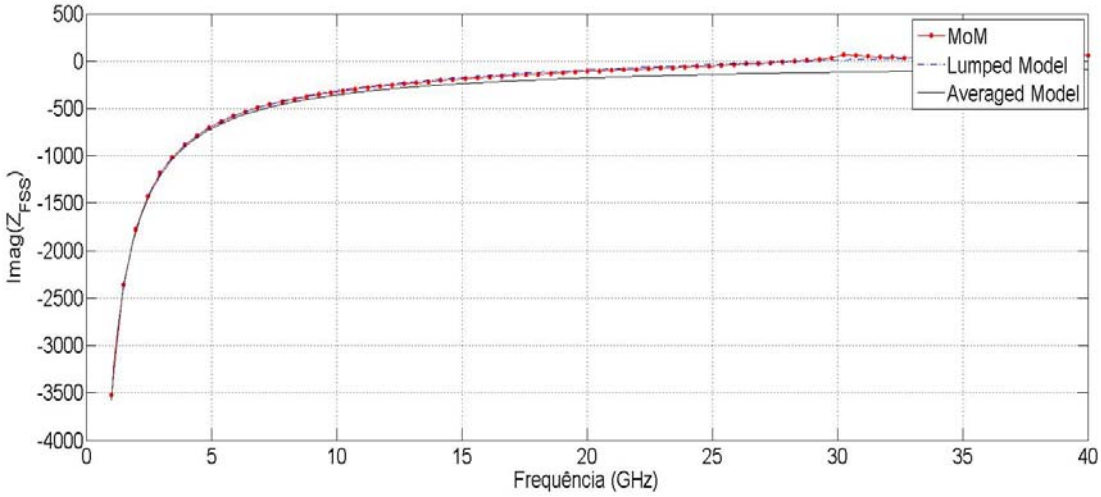

Figure 1. Impedance of a freestanding patch shaped FSS.

REFERENCES

1. Singh, D., A. Kumar, S. Meena, and V. Agrawal, "Analysis of frequency selective surfaces for radar absorbing materials," *Progress In Electromagnetics Research B*, Vol. 38, 297–314, 2012.
2. Harms, P., Mittra, R., and Ko, W., "Implementation of the periodic boundary condition in the finite-difference time-domain algorithm for FSS structures," *IEEE Transactions on Antennas and Propagation*, Vol. 34, No 9, 1317-1324, 1994.
3. T. F. Eibert, J. L. Volakis, D. R. Wilton, D. R. Jackson, "Hybrid FE/BI modeling of 3—D doubly periodic structures utilizing triangular prismatic elements and an MPIE formulation accelerated by the Ewald transformation," *IEEE Trans. Antennas Propagat.*, Vol. 47, pp. 843—850, 1999.
4. R. Mittra, C. H. Chan, and T. Cwik, "Techniques for Analyzing Frequency Selective Surfaces—A Review," *Proc. of the IEEE*, Vol. 76, pp. 1593—1615, 1988.
5. Bozzi, M., and Perregrini, L., "Frequency selective surfaces in the gigahertz and terahertz region: analysis and experimental results," *SPIE Proceedings*, Vol. 4111, Terahertz Electronics and Photonics II, No 41, 2000.

Printed MiMO Antenna implementations and challenges, by M. S. Sharaw

ON ELECTRODYNAMICS OF LIQUID WATER

A. A. Volkov[1*], **V. G. Artemov**[1], **and A. V. Pronin**[1,2]

[1] A. M. Prokhorov General Physics Institute, RAS, 119991 Moscow, Russia

[2] Dresden High Magnetic Field Laboratory, HZ Dresden-Rossendorf, 01314 Dresden, Germany

[*]corresponding author: aavol@bk.ru

Abstract

The dielectric spectrum of liquid water, $10^4 - 10^{11}$ Hz, is interpreted in terms of diffusion of short-living charges generated by self-ionization of H_2O molecules. This approach explains the Debye relaxation and the dc conductivity as two manifestations of the single microscopic mechanism. The high permittivity of water results from flickering dipoles of separated charges.

Water is a good insulator with a high static permittivity, $\varepsilon \approx 80$ at room temperature [1-3]. Potentiometric measurements reveal an appreciable proton conductivity, $\sigma_{dc} = 5.5\times10^{-8}$ Ω^{-1}cm^{-1} at room temperature [4]. This value is associated with the pH index, which is a key indicator of activity of protons in chemical reactions [5]. Normally, pH = 7; this water is regarded as neutral with the proton concentration $N_0 = 10^{-7}$ mole/liter. It is believed that under normal conditions, a given H_2O molecule will dissociate within 10^5 seconds (11 hours) [6].

The origin of the high static dielectric constant of water is commonly explained by the orientational motion of the molecular dipoles, which is referenced as the Debye relaxation [1-3]. The relaxation is particularly evident in the frequency spectrum of dielectric permittivity, $\varepsilon^*(\omega) = \varepsilon'(\omega) + i\varepsilon''(\omega)$, as a strong anomaly near a characteristic frequency (appox. 20 GHz at room temperature). The Debye relaxation is surprisingly well described by a simple relaxation formula:

$$\varepsilon^*(\omega) = \varepsilon_\infty + \frac{\varepsilon(0) - \varepsilon_\infty}{1 - i\omega\tau_D} \quad . \tag{1}$$

Here τ_D is the temperature-dependent relaxation time and $\Delta\varepsilon_D = \varepsilon(0) - \varepsilon_\infty$ is the contribution of the dielectric relaxation to the static dielectric constant.

For a long time, the Debye's idea about the orientational motion of water molecules has been exploited as the main microscopic mechanism responsible for the static permittivity. Basically, since its introduction, the model has been acknowledged as oversimplified. Therefore, it is being permanently modified. The present-day models involve dynamics of protons and large molecular clusters [7, 8]. Important is that in all these models, geometry of the water molecule is a substantial input parameter.

In our report, we propose an interpretation of the dielectric spectrum of water alternative to the Debye's approach. Instead of orientational motion of the molecular dipoles, as a basic factor in formation of the dielectric spectrum, we consider exclusively the diffusive motion of protons. Being expressed in terms of conductivity, $\sigma(\omega)$, the Debye relaxation [Eqs. (1)] looks like:

$$\sigma(\omega) = \omega^2\tau_D\varepsilon_0\frac{\Delta\varepsilon_D}{1+\omega^2\tau_D^2}. \tag{2}$$

Above a characteristic knee at $1/2\pi\tau_D$, $\sigma(\omega)$ is frequency-independent.

In accordance with the modern concept, protons, H^+, and hydroxyl ions, OH^-, are permanently generated and recombined in the volume of water due to the self-ionization of H_2O molecules [7-11]. Since free protons in water are not observed, they are considered to localize after their birth (on femtosecond time scale) on the neighboring neutral H_2O molecules. The excess proton converts the H_2O molecule into a charged complex H_3O^+ with a positive charge q^+, and leaves a "hole", OH^-, with a negative twin charge q^-. Subsequently, by a relay-race manner the q^+ and q^- charges wander diffusively over the H_2O molecules until they meet each other and recombine to produce a neutral H_2O.

Due to mutual Coulomb attraction, a charge usually recombines with its own twin partner. Sometimes, however, the "twins" fail to meet each other and recombine with "foreign" partners (from the first configuration sphere of the ionized molecules). Thus, there are two recombination processes for the charges: fast and slow. Accordingly, there are short- and long-living charge carriers in water. The electrodynamic response of the carriers reveals itself in the panoramic spectrum of conductivity.

By analogy with materials with high ionic conductivity (the superionics) [12], we have developed a model of hopping proton diffusion in water. This model comprehensively fits the experimental dielectric response of water in a broad frequency range (10^4 - 10^{13} Hz). The parameters of water, found by use of this model, bring us to the conclusion that the electrodynamics of water is mainly determined by the ability of H_2O molecules to dissociate rather than to form geometric structures.

Acknowledgements

We are grateful to S. D. Zakharov and G. M. Zhidomirov for useful and stimulating discussions.

REFERENCES

1. Eisenberg D. S. and W. Kauffmann, *The structure and properties of water*, Oxford University Press, New York, 1969.
2. *Water. A Comprehensive Treatise*, ed. by F. Franks, Plenum, New York, Vol. 1-7, 1972-82.
3. von Hippel A., “The Dielectric Relaxation Spectra of Water, Ice, and Aqueous Solutions and their Interpret at ion” *Transactions on Electrical Insulation*, Vol. 23, No. 5, 801, 1988
4. Light T. S., S. Licht, A. C. Bevilacqua, and K. R. Morash, “The Fundamental Conductivity and Resistivity of Water”, *Electrochemical and Solid-State Letters* 8(1), E16-E19 (2005)
5. Bockris J. O'M. and A. K. N. Reddy, *Modern Electrochemistry*, Kluwer Acad. Publishers, New York, 1998.
6. Geissler P. L., C. Dellago, D. Chandler, J. Hutter, and M. Parrinello, “Autoionization in Liquid Water”, *Science*, Vol. 291, 2121, 2001.
7. Agmon N., “Tetrahedral Displacement: The Molecular Mechanism behind the Debye Relaxation in Water”, *J. Phys. Chem.*, Vol. 100, 1072, 1996.
8. Walbran S.and A. A. Kornyshev, “Proton transport in polarizable water”, *J. Chem. Phys.*, Vol. 114, 10039, 2001.
9. Bakker H. J. and H.-K. Nienhuyst, “Delocalization of Protons in Liquid Water”, *Science*, Vol. 297, 587, 2002.
10. Agmon N., “Mechanism of hydroxide mobility”, *Chem. Phys. Lett.*, Vol. 319, 247, 2000.
11. Kornyshev A. A., A. M. Kuznetsov, E. Spohr, J. Ulstrup, “Kinetics of Proton Transport in Water”, *J. Phys. Chem. B*, Vol. 107, 3351, 2003.
12. *Physics of Superionic Conductors*, edited by M. B. Salomon, Springer, Berlin, 1979.

Isolation Enhancement Techniques Applied to a Dual-Band Printed MIMO Antenna System

Mohammad S. Sharawi
Electrical Engineering Department
King Fahd University of Petroleum and Minerals (KFUPM)
Dhahran, Saudi Arabia 31261
Email: msharawi@kfupm.edu.sa

***Abstract*—This paper represents a comparison between three isolation enhancement techniques for a printed dual-band multiple-input-multiple-output (MIMO) antenna system. The isolation enhancement techniques include a defected ground structure (DGS), a metamaterial (MTM) and a neutralization line (NL) based isolation structures. These structures were designed and optimized for a dual band printed MIMO antenna system. This work shows that certain types of isolation structures may not be able to enhance isolation of a specific antenna structure due to its radiation mechanism. The DGS and the MTM based isolation methods were able to enhance the isolation at both bands while the NL was only able to enhance it at the higher band of operation. Simulated and measured parameters are compared and discussed.**

I. Introduction

The shift to multiple antenna systems in 4G wireless systems is posing serious challenges in the design of efficient antenna systems. These systems will operate at low frequencies in the sub-GHz range. The antenna system usually consists of multiple resonators closely packed in a compact space for mobile device applications. Isolation improvement for closely packed antennas operating at low frequencies is a challenging task as the wavelength is very large and the spacing between the radiators is very small. The dimensions of the isolation enhancement structures are also a function of the wavelength. So larger isolation structures are required for lower frequencies, which will hit the area constraint that is very strict for hand-held devices. Multi-band operation of antennas further complicates the design process.

Several isolation enhancement techniques were studied in literature for printed multi-antenna systems. This paper focuses on three of them. These are, a defected ground structure (DGS) [1]-[2], a metamaterial based structure (MTM) [3]-[4] and a neutralization line(NL) [5]-[6] based structure. This paper compares the effect of these isolation methods when applied to a dual-band 4-shaped MIMO antenna system that appeared in [7]. This 4-shaped MIMO antenna structure operate at 800MHz and 2.6GHz.

The 4-shaped MIMO antenna structure suffers from low isolation between its radiating elements at both of its operating bands. Isolation structures based on DGS and MTM were designed and their performance was experimentally verified. On the other hand the performance of NL based isolation technique was evaluated based simulation results. A comparison of all these techniques is also provided in this paper in terms of resonance, isolation, gain and radiation efficiency.

II. Results and Discussions

The original dual-band dual-element MIMO antenna system is shown in Figure 1(a). It will be denoted as the reference model. Its dimensions are (in mm):W=50,L=100, Wt=2.2, H=2.5493, L1=40.75, L2=27, Ys=5.5, Xa2=1.6716, Lf=15.8, Xs=0.6716, Xf=2.6716, Wf=2.5, Yf=15.5, W1=10,Y=46, W2=17, Ws=1. The results for this MIMO antenna structure are taken as the reference since it does not have any isolation mechanism. Figure 1(b) shows the top layer of the NL geometry for isolation improvement. The antenna structure is the same as in Figure 1(a) except for an additional line connecting the two antenna elements on the top layer. Its bottom layer is similar to the reference model. The additional parameters for the NL structure are (in mm): Wnl=0.2, Hax=0,Hnl=8, Lnl=37.86. The additional line is placed at a location according to the criteria set by [5] that the NL should be placed at a point where the maximum current at the desired frequency occurs. The length of the NL should be such that it has an opposite current polarity (direction) at its ends such that the current of one antenna can cancel the current on the other.

The DGS that is inserted between the two antenna elements and etched out of the GND plane is shown in Figure 1(c). The dimensions of the structure are (in mm): L1=8, L2=16, L3=7, UEW=6.77, UEL=6.77, W1=7, W2=3, Wtrace=0.2, Gap=0.127. The dimensions of the CLL arrays on the top and bottom layers of the MTM based model are shown in Figure 1(d) (mm): L1=64.127, UEL1=8.927, UEW1=9, Gap1=0.127, Wtrace1=0.25, Xdist1=0.2, Ydist1=0.273, L2=35.8, UEL2=5.8 , UEW2=5.727 , Gap2=0.36, Wteace2=0.2, Xdist2=0.127, Ydist2=0.2.

Figure 2 shows the reflection coefficient comparison for the low band for the original antenna without any isolation enhancement mechanism and the three methods implemented. The graph shows that the central resonance frequency for the reference antenna and the one with a NL are almost the same while it is shifted for the DGS and MTM. This is because both DGS and MTM change the effective material properties (μ and/or ϵ). This change in material parameters affects the resonance of the system. The difference between the curves of

This work was supported by DSR at KFUPM through project No. RG12-19.

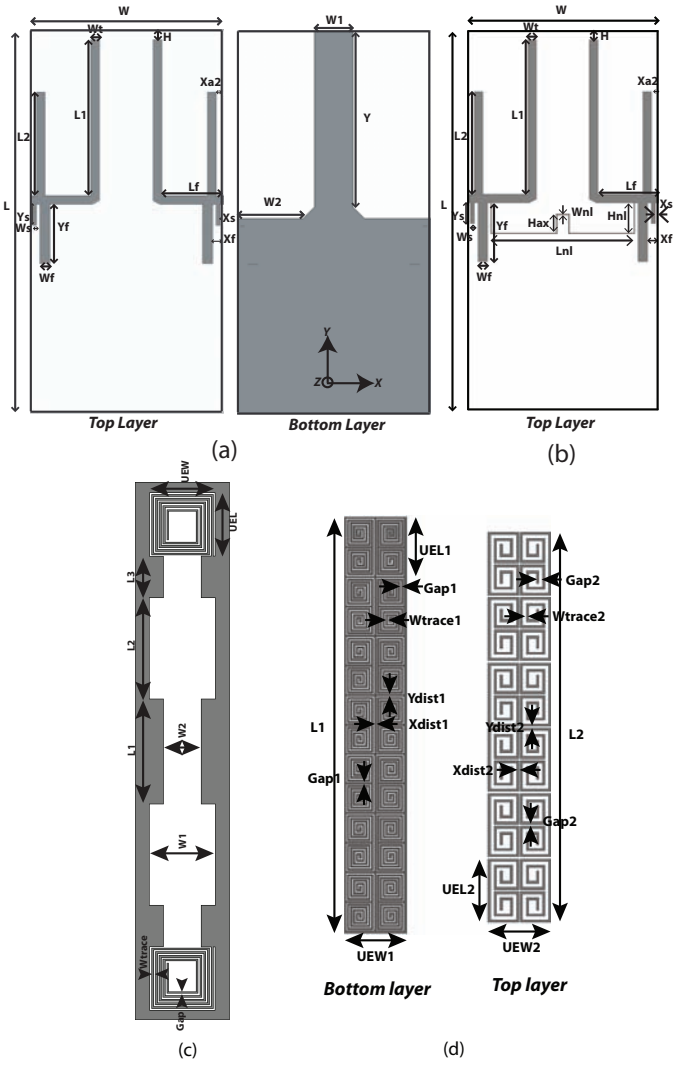

Fig. 1. Geometry of the 2×1 4-shaped MIMO antenna system without any isolation (a), with NL for second model (b), the DGS at bottom layer for third model (c) and the CLL arrays on top and bottom layers for fourth model (d).

the reference antenna and the NL model is due to the change in their input impedances.

TABLE I
ANTENNA PARAMETERS COMPARISON (SIMULATIONS-SIM. AND MEASUREMENTS-EXP.)

Antenna	Low band -6dB Bandwidth		High band -6dB Bandwidth		Low-band Isolation(min)		High-band Isolation(min)		High-band Gain		Low-band Gain		η_{low}	η_{high}
	Sim (MHz)	Exp (MHz)	Sim (MHz)	Exp (MHz)	Sim (dB)	Exp (dB)	Sim (dBi)	Exp (dBi)	Sim (dB)	Exp (dB)	Sim (dB)	Exp (dB)	Sim (%)	Sim (%)
Reference	29	25	190	120	6	9.6	7.1	7.1	4.16	2.53	-1.6	-4	37-28	74-64
DGS	20	20	510	540	16	17.48	9	8.5	5.67	1.86	1.39	-0.23	43-38	68-65
MTM	20	25	580	640	13.5	18	7	11	2.1	6.7	-1.12	-2.	32-25	70-40
NL	34	-	130	-	4.45	-	9	-	6.34	-	-4.6	-	37-25	68-61

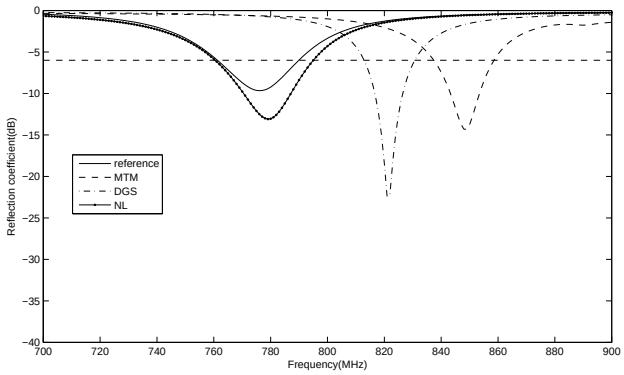

Fig. 2. Low band reflection coefficient for 2×1 antenna system.

Table I summarizes the results of the 4 models. The measurements from three prototypes; the reference model as well as the DGS and MTM are presented and compared. The results will be discussed in detail in the complete paper due to size limits of the summary. More curves and results will be presented in the complete paper.

REFERENCES

[1] H. T . Chou, H. C. Cheng, H. T. Hsu, and L. R. Kuo, "Investigations of isolation improvement techniques for Multiple Input Multiple Output (MIMO) wlan portable terminal applications," *Progress In Electromagnetics Research*, vol. 85, pp. 349-366, 2008.

[2] F. Zhu, J. Xu, and Q. Xu, "Reduction of mutual coupling between closely-packed antenna elements using defected ground structure," *Electronics Letters*,vol. 45, no. 12, pp. 601-602, 2009.

[3] C. Hsu, K. Lin, H. Su, H. Lin, and C. Wu, "Design of MIMO antennas with strong isolation for portable applications," *IEEE Antennas and Propagation Society International Symposium*, 2009, pp. 1-4.

[4] Y. Lee, H. Chung, J. Ha , and L. Choi, "Design of a MIMO antenna with improved isolation using meta-material," *International Workshop on Antenna Technology* (iWAT), 2011, pp. 231-234.

[5] A. Diallo, C. Luxey, P. L. Thuc, R. Staraj and G. Kossiavas, "Study and Reduction of the Mutual Coupling Between Two Mobile Phone PIFAs Operating in the DCS1800 and UMTS Bands," *IEEE Transactions on Antennas and Propagation*, vol. 54, no. 11, pp. 3063-3074, 2006.

[6] S. Su, C. Lee, and F. Chang, "Printed MIMO-Antenna System Using Neutralization-Line Technique for Wireless USB-Dongle Applications," *IEEE Transactions on Antennas and Propagation*, vol. 60, no. 2, pp. 456-463, 2012.

[7] M. A. Jan, D. N. Aloi and M. S. Sharawi, "A 2x1 Compact Dual Band MIMO Antenna system for Wireless Handheld Terminals," *IEEE Radio and Wireless Symposium* (RWS 2012), Santa Clara, California, January 2012.

LS-SVM Hyper-Parameter Optimization Based on PSO Algorithm for Microwave Characterization

T. Hacib[1*], H. Acikgoz[2], Y. Le Bihan[3]

[1]Laboratoire LAMEL, Univ. Jijel, Algérie

[2]Engineering Faculty, Karatay University, Turkey

[3]Laboratoire LGEP, Supélec, UMR 8507 CNRS, Univ. Paris 06, Univ. Paris-Sud, France

[*]corresponding author: tarik.hacib@gmail.com

Abstract-This paper presents the use of the least-square support vector machines (LS-SVM) technique, combined with the finite element method (FEM), to evaluate the microwave properties of dielectric materials. The FEM is used to create the data set required to train the LS-SVM. Approach based on particle swarm optimization (PSO) algorithm was also implemented to tune the hyper-parameters of LS-SVM models. Numerical simulations demonstrate that the LS-SVM method can determine the permittivity of materials with a high accuracy.

1. INTRODUCTION

SVM are a recent powerful machine learning method. They are developed on the basis of statistical learning theory. The SVM adjustment is obtained using complicated quadratic programming methods, which are often time consuming and difficult to implement [1]. LS-SVM are reformulations of the standard SVM which lead to solve linear equations instead of a quadratic programming problem [2].

In this paper, we propose a new method for the evaluation of the microwave properties of dielectric materials (complex permittivity) from the measured admittance. The method is based on the FEM and a LS-SVM hyper-parameter optimization based on PSO algorithm scheme.

2. LS-SVM FOR FUNCTION ESTIMATION

LS-SVM model for function approximation led to the optimization problem defined as:

$$min\ \boldsymbol{J}(\boldsymbol{w},\boldsymbol{e}) = \frac{1}{2}\boldsymbol{w}^T\boldsymbol{w} + \gamma\frac{1}{2}\sum_{i=1}^{N}\boldsymbol{e}_i^2 \tag{1}$$

Subject to the equality constraints:

$$y_i = \boldsymbol{w}^T\varphi(x_i) + b + \boldsymbol{e}_i \qquad i = 1,...,N \tag{2}$$

where φ is a nonlinear function, b is a bias term and $\boldsymbol{w} \in R^n$ is the weight vector. The fitting error is denoted by $\boldsymbol{e}_i$. The hyper-parameter γ controls the trade-off between the smoothness of the function y and the accuracy of the fitting. This optimization problem leads to a solution,

$$y(\boldsymbol{x}) = \sum_{i=1}^{N}\alpha_i K(\boldsymbol{x},x_i) + b \tag{3}$$

where α_i, b are the solution to the system obtained after constructing the Lagrangian and $K(\boldsymbol{x},x_i) = \varphi^T(\boldsymbol{x})\,\varphi(x_i)$ is the so-called kernel function. The most usual kernel functions are polynomial, gaussian or sigmoid.

3. MEASUREMENT SETUP AND NUMERICAL METHOD

The characterization cell, called SuperMit, consists in a junction between a coaxial waveguide and a circular waveguide which is filled by the dielectric material. In order to study liquids, a coaxial window is inserted between

the two guides (Figure. 1). The whole device is connected to an impedance analyzer.

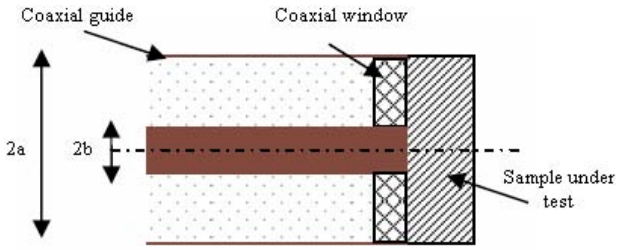

Figure. 1. SuperMit measuring cell

The electromagnetic problem is solved by using the FEM where the problem is expressed in terms of the electric field ***E***.

4. IMPLEMENTATION OF THE LS-SVM

Two single-output LS-SVM corresponding to the two estimated quantities ε' and ε'' are used. The inputs of a LS-SVM are the values of the complex admittance (real part *G*, imaginary part *B*) and frequency *f*.

The LS-SVMs were trained with 4500 examples. In this study, radial basis function (RBF) kernels are used,

$$K(\boldsymbol{x}, x_i) = exp\left(-\frac{\|\boldsymbol{x} - x_i\|}{\sigma^2}\right) \tag{4}$$

where $\sigma > 0$ is a constant defining the kernel width.

The predetermined parameters in LS-SVM algorithms with RBF kernel are γ and σ^2, which are less numerous than those in SVM. A PSO algorithm is used for tuning the LS-SVM parameters. PSO are heuristic techniques, which has a flexible and well-balanced mechanism to enhance local exploration abilities [3].

5. EXPERIMENTAL RESULTS

Measurements have been carried out by using an impedance analyzer Agilent 4291A on an ethanol sample whose dielectric characteristics are known. The measurement frequency band is from 1 MHz to 1.8 GHz. Hyper-parameters of LS-SVM obtained by PSO algorithm and root mean squared relative error (RMSRE) are given in Table 1. In this case, the obtained results on the test set are quite good then those obtained in [1].

Table 1. Parameters in LS-SVM with RBF kernel

Outputs	γ	σ^2	RMSRE (%)
ε'	$8.1113\ 10^{2}$	1.5380	$3.6055\ 10^{-1}$
ε''	$5.3367\ 10^{3}$	0.3921	$5.8539\ 10^{-2}$

CONCLUSION

The validity of the proposed LS-SVM based inversion method is being assessed by comparing the results obtained using the proposed method with those obtained from a multilayer perceptron NN and experiment.

REFERENCES

1. Hacib. T, Le Bihan. T, Acikgoz. H, Meyer. O, Pichon. L. “Microwave Characterization Using Least-Square Support Vector Machines,” *IEEE Transactions Magnetics*, Vol. 46, No. 8, 2811-2814, 2010.
2. Vapnik. V, *Statistical learning theory*, John Wiley and Sons, New York, 1998.
3. Parsonpoulos, K. E, Varhatis, M. N. “Recent approaches to global optimization problems through particle swarm optimization,” *Natural Computing*, Vol. 1, No. 2-3, 235-306, 2002.

A Compact Broadband MIMO Antenna for Mobile Terminals

X. X. Xia, Q. X. Chu*, and J. F. Li
School of Electronic and Information Engineering, South China University of Technology, Guangzhou, China.
* qxchu@scut.edu.cn

Abstract-A new broadband multiple-input multiple-output (MIMO) antenna with a good isolation and compact size is proposed. The proposed antenna consists of two G-shaped element in the upper layer and a protrude branch and T slot etched in ground which are used for reducing the mutual coupling. This planar antenna has a bandwidth of 100% with |S11| ≤ -10 dB from 2.26 to 6.78 GHz. The mutual coupling between the two antennas is below -22.5 dB in the whole band.

MULTIPLE-INPUT MULTIPLE-OUTPUT(MIMO)technology has been proposed for several years, which significantly improves the performance of wireless communication systems [1]. One important requirement for MIMO antenna systems is the need for good isolation between antenna elements. Various methods have been reported to improve isolation between the elements of a MIMO antenna. Parasitic elements are used to reduce mutual coupling [2], however it's sensitive to the position of parasitic elements. In addition, neutralization technique was proposed, which is adding a neutralization line between two antennas [3], [4]. All of the aforementioned techniques are only used in narrowband, and therefore not suitable for wideband application.

In this paper, a compact wideband planar diversity antenna for mobile terminals covering LTE 2300/2600, WLAN 2.4/5.2/5.8-GHz, and the lower UWB band (3.1-4.8 GHz) is proposed. It has a bandwidth of 100% with |S11| ≤ -10 dB from 2.26 to 6.78 GHz. The mutual coupling between the two antennas is below -22.5 dB in the whole band. The geometry of the proposed MIMO antenna system is show in Fig. 1(a). The design of the antenna is based on a FR-4 substrate with dimensions 55×50×0.8 mm^3 and relative permittivity 4.4. The MIMO antenna consists of two G-shaped symmetric face-to-face dual-branch monopoles printed on the upper part of the substrate. Each monopole occupies a surface of 17.5×13.5 mm^2. In order to increase the isolation between two monopoles, two inverted-L-shaped ground branches and a small T-shaped slot are etched in the ground.

In order to reach broadband, we devise a dual-branch monopole (branch 1 with length 40 mm and branch 2 with length 28 mm, which can produce a λ/2 resonate mode at 1.9 GHz, 2.87 GHz, respectively). when the two branches are integrated together, a wide operating band of 100% with |S11|≤ -10 dB extending from 2.26 to 6.78 GHz is produced. We can form a two antenna MIMO system by using two symmetric antenna elements without decoupling means. From Fig. 2(a), the isolation with the conventional ground plane is bad except at 4.6GHz which can be explained as the ground form a narrow filter that can trap the current at 4.6GHz. Aim to decrease the couple between the two antenna, we used two inverted L branches extend from the ground firstly. We can find in Fig.2 (a) that it can simply improve the isolation in lower band, but there is litter influence in higher band. In order to improve the isolation in the higher band, we additionally introduced a T-shape slot etched in the ground. As a result the isolation in the whole band especially higher band significantly improved (see in Fig. 2(b)).

The antenna was simulated using Ansoft simulation software HFSS v13. To verify the performance of the wideband MIMO antenna, a prototype was fabricated (see in Fig. 1(b, c)) and measured. The measure S-parameters are plotted in Fig. 2(b). The simulated radiation gain patterns of the decoupled active element at 2.5GHz are shown in Fig. 3.

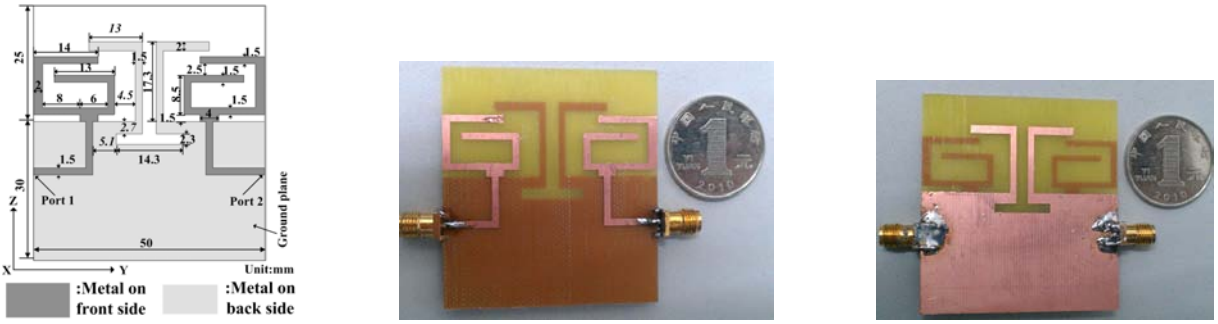

(a) (b) (c)

Fig1. (a) Detailed dimension of the proposed antenna (b) Front view of the prototype of the proposed antenna (c) Back view of the prototype of the proposed antenna

(a) (b)

Fig2. (a) Simulated S-parameters of the conventional ground plane and ground plane with L branch only (b) Simulated and measured S-parameters of the proposed MIMO antenna

(a) (b)

Fig3. Simulated radiation gain patterns at 2.5 GHz (a) x-y plane (b)y-z plane

REFERENCES

1. Foschini, Jr. G. J. and M. J. Gans, "On limits of wireless communication in a fading environment when using multiple antennas," Wireless Personal Commun., vol. 6, pp. 311-335, 1998.
2. Li, Z., Z. Du, M. Takahashi, K. Saito, and K. Ito, "Reducing Mutual Coupling of MIMO Antennas With Parasitic Elements for Mobile Terminals," IEEE Trans. Antennas Propag., vol. 60, no. 2, pp. 473-481, Feb. 2012
3. Diallo, A. C., Luxey, P. L. Thuc, T. Staraj, and G. Kossiavas, " study and reduction of the mutual coupling between two mobile phone PIFAs operating in the DCS1800 and UMTS bands," IEEE Trans. Antennas Propag., vol. 54, no. 11, pp. 3063-3073, Nov. 2006
4. Li, J. F. and Q. X. Chu， "Compact Conventional Phone Antenna Integrated with Wideband Multiple-Input-Multiple-Output Antenna" Microw. Opt. Technol. Lett., vol. 54, no. 8, pp.1958-1962, August. 2012